Numerical Simulation and modelling of substrate assimilation by microorganisms in a turbulent flow

Marion Linkes

To cite this version:

Marion Linkes. Numerical Simulation and modelling of substrate assimilation by microorganisms in a turbulent flow. Fluids mechanics [physics.class-ph]. Institut National Polytechnique de Toulouse - INPT, 2012. English. NNT : 2012INPT0149 . tel-04279754

HAL Id: tel-04279754
https://theses.hal.science/tel-04279754

Submitted on 10 Nov 2023

Université
de Toulouse

THÈSE

En vue de l'obtention du

DOCTORAT DE L'UNIVERSITÉ DE TOULOUSE

Délivré par :
Institut National Polytechnique de Toulouse (INP Toulouse)

Discipline ou sp®cialit® :
Dynamique des Fluides

Présentée et soutenue par :
Marion Linkes
Le 06 Décembre 2012

Titre :

Simulation numérique et modélisation de l'assimilation de substrat par des microorganismes dans un écoulement turbulent.

École doctorale :
Mécanique, Energétique, Génie Civil, et Procédés (MEGeP)

Unité de recherche :
IMFT - LISBP

Directeur(s) de Thèse :
Philippe Schmitz (Directeur)
Pascal Fede (Co-Directeur)

Rapporteurs :
Anne Tanière
Krist Gernaey

Autre(s) membre(s) du jury :
Jack Legrand (Président)
Marie-Isabelle Penet (Membre)
Eric Climent (Membre)
Jérôme Morchain (Membre)

Mais pourquoi ?
Et comment ça marche ?...

Je tiens tout d'abord à remercier chaleureusement mes encadrants, Jérôme Morchain, Pascal Fede et Philippe Schmitz, sans qui cette thèse n'aurait pas pu avoir lieu. Je les remercie de m'avoir fait confiance, de leur disponibilité et de leur patience également. Peut-être que nos réunions interminables me manquent déjà... Je souhaite remercier le Professeur Olivier Simonin de m'avoir un jour parlé de ces petites bêtes, et pour ses précieux conseils tout au long de ma thèse.

Je remercie tous les membres du jury d'avoir accepté de faire partie d'un des moments les plus importants de ma vie. Plus particulièrement, je remercie Anne Tanière et Krist Gernaey de s'être accrochés aux microorganismes en acceptant d'être rapporteurs de cette thèse, et pour les rapports riches qu'ils ont en fait. Merci au Professeur Jack Legrand d'avoir présidé ce jury. Un grand merci également à Marie-Isabelle Penet, qui m'a permis de me représenter ce que c'est qu'un bioréacteur quand on travaille tous les jours avec, et au Professeur Eric Climent pour ses questions, conseils et sa bonne humeur quotidienne. Je vous remercie pour les échanges qui ont eu lieu cette journée, tant du point de vue scientifique qu'humain.

J'ai effectué ma thèse au sein de l'Institut de Mécanique des Fluides de Toulouse, laboratoire bien vivant, où j'ai côtoyé un bon nombre de personnes qui m'ont beaucoup apporté. Je remercie tous les personnels du laboratoire : enseignants-chercheurs, techniques et administratifs, post-doctorants, doctorants, stagiaires. Un merci particulier à Muriel pour l'impression des manuscrits. Merci également à Florence pour la gestion administrative lors de la fin de thèse. Je remercie le service informatique d'avoir redémarré un nombre de fois incalculable cette chère Baker, mais également et surtout pour leur support et leur gentillesse. Merci au service COSINUS pour les scripts, debogages, trucs et astuces, et plus particulièrement, à Annaig et Hervé pour les pauses cafés !

Je remercie également l'ensemble de l'équipe enseignante du département hydraulique de l'ENSEEIHT, ainsi que de l'équipe pédagogique de la formation apprentissage de l'EMAC de m'avoir donné la chance de découvrir le métier d'enseignant durant ces trois ans. Un merci particulier à Gérald, Jean-Luc, Thomas, Véronique, Wladimir, Olivier Thual et Bénédicte. Et surtout Maryse, merci d'avoir été toujours là depuis 2006. Qu'est-ce qu'on ferait sans toi ?

Le groupe PSC, au sein duquel j'ai effectué ma thèse m'a également permis de rencontrer beaucoup de personnes. Merci aux permanents du groupe pour leurs conseils et à Olivier P. et Benoit de m'avoir laissé partager leur bureau. Merci aux "anciens" Nicolyx, Flo, Yannick, JF, Enrica, Zafer, Ali pour les supers moments partagés ensemble, pour la base de données à jour et votre soutien. Merci aux Djeuns, Marion, Niko, Aurélien, Guillaume, Daniel, Adrien pour votre bonne humeur, les pauses dans votre bureau, et à Blaise d'avoir instauré la coinche pendant les 6 derniers mois... la pause détente de la journée. Un merci particulier à MC et Romain, camarades d'année, et à qui je souhaite tout le meilleur pour la suite. Je remercie également mes nouveaux collègues qui ont connu la période de transition boulot et manuscrit puis boulot et présentation.

Je tiens à remercier tout particulièrement ma famille pour m'avoir soutenue et encouragée pendant ces trois années. Je remercie mes parents (all include) d'avoir été là (même si ça n'a pas été facile), de m'avoir supporté (au premier sens du terme), d'être venus le jour J et d'avoir été avec moi en ce jour particulier, un des jours les plus importants de ma vie. Merci à Josiane et Michel pour votre patience, et le réconfort que vous m'avez apporté. Enfin, je tiens à remercier mes amis, d'avoir été présents. Djé (et Cindy) pour tous les mails restés sans réponses et votre soutien, Marion, ma grande soeur, Audrey, ma petite soeur. J'espère que je ne t'ai pas dégouté de la physique... Crois-moi ça vaut le coup ! Marion L. pour ce qui nous lie et que je n'ai toujours pas réussi à définir et Anna, toujours là mais invisible à la fois.

Last but not least, je remercie Renaud. Je ne vais pas m'épancher sur le sujet au risque même qu'on finisse par m'en vouloir. Mais merci d'avoir été là, un soutien inébranlable malgré les difficultés rencontrées durant cette année. Merci pour le bricolage et les petits plats de cet été. BTW je crois me souvenir du poisson pané... Et ne t'inquiètes pas, ça va le faire ! xxx

Résumé & Abstract

Résumé

Une des problématiques majeures dans l'industrie des bioprocédés réside dans l'extrapolation des procédés biologiques à grande échelle. On observe généralement à l'échelle industrielle des écarts de rendement de croissance de la biomasse, ainsi que la formation de sous-produits comparativement à l'échelle du laboratoire. La formation de gradients de concentration à l'échelle des bioréacteurs est souvent évoquée. Dans ce travail, les interactions entre micromélange et assimilation du substrat sont abordées à l'échelle du microorganisme. Un modèle couplant transport et assimilation à l'échelle d'un microorganisme est proposé. L'existence de régimes physique et biologique, limitant l'assimilation du substrat est mise en lumière. Une approche basée sur le suivi Lagrangien de particules dans un champ de turbulence homogène isotrope est ensuite retenue. Les effets des hétérogénéités de concentration vues par les microorganismes, sont traduits à l'échelle de la population entière. Une loi analytique permettant de construire la distribution de flux reçus par les microorganismes à partir de la distribution de concentration en substrat dans le fluide, est proposée. Partant de cette distribution de concentrations vues, l'adjonction d'un modèle métabolique simplifié permet d'expliquer les baisses de vitesse spécifiques de croissance et la formation de sous-produits observées expérimentalement. Enfin, de premiers résultats sur le couplage inverse biologique sont présentés. L'effet des microorganismes sur le champ de concentration est caractérisé et une étude paramétrique sur les propriétés dynamiques et biologiques est réalisée.

Mots-clefs :assimilation de substrat, microorganismes, simulation numérique directe, turbulence homogène isotrope, couplage inverse biologique.

Abstract

The scale-up of biological process is a critical issue in the bioprocess industry. When passing from a laboratory to an industrial scale, the conversion yield of substrate into biomass is often overestimated and by-products are formed. Different existing works attempt to predict the effect of mixing on biomass growth and the emergence of substrate concentration gradients at the reactor scale are a first explanation of the degraded performances. In this work the interactions between micro-mixing and substrate assimilation are addressed at the microorganism scale. A coupled transport-assimilation model is proposed for an isolated microorganism. The emergence of physical and biological regimes limiting the substrate assimilation is enlightened. An approach based on the Lagrangian tracking of microorganisms in a homogeneous isotropic turbulent field is then chosen. The effects of local concentration heterogeneities seen by microorganisms are observed at the population scale. An analytical expression is proposed for the assimilated substrate flux distribution by the microorganisms, based on the substrate concentration distribution in the fluid. From these concentrations encountered by microorganisms, we coupled a simplified metabolic model that explains the decreased specific growth rate, and the by-products formation often observed in many experiments. Finally, first results on the biological two-way coupling are proposed. The effect of microorganisms on the substrate field is characterised and a parametric study on the dynamics as well as biological parameters is realised.

Keywords: substrate assimilation, microorganisms, Direct Numerical Simulation, Homogeneous Isotropic Turbulence, biological two-way coupling.

Contents

Nomenclature

Abreviations

DNS	Direct Numerical Simulation
DPS	Discrete Particle Simulation
LES	Large Eddy Simulation
PDF	Probability Density Function
RANS	Reynolds Averaged Navier-Stokes
SFM	Shape Function Method

Greek Symbols

μ_X	Specific growth rate	[h^{-1}]
Δ	Mesh size	[m]
η_B	Bachelor length-scale	[m]
η_C	Corrsin length scale	[m]
η_K	Kolmogorov length scale	[m]
$\hat{\Phi}(\mathbf{x},t)$	Filtered Eulerian mass flux	[$\mathrm{kg_S}\cdot\mathrm{s}^{-1}$]
κ	Wave number	[m^{-1}]
κ_{max}	Maximum wave number for fluid resolution	[m^{-1}]
Λ_f	Longitudinal integral length scale	[m]
λ_f	Taylor longitudinal length scale	[m]
Λ_g	Transversal integral length scale	[m]
λ_g	Taylor transversal length scale	[m]
Λ_S	Scalar integral length scale	[m]
λ_S	Scalar Taylor length scale	[m]
ν_f	Fluid kinematic viscosity	[$\mathrm{m}^2\cdot\mathrm{s}^{-1}$]
$\phi_p'^*$	Non-dimensionalised fluctuating part of the assimilated mass flux by one microorganism	[$\mathrm{kg_S}\cdot\mathrm{s}^{-1}$]

Φ_p^*	Non-dimensionalised substrate mass flux of one microorganism	$[\ \mathrm{kg_S \cdot s^{-1}}\ ]$
Φ_{int}	Interfacial mass flux	$[\ \mathrm{kg_S \cdot s^{-1}}\ ]$
Φ_{max}	Maximum mass flux	$[\ \mathrm{kg_S \cdot s^{-1}}\ ]$
Φ_p	Substrate mass flux assimilated by one microorganism	$[\ \mathrm{kg_S \cdot s^{-1}}\ ]$
ρ_f	Fluid density	$[\ \mathrm{kg \cdot m^{-3}}\ ]$
ρ_p	Particle density	$[\ \mathrm{kg \cdot m^{-3}}\ ]$
σ	Variance of the concentration signal	$[\ \mathrm{kg_S^2 \cdot m^{-6}}\ ]$
σ_X	Variance of the biomass concentration	$[\ \mathrm{kg_X^2 \cdot m^{-6}}\ ]$
τ_ε^s	Substrate dissipation time scale	$[\ \mathrm{s}\ ]$
τ_ε	Dissipation time scale	$[\ \mathrm{s}\ ]$
τ_B	Batchelor time scale	$[\ \mathrm{s}\ ]$
τ_C	Corrsin time scale	$[\ \mathrm{s}\ ]$
τ_D	Diffusion time	$[\ \mathrm{s}\ ]$
τ_K	Kolmogorov time scale	$[\ \mathrm{s}\ ]$
τ_M	Mixing characteristic time scale	$[\ \mathrm{s}\ ]$
τ_p	Particle relaxation time	$[\ \mathrm{s}\ ]$
τ_{R_S}	Reaction time scale based on the substrate consumption	$[\ \mathrm{s}\ ]$
τ_{R_X}	Reaction time scale based on the biomass growth	$[\ \mathrm{s}\ ]$
τ_R	Reaction characteristic time scale	$[\ \mathrm{s}\ ]$
ε_f	Fluid turbulent kinetic energy dissipation rate	$[\ \mathrm{m^2 \cdot s^{-3}}\ ]$
ε_s	Scalar dissipation rate	$[\ \mathrm{kg_S^2 \cdot m^{-6} \cdot s^{-1}}\ ]$
φ_{int}	Interfacial substrate gradient	$[\ \mathrm{kg_S \cdot m^{-4}}\ ]$
φ_{max}	Maximum interfacial substrate gradient	$[\ \mathrm{kg_S \cdot m^{-4}}\ ]$
ξ	Deviations	
ζ	Mean substrate concentration imposed gradient	$[\ \mathrm{kg \cdot m^{-4}}\ ]$

Non-dimensional numbers

Da	Damkhöler number
Re_p	Particle Reynolds number
Re_Λ	Reynolds number based on the integral length scale
Re_λ	Reynolds number based on the Taylor length scale
Sc	Schmidt number

St	Stokes number	

Roman Symbols

$\langle s'^2 \rangle$	Substrate concentration variance	$[\ \mathrm{kg_S^2 \cdot m^{-6}}\ ]$
$\mathbf{u}_f$	Fluid velocity vector	$[\ \mathrm{m \cdot s^{-1}}\ ]$
$\mathbf{u}_p$	Particle velocity vector	$[\ \mathrm{m \cdot s^{-1}}\ ]$
$\mathbf{x}_f$	Fluid position vector	
$\mathbf{x}_p$	Particle position vector	
$\mathcal{D}$	Molecular diffusivity	$[\ \mathrm{m^2 \cdot s^{-1}}\ ]$
$\mathcal{D}_{S,f}$	Molecular diffusivity of the substrate S in the fluid	$[\ \mathrm{m^2 \cdot s^{-1}}\ ]$
$\mathcal{N}$	Agitation velocity	
$\tilde{s}$	Substrate concentration deviation to the imposed gradient	$[\ \mathrm{kg_S \cdot m^{-3}}\ ]$
a_c	Microorganism surface	$[\ \mathrm{m^2}\ ]$
B	Batchelor constant	
C_i^S	Lagrangian constants for the substrate	
C_0	Lagrangian Kolmogorov constant	
C_{OC}	Obukhov-Corrsin constant	
D	Dilution rate	$[\ \mathrm{h^{-1}}\ ]$
$D_{\cdot}^L$	Second-order Lagrangian structure function	
D_c	Critical dilution rate	$[\ \mathrm{h^{-1}}\ ]$
d_A	Agitator diameter	$[\ \mathrm{m}\ ]$
d_p	Particle diameter	$[\ \mathrm{m}\ ]$
E	Kinetic energy spectral density	
F	Forcing random force	$[\ \mathrm{N}\ ]$
f	Longitudinal Eulerian spatial autocorrelation function	
f_i	Forcing term for the fluid dynamics	$[\ \mathrm{m \cdot s^{-2}}\ ]$
f_S	Forcing term for the substrate concentration field	$[\ \mathrm{kg_S \cdot m^{-3} \cdot s^{-2}}\ ]$
G	Substrate concentration fluctuations spectral density	
g	Transversal Eulerian spatial autocorrelation function	
K	Kolmogorov constant	
K^s	Scalar kurtosis	
K_S	Substrate affinity constant	$[\ \mathrm{kg_S \cdot m^{-3}}\ ]$

k_S	Microscopic substrate affinity constant	$[\ \mathrm{kg_S} \cdot \mathrm{m^{-3}}\ ]$
L	Length of the computational domain for the 1D configuration	$[\ \mathrm{m}\ ]$
L_{box}	Cubic box length for the HIT configuration	$[\ \mathrm{m}\ ]$
m_c	Mass of microorganisms	$[\ \mathrm{kg_X}\ ]$
N	Number of nodes of the mesh	
N_c	Circulation number	
N_p	Number of particles	
P	Metabolite P concentration	$[\ \mathrm{kg_P} \cdot \mathrm{m^{-3}}\ ]$
P_Φ	Distribution function of the mass flux	
p_f	Fluid pressure	$[\ \mathrm{Pa}\ ]$
P_M	Distribution function of the mass flux for Monod assimilation model	
P_{S1}	Distribution function of substrate concentration $S1$	
P_S	Distribution function of substrate concentration S	
q_f^2	Fluid kinetic energy	$[\ \mathrm{m^2} \cdot \mathrm{s^{-2}}\ ]$
$q_{s,f}^2$	Substrate concentration energy	$[\ \mathrm{kg_S^2} \cdot \mathrm{m^{-6}}\ ]$
q_P	Specific production rate for the metabolite	$[\ \mathrm{g_P} \cdot \mathrm{g_X^{-1}} \cdot \mathrm{h^{-1}}\ ]$
$q_{S,max}$	Maximum specific uptake rate for the substrate	$[\ \mathrm{g_S} \cdot \mathrm{g_X^{-1}} \cdot \mathrm{h^{-1}}\ ]$
q_S	Specific uptake rate for the substrate S	$[\ \mathrm{g_S} \cdot \mathrm{g_X^{-1}} \cdot \mathrm{h^{-1}}\ ]$
R	Microorganisms radius	$[\ \mathrm{m}\ ]$
r^E	Lagrangian to Eulerian dynamic time-scale ratio	
$R^E_{\cdot}(\tau)$	Eulerian temporal autocorrelation function	
$R^E_{\cdot}(r)$	Eulerian spatial autocorrelation function	
r_s^E	Lagrangian to Eulerian substrate time-scale ratio	
$R^L_{\cdot}(\tau)$	Lagrangian correlation function	
r_s^L	Lagrangian substrate to dynamic time-scale ratio	
r_s^L	Lagrangian time-scales ratio	
r_ε	Mechanical-to-scalar time scale ratio	
S	Substrate concentration	$[\ \mathrm{kg_S} \cdot \mathrm{m^{-3}}\ ]$
s'	Fluctuating substrate concentration	$[\ \mathrm{kg_S} \cdot \mathrm{m^{-3}}\ ]$
S_∞^{sat}, S^{sat}	Saturation far-field concentration	$[\ \mathrm{kg_S} \cdot \mathrm{m^{-3}}\ ]$
S^s	Scalar skewness	

S_0	Initial mean imposed substrate concentration	$[\ \mathrm{kg_S \cdot m^{-3}}\ ]$
S_1	Total substrate concentration corresponding to $S_0 + s'$	$[\ \mathrm{kg_S \cdot m^{-3}}\ ]$
S_∞	Far-field concentration	$[\ \mathrm{kg_S \cdot m^{-3}}\ ]$
s_g	Gradient contribution substrate concentration	$[\ \mathrm{kg_S \cdot m^{-3}}\ ]$
S_{int}	Interfacial concentration at the cell-liquid interface	$[\ \mathrm{kg_S \cdot m^{-3}}\ ]$
T	Period of the concentration signal	$[\ \mathrm{m}\ ]$
T^*	Period to diffusional time ratio	
T^E	Eulerian dynamic time scale	$[\ \mathrm{m}\ ]$
T_s^E	Eulerian time scale for the substrate	$[\ \mathrm{m}\ ]$
T^L	Lagrangian dynamic time scale	$[\ \mathrm{m}\ ]$
T_s^L	Lagrangian time scale for the substrate concentration	$[\ \mathrm{m}\ ]$
T_C	Circulation time	$[\ \mathrm{s}\ ]$
V_{box}	Volume of the computational domain	$[\ \mathrm{m^3}\ ]$
V_B	Working volume of the bioreactor	$[\ \mathrm{m^3}\ ]$
X	Microorganisms concentration	$[\ \mathrm{kg_X \cdot m^{-3}}\ ]$
Y_{XP}	Conversion yield of metabolite production	$[\ \mathrm{kg_X \cdot kg_P^{-1}}\ ]$
Y_{XS}	Conversion yield of substrate into biomass	$[\ \mathrm{kg_X \cdot kg_S^{-1}}\ ]$

Introduction

Les bioréacteurs, ou réacteurs biologiques sont des cuves agitées et aérées dans lesquelles la biomasse (des microorganismes) consomme des substrats (dont un sucre en général) et produit de nouveaux organismes et des produits d'intérêt. Ces réacteurs sont très répandus dans l'industrie agroalimentaire, chimique ou pharmaceutique. La recherche d'une productivité maximale conduit à la mise en œuvre de réacteurs de très grande taille (plusieurs dizaines de mètres cube) nécessitant une surveillance continue afin d'ajuster les paramètres de fonctionnement pour d'obtenir les performances souhaitées.

La mise au point du fonctionnement des bioréacteurs industriels repose sur une phase d'extrapolation depuis l'échelle du laboratoire jusqu'à l'échelle industrielle. La complexité des phénomènes biologiques à l'échelle cellulaire ainsi que notre capacité limitée à prédire les effets d'échelles résultants des interactions de la biomasse avec le milieu de culture sont autant d'obstacles à la définition de critères objectifs garantissant le maintien des performances lors du changement d'échelle. La montée en échelle d'un procédé biologique est donc toujours une démarche complexe mêlant empirisme, savoir-faire et incertitudes.

Parallèlement, la modélisation des bioréacteurs représente donc un enjeu majeur pour l'industrie, de même que l'identification de critères pertinents pour le suivi et l'analyse des cultures à grande échelle. De nombreuses approches expérimentales et numériques sont actuellement utilisées afin de produire des modélisations susceptibles a minima de représenter le fonctionnement à une échelle donnée. Parmi ces méthodes, le recours à la mécanique des fluides numériques pour prédire les transferts de masse, de quantité de mouvement et de chaleur dans des écoulements multiphasiques s'impose comme une voie prometteuse, notamment en raison des succès obtenus dans de nombreux autres domaines d'application.

Les mécanismes mis en jeu dans les réacteurs biologiques sont nombreux et souvent couplés. Parmi eux, on peut citer les principaux : le mélange dans la cuve (agitation, aération), le transfert de matière gaz-liquide, le transfert de matière du fluide vers les microorganismes et les réactions biologiques intracellulaires. De forts couplages existent entre ces différents mécanismes, par exemple :

- le transfert de matière gaz-liquide dépend de l'agitation et de l'aération du milieu, ainsi que de la réaction biologique,
- les différents champs de concentration (substrats et/ou produits formés) dans la phase liquide, dépendent à la fois du transport par le fluide (hydrodynamique du bioréacteur) et de la réaction biologique.

Les transferts de masse entre le liquide et la phase biologique sont extrêmement importants et se révèlent être à l'origine de la problématique même du fonctionnement des bioréacteurs. En effet, ces transferts dépendent de la qualité du mélange dans le bioréacteur, et plus particulièrement à l'échelle des microorganismes, et également de la capacité de ces derniers à assimiler le flux de matière transporté par le milieu de culture environnant.

La spécificité des réactions biologiques réside justement dans l'interaction directe du microorganisme avec son environnement. En effet, les schémas réactifs sont, en grande partie, conditionnés par les flux de masses échangés par le microorganisme avec le milieu environnant. Par conséquent, des hétérogénéités de concentration en substrat dans un bioréacteur vont directement influencer l'assimilation de ce dernier par les microorganismes. De plus, les microorganismes influencent directement ce même champ de concentration par leur consommation de substrat, menant ainsi à des mécanismes fortement couplés. D'un point de vue plus global, ces forts couplages influencent directement les performances des bioréacteurs, et des hétérogénéités sur la phase biologique sont observées en réponse aux hétérogénéités spatiales du réacteur. Ces dernières se traduisent par exemple par l'apparition de sous-produits de la réaction ou la diminution des vitesses spécifiques de croissance.

Dans la plupart des approches existantes, les hétérogénéités locales (du champ de concentration comme de la population microbienne) ne sont pas prises en compte. Il faut convenir que l'étude expérimentale est extrêmement complexe autant dans sa mise en œuvre que dans l'analyse d'hypothétiques résultats. C'est pourquoi ce travail mettra l'accent sur une approche numérique à l'échelle microscopique où les hétérogénéités de concentration vues par les microorganismes le long de leur trajectoire seront obtenues par le biais d'une résolution directe du champ fluide couplée au transport du scalaire. Cependant, compte-tenu du caractère fortement turbulent des écoulements dans les bioréacteurs, les gammes d'échelles mises en jeu sont très importantes. La comparaison entre la taille des bioréacteurs industriels de l'ordre de dizaines de mètres cube et la taille microscopique des microorganismes (de l'ordre du micromètre) donne la mesure de la difficulté de la modélisation complète d'un bioréacteur industriel et de la prise en compte de chaque phénomène mis en jeu.

La démarche théorique établie concernant ce type de problématique multi-échelle consiste à modéliser les phénomènes dont les échelles de tailles et de temps se situent en dessous de l'échelle retenue pour la simulation. Nous nous focaliserons donc dans cette étude sur un volume élémentaire équivalent à une maille d'un calcul CFD avec l'objectif d'étudier les conséquences des hétérogénéités spatiales dans ce volume et d'en représenter les conséquences à l'échelle de la maille tout entière. Cette étude s'inscrit globalement dans ce cadre et tentera aux travers de simulations numériques de caractériser l'impact de la dynamique de l'écoulement et du mélange sur l'assimilation de substrat par des microorganismes.

Aborder le problème à l'échelle microscopique dans le cas de microorganismes apparaît naturel mais ce choix se heurte à la difficulté suivante : comment décrire l'assimilation à l'échelle cellulaire quand la connaissance existante découle d'observations macroscopiques ? A l'inverse, le choix d'un modèle d'assimilation à l'échelle d'une cellule influence-t-il la loi d'assimilation macroscopique ? La description fine de la réaction biologique à l'échelle des microorganismes ne sera cependant pas l'objet de ce travail. Nous considérerons seulement les aspects physiques, et la loi d'assimilation du substrat à l'échelle du microorganisme, sans pour autant s'intéresser au devenir du substrat carboné dans la cellule. De ce fait, seul le transport du substrat carboné sera considéré, le transport de l'espèce gazeuse ne sera pas abordé. En d'autres termes, l'aération du milieu par injection d'oxygène ne sera pas considérée et on s'affranchira donc de l'effet des bulles sur l'hydrodynamique du réacteur ainsi que de la dissolution de l'oxygène dans l'eau.

Dans le premier chapitre, nous introduisons les notions biologiques nécessaires à la compréhension des phénomènes mis en jeu ainsi que les notions spécifiques à l'étude des bioréacteurs. L'étude bibliographique décrit différentes expériences mettant en évidence les interactions entre mélange et réaction biologique dans les bioréacteurs. Nous abordons les différents mécanismes de mélange en régime turbulent et présenterons les principaux travaux existants sur la modélisation des bioréacteurs par l'approche génie des réacteurs (basée sur des bilans globaux à l'échelle macroscopique) et par l'approche mécanique des fluides (basée sur la résolution d'équations locales). C'est sur cette dernière approche que nous nous appuyons tout au long de ce travail.

Le second chapitre (constitué d'une publication acceptée dans *Chemical Engineering Science*) propose une étude instationnaire de l'assimilation de substrat par un microorganisme isolé suivant l'idée que l'assimilation de substrat par les microorganismes est un phénomène ayant lieu à l'interface entre le liquide et la cellule. Le microorganisme est soumis à des fluctuations de concentration en substrat et le transport du substrat jusqu'au microorganisme est étudié. À l'interface de la cellule, on impose une loi d'assimilation du substrat qui dépend du flux de substrat lui arrivant. Cette configuration permet de mettre en évidence l'émergence d'une compétition entre transport et réaction biologique à l'échelle du microorganisme. L'analyse théorique du problème et des données de la littérature conduit à reconsidérer la notion de limitation par le substrat. En effet, une limitation de la vitesse d'assimilation par le transport ou par la réaction ne peut pas être identifiée en tant que telle sur la base de la seule connaissance du flux assimilé et de la concentration moyenne en substrat. En particulier cette partie montre l'importance de la prise en compte les fluctuations observées par les microorganismes le long de leur trajectoire, car ces dernières influent directement sur le taux d'assimilation.

Dans le troisième chapitre, nous présentons la configuration d'écoulement académique choisie : une turbulence homogène isotrope, et la méthode numérique utilisée. L'approche de simulation numérique directe choisie permet de s'affranchir de toute modélisation pour la détermination du champ de vitesse et on résout l'équation de transport d'un scalaire passif (n'agissant pas sur le fluide) qui représente le champ de concentration en substrat. Les résultats obtenus pour la dynamique et le scalaire sont confrontés aux résultats de la littérature dans le but de valider les simulations effectuées. Les simulations numériques réalisées dans ce chapitre servent de base de données pour les chapitres suivants en terme de champ dynamique et scalaire.

La chapitre quatre, propose d'étudier l'impact des hétérogénéités de concentration en substrat vues par les microorganismes sur la vitesse d'assimilation macroscopique à l'échelle de la population. Ces résultats sont obtenus par suivi Lagrangien de particules dans l'écoulement. Ces particules peuvent être assimilées à des microorganismes. Leur influence sur le champ fluide n'est pas considérée dans cette partie. Les statistiques à l'échelle de la population pour la phase biologique permettent de mettre en évidence l'influence de la dynamique et du mélange sur l'ensemble de la population de microorganismes. Une étude paramétrique est menée en considérant différentes populations de microorganismes caractérisées par leur affinité pour le substrat. Ainsi l'exploitation des distributions de flux assimilés pour chaque population considérée couplée à un modèle métabolique permet de prédire les taux de croissance et de production de métabolites d'*overflow* en fonction de l'affinité supposée pour le substrat.

L'étude proposée dans le dernier chapitre porte plus particulièrement sur des simulations instationnaires. Dans une première partie, l'influence des microorganismes n'est toujours pas prise en compte et la décroissance des fluctuations du substrat est étudiée ainsi que son impact sur l'assimilation par les microorganismes. Dans une seconde partie de ce chapitre, on aborde plus particulièrement le couplage inverse biologique, c'est-à-dire, quelle est l'influence de la consommation du substrat par les microorganismes sur le champ de concentration du fluide. Les résultats sont exploités en fonction des différents paramètres physiques pour l'écoulement et biologiques pour les microorganismes.

Enfin la dernière partie de ce travail récapitule les résultats essentiels obtenus et propose quelques perspectives dans la continuité de ce travail.

Chapitre 1

Etat de l'art de la simulation numérique des réacteurs biologiques

L'étude des réacteurs biologiques, ou bioréacteurs, a mis en évidence la difficulté de maîtrise des performances lors du passage de l'échelle du laboratoire à l'échelle industrielle. Les baisses ou augmentations de rendement observées lors d'un changement d'échelle, sont problématiques, tant au niveau coût que maîtrise du procédé. Ces écarts révèlent que les règles d'extrapolation actuellement utilisées sont inadaptées ainsi qu'une vision incomplète du fonctionnement cellulaire. Ce chapitre bibliographique, décrit dans un premier temps ce qu'est un bioréacteur et les différents types de fonctionnement. La problématique de changement d'échelle est alors présentée en se basant sur des résultats expérimentaux de la littérature. Les réactions biologiques sont introduites ainsi que leur forte interaction avec la phase extracellulaire. La nécessité de caractériser le mélange est démontrée par la littérature, et une classification des différents mécanismes de mélange turbulent et des échelles associées est présentée. Enfin, un état de l'art est proposé concernant la modélisation des bioréacteurs. Tout d'abord différents exemples de travaux utilisant l'approche génie des réacteurs pour la détermination de l'écoulement et de la réaction biologique sont cités. L'approche mécanique des fluides pour la simulation numérique des bioréacteurs est ensuite introduite. La situation de ce travail de thèse dans la problématique générale de modélisation des bioréacteurs est décrite plus en détail à la fin de ce chapitre.

Contents

Introduction

Les bioréacteurs, ou réacteurs biologiques sont d'immenses cuves dans lesquelles se trouvent de la biomasse dans un milieu de culture. La biomasse consomme des substrats présents dans le liquide et produit de nouveaux microorganismes ou des produits d'intérêts. Afin de maintenir une certaine homogénéité, ces réacteurs sont agités à l'aide de turbines, et aérées par injection d'oxygène.

Les performances des procédés biologiques dépendent de la composition du milieu de culture. Plus particulièrement, les microorganismes ont besoin d'éléments nutritifs nécessaires à leur développement. Ces éléments sont contenus dans le milieu de culture, dont la composition varie spatialement dans le réacteur. En effet, la composition de l'environnement dépend de l'hydrodynamique dans la cuve, mais aussi de la présence des microorganismes qui consomment les substrats et produisent de nouvelles substances. En raison de ces phénomènes fortement couplés, des problèmes récurrents lors d'extrapolation des procédés biologiques sont observés lors du passage de l'échelle du laboratoire à l'échelle industrielle. Cette problématique sera introduite après avoir présenté les bases nécessaires à la compréhension du fonctionnement des bioréacteurs.

Nous nous intéresserons ensuite aux travaux de la littérature qui mettent en évidence de manière expérimentale l'influence du mélange sur les performances biologiques, et aux différentes échelles de longueur et de temps mises en jeu dans les bioréacteurs. Nous présenterons ensuite une étude bibliographique des différents travaux modélisation des bioréacteurs en termes d'approche numérique Enfin, le cadre d'étude de ce travail sera présenté plus en détails.

1.1 Présentation générale des bioréacteurs

1.1.1 Contexte industriel

L'utilisation de micro-organismes à des fins alimentaires remonte à l'Antiquité. La production de pain grâce à des levures ou encore la fermentation pour la production de boissons alcoolisées étaient des procédés utilisés il y a déjà des millénaires par les Egyptiens par exemple. De nos jours, les technologies liées aux cultures microbiennes sont largement répandues, que ce soit dans l'industrie alimentaire ou pharmaceutique, et représentent un véritable enjeu industriel. Les rendements sont améliorés grâce à la maîtrise toujours plus accrues des procédés. Les avancées en recherche génétique permettent l'accès à une gamme de production toujours plus large, notamment en termes de création de nouveaux produits. Les procédés biologiques permettent ainsi d'obtenir de multiples produits dont les utilisations sont très variées (voir le tableau 1.1). Au cœur de ces procédés se trouvent les micro-organismes, qui réalisent les transformations chimiques des matières premières en produit d'intérêt.

1.1.2 Micro-organismes

Ce travail de thèse concerne les interactions entre les micro-organismes et leur environnement. Le terme général "micro-organisme" regroupe un ensemble important d'espèces dont la taille s'étend de $0,1$ à 10 μm environ. Une classification exhaustive des espèces de micro-organismes est complexe étant donnée leur diversité. Nous nous contenterons donc de citer les micro-organismes d'intérêt dans cette étude : *Escherichia coli* (*E. coli*) et *Saccharomyces cerevisiae*. La première est une bactérie utilisée pour la production de métabolites secondaires : produits d'intérêts alimentaires ou

Table 1.1: Exemple de productions industrielles obtenues par cultures bactériennes et fongiques.

Produits	**Utilisation**
biomasses	boulangerie, œnologie, industrie laitière
acides organiques	agroalimentaire, pharmacie, ciment, peinture
enzymes	fabrication de glucose, détergents
antibiotiques, vitamines	santé
protéines	thérapeutique (vaccins)
alcool	boissons, biocarburants
polymères	industrie pétrolière

pharmaceutiques. La seconde est une levure (champignon) de boulangerie dont les cultures visent principalement la production de la biomasse elle-même. On cherche à produire des levures à partir de la fermentation de levures. Mais, cette levure peut également être utilisée en bioréacteur pour la production de métabolites secondaires.

La figure 1.1 montre deux types de micro-organismes ainsi qu'une représentation schématique d'une cellule de levure de boulangerie. Une paroi perméable à structure semi-rigide protège l'intérieur de la cellule constituée de différents organites contenus dans la membrane cytoplasmique. Afin d'assurer leur maintenance, leur croissance, ou la production de métabolites extracellulaires, les micro-organismes utilisent des nutriments contenus dans le milieu de culture. En résultent différents mécanismes de transformation moléculaire et de transferts d'énergie intra-cellulaires. L'ensemble de ces mécanismes est appelé métabolisme microbien et correspond au fonctionnement d'un micro-organisme. Le catabolisme est associé à la maintenance et la croissance. La dégradation des matières consommées fournit alors l'énergie nécessaire pour le fonctionnement de la cellule. On parle sinon d'anabolisme pour les réactions de synthèse de molécules d'intérêt.

De manière générale, les micro-organismes ont besoin de l'apport extérieur de plusieurs éléments nécessaires à leur croissance (carbone, oxygène, hydrogène, azote, soufre, oxygène, phosphore). L'apport en nutriments est donc le plus souvent indispensable et peut représenter jusqu'à 50 % du coût du procédé. Il est donc nécessaire de choisir les nutriments les mieux adaptés. On décrira plus particulièrement les deux éléments les plus importants : le carbone et l'oxygène. En général le premier est sous forme de sucres (glucose, saccharose, amidon) car il ne nécessite que très peu de transformation pour l'assimilation par le micro-organismes et sera appelé substrat au cours de ce travail. Le second est amené par aération du milieu. On distingue alors deux types de métabolismes selon que le micro-organisme utilise ou non l'oxygène comme source directe d'énergie.

En culture aérobie (présence d'oxygène), les micro-organismes oxydent en totalité le substrat carboné générant la production de nouvelles cellules (croissance) et de dioxyde de carbone. Dans le cas où il n'y a pas d'oxygène, les micro-organismes sont en mécanisme fermentaire (ou anaérobie). La dégradation du substrat carboné n'est pas complète, et parallèlement à la croissance on observe l'apparition de métabolites, caractéristique du fonctionnement en absence d'oxygène. Ces sous-produits peuvent être excrétés par la cellule vers le milieu de culture.

La nature ainsi que le nombre de molécules d'intérêt produites dépend du type de micro-organisme et de son milieu de culture. Il est donc assez intuitif de penser que lors d'une culture aérobie, si le mélange n'est pas assez puissant pour maintenir un milieu homogènement aéré, certains micro-organismes puissent produire des métabolites secondaires en raison d'une oxygénation insuffisante ou d'une concentration trop importante en substrat.

On notera enfin que les réactions biologiques diffèrent extrêmement selon le type de culture, ou de micro-organismes utilisés. Dans les cultures en bioréacteur, un grand nombre de paramètres est

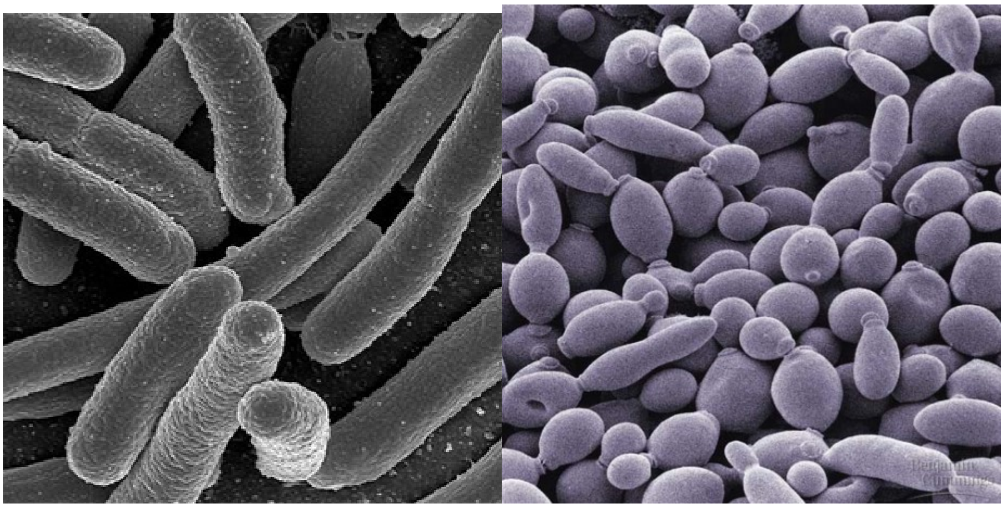

(a) *E. coli.* (b) *Saccharomyces cerevisiae.*

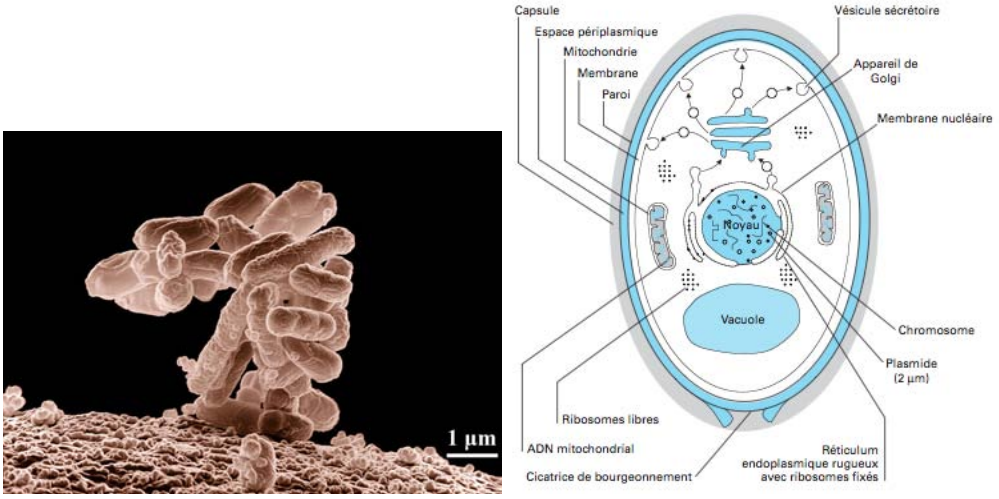

(c) Amas de *E. coli.* (d) Représentation schématique d'une cellule de levure.

FIGURE 1.1: Bactéries et levures.

donc à prendre en compte, et si un type de métabolisme est visé, il faut s'assurer de contrôler tous les éléments (concentrations en substrat et oxygène, température, mélange, agitation). En effet, la modification du milieu environnant par les réactions biologiques se traduit notamment par l'augmentation du pH de la solution (acidité du dioxyde de carbone), ou encore par l'augmentation de température du milieu (réactions exothermiques). Ces modifications du milieu de culture par les micro-organismes ont un impact direct sur ces derniers. On se trouve donc on présence de phénomènes locaux (à l'échelle d'un micro-organisme) fortement couplés. Du fait du nombre important de micro-organismes utilisés lors d'une culture biologique, des interactions à l'échelle globale du réacteur biologique interviennent également. Ces différentes interactions sont l'objet de ce travail de thèse et seront vues plus en détails ultérieurement. Le paragraphe suivant décrit le fonctionnement des réacteurs biologiques industriels.

1.1.3 Modes de fonctionnement des bioréacteurs

On peut distinguer plusieurs types de fonctionnement pour les bioréacteurs. Dans le cas de microorganismes aérobies, ceux-ci sont introduits dans une cuve agitée et aérée. Les bioréacteurs diffèrent alors par le mode d'apport en substrat.

On peut citer les fermentations discontinues des micro-organismes dîtes de type *batch* dans lesquelles le substrat est apporté en début de culture et n'est pas renouvelé. Dans ce type de réacteur, la quantité de biomasse bactérienne suit une évolution en 4 grandes phases comme le montre la figure 1.2a. On distingue en début de processus la phase de latence où la population microbienne s'adapte à son environnement. Les mécanismes intervenant pendant cette phase sont complexes et traduisent l'influence du milieu de culture sur la croissance, mais également des temps d'adaptation différents au milieu de culture selon l'état physiologique initial des micro-organismes. On discerne ensuite une phase de croissance exponentielle pendant laquelle la concentration de biomasse évolue rapidement. Cette phase de croissance est cependant limitée en temps à cause de l'apparition de facteurs intrinsèques au bioréacteur. On peut notamment citer l'épuisement des ressources en substrat disponible et l'apparition de métabolites bactériens inhibant la croissance des bactéries par exemple. Cette croissance s'amenuise donc pour arriver à une phase stationnaire. Cette phase apparaît comme une phase de croissance apparente nulle, or elle résulte de la compétition entre production et lyse de la biomasse. Enfin, une phase de déclin apparaît où la destruction des micro-organismes est le phénomène prépondérant résultant en une décroissance exponentielle de la biomasse.

On trouve également des bioréacteurs où la fermentation des microorganismes est menée en continu. Le principe d'une telle installation consiste en l'alimentation ininterrompue en substrat tout en soutirant simultanément en continu un volume du mélange biomasse-liquide de manière à conserver un volume de réacteur constant. Contrairement au réacteur batch, on peut dans ce cas maintenir à des valeurs choisies et constantes le taux de croissance des micro-organimes, la concentration de ces derniers, et/ou la production de métabolites d'intérêt. Expérimentalement deux conduites de procédé sont couramment utilisées : le turbidostat et le chemostat. Le principe de la première est basé sur l'asservissement de la concentration cellulaire à l'aide de mesures optiques de la turbidité du milieu. La seconde consiste à alimenter en nutriments en excès par rapport aux besoins des microorganismes excepté pour un nutriment, appelé facteur limitant et qui contrôle la concentration de biomasse à l'équilibre. Cette méthode est privilégiée pour l'étude des interactions d'un microorganisme avec son milieu environnant car on peut agir sur un seul paramètre mais n'est pas utilisée pour les applications industrielles. Elle est plus répandue et fait intervenir le taux de dilution D correspondant à l'inverse du temps de séjour, qui est aussi le taux de croissance de la biomasse. Celui-ci est alors fixé par l'expérimentateur et ne peut dépasser une valeur critique D_c pour laquelle le chemostat n'est plus réalisable. À chaque valeur du taux de dilution correspond alors un couple de concentration en micro-organismes X et en substrat S. La figure 1.2b montre l'évolution des concentrations en substrat et biomasse dans un réacteur continu en fonction du taux de dilution.

Enfin on peut trouver des réacteurs en fonctionnement discontinu-alimenté ou *fed-batch* (Figure 1.2c). Dans ces installations, le réacteur est alimenté continuellement en substrat et l'absence de soutirage du milieu conduit à une variation du volume du réacteur biologique. Pour conserver une concentration résiduelle constante en substrat, le débit d'alimentation est adapté. Cependant, les solutions de substrats utilisées sont très concentrées dans le but d'éviter une trop grosse augmentation du volume utile du bioréacteur. Toutefois, les forts gradients de concentration de substrat entre la région d'injection et le reste du réacteur, représentent une difficulté supplémentaire dans la prédiction des performances du procédé (Namdev et al., 1992; George et al., 1998). Le métabolisme du micro-organisme est fortement dépendant de son environnement.

Cette vision simplifiée des cultures de micro-organismes repose sur un certain nombre d'hypothèses. En premier lieu, le mélange des différents substrats apporté est considéré comme infiniment rapide

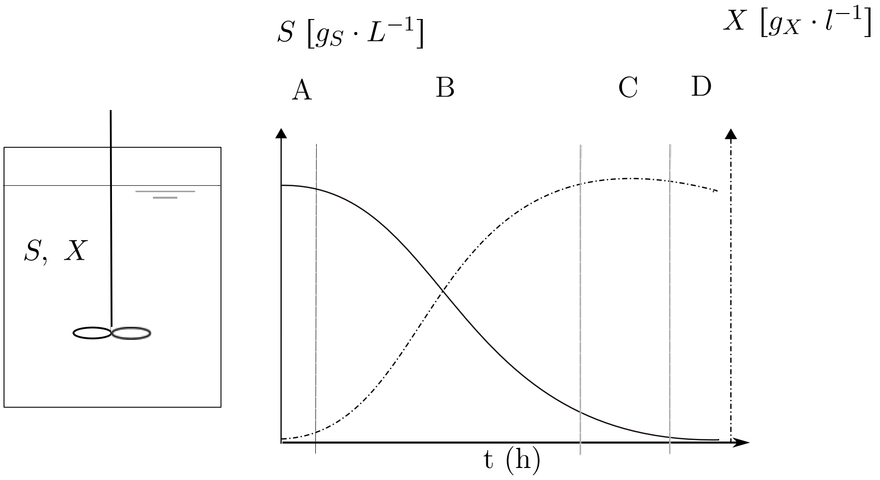

(a) Fonctionnement en bioréacteur *batch.* Les différences phases représentées : A- Phase de latence, B- phase exponentielle de croissance, C- phase stationnaire, D- phase de déclin.

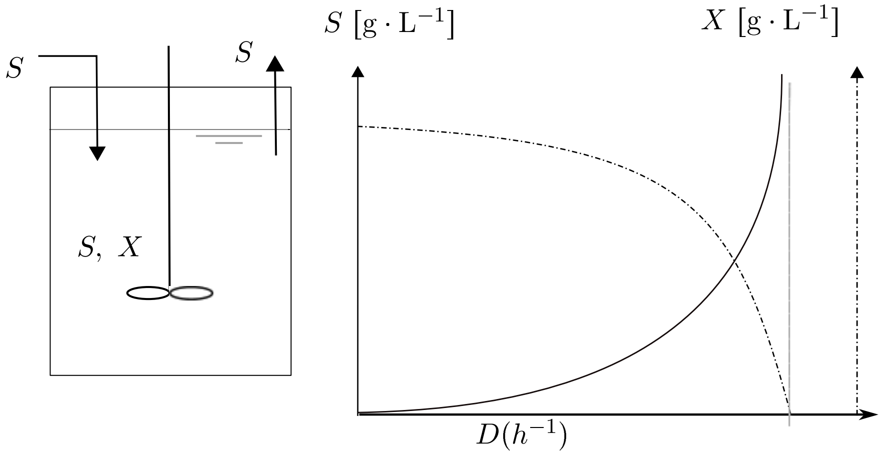

(b) Fonctionnement en bioréacteur continu. D_c correspond au taux de dilution critique.

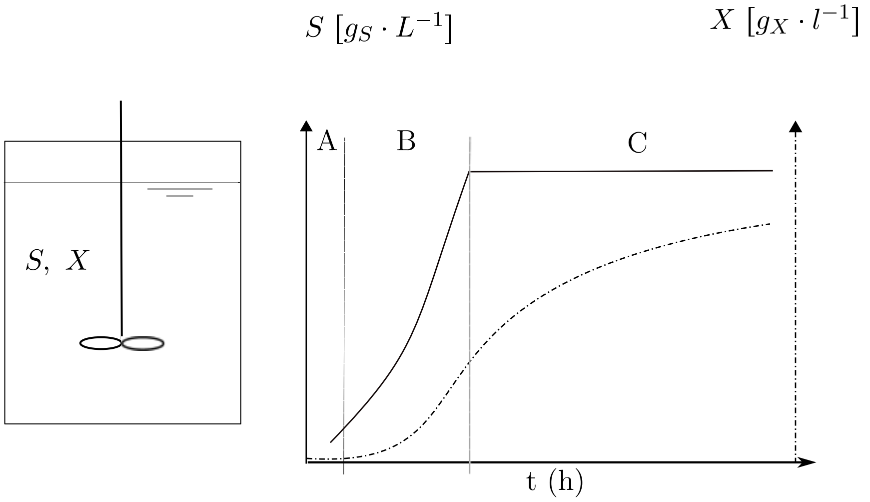

(c) Fonctionnement en bioréacteur *fed-batch.* Les différences phases représentées : A- Phase de latence, B- phase exponentielle de croissance, C- phase stationnaire.

FIGURE 1.2: Schéma de fonctionnement d'un bioréacteur et évolutions respectives des concentrations en biomasse X et substrat S.

par rapport aux réactions des consommation par les micro-organismes. Cette hypothèse forte signifie que le champ de concentration en substrat est parfaitement homogène dans tout le réacteur. Ensuite, les micro-organismes sont traités comme une espèce chimique dissoute, ainsi les termes réactionnels sont basés sur des concentrations de substrat et de biomasse en phase liquide. Enfin, les vitesses de transferts de matière (gaz-liquide) et thermiques sont également considérées comme lentes par rapport à la vitesse de mélange. Ces hypothèses sont très lourdes car la réalité peut être tout autre. Nous verrons par la suite qu'il s'agit d'une question relative aux temps caractéristiques du mélange, des transferts et de l'assimilation des différents substrats. Cette limitation est notamment observées dans le cas des réacteurs *fed-batch* car de forts gradients de concentration en substrat entre l'injection et le reste du réacteur existent.

1.1.4 Modélisation des réactions biologiques

Comme il a déjà été évoqué, les micro-organismes sont une véritable usine moléculaire où ont lieu de nombreuses réactions. De plus le métabolisme d'une cellule suit des mécanismes de régulations directement dépendant du milieu environnant de la cellule ainsi que de son histoire (Bailey and Ollis, 1986). Il est impossible de décrire rigoureusement les réactions biologiques de manière mathématique (Nielsen and Villadsen, 1992), et, même si il reste encore difficile d'intégrer les mécanismes de régulation, on est aujourd'hui capable de déterminer le fonctionnement interne de nombreux micro-organismes (Chassagnole et al., 2002). On trouve donc des modèles simplifiés qui s'appliquent pour des conditions de cultures spécifiques (température, pH, intervalles de concentrations fixes ...). Le choix d'un modèle se fait alors en se basant sur une analyse des phénomènes mis en jeu et de leur temps caractéristiques Esener et al. (1983). Du point de vue de l'environnement des cellules, on doit considérer les modifications liées au fonctionnement du bioréacteur, telles que l'état de mélange et les transferts thermiques et massiques. Pour la phase biotique on regarde les phénomènes de régulations qui permettent l'adaptation des micro-organismes à leur milieu environnant. Différents modèles ont été proposés dans la littérature (Bailey and Ollis, 1986; Nielsen and Villadsen, 1992) et peuvent être classifiés en plusieurs catégories.

Modèles non-structurés

Lorsque l'on s'intéresse uniquement à l'environnement extérieur, l'évolution de la composition interne des micro-organismes n'est pas prise en compte, on parle de modèles non-structurés. On considère alors l'adaptation des micro-organismes à une modification de leur environnement comme unique et instantanée. Cette modélisation revient à considérer les cellules comme des boîtes noires. Le modèles sont établis en faisant des bilans aux frontières des micro-organismes. Le système d'équations (1.1) représente un modèle non-structuré simple pour la croissance de la biomasse, la consommation du substrat et la production d'un métabolite P dans le cas où la concentration de substrat S est limitante.

$$\frac{dX}{dt} = \mu_X X, \tag{1.1a}$$

$$\frac{dS}{dt} = -q_S X, \tag{1.1b}$$

$$\frac{dP}{dt} = q_P X. \tag{1.1c}$$

X, S, P représentent respectivement les concentrations en biomasse, substrat et métabolite. Le facteur μ_X symbolise la vitesse, ou taux de croissance spécifique [s^{-1}]. On relie la vitesse spécifique de consommation du substrat et de production du métabolite au taux de croissance par :

$$q_S = \frac{\mu_X}{Y_{XS}}, \tag{1.2}$$

$$q_X = \frac{\mu_X}{Y_{XP}}, \tag{1.3}$$

les coefficients Y_{XS} et Y_{XP} correspondant aux rendements de croissance et de production. On peut également les définir comme la quantité de biomasse formée par quantité de substrat consommé, et la quantité de biomasse formée par quantité de métabolites produites. Ce système est relativement aisé à résoudre et ne considère donc que le milieu environnant des cellules. Cependant, la vitesse spécifique de croissance dépend directement de la concentration en substrat du milieu S. Plusieurs modèles ont été proposés. A titre d'exemple, citons le modèle de Monod (Monod, 1949) extrêmement répandu dans la littérature :

$$\mu_X = \mu_{X,max} \frac{S}{S + K_S}, \tag{1.4}$$

où $\mu_{X,max}$ est la vitesse spécifique maximale de croissance et K_S la constante de saturation du substrat considéré ou constante d'affinité du micro-organisme $[\ \mathrm{gS} \cdot \mathrm{L}^{-1}\ ]$. Cette constante est définie comme la concentration en substrat pour laquelle le taux de croissance spécifique de la population μ_X est égal à la moitié du taux spécifique de croissance maximal $\mu_{X,max}$.
On peut donc facilement relier la vitesse spécifique de consommation du substrat q_S à la concentration en substrat elle-même avec $q_{S,max} = \mu_{X,max}/Y_{XS}$:

$$q_S = q_{S,max} \frac{S}{S + K_S}. \tag{1.5}$$

On se trouve alors en présence d'une équation non-linéaire de la concentration en substrat. Le modèle de Monod a été beaucoup développé et de nombreuses variantes existent pour tenir compte de phénomènes supplémentaires tels que l'inhibition de la croissance par exemple. Il est largement utilisé dans de nombreuses applications, notamment dans les cultures continues et en régime permanent où les différents paramètres sont stables. Cependant, du fait de la nature même du modèle, lorsque qu'une modification de l'environnement conduit à une régulation cellulaire dont les temps caractéristiques sont similaires, les modèles non-structurés échouent complètement à prédire l'évolution du fonctionnement des micro-organismes et des bioréacteurs. Au vu de l'équation (1.1c), il est également intuitif de remarquer que si la production de métabolite n'est pas liée directement à la croissance de la biomasse, ce type de modèle ne pourra pas rendre compte raisonnablement de la production de métabolite P. Pour palier à ces limitations on peut donc distinguer un type de modèle qui prend en compte la composition interne des micro-organismes.

Modèles structurés

Dans ce type de modèle, en plus des concentrations environnantes, on introduit des concentrations intracellulaires (concentrations en métabolites et autres molécules dans la cellule). La connaissance de ces concentrations permet alors d'établir des modèles structurés qui décrivent le fonctionnement du micro-organisme. Cette formulation est donc intuitivement plus adaptée à la représentation d'un procédé biologique car elle permet de prendre en compte la dynamique du système. Il existe une grande variété de modèles structurés (Bailey and Ollis, 1986; Nielsen and Villadsen, 1992). Cependant, même si les schémas réactionnels biologiques sont désormais en partie connus, les cinétiques ne le sont toujours pas. Le développement de modèles dynamiques pour le fonctionnement des cellules reste donc un enjeu majeur.

Des modèles métaboliques existent également. À partir de la connaissance de l'ensemble des réactions intracellulaires possibles, et d'un nombre limité de mesures (telles que les flux de substrats assimilés ou excrétés), on peut prédire les vitesses des réactions intracellulaires. Cette approche correspond schématiquement à résoudre un bilan de matière en régime permanent à l'échelle de la cellule. Etant donné le nombre important de réactions intracellulaires, le degré d'indétermination du système est souvent très élevé. Cependant il peut être sensiblement réduit lorsqu'on lui adjoint un bilan enthalpique. Cette approche structurée est très prometteuse et met l'accent sur un point clef dans l'optique de la modélisation des bioréacteurs : la quantification des flux entrants dans la cellule.

Modèles de population

Lorsque que l'on étudie une population de micro-organismes dans son ensemble, on peut avoir deux approches différentes. Soit les cellules sont considérées comme étant chacune identique morphologiquement (du point de vue intracellulaire), et on parle alors de modèles de population non-structurés, soit on considère que chaque cellule est morphologiquement différente et on introduit des modèles de population dits structurés (segregated population model).

Basés sur une fonction de distribution du nombre de micro-organismes avec une caractéristique donnée (par exemple possédant le composé intracellulaire I), ces modèles sont statistiques. On utilise une équation de conservation pour cette fonction de distribution où l'ont fait intervenir un terme de formation pour I par exemple. Des termes probabilistes apparaissent également dans l'équation de conservation (Fredrickson et al., 1967). Pour plus d'information sur ces modèles, on pourra se référer à Ramkrishna (1979, 2011).

1.1.5 Conclusion

En regardant les différents approches pour modéliser la réaction biologique, il est important de savoir de quelle manière on va chercher à représenter les cellules. On peut alors regrouper les trois possibilités suivantes :

- soit les cellules sont toutes identiques et on utilise dans ce cas une approche non-structurée,
- les cellules peuvent également être identiques, mais en prenant en compte les variables intracellulaires,
- enfin, toutes les cellules sont potentiellement différentes.

Se pose ensuite la question de la représentation du fonctionnement des cellules. On peut adopter pour cela deux types d'approches selon que l'on va considérer les micro-organismes comme une population globale (c'est-à-dire sa concentration totale X dans la phase liquide) ou regarder un micro-organisme à l'échelle locale. Dans les deux cas, les approches peuvent être utilisées avec les trois représentations pour les cellules. La première approche, dite approche cinétique (de type Monod) utilise les variables extra-cellulaires, mais les vitesses de réactions peuvent être modulées par la prise en compte des variables intracellulaires. Dans la seconde représentation pour le fonctionnement des micro-organismes, on va considérer un réseau de réactions intracellulaires pour lesquelles on pourra observer des variations de vitesses et de rendements à l'échelle cellulaire. Ces variations peuvent trouver leur origine dans la quantité des flux de substrats reçus, et dans l'état de chaque cellule si elles sont différenciées. Cette approche, appelée approche métabolique, permet alors de prédire les bascules de métabolisme, apparition du mécanisme *overflow* par exemple, pour une population de micro-organismes en se basant sur les flux entrants (Xu et al., 1999). La figure 1.3 inspirée par Nielsen and Villadsen (1992) schématise les différents types de modélisations habituellement utilisés. En effet, la modélisation des procédés biologiques est complexe et fait intervenir des phénomènes à différentes échelles. D'un coté, le comportement biologique résulte des réactions

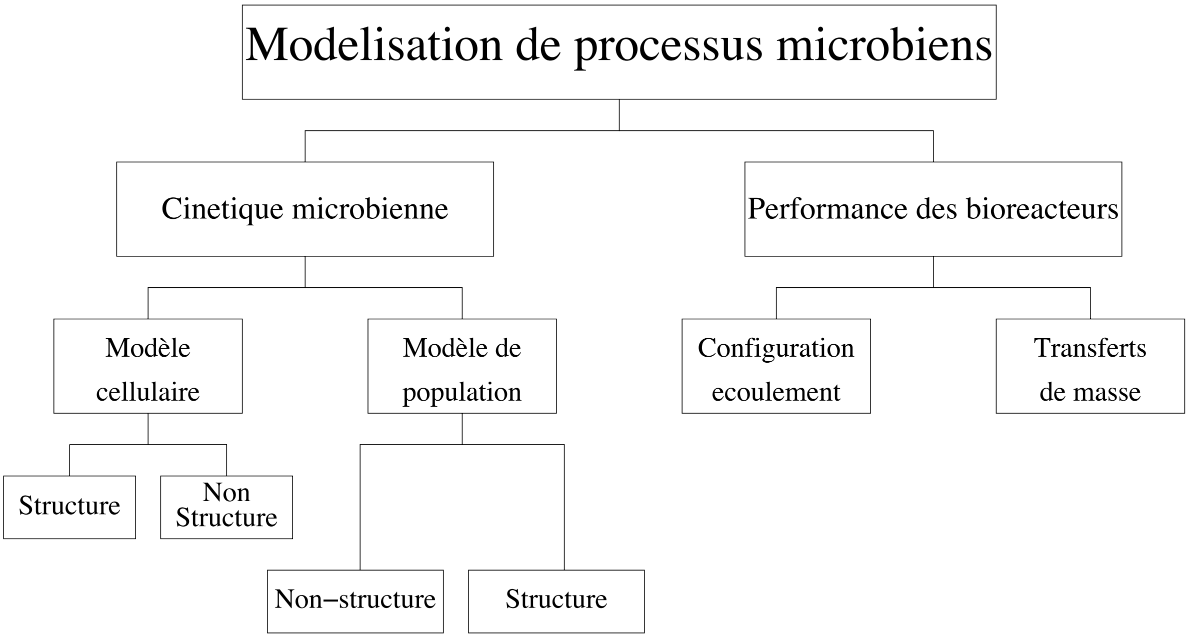

FIGURE 1.3: Schéma des différents aspects à considérer pour la modélisation des procédés de fermentation.

biologiques et des cinétiques microbiennes propre à chaque micro-organisme, et dépend directement du milieu environnant. D'un autre côté, la mise en place du bioréacteur nécessite la caractérisation du milieu environnant en terme de mélange, aération, agitation, dissipation, afin de caractériser les transferts de masse entre phase liquide et phase biotique. On se retrouve donc en présence de différents phénomènes fortement couplés qui font de la modélisation des bioréacteurs un challenge scientifique de taille. La partie suivante a pour but de développer plus en détails ces interactions et d'expliquer les problématiques principales qui y sont attachées.

1.2 Bioréacteurs : problématiques et enjeux

Comme il a été évoqué précédemment, les micro-organismes sont particulièrement sensibles à leur environnement, notamment si on modifie la composition de celui-ci. Il ne faut également pas oublier que les micro-organismes eux-mêmes agissent sur leur environnement.

1.2.1 Croissance de la biomasse, réaction biologique et adaptation

Comme nous avons pu le voir dans la section 1.1.4, les avancées technologiques permettent aujourd'hui d'accéder aux données intracellulaires et d'établir des schémas réactionnels à l'échelle d'une cellule. La connaissance des métabolismes est une donnée indispensable à la maîtrise des procédés biologiques à grande échelle, cependant, la cinétique des schémas réactionnels est encore inconnue ce qui ne permet pas une application à une population à grande échelle. L'enjeu des bioréacteurs étant la culture massive, les modèles non-structurés possèdent donc un attrait certain pour la modélisation de la croissance de la biomasse notamment.

En accord avec ces modèles, le comportement de la culture bactérienne évolue en fonction d'un nombre limité de constantes (par exemple $\mu_{X,max}$, K_S). Partant de cette hypothèse forte, la constante d'affinité d'un micro-organisme pour un substrat devrait être inchangée quelque soit la culture. Or, cette hypothèse est mise en défaut dans de nombreuses expériences sur la bactérie *E. coli* par exemple. En effet, pour ce type de cellule, la constante d'affinité pour le glucose varie de plusieurs ordres de grandeurs selon des conditions de culture différentes (Koch and Houston Wang, 1982; Senn et al., 1994). De plus, des auteurs ont montré d'importants écarts sur leurs résultats par rapport à la classique loi hyperbolique (Kovàrovà-Kovar and Egli, 1998), ce qui a conduit à proposer de nombreuses alternatives pour améliorer la loi de Monod. Il a également été montré que le rendement de croissance de biomasse Y_{XS} n'est pas constant et varie avec le taux de croissance dans les cultures.

Toutes ces observations expérimentales corroborent les limitations du modèle de Monod, car celui-ci impliquerait que le comportement biologique soit le même quel que soit l'environnement extérieur de la cellule. Or, des situations où le taux de croissance est limité par la phase abiotique sont fréquentes, et il a été montré que les cellules s'adaptent aux conditions de croissance ou de nutriments limitants par exemple (Ferenci, 1999b). On observe également des changements de métabolisme dans le cas de cultures de *E. coli* ou *S. cerevisiae*. Ces deux types de micro-organismes peuvent adopter les métabolismes oxydatifs s'ils se trouvent en milieu aéré ou bien fermentaire en l'absence d'oxygène. Il arrive que lors de cultures aérobies, utilisées notamment pour la croissance de la biomasse, la concentration en oxygène diminue fortement. Cette baisse entraîne l'adaptation des micro-organismes avec l'apparition d'un métabolisme fermentaire et de métabolites dans le milieu de culture. On observe également la production de métabolites similaires dans le cas où la concentration en substrat carboné est très importante. Ce mécanisme appelé « *overflow* »a été mis en évidence notamment par Lin et al. (2001); Xu et al. (1999).

Ces différentes observations montrent qu'un micro-organisme répond à des perturbations de son environnement en s'adaptant grâce à des mécanismes divers (Ferenci, 1999a). De plus, l'adaptation à ces perturbations n'est pas instantanée et le temps caractéristique varie selon le type de micro-organisme et le mécanisme d'adaptation (Bailey and Ollis, 1986). Dans les bioréacteurs, les micro-organismes sont donc soumis à des variations de leur milieu environnant. En effet, bien que les différents paramètres de culture soient optimisés, des hétérogénéités existent au sein des bioréacteurs. La section suivante est dédiée à une revue des expériences existantes sur les bioréacteurs ainsi que la mise en évidence des interactions entre réaction biologique et hydrodynamique interne.

1.2.2 Interactions entre réaction biologique et mélange

Un bioréacteur est une cuve agitée dans laquelle plusieurs phases sont en présence. L'agitation est donc indispensable pour homogénéiser le milieu. En effet, il est souhaitable que la phase biotique soit uniformément répartie dans tout le bioréacteur, mais également que la distribution du substrat carboné ou encore de l'oxygène soit homogène dans le bioréacteur. De plus, les réactions biologiques étant exothermiques, il est nécessaire de maintenir une agitation pour permettre une homogénéisation de la température dans le bioréacteur afin de conserver des conditions de culture optimales pour la biomasse. Il en est de même pour le pH du milieu de culture. Les cultures sont ainsi essentiellement conduites en régime turbulent.

On se trouve donc confronté à une problématique d'écoulements turbulents réactifs et polyphasiques (liquide, gaz, solide). Cette question est déjà compliquée dans le cas de réactions chimiques entièrement conditionnées par la thermodynamique. Dans le cas présent, une dimension supplémentaire apparaît du fait de l'inertie des micro-organismes qui répondent et s'adaptent aux variations de leur environnement local.

Les micro-organismes, extrêmement sensibles à leur milieu environnant, vont donc s'adapter à la configuration du procédé, et les rendements des réactions biologiques sont alors difficilement prédictibles. Ces écarts trouvent leur origine dans l'état de mélange du bioréacteur. On va brièvement introduire les expériences qui ont permis de mettre en évidence l'influence du mélange du substrat carboné sur les réactions biologiques.

1.2.2.1 Bioréacteurs de laboratoire

Les bioréacteurs de laboratoires sont des cuves de petits volumes ($\simeq$ 10 L) fortement agitées. Compte-tenu de leur petite taille, ils sont en général considérés comme parfaitement mélangés (Bailey and Ollis, 1986), bien que certaines études montrent que l'hydrodynamique du bioréacteur influence la réaction biologique. Une étude sur la croissance de biomasse de *S. cerevisiae* menée par Hansford and Humphrey (1966) a montré que le mélange agissait directement sur le rendement de production. En regardant l'effet de la localisation des points d'injection du substrat, ces auteurs ont montré l'impact du mélange sur le rendement, ainsi que l'effet de l'hydrodynamique sur le mélange. Par conséquent, ils préconisent une injection en des points multiples afin d'obtenir un mélange plus homogène du substrat carboné. Dunlop and Ye (1990b) ont repris cette étude et ont montré que la taille des micro-échelles turbulentes influence fortement le métabolisme cellulaire et montrant ainsi l'effet de micromélange sur les rendements de production.

D'autre études basées sur des mesures chimiques pour déterminer la qualité du mélange pour différents points d'injections ont été menées par Bourne et al. (1981). Ils ont montré que la production de biomasse est plus importante si le substrat est injecté dans une zone de forte dissipation d'énergie (où les plus petites échelles de mélange sont donc faibles), menant à une distribution plus homogène du substrat. Lors d'un apport en substrat moins important dans ces mêmes zones, les auteurs ont également montré que l'apport de substrat aux micro-organismes est plus rapide dans ces zones de forte dissipation. La problématique du mélange à l'échelle même des micro-organismes est donc soulevée. Cette question de l'influence directe du micro-mélange sur les micro-organismes a également été abordée par Al-Homoud and Hondzo (2008) et Hondzo and Al-Homoud (2007) dans le domaine des écosystèmes marins, pour de très faibles taux de dissipation de l'énergie cinétique turbulent ($\varepsilon \simeq 10^{-7}\ \mathrm{m}^2 \cdot \mathrm{s}^{-1}$). Ces auteurs ont observé une population d'*E. coli* placée dans un réacteur avec une turbulence de grille et ont fait varier les taux de dissipation dans le réacteur (dissipation allant de $10^{-7}\ \mathrm{m}^2 \cdot \mathrm{s}^{-3}$ à $5.10^{-5}\ \mathrm{m}^2 \cdot \mathrm{s}^{-3}$). Une demande accrue en oxygène pour les taux de dissipation les plus important a été observée traduisant une consommation plus rapide du substrat dans leur environnement direct pour ces mêmes taux de dissipation.

Enfin, grâce aux travaux de Garcia et al. (2009), une limitation en oxygène dans les réacteurs de laboratoires aérés et parfaitement mélangés (au sens macroscopique). On peut alors envisager que les vitesses apparentes de réaction biologique sont peut-être parfois des vitesses de micro-mélange. En effet, si un réacteur est bien macro-mélangé, il se peut qu'il soit cependant mal micro-mélangé comme l'ont montré Garcia et al. (2009), Akiti and Armenante (2004), et les hétérogénéités de mélange à l'échelle des micro-organismes doivent être prise en compte. Comme on peut s'y attendre, si des problèmes de mélange sont observés pour les réacteurs biologique de petite taille, les bioréacteurs industriels vont présenter des hétérogénéités de concentrations beaucoup plus importantes sur toute la gamme d'échelle du réacteur. C'est ce que nous allons voir maintenant.

1.2.2.2 Bioréacteurs industriels

De nombreuses études ont été menées sur les réacteurs industriels, qui ont mis en évidence l'existence de forts gradients de concentration en substrat carboné au sein des installations dans le cas de cultures *fed-batch* de production de levures (*S. cerevisiae*) (Larsson et al., 1996) ou de protéines recombinantes (*E. coli*) (Bylund et al., 1998; Enfors et al., 2001). Larsson et al. (1996) ont effectué des mesures de la concentration en glucose en différents endroits du bioréacteur, et ce pour deux positions d'injection en substrat carboné. Pour chaque injection, il a été montré que des gradients de concentration s'établissent le long de l'axe du bioréacteur : les gradients étant plus important lorsque l'injection se fait dans des zones où l'agitation est faible. Dans ce cas, le réacteur est mal macro-mélangé, et étant donné l'intensité des gradients de concentration, les bascules de métabolisme sont visibles (Dunlop and Ye, 1990a). L'impact négatif de ces gradients a également été étudié par Namdev et al. (1992) lors de culture de levures. Cependant, comme l'ont montré Larsson et al. (1996), grâce à des prélèvements rapprochés en un point du bioréacteur, la structure des fluctuations de concentration en ce point est directement liée à l'intensité de la turbulence au niveau du point d'injection. Ces observations révèlent un problème du méso-mélange comme nous allons le voir ultérieurement, et le micro-mélange non homogène qui en résulte peut mener à des bascules de métabolismes, dont la prédiction est difficile du fait des petites échelles mises en jeu.

Compte-tenu de ces observations, on peut donc dire que les micro-organismes dans un bioréacteur sont soumis à deux types de fluctuations pour les concentrations en substrat carbonés qui sont aussi bien d'origine hydrodynamique que biologique. On distingue donc des fluctuations de concentration rapides de faible amplitude liée à l'intensité turbulente, et les fluctuations de grande amplitude dont la fréquence est assez faible correspondant à l'écoulement moyen généré par le système d'agitation. Ces dernières sont responsables de la baisse de rendement observée dans les bioréacteurs (George et al., 1998; Bylund et al., 1998). Néanmoins, les micro-organismes peuvent aussi répondre à une contrainte fluctuante. C'est ce qu'on montré Lin and Neubauer (2000) dans une étude sur des cultures semi-continues d'*E. coli* avec des oscillations temporelles pour l'alimentation en substrat. Les cellules montrent une sensibilité à l'injection et répondent en s'adaptant à ces perturbations fluctuantes.

Afin de quantifier ces effets, des expériences ont été menées en laboratoire avec la mise en place de réacteurs mimant les réacteurs industriels à plus petite échelle. Ces réacteurs appelés *scale-down* (SDR) sont composés :

- d'un réacteur de petite taille agité et aéré, où les concentrations en substrat carboné sont relativement faibles
- d'un réacteur plus petit où on injecte le substrat limitant, qui représente donc la partie fortement concentrée correspondant à la zone d'alimentation des bioréacteurs industriels (Enfors et al., 2001).

Neubauer and Junne (2010) proposent un travail regroupant les principaux travaux sur ces SDR et proposent une représentation schématique pour ces derniers visible sur la figure 1.4. Ces bioréacteurs SDR donnent des résultats proches des observations à l'échelle industrielle et sont un bon outil pour l'étude en laboratoire des problèmes de changement d'échelle (George et al., 1998). Un autre paramètre important dans les réacteurs biologiques industriels, est la présence d'oxygène sous forme gazeuse. En effet, un double problème de mélange apparaît du fait de points d'injection différents entre substrat et oxygène. La présence de la phase gazeuse va également modifier l'hydrodynamique de la cuve et par la même occasion le mélange. Une baisse de rendement en biomasse de l'ordre de 20% a été observée par Bylund et al. (1998) entre des cultures fed-batch en bioréacteur industriel (12 m^3) et en laboratoire (1 L).

Enfin, la présence de gradients macroscopique de concentration en substrat à l'échelle du réacteur, peut entraîner la différenciation d'une population de micro-organismes en terme d'état physiologique. Il en est de même pour une population exposée à des fluctuations régulières de concentration. Delvigne et al. (2009) ont mis en évidence une ségrégation au sein de populations bactériennes, traduite par l'expression de certains gènes, dans le cas de réacteurs SDR. Ces travaux mettent en évidence une réponse des micro-organismes à leur environnement déjà abordée au cours de ce travail.

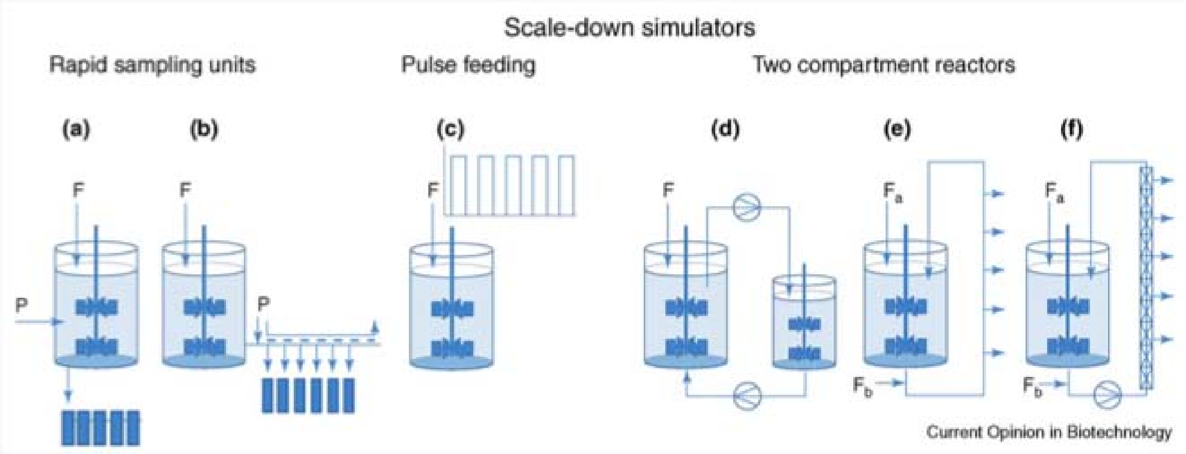

FIGURE 1.4: Représentation schématique de différents réacteurs *scale-down* SDR (Neubauer and Junne, 2010).

1.2.2.3 Conclusion : Effet des hétérogénéités de concentration en substrat carboné sur les micro-organismes

Il a déjà été évoqué que des baisses de rendements de croissance de la biomasse sont observées quand on passe d'un bioréacteur de laboratoire à l'échelle industrielle. De plus, pour les levures *S. cerevisiae*, George et al. (1998) mettent en évidence l'apparition du métabolisme *overflow* provoqué par l'existence de fortes concentrations en substrat carboné qui expliquent en partie la baisse de rendement en biomasse par la production d'éthanol proche de la zone d'injection en substrat (Bylund et al., 1998). Des observations similaires existent dans le cas des bactéries *E. coli*, où des baisses de rendement plus importantes ont également été observées. L'apparition des mécanismes d'*overflow* et anaérobie expliquent en partie cette diminution. Hewitt et al. (2000) ont de plus montré que la viabilité des micro-organismes était également liée au mélange.

Les cellules circulant dans les bioréacteurs sont soumises à différentes fluctuations de concentration. Des fluctuations de grandes amplitude sont observable à l'échelle du réacteur et dont la période est proche du temps de circulation, et des fluctuations de fréquence élevée et d'amplitude moindre ayant lieu à l'échelle microscopique. Ces deux types de fluctuations coexistent et peuvent être prépondérant l'un sur l'autre. De manière plus générale, les fluctuations à l'échelle microscopique seront toujours existantes, même si on est en présence d'un réacteur parfaitement mélangé à l'échelle macroscopique, comme l'ont montré Lin and Neubauer (2000). Les fluctuations de grande amplitude sont, quant à elle, aujourd'hui bien connues, et l'utilisation de SDR permet d'imiter à l'échelle du laboratoire l'alternance entre zones fortement et faiblement concentrées. Des résultats sur les pertes de performance des bioréacteur industriels ont ainsi pu être en partie obtenus, notamment en terme d'étude du comportement cellulaire face à l'intensité de la perturbation.

L'exposition répétée d'une population de micro-organismes à des fluctuations de concentration de plus ou moins grande amplitude peut également entraîner une ségrégation au sein-même de la population en terme d'état physiologique, montrant ainsi la capacité des cellules à s'adapter à leur milieu environnant. L'adaptation peut s'expliquer de la manière suivante. Le micro-organisme, en tant qu'usine cellulaire, doit gérer des flux de matière et d'énergie. De façon schématique, on peut dire que le micro-organisme maximise la production des éléments nécessaires à la croissance lorsque l'énergie est abondante. Le rendement de conversion de substrat en biomasse est fort, mais le rendement énergétique faible. A l'inverse, lorsque l'énergie est limitante, l'ensemble des réactions est mené avec un rendement énergétique maximal, parfois au détriment du rendement de conversion

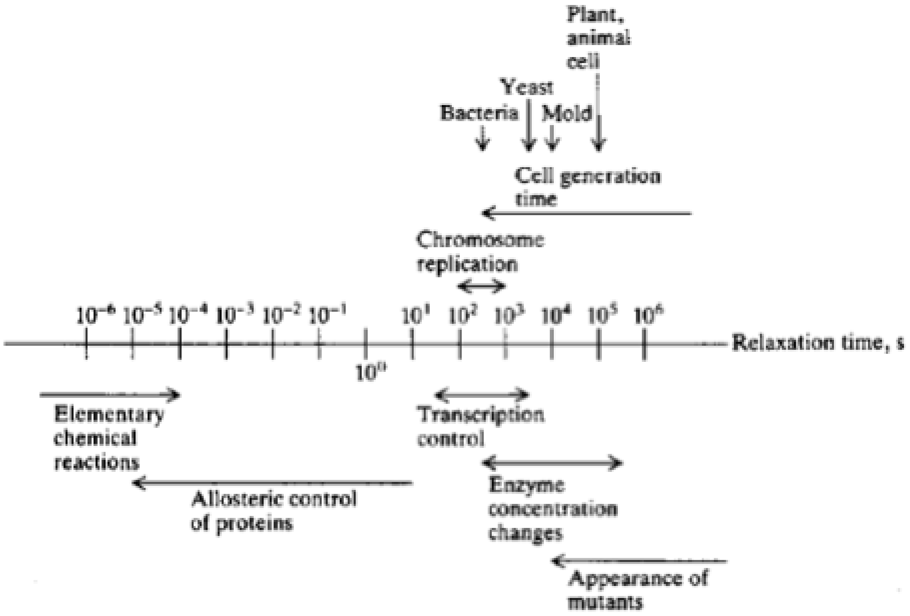

FIGURE 1.5: Ordre de grandeur des temps d'adaptation des micro-organismes (Bailey and Ollis, 1986).

du substrat. Dans un réacteur aéré, l'énergie est obtenue à partir de l'oxygène, On a pu observer que la réponse des micro-organismes à une variation de la concentration d'oxygène était rapide (Bylund et al., 1998).

Enfin, l'adaptation des micro-organismes requiert un temps caractéristique dont la détermination exacte n'est pas connue. À l'inverse des réactions chimique pour lesquelles les cinétiques sont connus, le temps caractéristique d'une cellule microbienne regroupe un grand nombre de facteurs. Par exemple ce temps dépendra du type de micro-organisme et de métabolisme considéré. Bailey and Ollis (1986) proposent une classification des temps de relaxation des micro-organismes, reportée sur la figure 1.5. On peut ainsi se demander quel temps caractéristique il est intéressant de considérer dans les bioréacteurs : réaction biologique ? consommation du substrat ? vitesse d'assimilation ? à l'échelle d'une population de micro-organismes ou d'une cellule ? Ces temps caractéristiques biologiques sont à comparer avec les temps caractéristiques du mélange dont les valeurs sont différentes localement et selon le mécanisme de mélange considéré. C'est ce que nous allons voir dans la partie 1.3.

1.2.2.4 Réponse biologique

Les exemples cités précédemment montrent que les cellules répondent aux variations de leur environnement en terme de concentration en substrats. D'autres études ont également montré que les micro-organismes sont sensibles aux contraintes mécaniques qu'elles subissent dans les bioréacteurs. Yim and Shamlou (2000) proposent une classification des contraintes subies par un micro-organisme suspendu dans un bioréacteur :

- collisions entre particules, et collisions particules-parois,
- contraintes de cisaillement et d'élongation,
- interactions physiques et physico-chimique aux interfaces gazeuses.

Étant donnée le faible écart de densités volumiques entre le fluide et les micro-organismes, les collisions sont en générales négligées. Les cellules étant transportées par l'écoulement subissent alors des contraintes hydrodynamiques, que l'on peut diviser en contraintes de pression, déformations visqueuses et contraintes turbulentes. Les cellules répondent ainsi en se déformant, et l'apparition d'états physiologiques différents est directement liée à ces déformations. Cependant, nous ne prendrons pas en compte ces phénomènes dans ce travail et nous attarderons uniquement sur l'effet de l'hydrodynamique sur le mélange du substrat.

Globalement, tout micro-organisme soumis a une contrainte (mécanique ou énergétique) va s'adapter en utilisant d'autre ressource, par exemple lorsque l'un des substrat est épuisé. Si la contrainte persiste, le micro-organisme modifiera son métabolisme et son matériel génétique de façon à résister à la contrainte. Ainsi, les micro-organismes ont la capacité de répondre aux contraintes de leur environnement, et de s'y adapter. Toutefois, cette réponse du micro-organisme modifie en retour l'environnement du micro-organisme. Ainsi lors de l'activation du métabolisme *overflow*, la production et l'excrétion de métabolites vers le milieu extérieur va entraîner une diminution du pH de celui-ci, et modifier les propriétés physico-chimique du fluide par exemple.

De manière plus critique, la culture de micro-organismes dans des milieux à concentration limitante en substrat, peut entraîner une augmentation de la capacité d'assimilation de ces derniers (Ferenci, 1996, 1999b,a). Une consommation plus élevée est alors observée lorsque ces micro-organismes se retrouvent dans un milieu de culture favorable (Lara et al., 2006a). Celle-ci entraîne donc l'apparition de gradients de concentrations à l'échelle du micro-organisme entre son interface et la concentration du bioréacteur. De manière plus générale, la consommation du sucre par les micro-organismes va agir directement sur le fluide environnant. C'est ce qu'on appelle le couplage inverse biologique. Celui-ci est la plupart du temps négligé mais fera l'objet du dernier chapitre de ce travail.

Nous allons maintenant nous attarder sur la description du mélange.

1.3 Caractérisation du mélange dans les bioréacteurs

Les réacteurs biologiques, tout comme les réacteurs chimiques, sont le théâtre de réactions biologiques/chimiques à l'échelle moléculaire. Le mélange à l'échelle microscopique, appelé micro-mélange, va donc précéder et influencer directement la réaction. Dans les réacteurs chimiques, l'apparition de produits différents de ceux attendus en terme de taille de précipités par exemple a été observée (Pohorecki and Baldyga, 1988). Cette influence du mélange sur les rendements a également été mise en évidence dans des procédés réactionnels, et notamment dans les bioréacteurs comme nous avons pu le voir précédemment. De plus, compte-tenu de l'hydrodynamique turbulente du bioréacteur, il est nécessaire d'analyser les différents mécanismes de mélange ainsi que les échelles associées.

1.3.1 Mécanismes du mélange turbulent

Le processus de mélange turbulent est très complexe, on y distingue trois niveaux : le macro-mélange, le méso-mélange et le micro-mélange. Le macro-mélange correspond au mélange à l'échelle du bioréacteur et détermine l'environnement pour le méso- et micro-mélange. Le fluide est convecté et subit le méso- et micro-mélange à travers différentes zones du bioréacteur où les propriétés de la turbulence varient. Le méso-mélange peut être défini comme l'échange, aux grandes échelles de la turbulence, entre les zones d'injections et l'environnement proche. Il concerne également le mélange

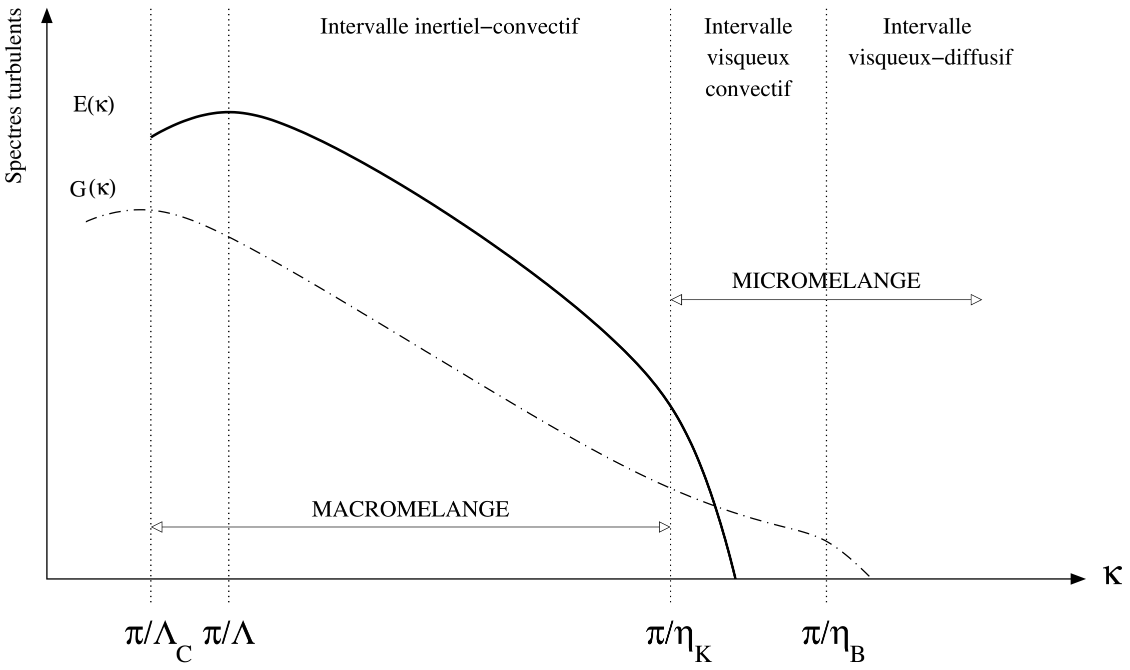

FIGURE 1.6: Spectres d'énergie cinétique $E(k)$ et de concentration $G(k)$ pour le cas $Sc \gg 1$ en représentation log-log.

dû à la désintégration des grands tourbillons dans la zone inertielle-convective. Enfin, le micro-mélange est le dernier stade du mélange turbulent et concerne la déformation visqueuse-convective d'éléments fluides, suivi de la diffusion moléculaire. Le processus de déformation visqueux-convectif a pour propriété d'accélerer la diffusion moléculaire et représente une des principales caractéristique du micro-mélange turbulent.

Les intéractions entre mélange et réaction ont lieu à l'échelle microscopique. Cependant, les macro- et méso-mélange ont un effet indirect sur la réaction car la structure des grands tourbillons détermine l'environnement pour le micro-mélange. Pohorecki and Baldyga (1983) a proposé une interprétation spectrale développée par la suite par Baldyga J. (1986); Baldyga and Bourne (1984). En regardant les spectres de fluctuations de vitesse et de fluctuations de concentration reportés sur la figure 1.6 qui expriment, en fonction du nombre d'onde (inverse de la taille des tourbillons), les densités spectrales d'énergie cinétique $E(k)$ et de fluctuations de concentration $G(k)$ pour un liquide, on peut alors distinguer plusieurs intervalles caractéristiques. Tout d'abord, l'intervalle inertiel pour la densité spectrale d'énergie cinétique compris entre l'échelle intégrale Λ et l'échelle de Kolmogorov η_K. Les tourbillons les plus énergétiques de taille Λ vont transmettre leur énergie aux tourbillons les plus petits et ce jusqu'à ce que la taille des tourbillons atteigne l'échelle de Kolmogorov η_K, où l'énergie sera dissipée par chaleur et où la viscosité domine. En ce qui concerne le scalaire, on distingue trois régions correspondant chacune à un mécanisme de mélange différent. Entre les échelles intégrales du scalaire (Λ_S) et de Kolmogorov, on se trouve dans le processus du méso-mélange inertiel-convectif où des paquets de fluides sont déformés et rompus par les mouvements du fluide, ainsi leur taille initiale est réduite, proportionnellement au taux de dissipation du scalaire ε_S, et sans effet de viscosité. C'est le cas pour des liquides dont le nombre de Schmidt est grand devant l'unité : les effets de la diffusion moléculaire sont négligeables. Ensuite, lorsque l'on se trouve entre les échelles de Kolmogorov et de Batchelor η_B, les tourbillons sont soumis à un cisaillement laminaire et leur taille est donc réduite par déformation visqueuse, tandis que la diffusion moléculaire commence elle aussi à jouer un rôle dans le mélange : c'est ce qu'on appelle la zone visqueuse-convective. Enfin, sous l'échelle de Batchelor, on trouve l'intervalle visqueux-diffusif où la diffusion moléculaire et le cisaillement laminaire sont du même ordre de grandeur. Ce spectre correspond aux fluides à fort nombre de Schmidt, (liquides comme dans les bioréacteurs), mais nous verrons ultérieurement que le spectre des fluctuations de concentrations dans le cas de fluides ayant un nombre de Schmidt de l'ordre de 1 est différent. La figure 1.7 donne une représentation schématique des mécanismes de mélange turbulent.

1.3.2 Echelles de longueur de mélange

Deux échelles précédemment citées sont importantes pour la description du mélange turbulent d'un scalaire passif. Premièrement, l'échelle de longueur intégrale du scalaire Λ_S. Elle caractérise les plus grandes structures dans le champ du scalaire. Elle est généralement déterminée par les conditions initiales du champ scalaire ou bien par le mélange turbulent lui-même qui créé des tourbillons du scalaire avec une taille caractéristique proche de celle de l'échelle intégrale du fluide Λ. Généralement, on observe des inhomogénéités de distribution pour Λ_S qui résultent des gradients de scalaire à grande échelle, ainsi que du mélange turbulent lui-même.
On trouve ensuite l'échelle de Batchelor qui caractérise la taille des plus petits tourbillons où la diffusion moléculaire joue le rôle principal. L'échelle de Batchelor est exprimée en fonction de l'échelle de Kolmogorov :

$$\eta_B = Sc^{-1/2}\eta_K, \tag{1.6}$$

où Sc, appelé le nombre de Schmidt, représente le rapport entre la viscosité cinématique et la diffusivité du scalaire $\mathcal{D}_S$. On remarque alors que pour des nombres de Schmidt de l'ordre de 1^1, les plus petites échelles du scalaire sont du même ordre que celle de Kolmogorov. En revanche, pour des nombres de Schmidt plus importants (pour des liquides), le champ du scalaire comportera plus de petites structures que le champ de vitesse. La réaction se faisant au niveau moléculaire, il est donc indispensable de prendre en compte ces petites structures. Nous verrons que ces petites structures du scalaire représentent une limitation pour la simulation numérique directe des écoulements turbulents dans le cas de liquide notamment. Tout comme on peut trouver une échelle de longueur caractéristique pour chaque mécanisme de mélange, on peut leur associer une échelle de temps.

1.3.3 Echelles de temps de mélange

Comme on a pu le voir, le macro-mélange est associé à l'échelle du bioréacteur agité dans son ensemble. Le temps caractéristique associé est alors en général assimilé au temps de circulation ou temps de séjour T_C. Cela correspond au temps mis par un élément fluide pour parcourir le réacteur avant de revenir dans la zone initialement prédéfinie (Figure 1.7a). On le calcule en général à partir du volume utile du réacteur V_B, divisé par la capacité de circulation (produit du nombre de circulation N_C, de la vitesse d'agitation $\mathcal{N}$ et du diamètre de l'agitateur d_A, voir équation (1.9)). Expérimentalement, on détermine également le temps de macro-mélange à partir du point de l'injection du scalaire. Les résultats obtenus sont du même ordre de grandeur dans les deux cas, donc le calcul à partir de la capacité de circulation est conservé. Ce temps de circulation augmente notablement lorsque l'on passe d'un réacteur à l'échelle de laboratoire à l'échelle industrielle jusqu'à être de l'ordre de la minute pour de très gros volume. De ce fait, des gradients macroscopiques de concentration apparaissent et provoquent une diminution du rendement de production (Larsson et al., 1996; Bylund et al., 1998). Cependant un scale-up entraîne également une diminution du taux de dissipation en raison des grands volumes et puissances d'agitation utilisées. On peut également penser que cette baisse de la puissance dissipée intervient également dans les baisses de rendement

---

[1] Pour des nombres de Schmidt inférieurs à 1, on définit une échelle diffusive comme $\eta_D = (\mathcal{D}^3/\varepsilon)^{1/4}$.

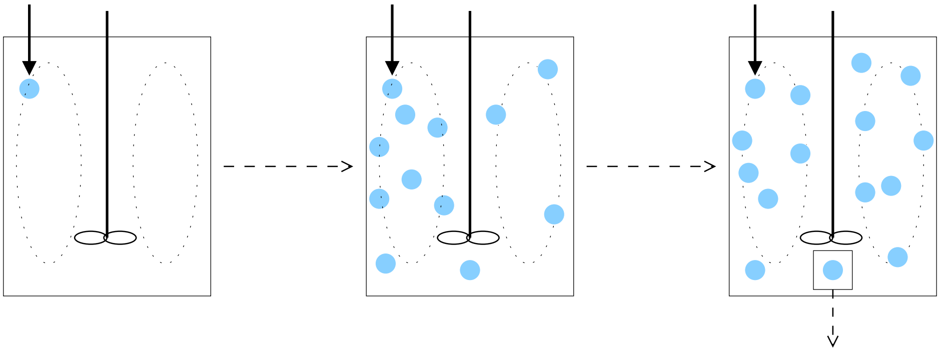

(a) Macromélange

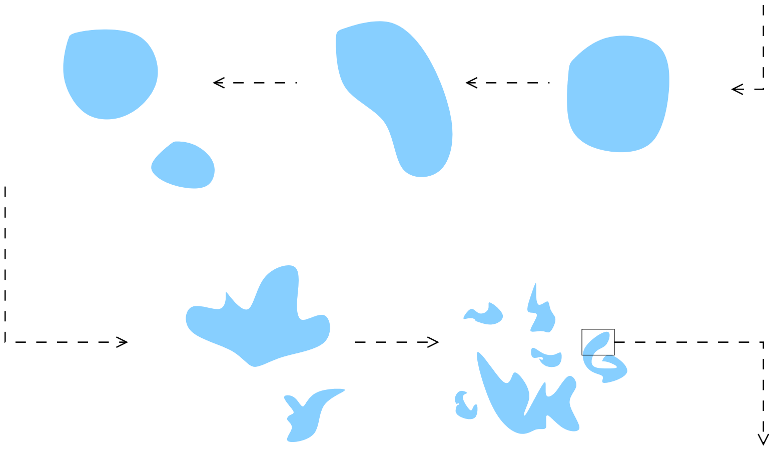

(b) Mésomélange

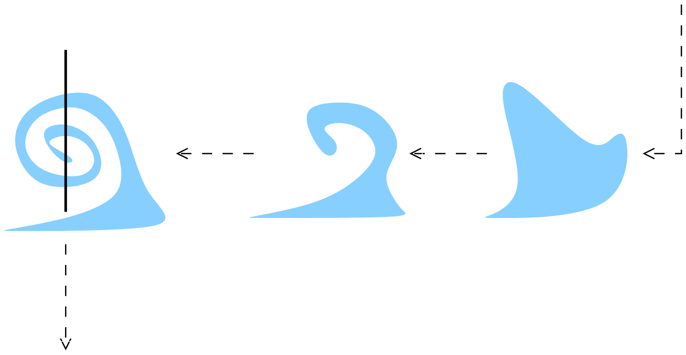

(c) Micro-mélange par incorporation

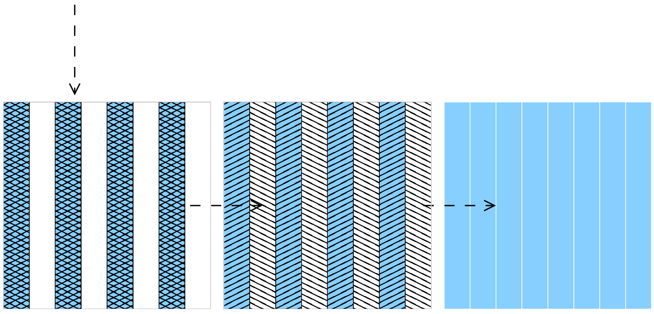

(d) Mésomélange

Figure 1.7: Représentation schématique des mécanismes de mélange turbulent (Baldyga and Bourne, 2003).

observées. Plus particulièrement, Wenger and Dunlop (1994) ont montré une influence directe de la vitesse d'agitation (et donc du macro-mélange), à l'échelle d'un bioréacteur de laboratoire, sur le rendement de croissance de la biomasse.

En ce qui concerne l'échelle de temps du méso-mélange (Figure 1.7b), on la définit comme la durée nécessaire pour réduire la taille d'un paquet de fluide de l'échelle intégrale du scalaire Λ_S à l'échelle de Kolmogorov η_K. Il correspond également au temps de retournement d'un tourbillon de taille Λ_S, et est donc relié au temps de dissipation de l'énergie $\tau_\varepsilon = q_f^2/\varepsilon_f$ (équation (1.11)).

De même, on définit le temps du micro-mélange visqueux-convectif (Figure 1.7c) : le temps nécessaire pour réduire les tourbillons de l'échelle de Kolmogorov à l'échelle de Batchelor sans considérer la diffusion moléculaire τ_K (Equation (1.13)). Baldyga J. (1986) proposent une formulation qui prend en compte les effets moléculaires et de cisaillement laminaire :

$$\tau_{Ds} = 2\left(\frac{\nu}{\varepsilon_f}\right)^{1/2} \text{arcsinh}(0,05Sc). \tag{1.7}$$

Toutes ces échelles de temps sont donc caractéristiques du mélange turbulent, et même si les réactions chimiques ont lieu à l'échelle microscopique, le temps de mélange total est contrôlé par le processus le plus lent (Fox, 2003). On peut d'ailleurs ordonner tous ces temps de la manière suivante :

$$\tau_{Ds} < \tau_K < \tau_\varepsilon < T_C. \tag{1.8}$$

Le tableau 1.2 regroupe les différentes échelles de temps et de longueurs caractéristiques pour le mélange turbulent. Pour plus de détails, Delafosse (2008) reporte des valeurs de ces mêmes échelles pour deux types de bioréacteurs, et différents taux moyens de dissipation visqueuse (agitations différentes). Un tableau regroupant les temps caractéristiques de la réaction associée à la consommation de substrat pour la croissance de micro-organismes est également fourni. En effet, une fois les différents mécanismes de mélange listés, il faut ensuite s'intéresser à la compétition entre réaction et mélange turbulent.

TABLE 1.2: Expression des échelles de longueur et des temps caractéristiques pour les mécanismes de mélange turbulent.

Mécanismes	**Echelles de longueur**	**Echelles de temps**
Macro-mélange	d_A	$T_C \approx \dfrac{V}{N_c \mathcal{N} d_A^3}$ (1.9)
Méso-mélange inertiel-convectif	$\Lambda_S \approx \dfrac{{q_f^2}^{3/2}}{\varepsilon_f}$ (1.10)	$\tau_\varepsilon \approx \dfrac{q_f^2}{\varepsilon_f}$ (1.11)
Micro-mélange visqueux-convectif	$\eta_K \approx \left(\dfrac{\nu^3}{\varepsilon_f}\right)^{1/4}$ (1.12)	$\tau_K \approx \left(\dfrac{\nu}{\varepsilon_f}\right)^{1/2}$ (1.13)
Micro-mélange visqueux-diffusif	$\eta_B \approx \text{Sc}^{1/2}\eta_K$ (1.14)	$\tau_{D_s} \approx \left(\dfrac{\nu}{\varepsilon_f}\right)^{1/2} \ln(Sc)$ (1.15)

1.3.4 Compétition entre réaction biologique et mélange

Avant toute modélisation, il est nécessaire de savoir quel mécanisme de mélange peut affecter la réaction biologique. On peut pour cela raisonner en terme de temps caractéristique de la réaction biologique et le comparer aux échelles de temps du mélange turbulent. Dans un premier temps, si on considère τ_M un temps caractéristique quelconque du mélange et le temps de réaction biologique τ_R, on va distinguer trois cas : $\tau_M \ll \tau_R$, $\tau_M \approx \tau_R$ et $\tau_M \gg \tau_R$. Dans le premier cas, la réaction biologique est très lente devant l'échelle de temps du mélange, et il n'y a alors pas d'effets du mélange sur la réaction. Dans les deux derniers cas cependant, il est nécessaire de comparer chaque temps caractéristique du mélange à la vitesse de réaction biologique :

- $T_C < \tau_R$: le réacteur est parfaitement macro-mélangé et micro-mélangé pour la réaction. En effet, compte-tenu de la classification des temps caractéristiques dans le bioréacteur (équation (1.8)), la réaction biologique sera plus lente que n'importe quel mécanisme de mélange. On peut s'attendre à avoir ce genre de réacteur parfaitement mélangé dans le cas d'expérience en laboratoire où les hétérogénéités en substrat sont faibles par exemple.
- $\tau_\varepsilon < \tau_R < T_C$: la réaction biologique est plus rapide que le macro-mélange, ce qui conduit à l'apparition de gradients de concentration en substrat. Le réacteur est composé de zones macroscopiques mal mélangées tandis que chaque région est bien homogène (micro-mélangée). Les micro-organismes contenus dans un tel environnement voient donc dans leur environnement des changements de concentrations qui fluctuent à la période T_C, correspondant au temps de circulation. Ce type de situation est typique des réacteurs industriels *fed-batch.*
- $\tau_K < \tau_R < \tau_\varepsilon$: ici, la réaction biologique se fait dans un temps plus faible que celui pour réduire l'échelle intégrale de concentration. Cela signifie que les micro-organismes voient leur environnement "rechargé" en substrat à une fréquence $1/\tau_\varepsilon$. Cependant, la distribution de concentration est totalement dépendante de la turbulence et les micro-organismes seront fortement influencés par le mélange dans ce cas. Cette situation, bien que difficile à caractériser, est plus qu'envisageable dans les bioréacteurs industriels compte-tenu des taux de dissipation variables spatialement dans le bioréacteurs, et de la dépendance directe des échelles du méso- et micro-mélange à cette variable spatiale (équation (1.11) et (1.13)).
- $\tau_{Ds} < \tau_R < \tau_K$: enfin la situation où la réaction est très rapide par rapport à la vitesse de micro-mélange. Les micro-organismes consomment plus vite le substrat que celui-ci n'est renouvelé dans l'environnement proche de la cellule. On va alors trouver des zones dans lesquelles le substrat est épuisé dans l'environnement proche de la cellule. Le régime est alors limité par le mélange.

On peut donc répertorier plusieurs situations où le mélange et la réaction biologique entrent en compétition et il est nécessaire de savoir dans quel régime on se trouve afin de modéliser au mieux un bioréacteur.

Temps caractéristique de la réaction biologique

On a précédemment introduit la notion de temps caractéristique de la réaction biologique. Or, à l'inverse d'un réacteur chimique où l'on peut arriver à connaître exactement les réactions ayant lieu, ainsi que leur cinétiques respectives, les micro-organismes sont le théâtre d'un grand nombres de réactions, qui varient en fonction du milieu environnant et de l'histoire des cellules. Une cinétique complète est donc impossible. On exprime alors en général le temps de la réaction biologique pour un composé et pour la culture associée. Par exemple, pour la croissance de la biomasse, on prend en général :

$$\tau_{R_X} = \frac{1}{\mu_{Xmax}}, \tag{1.16}$$

ce qui donne des temps de réaction de l'ordre de quelques heures. On ne devrait donc jamais avoir d'effet du mélange car on a vu que dans les bioréacteurs industriels le temps de circulation s'élevait au maximum à quelques minutes. Or , les expériences de la littérature ont montré un effet de mélange. Cette approximation pour le temps de réaction n'est donc pas pertinente.

On peut également se baser sur le temps caractéristique de consommation du substrat carboné en reprenant l'équation (1.1b) :

$$\tau_{R_S} = \frac{S}{q_{Smax} X}. \tag{1.17}$$

Le temps de réaction varie alors en fonction de la concentration en biomasse X et en substrat S. Cette dernière étant transportée par l'écoulement, le mélange aura alors une influence directe sur le temps de réaction. Il est possible de déterminer la vitesse maximale de consommation de manière globale expérimentalement, mais on n'attend pas les valeurs locales de celles-ci. Or, la littérature rapporte des disparités sur ces valeurs, notamment concernant les milieux de culture et l'hydrodynamique du milieu. Ferenci (1999b) a par exemple montré que si des cellules sont cultivées dans un milieu où le substrat est limité, l'affinité K_S pour le substrat augmente. Selon le fonctionnement du réacteur, Neubauer et al. (1995a) ont aussi mis en évidence des déviations dans les vitesses maximales d'assimilation mesurées entre un bioréacteur *batch* et *fed-batch*.
Ces exemples montrent bien la difficulté de définir des cinétiques qui soient transposables quel que soit le type de procédés, les conditions de cultures et l'histoire des micro-organismes.

1.3.5 Conclusion

Au cours de cette partie, une brève étude sur les mécanismes de mélange en régime turbulent a été introduite. Une analyse spectrale en terme d'échelle de longueur a été proposée et les temps caractéristiques du mélange ont été défini pour les différents processus entrant en jeu. Ces temps caractéristiques du mélange ont été confrontés au temps caractéristique de la réaction biologique, et la difficulté de définir cette dernière a été mise au jour. Une revue non-exhaustive des résultats expérimentaux mettant en évidence l'effet du mélange sur les procédés biologiques avait auparavant été introduite. De plus, l'adaptation de la phase biotique à son milieu environnant est un phénomène encore mal connu et dont la prédiction se relève être impossible dans un procédé biologique. En pratique, les observations expérimentales sur les propriétés biologiques montrent une grande variabilité d'une étude à une autre.

Ensuite, la plupart des données sur les vitesses maximales d'assimilation, affinité pour le substrat, consommation du substrat sont déterminées à partir de bilan de matière sur l'ensemble du bioréacteur. On accède donc seulement à une valeur globale des paramètres régissant la croissance. Or, il a été montré que les effets locaux sont extrêmement importants dans les procédés biologiques, du fait de la compétition entre mélange et réaction biologique notamment. Il apparaît ici une première conclusion importante du point de vue de la modélisation des bioréacteurs : considérer une réaction biologique à l'échelle globale d'un bioréacteur c'est à dire en se basant sur la concentration moyenne dans le bioréacteur $< S >$, n'est pas une solution valable dans le cas où des inhomogénéités de concentrations en substrat sont présentes dans le milieu. Un enjeu majeur, au delà de la modélisation de la réaction biologique, se situe donc également dans la modélisation de l'hydrodynamique de la cuve et du mélange. La partie suivante a pour but de recenser de manière la plus exhaustive possible les différentes approches existantes pour la modélisation des bioréacteurs.

1.4 Modélisation des bioréacteurs - Approche « génie des réacteurs »

L'état physiologique d'un micro-organisme situé dans l'environnement dynamique d'un bioréacteur est le résultat d'interactions importantes entre le milieu extracellulaire (de l'environnement proche des micro-organismes) et les mécanismes cellulaires propres au micro-organisme considéré. Le fonctionnement d'un système biologique pour la production de biomasse par exemple est donc régi simultanément par des stimuli extérieurs à la cellule, les propriétés des cellules et à leur réponse dynamique à l'environnement extérieur.

Compte-tenu de ces remarques, il apparaît que l'amélioration des performances des bioréacteurs, et, en particulier le choix des conditions de culture, nécessite une description des phénomènes à l'échelle locale (échelle du micro-organisme). D'un côté, la formulation mathématique des réactions intracellulaires, mais aussi des mécanismes d'adaptation aux variations de l'environnement extérieur doivent être abordées. De plus, la caractérisation complète de l'hydrodynamique dans le bioréacteur est nécessaire afin d'étudier l'impact des variations spatiales et temporelles de l'intensité du mélange ou du transfert de matière sur les performances du bioréacteur.

Une modélisation correcte se baserait donc sur la résolution exacte des réactions internes aux cellules en tenant compte des variations du milieu extérieur. La première résolution est basée sur la modélisation des réseaux métaboliques et permet d'expliquer certaines propriétés des systèmes biologiques complexes (Kitano, 2002). En ce qui concerne la détermination de la phase porteuse liquide, la mécanique des fluides numérique est le candidat idéal car elle détermine entièrement l'hydrodynamique par la résolution des équations de Navier-Stokes. Nous aborderons cette approche dans la partie suivante et allons nous intéresser ici à une approche mécanistique pour la modélisation des bioréacteurs.

Cette dernière se base sur une analyse mécanistique du mélange et simplifie le problème en ne considérant qu'une partie des mécanismes intervenants. Par exemple dans le cas du mélange turbulent, on peut choisir de modéliser soit le mélange macroscopique, soit le mélange microscopique. On va ici s'attarder sur la prise en compte du mélange macroscopique en présentant les différents types de modélisation existants dans la littérature.

1.4.1 Modélisation de l'hydrodynamique

Association de réacteurs idéaux

Basé sur la Distribution des Temps de Séjour (DTS) initialement introduite par Danckwerts (1958), ce type d'approche représente un réacteur continu comme l'association de plusieurs réacteurs parfaitement mélangés et de réacteurs piston dont la DTS est connue. En agençant différents types de réacteurs on peut à modéliser la DTS du réacteur continu.
L'extension de la méthode aux réacteurs *fed-batch* a été proposée par Villermaux (1995) où la détermination des DTS dans ces bioréacteurs est nécessaire. L'approche a également été utilisée dans le cas des bioréacteurs continus afin de prédire les taux de dilution critique D_c (Bailey and Ollis, 1986).

Modèles de compartiments

Une autre approche largement répandue consiste à découper le bioréacteur en un nombre fini de volumes parfaitement macro-mélangés, c'est-à-dire dans lesquels tout scalaire passif est homogène

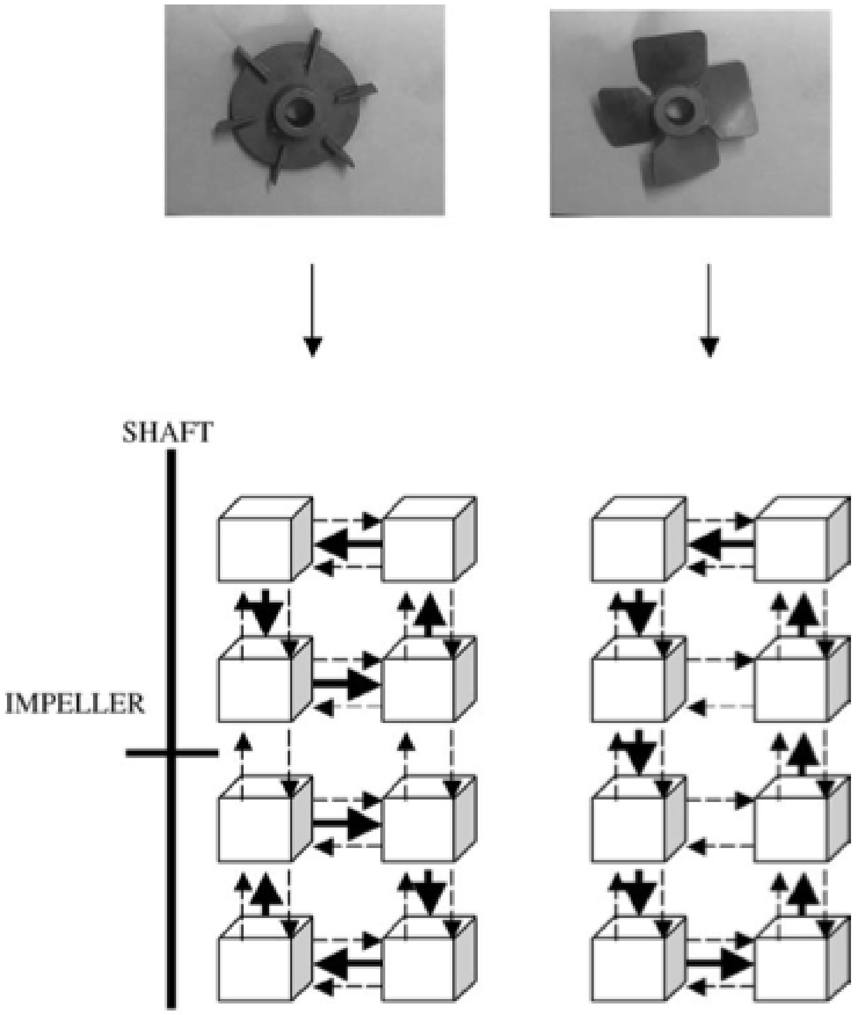

Figure 1.8: Schéma simplifié de l'association de compartiment dans le cas d'une turbine radiale (RDT6 à gauche) et axiale (A315 à droite) (Delvigne et al., 2005a). Les flèches --→ et ←-- représentent les flux diffusifs et -▸les flux convectifs.

(concentration, température). Le principe de cette approche est ensuite de relier chaque volume élémentaire à son voisin par un flux convectif et un flux diffusif représentant l'effet de la turbulence. La figure 1.8 illustre le principe de fonctionnement d'une telle approche.

Les différents échanges de matière sont basés sur les grandeurs globales connues du réacteur modélisé. Ainsi, on peut remarquer que les compartiments seront reliés différemment selon le type de cuve ainsi que selon le nombre et le type d'agitateur (voir la figure 1.8, (Delvigne et al., 2005b)), mais également selon la dimension de la cuve, et la vitesse d'agitation. Les flux convectifs en dépendent directement (Reuss and Jenne, 1993; Guillard, 1999). La détermination des flux diffusifs est quant à elle plus complexe et représente la principale limitation de ce type de modélisation. En effet, ces derniers caractérisent les échanges liés à la turbulence et sont difficiles à évaluer dans une cuve agitée.

De plus, malgré la diversité des modèles de compartiment, ils sont général en deux dimensions et ne rendent pas compte de toutes les éventuelles dissymétries de l'écoulement. En revanche, leur mise en place assez simple permet de modéliser de grands volumes, c'est pourquoi ils sont très répandus pour l'étude des bioréacteurs.

Extension des modèles de compartiment : approche stochastique et approches hybrides

Afin de palier aux limitations des modèles de compartiments, notamment en terme de détermination des flux diffusifs, de nouvelles approches ont été développées. Delvigne et al. (2005a) proposent un modèle probabiliste stochastique pour le mélange. En effet, le passage de paquets de fluide d'un compartiment à un autre sera gouverné de manière probabiliste. De plus son implémentation simple et peu coûteuse permet d'envisager de coupler ce type d'approche avec un modèle cinétique pour la réaction biologique. Cette approche se base sur les paramètres obtenus avec des modèles de compartiments et Delvigne et al. (2005b) montrent que les résultats obtenus par les deux approches sont similaires. Elle permet donc de pouvoir modéliser le processus de mélange, ainsi que la circulation de micro-organismes dans le bioréacteur (Delvigne et al., 2005a). Les profils de concentration vus par les micro-organismes dans le bioréacteur peuvent ainsi être déterminés. Delvigne et al. (2005a) ont ainsi pu simuler une culture *fed-batch* d'*E. coli*.

Toujours dans le but d'améliorer les modèles de compartiments, des méthodes hybrides ont également été développées, dans lesquelles l'approche compartiment est combinée avec des calculs CFD, notamment pour la détermination des flux de matière et d'énergie. Bauer and Eigenberger (1999) ont proposé une étude hybride dans le cas d'une colonne à bulle. Les compartiments sont des zones verticales auxquelles on ajoute un modèle de transfert de masse dans la direction horizontale entre chaque zones. Ces flux latéraux sont calculés à l'aide d'un calcul CFD diphasique. Les paramètres requis pour le calcul numérique sont, quant à eux, déterminés par le modèle de compartiment. Plus récemment, Bezzo et al. (2003) ont appliqué cette stratégie hybride au calcul de la production de gomme xanthane en bioréacteur agité. Les auteurs ont couplé une description Eulérienne de l'écoulement du fluide à un modèle de compartiments en considérant un nombre fini de volumes parfaitement homogènes et capable d'échanger de la matière avec les volumes voisins.
Nous allons maintenant voir comment certains auteurs ont pu également coupler la réaction biologique avec ces approches génie des réacteurs pour l'hydrodynamique.

1.4.2 Couplage de l'hydrodynamique avec la réaction biologique

Certains auteurs ont fait des simulations numériques en couplant les différents modèles précédents à une réaction biologique pour la biomasse. Dans la plupart des cas, des modèles de compartiments sont utilisés pour l'hydrodynamique auxquels sont ajoutées des équations de cinétique pour la réaction biologique. Dans leur travaux Nagy et al. (1995) ont effectué des simulations sur la fermentation de l'acide glutamique en bioréacteur en fonction des conditions de mélange et de la configuration des cuves. En utilisant un modèle de compartiment, dont les paramètres avaient au préalable été déterminés par Mayr et al. (1993), un modèle non-structuré pour la cinétique a été ajouté. Les auteurs ont caractérisé les effets du pH et de la concentration en oxygène sur la fermentation.

Dans une autre étude, Vlaev et al. (2000) se sont intéressés à la production d'un antibiotique, la tylosine, en utilisant un modèle de compartiments composé de 600 zones. Ils ont caractérisé le transfert d'oxygène et une réaction biologique avec une cinétique du second ordre. A l'aide de ces outils, ils ont obtenus une prédiction des distributions spatiales des différents champs de concentration. Une des conclusions majeures de ce travail consiste en l'obtention de résultats propres à une cinétique du second ordre pour la réaction biologique. Or, un changement d'ordre des réactions est fortement envisageable, notamment dans le cas de concentrations très importantes en oxygène et substrat carboné, où une réaction d'ordre zéro paraît plus probable. De plus, les auteurs insistent sur les

variations brusques et de grandes ampleurs des concentrations subies par les micro-organismes lors de leur passage en différentes zones du bioréacteur.
Cependant, les différentes études citées ne s'attardent malheureusement pas sur la réaction biologique, mais sont principalement utilisés pour caractériser l'hydrodynamique liquide et le transfert d'oxygène dans les bioréacteurs de grande taille, à l'instar de l'étude menée par Zahradnik et al. (2001).

Bilan de population

Une autre approche peut également être utilisée pour modéliser les réactions biologiques en prenant en compte l'historique des trajectoires des micro-organismes par exemple. En effet, un bilan de population sur les micro-organismes (en Anglais PBE pour Population Balance Equation) permet de prendre en compte les variations observées par les micro-organismes. Fredrickson et al. (1967); Subramanian et al. (1970) ont introduit cette modélisation qui permet de décrire les distributions d'un certain nombre de paramètres intrinsèques à une population de micro-organismes. La plupart des modèles sont basés sur un état propre de la cellule, telle que la masse (Mantzaris et al., 1999), et les hétérogénéités sont constitutives des cellules elles-mêmes. Morchain et al. (2012) ont proposé une approche de bilan de population où les hétérogénéités de population sont induites par l'environnement des cellules, menant à des états cellulaires multiples en fonction de l'état de mélange par exemple, et à autant de réponses biologiques. Une modélisation complète d'un bioréacteur peut alors être envisagée en couplant ces bilans de population à un modèle hydrodynamique. Bezzo et al. (2003) utilise l'approche hybride modèle de compartiment / CFD appliquée à un modèle de bilan de population pour déterminer la distribution de masse des cellules dans le cas de la croissance de population. Morchain et al. (2012) couple l'approche bilan de population à des calculs CFD dans le cas d'un réacteur idéal.
Cependant, quelle que soit l'approche choisie pour les bilans de population, un problème inhérent à cette formulation du problème réside dans la limitation numérique, car un grand nombre de fonctions intra- ou extra-cellulaire nécessitent d'être calculées.

Modèle de cellule isolée (Single Cell Model)

Une alternative au bilan de population a été introduite notamment par Ataai and Shuler (1985) et Kim and Shuler (1990), et reprise plus tard par Henson et al. (2002). Elle consiste à considérer chaque micro-organisme individuellement avec ses caractéristiques propres et de regarder la population de micro-organismes comme un ensemble de cellules isolées. Cette formulation présente l'avantage d'être plus facile à implémenter et de déterminer la structure intra-cellulaire et la dynamique des cellules par exemple. Ce type de modélisation se rapproche donc de la modélisation Lagrangienne où chaque inclusion est suivie. Néanmoins, ces modélisations considèrent un environnement parfaitement mélangé, ce qui est loin de rendre compte de la réalité, car on a pu voir précédemment que les variations spatiales de concentration dans les bioréacteurs ne peuvent pas être négligées.

L'approche mécanistique a été largement utilisée pour la modélisation des bioréacteurs. Cependant, comme nous avons pu le voir, elle possède bien des limitations, notamment la détermination des flux diffusifs dans le cas des modèles de compartiments. Des approches hybrides impliquant la mécanique des fluides sont développées car elles permettent une meilleure prédiction de l'hydrodynamique des bioréacteurs. Nous allons maintenant introduire l'approche mécanique des fluides pour la modélisation des bioréacteurs.

1.5 Simulation numérique des bioréacteurs à l'aide de la mécanique des fluides numérique

1.5.1 Introduction/État de l'art

La mécanique des fluides numérique est un outil de modélisation pour les bioréacteurs de plus en plus utilisé. Elle consiste en la résolution des équations de Navier-Stokes et est largement utilisée pour la modélisation d'écoulements réactifs. Dans le cas des bioréacteurs, les écoulements sont fortement turbulents, impliquant une large gamme d'échelles spatiales et temporelles. La résolution de toutes ces échelles directement à partir des équations générales de Navier-Stokes n'est alors possible que pour des cas d'écoulements académiques. Cependant, il est possible de déterminer l'hydrodynamique des bioréacteurs grâce à l'approche RANS (Reynolds-Averaged Navier-Stokes) et l'utilisation de modèles de turbulence. Ces modèles sont largement utilisés Fox (2003) et on les trouve notamment dans les codes de calculs commerciaux.

Du fait de l'aération des cuves des bioréacteurs, l'injection de bulles d'oxygène nécessite une résolution diphasique du problème. Dans le cas de l'approche RANS, des modèles à N-fluides ont été développés permettant ainsi de caractériser l'hydrodynamique et les interactions entre la phase liquide et la phase gazeuse. De plus, la présence des micro-organismes dans les bioréacteurs complexifie l'étude du fait des réactions biologiques à prendre en compte. En effet, le substrat est transporté par l'écoulement, mais des termes réactifs apparaissent à cause de l'assimilation de celui-ci par les micro-organismes.

Des modèles supplémentaires sont donc nécessaires, d'une part pour caractériser le mélange et l'assimilation à l'intérieur d'une maille du fluide. On peut rappeler ici que si la réaction biologique est rapide par rapport au temps de mélange, l'erreur sur la réaction sera importante si tous les mécanismes de mélange ne sont pas modélisés. L'utilisation de modèles de sous-maille est donc nécessaire dans le cas d'écoulements turbulents réactifs si la résolution ne se fait pas de manière directe, afin de prendre en compte les hétérogénéités à l'intérieur d'une maille. Ces dernières sont généralement décrites à l'aide d'une fonction de densité de probabilité (PDF pour Probability Density Function). Le tableau 1.3 inspiré par Fox (2003) présente les relations entre l'approche génie des réacteurs et Mécanique des Fluides.

TABLE 1.3: Caractérisation des approches de modélisations et équivalence entre approche génie des réacteurs et Mécanique des Fluides.

Processus Physique	Approche génie des réacteurs	Approche mécanique des fluides
Macro-mélange	DTS Modèles de compartiment	Modèles de turbulence pour le transport du scalaire
Méso-mélange	modèles de micro-mélange pour la ségrégation	méthodes PDF
Micro-mélange	modèles de micro-mélange temps de micro-mélange	Valeurs conditionnées de propriétés du scalaire

On va maintenant présenter les résultats de différents travaux de la littérature concernant la caractérisation de l'hydrodynamique dans des bioréacteurs, ainsi que les différentes approches pour modéliser la phase biotique dans le cas de simulations RANS.

1.5.2 Simulation RANS et couplage biologique

L'étude de l'hydrodynamique des bioréacteurs à l'aide de la mécanique des fluides s'est développée au cours des dernières années, et plusieurs travaux y sont dédiés. L'utilisation de l'approche RANS avec des modèles de turbulence adaptés lors d'études numériques semble donner des résultats encourageants. Cependant, plusieurs paramètres nécessitent d'être pris en compte pour l'étude numérique des bioréacteurs.

Hydrodynamique du bioréacteur - Phase porteuse

Tout d'abord, la géométrie de la cuve est un paramètre important dont il ne faut pas négliger l'impact sur les résultats hydrodynamiques. De plus, les cuves des bioréacteurs sont mélangées à l'aide d'agitateurs dont le nombre et la forme peuvent également varier. La turbine Rushton a été longuement étudiée et apparaît comme le type d'agitateur de référence car elle permet une recirculation du liquide dans l'ensemble du bioréacteur. Même si les résultats de différentes études numériques sont prometteurs, elles diffèrent selon les paramètres de simulation utilisés tels que le modèle de turbulence, l'approche de modélisation de la turbine, la taille du maillage. Jenne and Reuss (1999) proposent une analyse critique des différentes simulation effectuées par comparaison avec des résultats expérimentaux.

Le comportement de la phase liquide est donc obtenu par résolution des équations de Navier-Stokes moyennées, auxquelles on ajoute un modèle de turbulence (Pope, 2000). Les résultats obtenus sont généralement analysés en terme d'énergie cinétique et de champ de vitesse (Ranade, 1997; Hartmann et al., 2004), mais des études plus récentes ont permis de caractériser également le taux de dissipation dans la cuve (Delafosse, 2008).
D'autres études ont également permis de caractériser l'hydrodynamique de cuves agités avec des agitateurs de types différents ou en nombre plus important. Intuitivement, la complexité de la résolution augmente avec le nombre d'agitateurs (John et al., 1997).

Ecoulement gaz-liquide

L'aération des bioréacteurs étant un phénomène important pour les cultures aérobies. La modélisation des écoulement diphasiques turbulents peut alors se faire de deux manières distinctes. Dans l'approche Euler-Lagrange, les bulles d'oxygène sont suivies individuellement tandis que la phase continue est traitée de manière continue (Lapin and Lübbert, 1994), tandis que dans l'approche Euler-Euler, les deux phases sont traitées de manière continue (Schmalzriedt et al., 2003).
Il est à noter ici que l'oxygène ne sera pas considéré dans ce travail, et que l'on se focalisera sur le substrat transporté par la phase continue, et consommé par les micro-organismes.

Couplage de modèles non-structurés pour la réaction biologique

Le substrat est considéré comme un scalaire passif, c'est-à-dire qu'il n'influence pas l'hydrodynamique du bioréacteur. On peut cependant penser que du fait de la présence de substrat, de légères différences de masse volumique peuvent apparaître au sein de la phase porteuse. Mais, le mélange étant assuré au sein du bioréacteur, et les concentrations dans le bioréacteur restant peu élevées, on admettra que la phase porteuse reste à masse volumique constante.

Une équation de transport est donc résolue pour le substrat, dans laquelle on utilise un modèle non-structuré pour rendre compte du terme réactif. La cinétique de Monod est généralement utilisée.

Ainsi, Larsson et al. (1996) ont pu étudier l'impact de gradients de concentration en substrat sur la croissance de la biomasse et la formation de sous-produits. D'autres travaux ont également mis en évidence l'influence du point d'injection du substrat sur la distribution spatiale de celui-ci dans les bioréacteurs. Dans le cas d'un bioréacteur d'un volume de 68 L, Schmalzriedt et al. (2003) ont montré que pour une répartition plus homogène du substrat, l'injection dans une région proche de l'agitateur est préférable. Les auteurs ont également montré l'influence que peut avoir le type d'agitateur sur le mélange et donc la distribution du substrat.

1.5.3 Vers une résolution plus fine des réactions biologiques et de l'hydrodynamique

Modèles structurés et suivi lagrangien pour les micro-organismes

Les approches classiques de caractérisation de la réaction biologique par les modèles non-structurés du type Monod sont largement utilisées et permettent en première approche une bonne approximation pour la détermination de paramètres de fonctionnement par exemple. Cependant, il a été montré qu'elles échouent à prédire la croissance de la biomasse lors de brusques variations de concentration en substrat dans le milieu environnant des cellules. En effet, l'existence de concentrations différentes peut induire l'activation de transporteurs différents selon l'affinité au substrat. Cette réponse intracellulaire aux stimuli extracellulaires doit donc être prise en compte.

Schmalzriedt et al. (2003) proposent deux exemples de cette application, dont un modèle structuré pour *S. cerevisiae* avec la prise en compte de 15 métabolites intracellulaires et les concentrations extracellulaires en glucose et éthanol.

En utilisant des modèles structurés, des auteurs ont pu caractériser le comportement d'une population de cellules hétérogènes dans un bioréacteur agité à l'aide d'une approche lagrangienne. Partant de l'idée que le comportement d'une population de micro-organismes dépend du passé de chaque individu, Lapin et al. (2004) ont considéré l'évolution de l'état intracellulaire de cellules dont l'état initial est spécifié, couplé à une résolution eulérienne du fluide par la méthode RANS. Les micro-organismes sont donc suivis de manière lagrangienne et leur mouvement résulte de la convection déterminée par la simulation numérique couplée à la dispersion turbulente. L'état intracellulaire est déterminé par la résolution d'équations de conservation des espèces, équations couplées à la concentration de glucose dans le milieu extérieur notamment. L'application de cette méthode pour modéliser le comportement d'une population d'*E. coli* (Lapin et al., 2006) a démontré que l'activité du système PTS (Phosphotransferase System) dépend de la concentration locale de glucose mais aussi des concentrations en métabolites intracellulaires. Lapin et al. (2004) ont également appliqué cette approche dans le cas de *S. cerevisiae* en suivant les micro-organismes de manière continue (approche Euler-Euler). Ils ont alors pu mettre en évidence, pour deux bioréacteurs différents (laboratoire - 68 L et réacteur industriel - 900 L), l'existence de zones à très fortes concentrations en glucose menant à la production d'éthanol par le mécanisme *overflow*. De plus, des zones à très faibles concentrations en glucose, peuvent être à l'origine d'épisodes où les cellules sont affamées si leur passage est y est fréquent.

Simulation aux grandes échelles

Malgré des résultats satisfaisants des simulations RANS pour la caractérisation de l'hydrodynamique dans les cuves des bioréacteurs, une dépendance au modèle de turbulence utilisé existe. Singh et al. (2011) proposent une analyse des performances de différents modèles de turbulence pour la simulation d'un bioréacteur agité. Ils concluent que même si les résultats obtenus pour les vitesses moyennes axiales et tangentielles dans le réacteur sont satisfaisants, la prédiction de l'énergie cinétique turbulente et de la dissipation de celle-ci varie d'un modèle à l'autre.

C'est pourquoi la simulation aux grandes échelles (ou LES pour *Large Eddy Simulation*) a été utilisée dans différents travaux. À l'inverse de l'approche RANS, qui permet de calculer uniquement le mouvement moyen, la LES résout les champs instantanés jusqu'à une certaine échelle de longueur (appelée échelle de coupure), qui correspond en général à la taille des mailles, et qui fait intervenir un modèle de sous-maille pour modéliser les phénomènes sous cette échelle.

Dans leur travaux, Enfors et al. (2001) ont réalisé des simulations numériques aux grandes échelles pour un réacteur de 22 m^3, alimenté par une solution de substrat. N'incluant pas la consommation du substrat par les micro-organismes, ces simulations ont pu caractériser l'état de mélange du substrat dans la cuve. Les zones proches de l'injection sont très concentrées tandis que la concentration dans le bas de la cuve est très faible. Ils ont également montré l'existence d'importantes fluctuations de concentration en substrat au voisinage du point d'injection.

Delafosse et al. (2008) utilisent la LES pour décrire l'hydrodynamique d'une cuve agitée à l'aide d'une turbine Rushton, et comparent les résultats obtenus avec des résultats expérimentaux (Escudié and Liné, 2003; Ducci and Yianneskis, 2005). Comparativement aux résultats obtenus par l'approche RANS, la LES est plus proche de l'expérience et paraît ainsi être un excellent candidat pour la détermination de l'hydrodynamique des bioréacteurs.

La simulation de traceurs inertes a également été étudié par Delafosse (2008). Une influence de la position de l'alimentation du traceur sur les hétérogénéités de concentration au sein du bioréacteur a été mise en évidence : plus l'injection est loin de l'agitateur, plus importantes sont les hétérogénéités de concentration observées par les micro-organismes. Cette observation a été faite en assimilant les micro-organismes à des particules et en les suivant de manière lagrangienne. Une étude sur l'assimilation du substrat par une population de micro-organismes en considérant une loi de Monod pour chaque micro-organisme a également été menée. La vitesse d'assimilation moyenne obtenue présente alors des écarts par rapport à la vitesse d'assimilation attendue dans un milieu parfaitement homogène. Cette observation est le point de départ de ce travail dont nous allons détailler les approches dans le paragraphe suivant.

1.6 Cadre de l'étude

Compte-tenu de l'étude bibliographique menée jusqu'à présent, nous allons expliquer dans cette partie l'organisation de cette thèse. Ce travail est plus particulièrement basé sur le mélange du substrat et l'effet du mélange sur l'assimilation par les micro-organismes. Il propose également une étude du couplage inverse biologique en étudiant l'impact de l'assimilation par les micro-organismes sur le champ de concentration du substrat. Dans un premier temps nous allons nous concentrer sur la modélisation de l'assimilation.

1.6.1 L'assimilation du sucre, avant tout un phénomène microscopique

Au cours de ce chapitre, nous avons pu voir l'existence de plusieurs types de modélisations pour la réaction biologique. Les modèles cellulaires se divisent en deux catégories : les modèles non-structurés et structurés.

Les modèles non-structurés permettent de déterminer la croissance de la biomasse, la consommation du substrat et la formation de métabolites secondaires de manière simple. Cette approche est particulièrement bien adaptée dans le cas de réacteurs idéalement mélangés où les temps caractéristiques du mélange et du transfert de masse sont négligeables devant celui de la réaction biologique. Ces modèles s'appliquent de manière globale sur l'ensemble des bioréacteurs.

Si on analyse plus particulièrement le modèle de Monod pour la vitesse spécifique de croissance (équation (1.5)), à partir du système d'équation (1.1), on peut remarquer que :

- le taux de croissance de la biomasse dépend de la concentration en biomasse,
- il existe une limite de saturation maximale pour le taux de croissance vis-à-vis d'un substrat donné,
- les cellules ont besoin de substrat que ce soit pour se développer, ou produire des métabolites.

Ces propriétés des modèles non-structurés sont parfaitement en accord avec les observations expérimentales de croissance de la biomasse. Cependant, ces modèles ne tiennent pas compte de l'état intracellulaire des micro-organismes, ou de la diversité des métabolismes présents dans une population de micro-organismes. Ces modèles échouent donc pour la prédiction de la croissance de la biomasse, dans le cas où l'environnement des cellules varie rapidement. De plus, cette approche de la réaction biologique est appliquée à l'échelle d'une population de micro-organismes dans un bioréacteur, et les paramètres intrinsèques du modèle (μ_{max}, K_S) sont déterminés à partir d'observations expérimentales. La grande variété de cultures mène ainsi à un grand nombre de constantes d'affinité pour un même substrat (Lendenmann and Egli, 1998; Lin et al., 2001). La proposition d'un modèle global se révèle alors impossible.

Si l'on se place maintenant à l'échelle d'un micro-organisme, celui-ci subit de fortes variations dans son environnement en terme de concentration en substrat (George et al., 1998; Bylund et al., 1998). Partant de cette observation, on peut facilement conclure que la multitude de cellules présente dans une culture en bioréacteur verra des concentrations différentes en chaque point du bioréacteur. Selon la valeur de la concentration en substrat dans l'environnement direct d'un micro-organismes et de son histoire, on pourra observer des métabolismes différents d'un point à un autre de la culture. C'est pourquoi, de nombreux modèles structurés ont été proposés afin de pouvoir approcher les mécanismes intracellulaires.

Dans les approches structurées, on regarde les réactions biologiques à l'échelle d'une cellule. On considére les substrats extracellulaires qui vont interagir, après passage de la membrane, avec les composants intracellulaires. On observe la production de métabolites, dont la nature va différer selon le métabolisme considéré, et le passage de ces métabolites dans le milieu extracellulaire. Cette modélisation nécessite la connaissance fine de chaque métabolisme possible. Des modèles compartimentaux ont par exemple été développés pour palier à cette difficulté. On pourra se référer à Nielsen and Villadsen (1992) pour plus d'information sur les modèles structurés.

Le nombre de réactions possibles pour la consommation du substrat est considérable, et la détermination de chacune reste inaccessible. C'est pourquoi le choix d'un modèle structuré ne sera pas envisagé dans ce travail. En revanche, l'idée que la réaction biologique ait lieu dans un micro-organisme, et que le substrat traverse la membrane cytoplasmique du micro-organisme encourage une modélisation locale pour l'assimilation. C'est à partir de cette observation que ce travail cherchera à caractériser l'assimilation du substrat à l'échelle du micro-organisme.

À partir d'un modèle simple de transport pour le substrat couplé aux lois classiques pour la vitesse spécifique de croissance, imposée à l'interface de la membrane du micro-organisme, on regarde l'effet du transport sur l'assimilation. Des concentrations fluctuantes en substrat sont appliquées et l'effet de ces fluctuations sur l'assimilation par le micro-organisme est caractérisé. Cette approche correspond grossièrement à l'idée de suivre un micro-organisme dans un bioréacteur et de regarder la quantité de sucre qu'il consomme à chaque instant. L'étape suivante va donc consister à suivre une population de micro-organismes dans une configuration simple d'écoulement.

1.6.2 Etude de l'assimilation de substrat par une population de microorganismes dans une configuration académique d'écoulement turbulent

L'étude des bioréacteurs a montré que l'existence de forts gradients de concentration en subtrat (Larsson et al., 1996; Enfors et al., 2001) influençait fortement la croissance de la biomasse. L'idée que les micro-organismes soit sensibles au macro-mélange est donc renforcée. Or, des études expérimentales ont également montré que les micro-organismes sont sensibles au micro-mélange (Bergstedt et al., 2004; Warnaars and Hondzo, 2006). En d'autres termes, les petites échelles de la turbulence impactent directement la croissance de la biomasse. Al-Homoud and Hondzo (2008) concluent dans le cas de la bactérie *E. coli* que l'assimilation de substrat est favorisée pour de plus grandes énergies dissipées dans un écoulement turbulent.

Afin de caractériser les effets de mélange et de la dynamique sur l'assimilation de substrat par une population de micro-organismes à petite échelle, une approche numérique basée sur la résolution directe des équations de Navier-Stokes a été choisi. Un outil de DNS initialement utilisé pour caractériser les échanges de température entre des particules solides et une turbulence gazeuse homogène isotrope anisotherme a été adapté pour l'étude des échanges dans les bioréacteurs compte-tenu de la forte analogie entre température du gaz et concentration en substrat. L'approche se base sur l'analyse de simulations numériques directes couplées avec le calcul des trajectoires de milliers de micro-organismes. Elle permet de résoudre la dynamique de l'écoulement et le mélange du substrat et ne demande qu'un seul modèle, celui pour l'assimilation du substrat à l'échelle d'un micro-organisme et permet de déterminer une vitesse d'assimilation globale à l'échelle de la population. Cette dernière peut se coupler avec une simulation RANS ou LES dans le but d'une meilleure prédiction de l'assimilation de substrat par la biomasse.

Enfin, jusqu'ici, l'effet de l'assimilation du substrat par les micro-organisme, sur le mélange du substrat n'avait pas été envisagé. La dernière partie de ce travail est dédiée aux conséquences de la consommation de substrat dans le milieu sur l'assimilation.

1.6.3 Etude de l'effet de la phase biotique sur la phase porteuse - Effet de la consommation de substrat par les micro-organismes

L'impact d'hétérogénéités de concentration en substrat sur la vitesse d'assimilation d'une population de micro-organismes est caractérisée dans le cas d'un écoulement simple. On peut également penser que du fait de l'assimilation locale du substrat par les cellules, des gradients de concentration à l'échelle locale vont apparaître. Ces gradients locaux auront en retour un effet sur l'assimilation. Ce couplage inverse biologique fera l'objet du chapitre 5.

Ce travail de thèse constitue une première approche pour la modélisation des processus biologiques à l'échelle microscopique et mésoscopique en terme de caractérisation de l'assimilation du substrat. Des modèles pour la détermination de l'assimilation par un micro-organisme sont proposés à l'échelle microscopique, ainsi qu'à l'échelle mésoscopique. Enfin, de nombreuses perspectives pour l'amélioration de la modélisation des bioréacteurs seront proposées.

Figures

Chapter 2

Numerical study of substrate assimilation by a microorganism exposed to fluctuating concentration

In most modelling works on bioreactors, the substrate assimilation is computed from the volume average concentration. The possible occurrence of a competition between the transport of substrate towards the cell and the assimilation at the cell level is generally overlooked. In order to examine the consequences of such a competition, a diffusion equation for the substrate is coupled with a specific boundary condition defining the uptake rate at the cell-liquid interface. Two assimilation laws are investigated, whereas the concentration far from the cell is varied in order to mimic concentration fluctuations. Both steady and unsteady conditions are investigated. The actual uptake rate computed from the interfacial concentration is compared to the time-averaged uptake rate based on the mean far-field concentration. Whatever the assimilation law, it is found that the uptake rate can be correlated to the mean far-field concentration, but the actual values of the parameters are affected in case of transport limitation. Moreover, the structure of the far-field signal influences the substrate assimilation by the microorganism, and the mean interfacial uptake rate depends on the ratio between the characteristic time of the signal and the diffusional time scale, as well as on the amplitude of the fluctuations around the mean far-field concentration in substrate. The present work enlightens few experimental results and helps in understanding the differences between the concentration measured and that present in the microenvironment of the cells.

Résumé

La plupart des travaux réalisés sur la modélisation des bioréacteurs s'appuient sur une approche macroscopique pour la détermination de l'assimilation du substrat. Par approche macroscopique, on entend que l'assimilation du substrat est calculée à partir de la concentration moyenne dans le volume élémentaire de contrôle (maille d'un calcul CFD). Or, en réalité la concentration en substrat dans cette maille n'est pas nécessairement uniforme. Ainsi, en modélisant la vitesse d'assimilation à partir de la concentration moyenne, on ne tient pas compte de l'état de mélange dans le volume considéré. De la même manière, on suppose en général que tous les microorganismes présents dans le volume de contrôle possèdent la même capacité d'assimilation. Des approches LES avec un modèle de sous-maille tentent de prendre en compte ces hétérogénéités, mais leur impact sur l'assimilation par les microorganismes n'a été que très peu étudié.

De plus, dans la plupart des travaux de modélisation, la réaction biologique est toujours le phénomène limitant pour l'assimilation. Or, on peut observer que l'assimilation est avant tout un phénomène microscopique, qui survient à l'échelle du microorganisme. Les molécules de substrat sont assimilées par un microorganisme à travers sa membrane. Il s'agit donc par nature d'un transfert de masse à l'échelle locale.
En pratique, la détermination à l'échelle de chaque microorganisme est impossible compte-tenu du nombre d'individus en présence dans les bioréacteurs et des limites des techniques expérimentales. On mesure donc l'assimilation de manière globale, en moyenne sur l'ensemble d'une population de microorganismes, et on la relie à la concentration moyenne dans le milieu de culture.

Mais, ces lois d'assimilation globales échouent à prédire l'assimilation d'une population de microorganismes lors de passage de réacteurs de laboratoires à des réacteurs industriels. En effet, celles-ci étant uniquement basées sur la concentration moyenne en substrat ne prennent pas en compte les fluctuations de concentration. Or, les microorganismes eux, individuellement sont sujets à ces fluctuations de concentration le long de leur trajectoire.

L'approche proposée dans cette partie consiste à se placer à l'échelle d'un microorganisme soumis à des fluctuations temporelles de concentration. Ainsi l'assimilation en moyenne dans le temps peut être vue comme la conséquence des différentes concentrations rencontrées par un microorganisme au cours de son parcours dans un bioréacteur imparfaitement micro-mélangé. En combinant un modèle de transport pour la concentration depuis le champ lointain jusqu'à l'interface microorganisme-liquide et en se donnant la loi de vitesse d'assimilation à l'interface, on introduit la possibilité d'étudier différents régime d'assimilation : soit le flux de substrat est suffisant et la réaction biologique contrôle l'assimilation, soit l'assimilation est limitée par l'apport en sucre. Ce dernier régime peut être qualifié de régime physique. Dans ce cas, la concentration à l'interface est très petite devant la concentration lointaine. Le microorganisme *voit* de très faibles concentrations. Quelles sont les conséquences d'une compétition entre transport de substrat jusqu'au microorganisme et assimilation ? C'est sur ce dernier point que cette partie du travail se focalise.

Nous étudions donc l'assimilation d'un seul microorganisme soumis à des fluctuations de concentration en substrat dans une configuration simple. Le substrat est transporté de manière purement diffusive jusqu'au microorganisme, et ce dernier, à travers une loi d'assimilation prescrite à son interface, assimile le substrat. La concentration en substrat est donnée pour le champ lointain et celle-ci peut varier en temps. Les deux approches stationnaire, où la concentration est uniforme, et instationnaire sont étudiées. Le taux d'assimilation par le microorganisme est déterminé à son interface ainsi que la concentration interfaciale (à l'interface du microorganisme).

Deux modèles d'assimilation sont considérés. Le premier est le modèle d'assimilation de Monod avec une constante d'affinité pour le substrat définie à l'échelle du microorganisme. Ce modèle relie algébriquement la vitesse d'assimilation à la concentration interfaciale et suppose donc une adaptation instantanée du microorganisme aux variations de concentration à son interface. Le second modèle proposé est un modèle bilinéaire basé sur la capacité d'assimilation maximale du microorganisme. Dans ce second modèle, on admet que la totalité du flux arrivant à l'interface est assimilé tant que celui-ci reste inférieur à la capacité maximale d'assimilation du microorganismes (supposée connue et constante). Lorsque le flux est saturant, le microorganisme ne peut pas absorber plus de sucre que sa capacité maximale d'assimilation et on observera une accumulation de sucre à son interface. Ce flux de sucre dépend directement de la concentration en sucre du champ lointain.

Nous avons étudié différents types de signaux pour la concentration lointaine. L'analyse menée est statistiquement stationnaire et permet d'obtenir des moyennes temporelles pour le flux assimilé et la concentration en substrat à l'interface du microorganisme.

Le flux assimilé est comparé au flux basé sur la concentration lointaine moyenne. Dans tous les cas, les résultats obtenus sont inférieurs au flux basé sur la concentration moyenne. Ce résultat s'explique par la non-linéarité de la relation entre le flux et la concentration. On remarque cependant que les flux calculés peuvent être reliés à la concentration lointaine moyenne par une loi hyperbolique (similaire dans sa forme à une loi de Monod), mais la constante d'affinité de cette loi globale est influencée par l'occurrence du régime physique pour l'assimilation.

D'autre part, différents signaux temporels pour la variation de concentration lointaine ont été étudiés en termes d'assimilation par le microorganisme. Il apparaît une dépendance du flux assimilé à la structure du signal, ainsi qu'à la période du signal. En d'autres termes, la variance et le temps caractéristique du signal influencent directement le taux de sucre assimilé par le microorganisme. Jusque-là, ce résultat intuitif n'était pourtant pas pris en compte dans les différents types de modélisation existants. Une étude sur le rapport entre temps caractéristique de diffusion sur le domaine et période du signal de concentration permet de montrer le caractère passe-bas du système, mais également montre un effet important de la compétition entre transport et assimilation. De plus, l'amplitude des fluctuations a un effet important sur l'assimilation du microorganisme. Typiquement, pour une même concentration moyenne dans le temps, si une cellule est exposée à un pic de concentration sur une durée très courte, elle assimilera une quantité de sucre plus faible sur la période du signal que si elle est exposée à une concentration moins importante mais sur une durée plus longue.

Ces différents résultats à l'échelle d'un microorganisme sont encourageants. Ils fournissent une base d'explication physique à certains résultats de la littérature. En particulier, le fait que la constante d'affinité pour le substrat varie sensiblement d'une expérience à l'autre. Les résultats montrent que l'état de micro-mélange a une influence directe sur la valeur de cette constante. De plus, le fait que des souches « rapporteuses » émettent une fluorescence dans une culture où la concentration mesurée est considérée comme non-limitante (car très supérieure à la constante d'affinité) indique que des limitations à l'échelle du microorganisme sont perçues. Ceci supporte l'idée que le recours à une loi macroscopique occulte l'existence d'une possible limitation par le transport (l'existence de régime physique). Parce qu'elle dépend potentiellement des conditions locales de mélange, une loi d'assimilation prescrite à l'échelle globale n'est pas donc invariante lors du changement d'échelle. On peut ainsi penser que l'existence d'une compétition transport/assimilation explique en partie les déviations observées expérimentalement pour la croissance de la biomasse. De plus, cette approche permet une meilleure compréhension des écarts de comportement de microorganismes par rapport aux comportements attendus basés sur la concentration moyenne mesurée dans le bioréacteur. En effet, c'est plutôt le signal dans son environnement très proche (concentration à l'interface du microorganisme) qui va piloter l'assimilation.

Ces conclusions sont tirées d'une étude où seule la diffusion contrôle le transport mais elles peuvent être transposées à une configuration plus réaliste pour le microorganisme où le transport du substrat est assuré par un mécanisme de convection/diffusion. Par ailleurs si l'on suppose la loi d'assimilation locale connue, on pourrait alors envisager une étude en terme de nombres sans dimension pour le transfert de masse, ainsi que pour la compétition transport/réaction biologique. Cette étude pourrait représenter un réel avantage pour déterminer le régime dans lequel se trouve le microorganisme par exemple.

Contents

Introduction

Scale-up problems are frequent in fed-batch bioreactors when passing from a laboratory ($\sim$ 1 L) to an industrial scale ($\sim$ 10 m^3). It is therefore crucial to understand the reasons for the often observed reduced conversion yield of substrate into biomass, with by-product formation (Larsson et al., 1996; Bylund et al., 1998). One of the first studies on the effect of mixing on microbial behaviour was addressed by Hansford and Humphrey (1966) for Baker's yeast. These degraded performances are attributed to the presence of concentration gradients of substrate, pH and/or oxygen within the reactor. In a fluctuating environment, cells may be unable to adapt dynamically to the local environment and their behaviour thus deviates from that identified at the laboratory scale, i.e. in a steady and homogeneous environment. As pointed out by Enfors et al. (2001) and later by Lara et al. (2006b), the behaviour of microorganisms is an integrated consequence of all the fluctuations experienced during their transport within the bioreactor. The difficulty in predicting the changes during scale-up of fermentations is related to the variety of strongly coupled phenomena such as hydrodynamics, two-phase mass transfer and biological reaction. Beside the experimental approach, the modelling and simulation of bioreactors have been developed; and the progression tends to a full integration of the most influential phenomena in a commercial Computational Fluid Dynamics code is possible whilst rare (Schmalzriedt et al., 2003). Unfortunately, the results are somewhat disappointing despite the use of well-established models in each domain of concern. In most cases, the macroscopic gradients at the reactor scale and the amount of by-products are underestimated (Enfors et al., 2001; Schmalzriedt et al., 2003), whereas the biomass production is overestimated.

In many modelling works on bioreactors, the specific substrate uptake rate q_S (grams of substrate by unit of time and cell mass, [$\mathrm{g_S.g_X^{-1}.s^{-1}}$]) is modelled using a Monod equation based on the average concentration $< S >$. The symbols $< \cdot >$ represent a spatial averaging over a volume of control on which mass balances are written. This volume of control can be either the whole reactor if an ideal reactor approach is used, or a portion of the reactor if a compartment model or a CFD approach is used.

$$< q_S > = q_{S,max} \frac{< S >}{K_S + < S >}, \tag{2.1}$$

q_{max} is defined as the maximum specific uptake rate and K_S is the affinity constant for the substrate.

Based on zone models, several studies focused on the macro-mixing issues for bioreactors. **?** investigated the effect of dynamics of the mixing process in mechanically stirred bioreactors by using a circulation-model for flow of fluid and a two-environment-model to account for micro-mixing in the vessel. The biological reaction obeys a kinetic model. They obtained a circulation time distribution which is more a macro-mixing issue. Namdev et al. (1992) also studied the circulation time distribution. They evaluated the effects of the feed zone by conducting aerobic fed-batch fermentations of *Sacharromyces cerevisiae* with a recycle loop and a bench-scale fermentor. The intermittent feed in the recycle loop simulates the circulation of cells through the feed zone for different residence times and the biomass yield is increased in the feed zone for long-time exposure. Considering zone models, those works assume that the micro-mixing is perfect, because they consider a homogeneous concentration <S> in the zone. But, the effect of micro-mixing has been enlighten by Akiti and Armenante (2004) for a chemical reaction in a fed-batch stirred reactor.

In these approaches, all species are treated as dissolved species, but as far as microbial populations are considered, it might be more meaningful to make an analogy with heterogeneous catalysis considering suspended particles in a liquid phase.

Therefore, two asymptotic regimes can be distinguished: the biological regime if the transport rate towards the particle is larger than the reaction rate, and the physical regime if it is smaller. Experimental evidences of assimilation taking place in the physical regime have been given by Hondzo and Al-Homoud (2007). These authors showed that, at a very low dissipation rate ($7\ 10^{-6} \leqslant \varepsilon \leqslant 180\ 10^{-6}$, ε dissipation rate in $[\ \mathrm{m}^2 \cdot \mathrm{s}^{-3}\ ]$), the oxygen uptake rate is correlated to the energy dissipation rate and therefore controlled by the rate of transport towards the cell surface. From the cell position, the competition between transport towards the cell and substrate assimilation results in a heterogeneous concentration field: the concentration at the cell surface differs from the average concentration $< S >$. The latter is sometimes referred as the bulk concentration or far-field concentration (concentration far from the cell).

In the classical approach, the substrate concentrations are treated as spatial or temporal averages. The present work focuses on dynamic simulations where the influence of temporal fluctuations of the substrate concentration on the assimilation by one microorganism is scrutinised. These temporal evolutions can be thought as the different substrate concentration experienced by a microorganism transported in a bioreactor. The assimilation is of prime interest and requires a precise modelling.

From a biological point of view, assimilation has been studied by Koch and Houston Wang (1982), Ferenci (1996), Natarajan and Srienc (1999, 2000), Lin et al. (2001) and Chassagnole et al. (2002), among others. One important conclusion concerns the ability of cells to modify their assimilation capacity in response to the concentration fluctuations encountered. Without ignoring these particular features of biological systems, only the physical aspects of the problem will be considered in this paper, and no adaptation or regulation of the uptake systems is taken into account. In other words, the parameters of the assimilation law, q_{max} and K_S, will be regarded as pure constants.

The originality of the work concerns the microscopic description of the assimilation at the microorganism's interface. The uptake rate is based on local quantities such as the interfacial concentration that is different from the bulk concentration and results as a competition between transport and assimilation.

As a first step, we propose to investigate the case where the substrate transport towards the cell is controlled by a molecular diffusion process. The aim of this work is to scrutinise the influence of a time-varying far-field concentration on both the interfacial concentration and assimilation rate dynamics at the cell scale. This question is addressed through the resolution of a scalar diffusion equation in spherical coordinates. The analytical resolution for such a problem is known for some particular boundary conditions (Truskey et al., 2004) and used to validate the tool. Then, a numerical resolution with various boundary conditions at the cell surface is performed, allowing the calculation of both the interfacial flux and concentration under transient conditions. First, an assimilation law based on a Monod equation is used. It is shown that it is not possible to correlate the mean assimilation rate to the mean far-field concentration without adapting the constant of the assimilation law. We propose an alternative bi-linear formulation of the assimilation law that reproduces the asymptotic behaviours (biological and physical regimes). This model is applied under transient conditions and the influence of different parameters of the concentration field on the assimilation rate is enlightened. At steady state, the interfacial concentration can be obtained by equating the reaction rate to the mass transport rate, and an overall reaction rate can be expressed as a function of the bulk concentration. Under transient conditions, the elimination of the unknown interfacial concentration is no longer possible, and the full set of partial-differential equations for scalar transport and assimilation at the particle has to be considered.
Using this procedure, it is shown that the microorganism will be exposed to highly substrate-limited events whereas the bulk concentration is highly non-limiting.

2.1 Model framework

2.1.1 Geometry and boundary conditions

The computational domain can be seen as a sphere of stagnant fluid, and the microorganism, spherical as well, is located at its centre. The external boundary of the domain, indicated by a long-dashed line in Figure 2.1 is homogeneously supplied in substrate with the concentration S_∞, while the short-dashed line represents the microorganism interface. The scalar transport towards the cell is purely diffusive and follows the spherical diffusion equation. In view of the present geometry and the homogeneous distribution of concentration at the domain boundaries, the concentration is the same all over the cell surface, then the radial component of the equation is sufficient for solving the substrate transport in a satisfactory manner. The diffusion equation in the radial coordinate r, $[\ \mathrm{R} \leqslant \mathrm{r} \leqslant \mathrm{L}\ ]$, yields:

$$\frac{\partial S}{\partial t} = \frac{\mathcal{D}}{r^2}\frac{\partial}{\partial r}\left(r^2\frac{\partial S}{\partial r}\right), \tag{2.2}$$

where S is the substrate concentration in the domain, $\mathcal{D}$ is the molecular diffusivity, R is the microorganism radius which is set constant[1] and L is the length of the domain (large compared to R)[2]. Three typical boundary conditions associated to equation (2.2) are investigated in the present work:

- imposed time-varying far-field concentration

$$S_{r=L} = S_\infty(t), \tag{2.3}$$

- Neumann boundary condition: specified flux at the cell-liquid interface

$$\frac{\partial S}{\partial r}\Big|_{r=R} = \varphi_{int}, \tag{2.4}$$

- Dirichlet boundary condition: specified concentration at the cell-liquid interface

$$S_{int} = S_{r=R} = C. \tag{2.5}$$

If a Neumann boundary condition along with a Monod assimilation law is chosen, the uptake rate depends on the substrate concentration at the cell-liquid interface and one actually gets $\varphi_{int} = \varphi_{int}(S_{r=R})$. Note that boundary conditions (2.4) and (2.5) are mutually exclusive, but can be used to reproduce the asymptotic behaviour of substrate assimilation at high and very low concentrations.

As already mentioned, whatever the actual phenomena ensuring the passage of the substrate through the cell membrane, the latter is preceded by the transport of the substrate to the cell-liquid interface. These two phenomena occur in series and two asymptotic regimes can then be distinguished. On the one hand, when the transport of substrate towards the cell governs the process, typically when the microorganism grows in a nutrient-limited culture, the physical regime stands and the actual uptake rate is indeed limited by the transport rate. The interfacial concentration tends to zero $S_{r=R} \mapsto 0$ which can be translated in terms of boundary conditions by $C = 0$ in equation (2.5).

---

[1] Notice that, in general, the microorganism can grow up to a mass, i.e. to a volume, which is about the double of its initial value, and then usually subdivides into two cells. The maximum cell diameter or radius attained is thus of the order of $\sqrt[3]{2} \simeq 1.26$ times the initial value, therefore it can be considered as constant with a good approximation.

[2] The length of the domain is important because the substrate is carried on this length. A direct influence of L can be found on the characteristic transport rate. The chosen length L is large compared to R but remains small enough to consider characteristic times of order 20 s

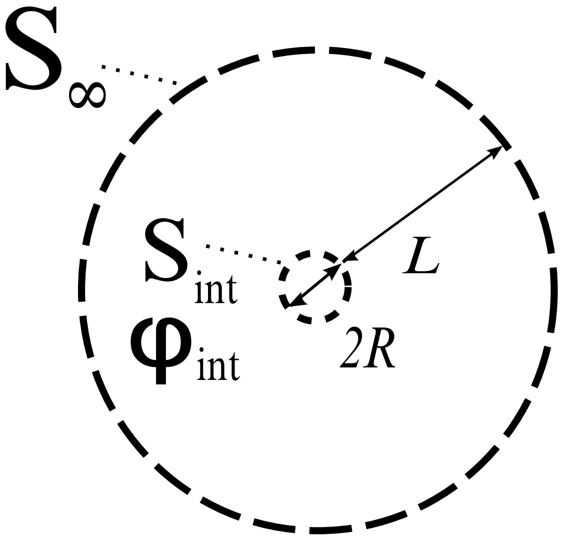

Figure 2.1: Schematic representation of the 1D calculations Cconfiguration.

On the other hand, in the biological regime the uptake rate is slower than the transport rate and the transfer through the membrane controls the process. This situation typically occurs at high substrate concentration and results in a saturated assimilation capacity. Here, the corresponding boundary conditions is a constant gradient at the cell surface such that the specific uptake rate, q_S, is maximum. The relationships between concentration gradients, mass fluxes and uptake rates are detailed in section 2.1.4.

2.1.2 Numerical framework

Equation (2.2) can be spatially discretised in various ways. In order to be as consistent as possible, a conservative form was used, rewriting the radial diffusion equation as:

$$\frac{\partial S}{\partial t} = \mathrm{div}(\mathcal{D}\mathbf{grad}S). \tag{2.6}$$

This form allows to keep the operator div($\mathcal{D}$**grad** .) in the discretisation, and the interfacial gradient $\varphi_{int} = \frac{\partial S}{\partial r}\big|_{r=R}$ then appears directly and does not have to be recalculated from the concentration field. This formulation simplifies the imposition of a given flux boundary condition (Neumann boundary condition). Further information on the discretisation can be found out in the Appendix. A first-order implicit time integration was employed for the temporal resolution of the problem. Higher-order temporal schemes have been tested with no significant impact on the results.

2.1.3 Analytical solutions

Steady-state analytical solutions of equation (2.6) are known for various boundary conditions. Only that of interest, obtained with two Dirichlet boundary conditions, will be reported here. Let S_∞ be the constant concentration at $r = L + R$ and $C = 0$ so that the concentration at the cell surface $r = R$ is null, then the steady-state solution of the problem is given by:

$$S(r) = S_\infty \left(1 + \frac{R}{L}\right)\left(1 - \frac{R}{r}\right). \tag{2.7}$$

The concentration gradient at the cell-liquid interface is:

$$\varphi_{int} = \frac{\partial S}{\partial r}|_{r=R} = \frac{S_\infty}{R}\left(1 + \frac{R}{L}\right). \tag{2.8}$$

If $L >> R$ the above expression simplifies into the following:

$$\varphi_{int} \approx \frac{S_\infty}{R}. \tag{2.9}$$

The result of equation (2.9) shows that the concentration gradient at the cell surface can be, in some particular conditions ($S_{r=R} = 0$), independent of the actual length of the domain, provided that the latter is much larger than the cell radius.

An analytical solution can also be found for the unsteady case if one considers a Dirichlet boundary condition, S_∞ at $r = L + R$, a Neumann boundary condition , $\partial S/\partial r\big|_{r=0} = 0$, and a uniform initial condition, $S(r, 0) = 0$ (Truskey et al., 2004):

$$S(r,t) = S_\infty\left(1 + 2\sum_{n=1}^{\infty}(-1)^n \frac{\sin(n\pi r/L)}{n\pi r/L}\exp^{-n^2\pi^2 t\mathcal{D}/L^2}\right). \tag{2.10}$$

In our case, the Neumann boundary condition is not imposed at $r = 0$ but at $r = R$; nevertheless, if $L \gg R$, the analytical solution above will provide a good approximation of the concentration profile in the early step of the process. It will be used as a reference to test our model under transient conditions. In equation (2.10), the length of the domain L appears explicitly in the characteristic time $\tau_D = L^2/\mathcal{D}$. As such it impacts the dynamics of the scalar transport, but has no impact on the concentration profile $S(r/L, t) = f(t/\tau_D)$. The scalar transport dynamics is indeed controlled by the characteristic time rather than by the length of the domain L. Provided that the latter is large compared to the cell radius, numerical solutions should be independent of L and can be compared to analytical solutions. Under transient conditions (time-varying far-field concentration) a key parameter will be the ratio of the concentration fluctuation time scale to the transport time scale τ_D.

2.1.4 Relating concentration gradient to biological constants

The substrate assimilation is generally defined by a specific uptake rate, in $g_S.g_X^{-1}.s^{-1}$, which can also be regarded as a mass flux through the cell membrane, q_{int}, per unit cell mass . This quantity is upper bounded since the cell has a maximum uptake capacity. In practice, the maximum specific uptake rate for a given substrate $q_{S,max}$ is deduced from experiments:

$$q_{S,max} = \frac{\mu_{max}}{Y_{XS}}, \tag{2.11}$$

where μ_{max} is the maximum specific growth rate of the microorganism and Y_{XS} is a conversion yield of substrate into biomass. The interfacial mass flux Φ_{int} is the equivalent mass of substrate assimilated per unit time. The related maximum mass flux is:

$$\Phi_{max} = m_c q_{S,max}, \tag{2.12}$$

where m_c is the cell mass.

Finally, if one assumes that the transfer through the membrane is uniform over the cell surface, the concentration gradient at the cell surface φ_{int} can be written as :

$$\Phi_{int} = a_c \mathcal{D} \varphi_{int}, \tag{2.13}$$

where a_c is the cell surface. The maximum concentration gradient at the microorganism interface corresponding to the saturation of the uptake capacity is thus given by φ_{max}:

$$\Phi_{max} = a_c \mathcal{D} \varphi_{max}. \tag{2.14}$$

In the following, the different interfacial quantities are non-dimensionalized by the corresponding above-mentioned maximum interfacial values (see Table 2.1) and it is outlined that the following ratios are equivalent:

$$\frac{\varphi_{int}}{\varphi_{max}} = \frac{q_{int}}{q_{S,max}} = \frac{\Phi_{int}}{\Phi_{max}}. \tag{2.15}$$

As far as boundary conditions are expressed in terms of concentration gradients, the first ratio of equation (2.15) will be used to present the results in the present work.

Table 2.1 and 2.2 summarise the different biological and physical parameters for the forthcoming calculations.

Table 2.1: Reference parameters for biological condition. (^{a} from Lendenmann and Egli (1998))

Y_{XS}	μ^*_{max}	$q_{S,max}$	ρ_{cell}	Φ^*_{max}	φ_{max}
0.5	0.6^a	0.33	1000	$1.4\ 10^{-18}$	223
$[\ g_X \cdot g_S^{-1}\ ]$	$[\ h^{-1}\ ]$	$[\ g_S \cdot g_X^{-1} \cdot s^{-1}\ ]$	$[\ g_X \cdot L^{-1}\ ]$	$[\ kg_S \cdot s^{-1}\ ]$	$[\ kg_S \cdot m^{-4}\ ]$

Table 2.2: Reference parameters.

R^*	L^*	$\mathcal{D}^*$
10^{-6}	10^{-4}	5.10^{-10}
[m]	[m]	$[\ m^2 \cdot s^{-1}\ ]$

2.2 Results

Steady-state and transient simulations are presented in the following part of the work. The results of transient simulations (time-varying far-field concentration) are presented in terms of time-averaged normalized concentration gradients, as a function of the time-averaged far-field concentration $\overline{S_\infty(t)}$. In this work, two periodic signals are used for the far-field concentration, so a stationary periodic solution is finally obtained. These signals are shown in Figure 2.2. The reason for this choice is to impose far-field signals with a marked difference in terms of variance in order to study the effect of the signal structure on the assimilation dynamics. Time averaging is performed over a full period once the stationary regime has been reached. When temporal evolutions are presented, the time is normalised by the diffusion time τ_D and the ratio $T^* = T/\tau_D$ is used for a parametric study. This parameter compares the period, T, of the far-field concentration signal to the diffusion time. For small values of T^*, the far-field concentration changes faster than the time required for the concentration profile to get established. For large values of T^*, there is enough time for the concentration profile to get established between two concentration changes, so that a pseudo-steady-state approximation can be made.

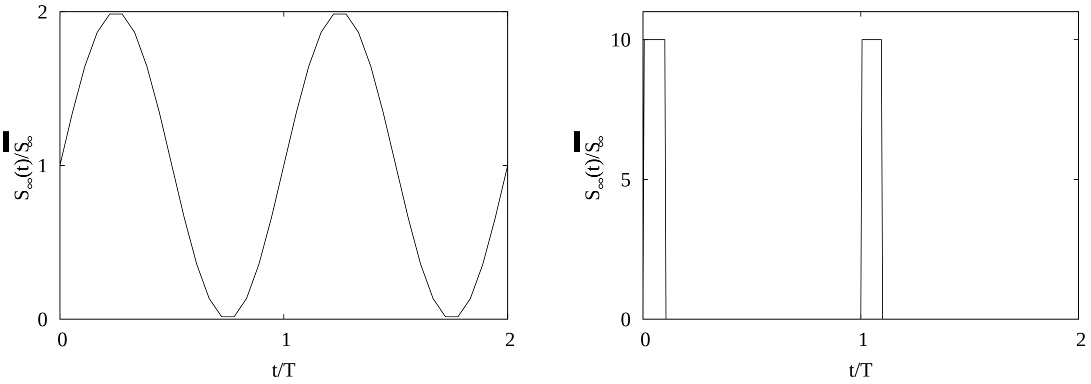

(a) Sinus (b) Top-hat

Figure 2.2: Evolution of the two far-field signals used in transient simulations. For a given period T, the two signals differ in terms of the variance ratio $\sigma/\overline{S_\infty}^2 = 0.5$ for sine, $\sigma/\overline{S_\infty}^2 = 9$ for top-hat.

2.2.1 Monod assimilation model at the cell interface

Constant far-field

A first set of calculations is performed with an imposed far-field concentration and the usual Monod equation at the cell interface which corresponds to a Neumann boundary condition, see equation (2.4):

$$\varphi_{int} = \varphi_{max} \frac{S_{int}}{k_S + S_{int}}, \tag{2.16}$$

where S_{int} refers to the interfacial concentration and k_S is the half-saturation constant of the enzymatic reaction controlling assimilation at the cell-liquid interface. The results are presented in terms of normalised concentration gradients, $\varphi_{int} / \varphi_{max}$, as a function of the normalised far-field concentration S_∞ / k_S. It can be reminded here that the normalised gradients are equivalent to the normalised uptake rates. In the present case, an analytical solution for the interfacial concentration and interfacial uptake rate can be found (see A). The resulting normalised uptake rate is shown by Figure 2.3 with dashed lines. Note that identical results are obtained when solving the unsteady problem with the same boundary conditions. Since the results are plotted as a function of the bulk concentration S_∞, one observes that the half saturation is not obtained for $S_\infty / k_S = 1$ but for a higher value of the far-field concentration. The reason why the results are plotted against the bulk concentration is that in experimental situations the interfacial concentration is not measurable. If one dismisses the possible limitation by transport phenomena down to the cell scale, the uptake rate is directly computed from the bulk concentration. The corresponding uptake rate, $\varphi_{S_\infty} / \varphi_{max} = S_\infty / (k_S + S_\infty)$, is shown by Figure 2.3 with solid lines. The comparison shows that significant differences can exist between the actual uptake rate and the values obtained neglecting the transport limitations. This discrepancy results from the concentration difference between the bulk and the microorganism surface. Such a situation is typical of an assimilation process taking place in the physical regime, when transport limits the assimilation rate. In case of severe transport limitation, an interfacial concentration close to zero can be reached as explained in section 2.1.1. From the analytical solutions, it is possible to evaluate the difference between the uptake rate based on the far-field concentration and the actual uptake rate. This error is presented by Figure 2.4 as a function of S_∞ for different k_S, and proves to be strongly dependent on the value of the half-saturation constant. For high values of k_S (10^{-3} $\mathrm{kg_S \cdot m^{-3}}$) the deviation always remains lower than 5% whatever the bulk concentration. For small values of k_S (10^{-6} $\mathrm{kg_S \cdot m^{-3}}$) the deviation can reach 100 % of the maximum uptake rate when the bulk concentration lies in the range of 1 to

10 k_S. In the intermediate range of k_S, the maximum deviation is reached for far-field concentration equivalent to the half-saturation constant. Figure 2.4 thus shows that, if the overall assimilation process is partly limited by the transport to the cell surface, then evaluating the uptake rate from the bulk concentration and a previously identified value of k_S (at the cell scale) leads to overestimate the actual uptake rate in the range $k_S \simeq \overline{S_\infty}$, especially for low k_S values. These results can also be analysed in the following way: let us consider $\varphi_{int} = f(\overline{S_\infty})$ (dashed line in Figure 2.3) as an experimental data set from which the assimilation law has to be identified. This curve can be approximated using the Monod formulation:

$$\varphi = \varphi_{max} \frac{\overline{S_\infty}}{K_S + \overline{S_\infty}}, \tag{2.17}$$

and it leads to an apparent affinity constant K_S close to 2 10^{-4} $\mathrm{kg_S \cdot m^{-3}}$. This value is different from that imposed in the calculations at the cell surface. It is therefore an apparent K_S which indeed reflects some transport limitation (purely physical phenomena). In other words, changing the efficiency of the mass transfer to the cell level can affect the identification of the apparent affinity constant K_S, even though the physics of the assimilation at the cell scale remains unchanged (same k_S).

Time-varying far field

Further calculations were performed with time-varying far-field concentration $S_\infty(L,t)$. Transient simulations are performed since there is no analytical solution in this case. The two types of signals shown by Figure 2.2 were used. Both signals share the same period and the same mean far-field concentration. The results of numerical simulations for time-varying far-field concentration are examined in terms of time averages of the instantaneous interfacial uptake rate as defined in equation (2.16). Time-averaged values of the interfacial flux are reported in Figure 2.3 for the particular case of $T^* = 0.9$ (line with circle). The main striking result is that, for a given mean far-field concentration, the assimilation rate differs when the surrounding medium is exposed to fluctuating concentrations. Moreover, comparing the sine and top-hat signals, the resulting assimilation rate is influenced by the structure of the far-field signal. This result suggests that, not only the mean concentration, but also the variance has an influence on the assimilation process. As already mentioned in the previous section, the interfacial concentration is hardly accessible in practical situations. It is therefore interesting to examine the consequences of using the far-field concentration for the prediction of the uptake rate (k_S is assumed to be known). Two different situations occur. If the concentration fluctuations are measurable, a possible approach is to perform a time average of the instantaneous uptake rates evaluated from the instantaneous far-field concentrations (line with ∇ in Figure 2.3):

$$\overline{\varphi(S_\infty(t))} = \varphi_{max} \overline{\frac{S_\infty(t)}{k_S + S_\infty(t)}}. \tag{2.18}$$

If the concentration fluctuations are filtered by the measuring probe, the only information available is the mean far-field concentration $\overline{S_\infty}$. So one can only evaluate the mean uptake rate from the mean far-field concentration through equation (2.19):

$$\varphi(\overline{S_\infty}) = \varphi_{max} \frac{\overline{S_\infty}}{k_S + \overline{S_\infty}}. \tag{2.19}$$

When this latter approach is used, the same results are obtained for both signals (because of identical $\overline{S_\infty}$, whatever the period or the variance) and they correspond to those for the constant far-field case at the same S_∞ (solid line, Figure 2.3). In both situations, the prediction of the mean uptake

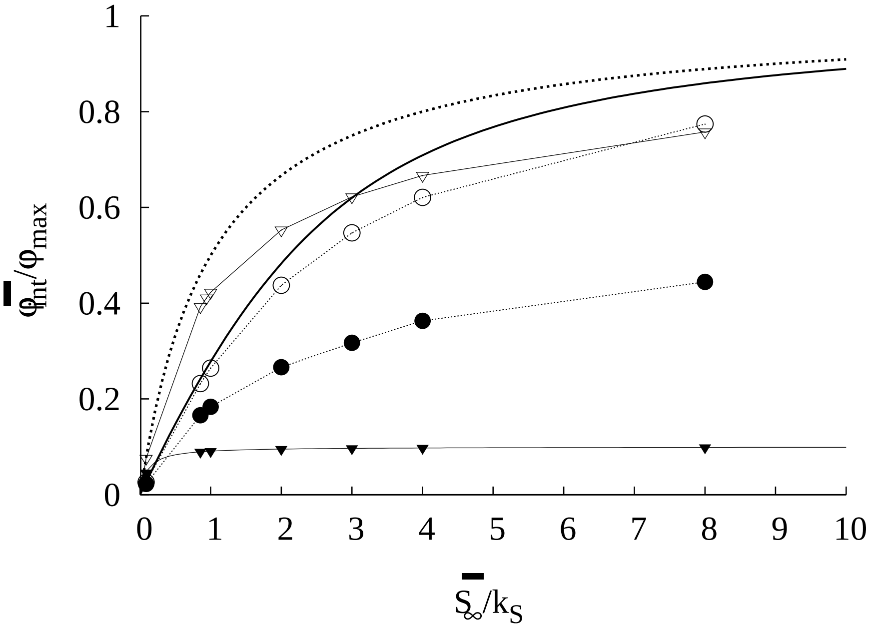

Figure 2.3: Mean interfacial uptake rate as function of the normalised mean far-field concentration (results obtained with $k_S = 10^{-4}$ $\mathrm{kg_S \cdot m^{-3}}$). Constant far-field: (········), sine evolution: ○ and top-hat signal: • (both at $T^* \simeq 0.9$). Mean uptake rate based on the mean far-field concentration $\varphi(\overline{S_\infty})$: (———) and on the instantaneous far-field concentration $\overline{\varphi(S_\infty(t))}$ for sine: ▽ and top-hat: ▾.

rate is not correct. In equation (2.19) the temporal variations of the far-field concentration are not taken into account. In equation (2.18) the instantaneous uptake rate is algebraically linked to the far-field concentrations, which indeed reflects an immediate change of the uptake rate in response to a change in the far-field concentration. The real uptake rate lies in between.

Similarly to what was proposed in the previous section, one can try and estimate the parameter of the assimilation law. Indeed, whatever the type of signal, a hyperbolic relationship is observed between the mean uptake rate and the mean far-field concentration. Therefore it is still possible to correlate the mean uptake rate to the mean far-field concentration, but the affinity constant is only an apparent K_S and reflects to a certain extent the existence of physical transport limitation. Here again, the identified value for K_S is higher than the actual k_S controlling the assimilation at the cell surface. For the same period of the fluctuations, it is also dependent on the type of signal.

2.2.2 First limitations

Limitations of the standard assimilation model

From numerical experiments it was shown that the apparent affinity constant K_S coming out from a data fitting of $\varphi = f(\overline{S_\infty})$ using a Monod expression is an apparent constant which can, in some cases, be affected by the existence of transport limitations and/or temporal concentration fluctuations. This constitutes an extension of the work of Merchuk and Asenjo (1995) that was limited to a constant assimilation rate (zero-order reaction at the cell surface). As a result, the apparent affinity constant was found to depend on the rate of transport only. In the present study, it is shown that the apparent affinity constant can reflect both biological and physical effects.

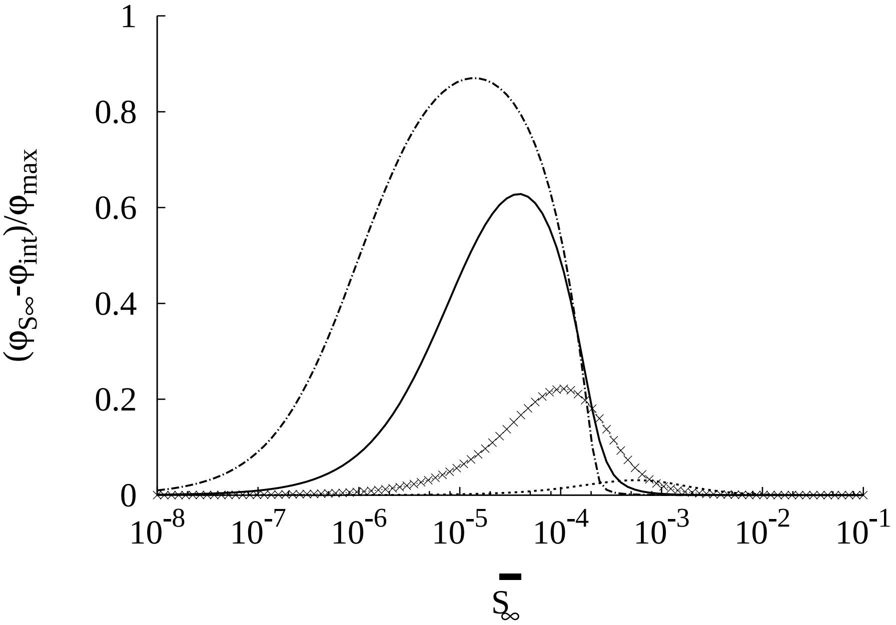

Figure 2.4: Difference between the uptake rate based on the far-field concentration and the interfacial uptake rate for constant far-field concentrations for different affinity constants. $k_S = 10^{-6}$: (-··-·-), $k_S = 10^{-5}$: (——), $k_S = 10^{-4}$: (×) and $k_S = 10^{-3}$: (········) (all affinity constants in $\mathrm{kg_S \cdot m^{-3}}$).

Beyond the fact that cells are known to modify their affinity for the substrate using different type of transporters (Ferenci, 1999b), this part of the work gives a physical explanation for the difficulty in identifying the parameter K_S. Consequences are twofold:

1. from an experimental point of view it questions the identifiability of the affinity constant. In the biological regime, the concentration at the cell surface is similar to the bulk concentration. Therefore a real k_S is identifiable from experiments. Apart from this biological regime, a concentration gradient between the microorganism and the bulk develops because of the competition between the rate of transport and the rate of assimilation. However it is still possible to relate the uptake rate to the bulk concentration through a standard Monod equation, but the parameters are actually affected by the operating conditions of the experiment. In particular, the rate of transport is dependent on the mixing efficiency in the bioreactor.
2. From a modelling point of view, the calculation of the mean interfacial uptake rate $\overline{\varphi_{int}}$ based on the far-field concentration $\varphi(\overline{S_\infty})$ is correct in the biological regime only since $S_{int} \simeq S_\infty$ and $K_S \simeq k_S$. But if assimilation does not proceed in the biological regime, the correct calculation of the uptake rate requires the transport to be solved down to the cell scale. The error in the calculation of the uptake rate based on the far-field concentration increases when k_S decreases. The smaller the affinity constant, the bigger the error on the uptake rate. In most modelling works, a predefined Monod law is used to quantify substrate assimilation in bioreactors, irrespective of a possible limitation by physical transport.

Although this demonstration was conducted considering a purely diffusive transport, the same conclusions are expected if a convective motion around the cell is present. This would modify the expression for the transport rate, but the dependance of K_S on the Damköhler number would remain. This suggests that mixing at the micro-scale can influence the assimilation, which is indeed confirmed by experiments (Dunlop and Ye, 1990a). It will now be shown that the reference to an affinity constant is not necessary to predict the assimilation rate from the bulk concentration.

2.3 A new assimilation model for microorganisms in a substrate-limiting medium

2.3.1 Substrate assimilation model

Many experimental observations indicate that the so-called substrate limiting conditions are indeed situations where assimilation takes place in the physical regime. Lendenmann and Egli (1998) found that the uptake rate of *E.coli* cells initially cultivated in a chemostat and then transferred in a substrate-rich medium was indeed constant, approximately equal to two thirds of the maximum uptake rate in batch culture and independent of the dilution rate in the chemostat. Neubauer et al. (1995b) showed that after a prolonged starvation (27 min), the specific uptake rate of *E.coli* cells suddenly exposed to high substrate concentration could be an order of magnitude higher than the maximum uptake rate measured in a batch culture. Natarajan and Srienc (1999) found that the uptake rate of *E.coli* cells cultivated in a chemostat and then transferred into a substrate-rich medium was independent of the previously experienced dilution rate. All these results show that cells grown under substrate limiting conditions are potentially able to uptake the substrate at a higher rate. In fact, they actually do so as soon as they encounter more favourable conditions. This demonstrates that assimilation was previously taking place in the physical regime. It is therefore proposed to consider that assimilation is either limited by the transport to the cell level or by the maximum uptake capacity of the cell. These two independent ideas are necessary to establish the model. In our case, diffusion controls the transport towards the cell surface. It will be shown that this choice does not limit the extent of our conclusions. The maximum uptake rate is assumed to be constant and given by equation (2.11). Steady and unsteady simulations will be performed and the results compared to those obtained with a standard Monod model.

2.3.2 Imposing boundary conditions

The choice of this assimilation model results in the setting of a specific boundary condition at the cell-liquid interface. This clearly appears if one considers these following asymptotic behaviors.

- Non-limited culture: by definition, this suggests that the uptake rate is maximum. Then, a fixed flux (Neumann boundary condition) corresponding to the maximum uptake rate is imposed.
- Limited culture: the mass flux at the cell interface is lower than the maximum uptake capacity. Then, one can assume that the interfacial concentration is constant and almost zero (Dirichlet boundary condition).

If a constant far-field concentration is set, the type of boundary condition to be used is uniquely determined by the values of φ_{max} and S_∞ as it will be shown in the following section. If a time-varying far-field concentration is imposed, one must consider the switch between the two boundary conditions. A so-called Robin boundary condition, which encompasses the case of Dirichlet and Neumann boundary conditions, is used at the microorganism surface $S(R,t)$. The switch between these two conditions is based on the value of the flux computed at the cell-liquid interface. Thus, the boundary condition is dynamically updated as the calculation proceeds depending on the instantaneous value of the interfacial mass flux.

2.3.3 Uniform environment

The focus was first put on the interfacial response for a constant far-field signal. This configuration mimics the medium surrounding a microorganism in a homogeneous macroscopical environment. Starting from a zero concentration field $S(r,0)=0$, a constant value is imposed at $S(r=L,t>0)=S_\infty$ and equation (2.2) is time-integrated until the steady state is reached. The transient behaviour of both the interfacial concentration and flux is not reported and is not of prime interest in the present work. The analytical solution for the transient case was used to validate the program. The results for different far-field concentrations are presented by Figure 2.5. The normalised interfacial uptake rate, $\varphi_{int}/\varphi_{max}$, is plotted against the far-field concentration. The evolution of the interfacial flux is bilinear as a result of the imposed boundary condition at the cell surface. It is quite interesting to observe that this result resembles the Blackman bilinear model which gives the best fit for Koch and Houston Wang (1982) experimental data in the range of low concentrations. In this case the uptake rate can be expressed as a function of the far-field concentration: at low concentration, the interfacial concentration falls to zero and the flux is proportional to the far-field concentration as indicated in equation (2.7); above a saturation concentration S_∞^{sat} it becomes constant. This saturation concentration S_∞^{sat} corresponds to the limit case when $\varphi_{int}=\varphi_{max}$. Combining equation (2.8) and (2.14), it comes:

$$S_\infty^{sat}\left(1+\frac{R}{L}\right)=\frac{\Phi_{max}}{4\pi\mathcal{D}R}, \tag{2.20}$$

which simplifies into the following for $R \ll L$:

$$S_\infty^{sat}\approx\frac{\Phi_{max}}{4\pi\mathcal{D}R}. \tag{2.21}$$

The far-field concentration below which a limitation of the uptake rate occurs is relatively low, but one must consider that the cell concentration is also very small. Indeed, in our modelling one cell occupies the centre of a sphere of diameter $L+R\simeq L$, thus the approximate corresponding cell concentration is given by $\rho_{cell}(R/L)^3$, i.e. $1\ \mathrm{mg}\cdot\mathrm{L}^{-1}$. It is not surprising that such a low concentration is required to limit such a small amount of cells. Adversely it also shows that defining a limiting concentration irrespective of the cell density is probably incorrect. Although it is not the central point of this paper, one can wonder if a normalised definition based on the ratio of the substrate concentration to the cell concentration would not be more appropriate to establish a comparison between various experimental data. In the present case we would get a ratio $S_\infty/X\simeq 10^{-1}$, for the switch between the diffusion-limited regime and the biological regime (assimilation rate limited by the assimilation capability of the cell).

Finally a short comparison with results for the Monod assimilation model are given by Figure 2.5 for a small affinity constant $k_S=10^{-6}\ \mathrm{kg_S}\cdot\mathrm{m}^{-3}$. The results are very similar, encouraging the possibility to get rid of the macroscopic parameter K_S, especially if most of the substrate is assimilated by high-affinity transporters.

2.3.4 Time-varying far-field concentrations

A relationship between the far-field concentration and the uptake rate was found for a constant far-field. Is this also possible for time-dependent far-field concentration? In order to examine this point, a parametric study is performed on the ratio $T^*=T/\tau_D$, where T is the period of the signal and τ_D is the diffusional time. The parameters corresponding to each simulation are given in Table 2.1 and 2.2. The far-field concentration is chosen so that over one period two sub-periods can be identified: one with the far-field concentration above the saturation concentration and the other

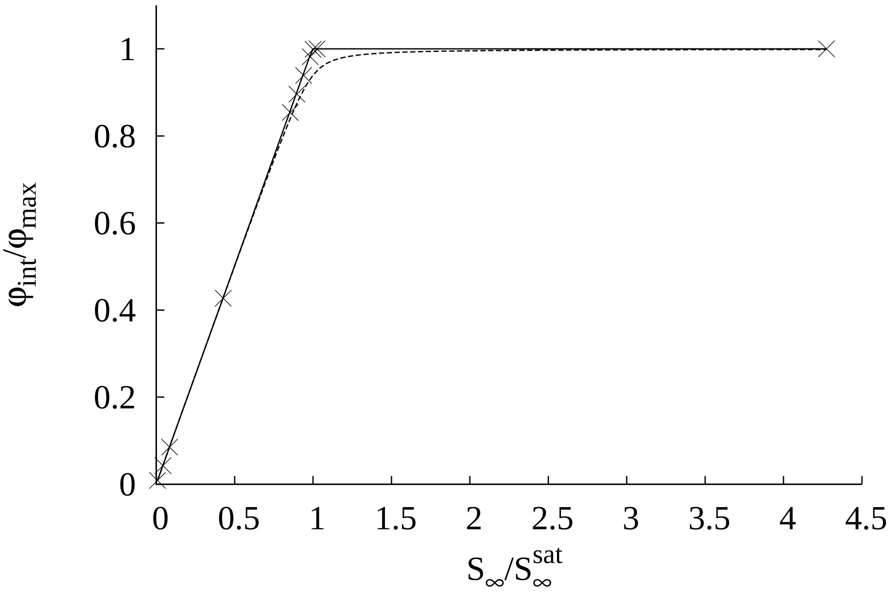

Figure 2.5: Normalised interfacial uptake rate in the steady state for different constant far-field concentrations. (——) analytical solution, × numerical values extracted from the simulations. (········) numerical values using a Monod assimilation model with a high-affinity constant $k_S = 10^{-6}\ \mathrm{kg_S \cdot m^{-3}}$.

one with the far-field concentration below the saturation concentration.

Figure 2.6 shows the temporal evolutions of the concentration (dashed line) and the uptake rate (solid line) at the microorganism interface calculated with a top-hat far-field concentration signal (dotted line). The effect of the Robin-like boundary condition at the microorganism interface is visible: once the interfacial flux has reached its maximum value, the interfacial concentration rapidly increases. Adversely, when the cell is exposed to a severe limitation, the interfacial concentration falls down to zero first and the flux decreases afterwards. The logic of the switch can be explained considering a step-up of the far-field concentration followed by a step-down. As long as the flux reaching the cell surface is lower than the maximum uptake rate, a zero concentration boundary condition is used. Then, when the interfacial flux equals the maximum uptake rate, a constant flux condition is imposed and the interfacial concentration progressively increases. Then, the far-field concentration falls suddenly. Shortly after, the interfacial concentration starts decreasing whilst the flux reaching the cell is unaffected (still maximum). In the end, the interfacial concentration reaches zero and it is no longer possible to internalize the substrate at the maximum uptake rate because transport towards the cell is limiting. So, a zero-concentration boundary condition is applied and the interfacial flux also starts decreasing. It can be noticed that the interfacial concentration and flux variations are interdependent but not strictly correlated. The concentration at the cell interface $S_{int}(t)$ varies whilst the interfacial flux φ_{int} is constant and maximum. Inversely the interfacial uptake rate can vary while the related interfacial concentration remains zero. The duration of those events is expected to change with the far-field signal (period and structure). Considering this fact, we decided to investigate in more detail the complex relationship between the structure of the far-field signal and the resulting interfacial signals. A sensitivity analysis on the influence of T^* on assimilation is conducted. Small values of T^* indicate that the concentration far from the cell changes rapidly in comparison with the time required to bring the substrate to the cell surface by diffusion. In this case, a direct relationship between the uptake rate and the far-field

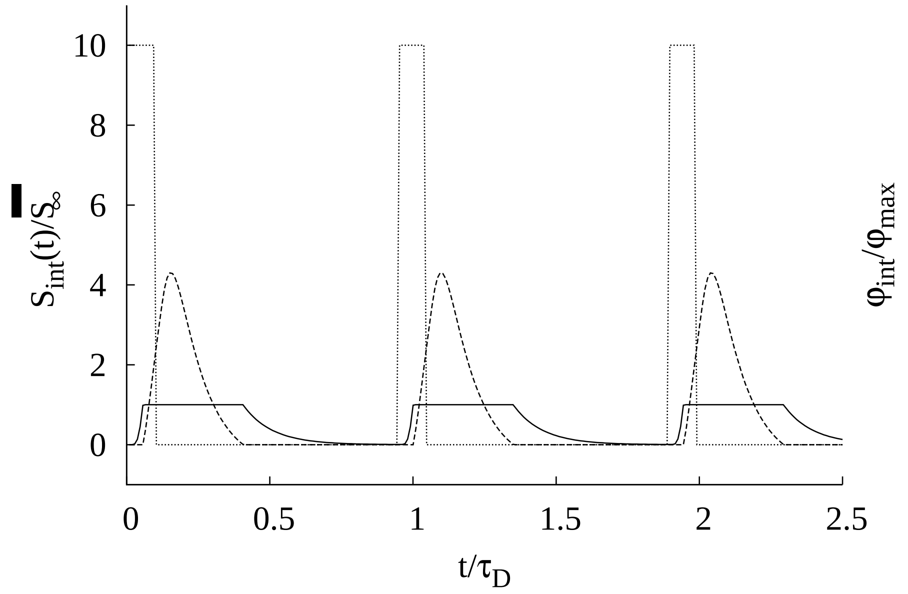

Figure 2.6: Temporal evolution of the top-hat far-field concentration (········) and the corresponding interfacial concentration (- - - -) and interfacial uptake rate (——). $\overline{S_\infty} = 2.10^{-4}\ \mathrm{kg_S \cdot m^{-3}}$, $T^* \simeq 1.1$.

concentration can be established: the fluctuations of the far-field signal are actually filtered by the diffusion process and the resulting mean interfacial uptake rate is given by equation (2.22), based on equation (2.8):

$$\varphi_{int} \simeq \frac{\overline{S_\infty}}{R}. \tag{2.22}$$

For large T^*, the concentration profile has enough time to get established before the far-field concentration changes. Therefore, a quasi-steady-state hypothesis can be used. The mean uptake rate can be estimated from the averaging of the instantaneous uptake rates computed from instantaneous far-field concentrations. In the intermediate case, a strong competition between fluctuations and transport takes place. The effect of these interactions on the microorganism uptake rate is not easily predictable.

In order to analyse the influence of the far-field concentration variation on assimilation, the time-averaged values of the interfacial flux are plotted against the mean far-field concentration for various T^* ratios. The results obtained with the sine and top-hat signals are presented by Figure 2.7 and Figure 2.8 respectively. The consequences of concentration fluctuations in the environment of the microorganism on the mean uptake rate are significant. Indeed, for a given mean far-field concentration, the mean normalised uptake rate in presence of concentration fluctuations is lower than that obtained in a uniform environment. A first consequence of the inhomogeneous concentration field is a decrease in the uptake rate of the cell.

At first sight, this conclusion seems to be in contradiction with the conservation of mass. The mean concentration is the same for all simulations so, where is the substrate which was not assimilated? In fact, one must remember that diffusion operates in two directions: it can bring the substrate towards the cell, or it can take it away from the cell if the substrate concentration at the cell surface is higher than that far from the cell. This is what happens, especially in the case of a top-hat signal because the pulse of high concentration is followed by a zero concentration period. Thus, the effects are much more pronounced for the top-hat signal than for a sine (see Figure 2.7 and 2.8). The substrate which is not assimilated vanishes in the far field and it is lost for the cell

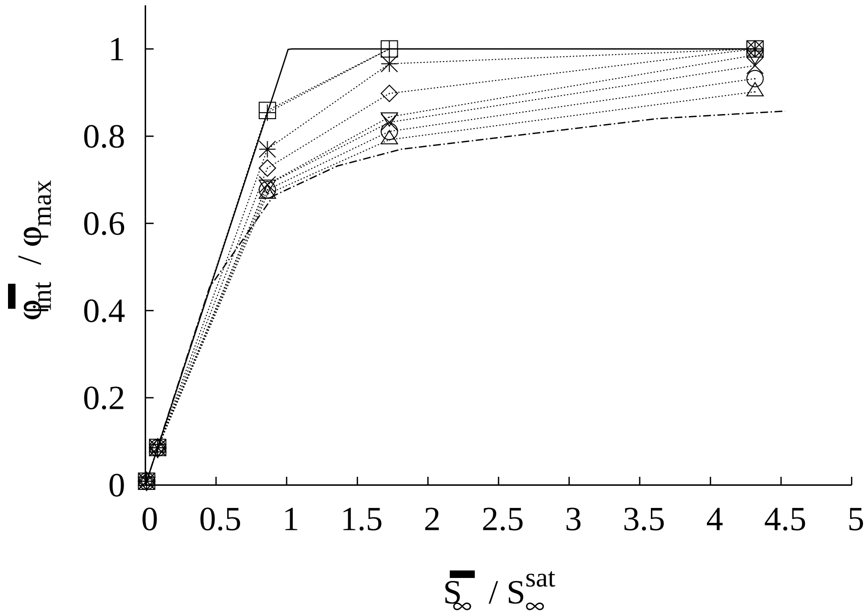

Figure 2.7: Effect of characteristic timescale of the sine time-varying far-field concentration signal on the time-averaged interfacial uptake rate in the established state. (———) constant far-field, + : $T^* \simeq 0.1$, □: $T^* \simeq 0.2$, ∗ : $T^* \simeq 0.5$, ◇: $T^* \simeq 0.7$, ▽: $T^* \simeq 0.9$, × : $T^* \simeq 1.1$, ○: $T^* \simeq 1.4$, △: $T^* \simeq 2$, (-·-·-) : $T^* \to \infty$ corresponding to the mean uptake rate based on the far-field concentration $\overline{\varphi(S_\infty(t))}$.

under consideration. One can observe that the cell was unable to internalize the substrate more rapidly despite the concentration peak because it has already reached its maximum uptake rate. It is remarkable to observe that this particular observation indicates that cells would take advantage of being able to increase their substrate uptake capacity. During the starvation period this additional capacity would remain unexploited, but it would allow them to uptake large amounts of substrate during the period of feast. A comparison between Figure 2.7 and Figure 2.8 shows that the higher the variance of the signal, the smaller the mean interfacial uptake rate. These can be regarded as the consequences of the competition between the assimilation and the mixing processes. Thus our simulations prove that the microorganism assimilation behaviour is strongly dependent on the mixing state of the surrounding medium. Despite the fact that the assimilation law at the cell level does not obey to a Monod equation, the averaged assimilation could be fitted with a Monod equation while both φ_{max} and K_S would depend on the characteristics of the far-field signal. In other words, the relationship between the observed uptake and the mean concentration might obey a Monod equation. But this is a macroscopic observation which reflects the interaction between transport phenomena and assimilation at the cell scale.

2.4 Discussion

The prediction of the substrate uptake rate is of crucial importance in modelling bioreactors because it couples the liquid phase to the biological reactions. Once the uptake rate is known, kinetic or metabolic models can be used to describe the intra-cellular reactions and the fate of the carbon within the cell. The concentration at the cell-liquid interface where assimilation actually takes place is not accessible through experiments, and it is therefore necessary to establish a relationship

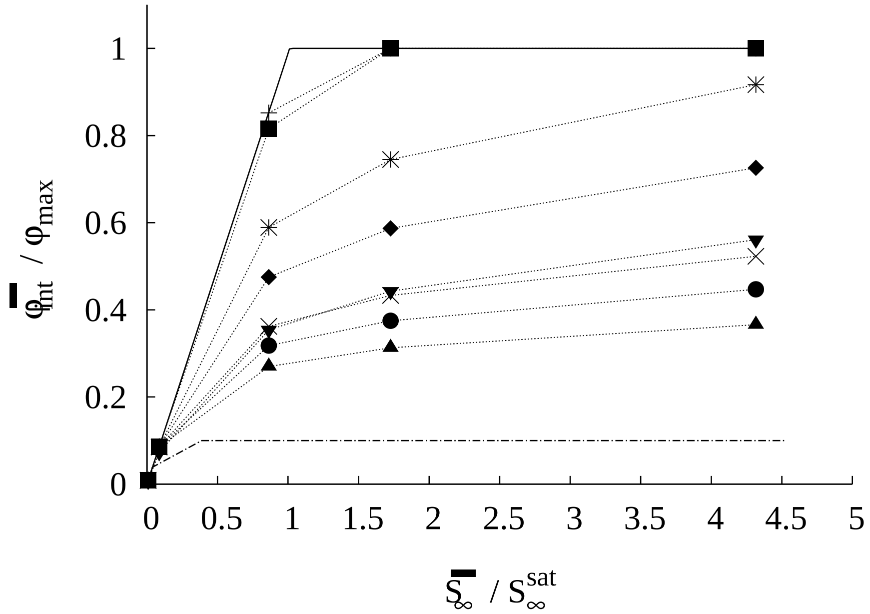

Figure 2.8: Effect of characteristic timescale of the top-hat time-varying far-field concentration signal on the time-averaged interfacial uptake rate in the established state. (——) constant far-field, + : $T^* \simeq 0.1$, ■ : $T^* \simeq 0.2$, ∗ : $T^* \simeq 0.5$, ◆ : $T^* \simeq 0.7$, ▾ : $T^* \simeq 0.9$, × : $T^* \simeq 1.1$, • : $T^* \simeq 1.4$, ▲ : $T^* \simeq 2$, (-·-·-) : $T^* \to \infty$ corresponding to the mean uptake rate based on the far-field concentration $\overline{\varphi(S_\infty(t))}$.

between the uptake rate and the average concentration in an elementary volume of fluid.

In most studies, experimental or numerical, dealing with fluid transport and biological reaction, the substrate consumption is ascribed to obey a general Monod law derived from macroscopic observations (Al-Homoud and Hondzo, 2008; Schmalzriedt et al., 2003; Lin et al., 2001). The survey of the literature reveals that the two constants used in this law are indeed dependent on the culture conditions (Lendenmann and Egli, 1998; Lin et al., 2001), which is obviously detrimental to the predictive capacities of the whole model. It was also found that different parameters are identified for the same strain (Koch and Houston Wang, 1982). The exact identification of these constants from experimental data is made difficult because of the strong interactions between assimilation and mixing taking place in bioreactors.

These considerations motivated the present work which aims at enlightening this scientific issue. It was decided to perform numerical simulations in a simplified case by taking into account only two well identified phenomena: mass transport and assimilation at the cell scale. One important thing to observe is that these two phenomena happen consecutively. Therefore, the observed rate results from the combination of both effects. In this paper, our choice was to solve directly the diffusive mass transport of substrate down to the cell level. Assimilation was described at the cell surface using two different assimilation laws (hyperbolic Monod and bilinear model). Thus these models correspond to the true biological uptake rate which is achieved without transport limitation. According to our simulation results, a hyperbolic relationship between the uptake rate and the mean concentration is systematically observed. But the effective affinity constant is clearly dependent on the physics of substrate transport. This conclusion stands for the two investigated models. The parameters of the hyperbolic relationship can be identified in the following cases:

- the imposed substrate concentration is constant $\varphi = \varphi(S_\infty)$,

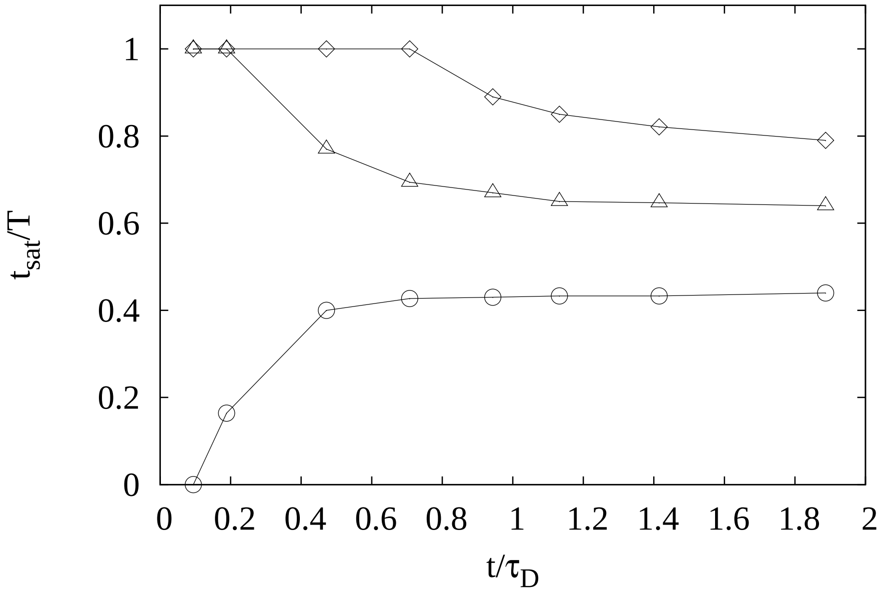

Figure 2.9: Saturation time at the maximum uptake rate over the corresponding period, as function of the characteristic time ratio for the sine far-field signal. ◇: $\frac{\overline{S_\infty}}{R\varphi_{max}} = 4.3$, △: $\frac{\overline{S_\infty}}{R\varphi_{max}} = 1.7$, ○: $\frac{\overline{S_\infty}}{R\varphi_{max}} = 0.85$.

- the characteristic time of transport is small compared to that of concentration changes ($T^* \ll 1$), leading to a quasi-steady state $\overline{\varphi} = \overline{\varphi(S_\infty(t))}$,
- the characteristic time of transport is very large compared to that of concentration changes ($T^* \gg 1$), resulting in a filtering of high frequencies $\overline{\varphi} = \varphi(\overline{S_\infty})$.

In order to perform this identification, the rate of transport has to be known and one must then solve the continuity of mass fluxes at the cell interface. An example is provided in the case of diffusion-controlled transport and a Monod assimilation law. It was found that the apparent affinity constant is only dependent on the rate of transport. For the intermediate cases ($T^* \approx 1$) the relationship between the uptake rate and the mean concentration still obeys a hyperbolic equation, but the affinity constant is now also impacted by the ratio T^*. In that case, it was observed that the temporal characteristics of the interfacial uptake rate and concentration are decoupled from those of the far-field signal. Moreover they also depend on the type of signal itself (mean value and variance). This is illustrated by Figure 2.6. It is particularly interesting to observe that for a top-hat signal with a mean value corresponding to a non-limiting concentration ($\overline{S_\infty} > S_\infty^{sat}$), the interfacial concentration periodically falls down to zero and the uptake rate is not maximum. Moreover the duration of these events (zero concentration and sub-optimal uptake rate) are impacted by the time constant ratio as shown by Figure 2.9. The same kind of observations can be made for a sine evolution of the far-field concentration and they are not restricted to a particular type of assimilation model. This suggests that cells may locally be exposed to starvation whereas the mean concentration is above the supposed limiting value.

This model developed for purely diffusive transport aimed to analyse the behaviour of cells in bioreactors. Further development can be envisaged with more realistic configuration for the substrate transport. Indeed, numerous studies of heat and mass transfer rates from spherical particles immersed in low-Reynolds numbers velocity fields have been performed over the years (Acrivos and Taylor, 1962; Frankel and Acrivos, 1968). Theoretical analysis have led to the development of asymptotic expressions for the Nusselt or Sherwood numbers as function of the Péclet number Pe for the cases of uniform to simple shear flow at infinity. For small Péclet numbers, the diffusion effects are dominant near the particle but an additional transfer, due to convection effects at large distances of the particle, enhances the purely diffusive mass transfer rate Sh0 and the added non-dimensioned transfer rate is equal to $\alpha Sh_0 Pe^{1/2}$. At large Péclet numbers the transfer rate depends on the velocity distribution at the particle (Poe and Acrivos, 1976), and can be either a constant or depending on the Péclet number as $\beta Pe^{1/2}$. Batchelor (1980), later derived a general method to determine the numerical values of the constants α and β for different given types of shear flow. The usual transfer rate is studied from the particle to the surrounding medium but previous studies (Purcell, 1978) have shown that results are similar for mass transfer towards a particle. Further numerical studies (Feng and Michaelides, 2000) concern the transient heat transfer from a spherical particle at high Reynolds and Péclet numbers and three-dimensional simulation could be envisaged in order to account for shear flow around the microorganism and substrate transport and assimilation. Considering the previous results for convective flows, in comparison with diffusive transport, smaller characteristic time scales are expected for convective transport on the domain length L. Nevertheless, the same interfacial responses are expected for the microorganism.

These conclusions help in understanding the experimental results of Garcia et al. (2009) showing that GFP (Green Fluorescent Protein) reporting strains sensitive to oxygen limitation were illuminated whilst cultivated in an agitated bioreactor with the DO (Dissolved Oxygen) maintained above 20%. It is known that starvation activates high-affinity transporters (Ferenci, 1999b). Transposing the observations of Garcia and co-workers to the glucose assimilation, one can also imagine that the repeated exposure of cells to low-concentration events can activate high-affinity transporters even if the measured substrate concentration is above the limiting value. This would partly explain the extra-assimilation capacity observed in poorly micro-mixed industrial bioreactors and the failure of standard models to accurately predict both the assimilation rate and the amount of over-flow metabolites. Ferenci (1999b) observed that in a batch culture, the gene coding for the high affinity transporters are activated at relatively high substrate concentration ($60\ \mathrm{mg \cdot L^{-1}}$), much higher than Ks ($1\ \mathrm{mg \cdot L^{-1}}$). Under these conditions it is difficult to understand the triggering factor for gene activation: the substrate influx is not limiting and the concentration is far above the affinity constant Ks. Considering the present work, one can analyse the experimental data in a slightly different way. First of all, the substrate concentration is not the accurate quantity; one must rather follow the ratio S/X which can be regarded as the ratio between the transport rate $\mathcal{D}_m(S - Si)/L$ and the assimilation rate μX. In the exponential growth phase, μ is constant. The rate of transport is also constant if the agitation speed is maintained. As the batch culture proceeds, the substrate concentration decreases and the amount of cells increases, so the ratio S/X progressively decreases indicating that transport limitation is more and more likely to occur. From the cell point of view, it means that the interfacial concentration is also progressively falling down to zero. When this lower value is reached, it can surely be considered as a signal for activating high affinity transporter. Our results show that the uptake flux can be maximal while the far field concentration is high above Ks and the interfacial concentration is close to zero. Insel et al. (2007), have shown that the initial substrate to microorganism ratio directly influence the population growth in batch cultures. By setting constant mean cell residence time and top-hat feed, they observed the kinetic response of *E. coli*. Regulation of growth metabolism by decreasing the maximum growth rate and increasing the substrate affinity constant results in a higher assimilation capacity.

Finally, in the conclusion of their work, Schmalzriedt et al. (2003) pointed out two directions for future improvements: dynamic metabolism modelling and micro-mixing. The former point has been addressed by Lapin et al. (2004). The experimental evidence of micro-mixing issues in biological reactors was brought some years ago by Dunlop and Ye (1990a) and Amanullah et al. (2001). In the field of chemical-reactor engineering, the term micro-mixing is used to depict the situation where the characteristic mixing time is similar or lower than the characteristic reaction time. When mixing competes with the reaction a concentration distribution occurs, so that homogeneity down to the molecular scale is not achieved in the reactor. The concentration distribution within the volume of control results from the combined effects of mixing and reaction. If the relationship between the reaction rate and the concentration is not linear, the actual average reaction rate differs from the reaction rate based on the average concentration. Since equation (2.1) is not linear one can effectively suspect that biological reactions (and substrate assimilation in particular) may lead to micro-mixing issues.

2.5 Conclusion

In this work a dynamic model for the assimilation of substrate by a microorganism subjected to concentration variations in its microenvironment is proposed. The transport of substrate towards the cell is represented by a purely diffusive process. Different assimilation models were scrutinised at the micro-organism interface. These models result in specific boundary conditions at the micro-organism interface. Firstly a classical Monod assimilation model was used, assuming the maximum specific growth rate and the affinity constant to be known. As expected a hyperbolic relationship between the uptake rate and the mean far-field concentration is found, but different effective affinity constants are observed depending on whether transport limits assimilation or not. An alternative model for substrate assimilation was developed in order to get rid of this parameter. The only biological parameter needed in this second approach is the maximum specific growth rate, from which the maximum interfacial mass flux can be estimated. A specific time-varying boundary condition, based on the substrate flux at the cell surface, is set. The results were similar to those obtained with a standard Monod law: a general hyperbolic evolution for the uptake rate is obtained for various far-field signal evolutions. However it was shown that the results differ depending on the type of fluctuations imposed in the microenvironment of the cell. This supports the idea that if assimilation takes place in the physical assimilation regime (the transport limits the assimilation) the uptake rate can not be directly derived from the biological assimilation. Finally, it was shown that the magnitude and duration of critically low-concentration events (at the cell surface) are dependent on the concentration fluctuations to which the cell is submitted. In that sense this work is helpful in understanding how the concentration fluctuations in the microenvironment of cells (caused by imperfect mixing at the cell level) may be responsible for the activation of high-affinity transporters.

Figures

Chapter 3

Numerical simulation of fluid turbulence, substrate transport

This chapter introduced the theoretical background for the direct numerical simulations of the present work. Firstly, the main assumptions and adaptations for handling biological flows are exposed. The fluid-flow configuration is presented as well as the numerical and statistical tools necessary for the analysis of the Homogeneous Isotropic Turbulent flow.
In order to validate and present the different simulations, a statistical analysis is performed for both the dynamic and the scalar field. Indeed, the mixing is completely obtained for the scalar. The different integral length scales of the flow are defined by means of Eulerian correlations. A spectral analyse is proposed in order to establish a reference case, especially for the scalar energy spectrum. With the aim of validated the different simulations and to introduced the Probability density functions, the usual fluid PDF are given and confronted with results from literature. A study on Lagrangian quantities of the flow is also performed in order to define different Lagrangian statistics.
This chapter is a data-base for the further work, that defines and presents all the statistics of the carrier-phase that will be later used for two-phase simulations.

Résumé

Après avoir étudié l'assimilation de sucre par un microorganisme soumis à des variations temporelles de concentration à l'échelle microscopique, nous avons décidé d'étudier le comportement d'une population de milliers de microorganismes dans un écoulement turbulent stationnaire en présence de fluctuations locales de concentration en substrat.

Une approche par simulation numérique directe a été choisie afin de s'affranchir de toute modélisation du transport turbulent. Toutes les échelles du champ dynamique sont donc résolues. On y adjoint la résolution du transport du substrat, assimilé à un scalaire passif.

Après avoir introduit les équations générales de Navier-Stokes et l'équation de transport du substrat, l'outil de simulation numérique direct JADIM est présenté. La configuration retenue pour la simulation des écoulements porteurs dans les bioréacteurs est ensuite expliquée. Tout d'abord, dans le but d'obtenir une connaissance totale des phénomènes mis en jeu dans le domaine simulé, une configuration statistiquement stationnaire est choisie pour l'agitation et le substrat afin de dériver des statistiques à l'échelle du domaine de calcul. Les limitations de l'approche pour les écoulements porteurs biologiques sont également abordées, notamment les limitations numériques.

Dans le but d'obtenir une étude de l'assimilation à l'échelle de la boîte, ou macroscopique, les outils statistiques sont introduits, et les équations moyennées pour les différentes grandeurs dynamiques et relatives au scalaire sont développées. On récapitule ensuite les différents paramètres physiques des simulations menées. En effet, différentes simulations ont été choisies afin de pouvoir comparer l'effet de la dynamique sur le mélange du substrat, ou encore à même champ dynamique, différents paramètres pour le mélange.

Afin de valider les simulations, une large gamme d'analyse statistique est proposée. Les différentes statistiques "classiques" sur l'énergie cinétique turbulente, la dissipation, l'énergie du scalaire et les plus petites échelles de l'écoulement sont résumées dans un tableau. On y trouve également les échelles intégrales de l'écoulement, basées sur une étude des corrélations Eulériennes.

Cette étude sur les corrélations Eulériennes permet d'introduire la définition de ces échelles intégrales pour le fluide et le scalaire. Les corrélations Eulériennes sont comparées aux expressions analytiques obtenues dans la littérature. Les temps Eulériens sont également calculés et comparés aux temps Lagrangiens obtenus à l'instar de l'étude proposée par Yeung et al. (2000). Basée sur les corrélations Eulériennes, la définition des spectres d'énergie pour la vitesse et le scalaire sont ensuite introduites et les différents spectres obtenus sont comparés à la loi universelle de Kolmogorov pour la zone inertielle. Les différents spectres pour l'énergie des fluctuations de concentrations du scalaire sont également comparés à la loi en $^{-5/3}$ et une comparaison de chaque spectre est proposée pour les différentes simulations pour le mélange du scalaire. Ces spectres servent de référence pour la suite du travail et l'analyse spectrale proposée dans le dernier chapitre se référera à ces spectres.

Afin de valider de manière un peu plus fine la dynamique du champ scalaire, on étudie également les distributions de fluctuations ce dernier. Le caractère gaussien des fluctuations, déjà mis en évidence par différents auteurs, est retrouvé pour nos simulations. Même si les fluctuations du scalaire sont gaussiennes, les distributions des gradients de fluctuations, elles, ne le sont pas. Il est, de plus observé un écart de distribution dans la direction de l'anisotropie pour le gradient du scalaire. Nos résultats sont confrontés à ceux obtenus par Pumir (1994) and Overholt and Pope (1996). Les coefficients d'asymétrie et d'aplatissement sont calculés et les valeurs obtenues sont en bon accord avec les travaux précédemment cités.

Enfin, on définit les corrélations Lagrangiennes utiles à l'analyse Lagrangienne de l'écoulement. Ces corrélations Lagrangiennes permettent de définir, notamment, les temps caractéristiques Lagrangiens du fluide et du substrat. Ceux-ci sont confrontés aux résultats principaux de Yeung et al.

(2000), et les différents temps caractéristiques des simulations sont comparés. Enfin, les fonctions de structures Lagrangiennes du second ordre sont définies et leurs évolutions tracées. Basé sur l'hypothèse de Kolmogorov (1962), selon laquelle il existe une zone d'évolution linéaire en temps de ces fonctions de structure, nous avons déterminé les constantes Lagrangiennes de Kolmogorov d'après nos simulations. Malgré la difficulté d'évaluer cette constante, l'évolution des valeurs obtenues est en relativement bon accord avec Fox (2003) ou Lien and D'Asaro (2002). Cette analyse est également menée pour les fonctions de structures relatives à la concentration en substrat. Finalement ce chapitre se présente comme un chapitre de présentation de l'approche DNS pour les simulations de la phase continue, mais aussi comme un chapitre de validation de l'outil numérique. Il fait également le récapitulatif des simulations monophasiques effectuées qui serviront de phase porteuse pour les microorganismes. Les différentes simulations effectuées permettent de proposer une gamme d'écoulements où la dynamique aussi bien que le mélange diffèrent mais dont les effets peuvent être comparés d'une simulation à une autre. L'avantage est donc de pouvoir ensuite caractériser l'impact de la dynamique et du mélange sur l'assimilation du substrat par les microorganismes dans une configuration stationnaire comme nous le verrons au chapitre 4.

Contents

Introduction

The second chapter of this work is devoted to the study of assimilation by one microorganism at the microscopic scale. The effect of fluctuating substrate concentrations on assimilation was enlightened and the competition between transport and assimilation was depicted with an elementary 1D framework. During this previous part of the work, the temporal evolution of substrate concentration and uptake rate by the microorganism were studied. Even if the knowledge of assimilation by one microorganism is of extreme importance for understanding local interactions, a more realistic study consists in considering a whole population of microorganisms. Therefore, from now on, and based on the observations made in chapter 2 the present chapter will focus on assimilation of substrate by populations of thousands of microorganisms in a homogeneous turbulent flow.

Moreover, pursuing the idea that the assimilation is a microscopic phenomenon which consequences are observable at the macroscopic scale, the knowledge of the mixing at the microscopic scale is needed. In order to get rid of any model for turbulence or mixing we chose to perform direct numerical simulations of a turbulent flow with a scalar transport. In so doing, the micro-mixing is entirely known and its consequence on substrate assimilation is scrutinised in the following of the work.

The different equations, the numerical tool and the configuration of the study are presented, a deep statistical analysis of both the velocity and substrate concentration fields is carried out. The aim of this chapter is to introduce and summarise the different flow fields and the different statistical tools employed during this work.

3.1 Direct numerical simulation of substrate transport

The Fluid Mechanics approach for the numerical simulation of bioreactors was introduced in chapter 1. The RANS or LES approaches are generally chosen for the carrier flow determination and the substrate mixing in the study of bioreactors (Enfors et al., 2001; Schmalzriedt et al., 2003; Lapin et al., 2004, 2006; Delafosse, 2008). But, the interactions between the carrier phase and the biomass are dependent on the applied models. Therefore, in order to get rid of any models on the velocity field and substrate concentration field, we chose to perform Direct Numerical Simulations (DNS) for a simple configuration of homogeneous isotropic turbulent flow.

We first present the general framework for the fluid turbulence and substrate transport simulations. The general governing equations are given and the numerical tool is presented. The specificities of the chosen configuration are explained as well as the limitations of the approach.

3.1.1 General equations

Based on the idea to avoid any modelling of the velocity field or for the substrate mixing, our approach can be seen as the idea to simulate the flow and substrate transport in one computational cell of a RANS or LES calculation in an industrial reactor. Based on this idea, the numerical study of substrate turbulent transport in an incompressible fluid flow is investigated. The general equations for the velocity field and substrate transport are given hereafter.

Fluid flow equations

For turbulent incompressible Newtonian fluids, the local instantaneous governing incompressible Navier-Stokes equations are:

- Mass balance:

$$\frac{\partial u_{f,i}}{\partial x_i} = 0. \tag{3.1}$$

- Momentum Equation (Navier-Stokes equation):

$$\frac{\partial u_{f,i}}{\partial t} + u_{f,j}\frac{\partial u_{f,i}}{dx_j} = -\frac{1}{\rho_f}\frac{\partial p_f}{\partial x_i} + \nu_f \frac{\partial^2 u_{f,i}}{\partial x_j \partial x_j}, \tag{3.2}$$

where $\mathbf{u}_f$ is the fluid velocity at the position $\mathbf{x}$, p_f the pressure, ρ_f the fluid density, and ν_f the fluid kinematic viscosity. The subscripts i and j refer to the i^{th} and j^{th} directions. Because we decide to perform direct numerical simulations, the exact Navier-Stokes equations are resolved and the whole scales involved in the turbulent flow are solved.

Substrate concentration transport equation

Concerning the substrate, it is regarded as a passive scalar, which general transport equation is given by equation (3.3). The passive property for the scalar means that it does not influence the velocity field. So, the general form of equation (3.3) for the substrate transport is a convection-diffusion equation:

$$\frac{\partial S}{\partial t} + u_{f,j}\frac{\partial S}{\partial x_j} = \mathcal{D}_{S,f}\frac{\partial^2 S}{\partial x_j \partial x_j}, \tag{3.3}$$

where S is the substrate concentration, and $\mathcal{D}_{S,f}$ is the molecular diffusivity of the substrate S in the fluid.

3.1.2 Numerical tool and flow configuration

Numerical tool

The Navier-Stokes equations are solved with the JADIM code developed at the IMFT. JADIM is a Finite Volume numerical code for the direct simulation of incompressible turbulent fluid flows with passive scalar transport. The fluid turbulence can also be solved by means of Large Eddy Simulations (LES). JADIM offers the possibility to solve multiphase flow with Volume Of Fluid method or Lagrangian particle tracking. JADIM is based on a finite volume method and the spatial derivatives are evaluated with a second-order centred scheme in space (Magnaudet et al., 1995) and integrated in time with an explicit second order Runge-Kutta method. Further information is given in Legendre (1996).

The computational domain is a three-dimensional cubic box of length L_{box} as shown in Fiugre 3.1a. A cartesian mesh with constant grid-space Δ in the three directions is used. All simulations are performed with 128 nodes in each direction, and the analytical development of the last chapter is investigated with a 64^3 grid.

Stationary Homogeneous Isotropic Turbulence

In this work, we decided to focus on a simple configuration for the turbulent flow field. Indeed, the exact resolution of the flow dynamics and substrate mixing is not reachable in industrial configurations. With the aim to explore the local interactions between substrate mixing and biological

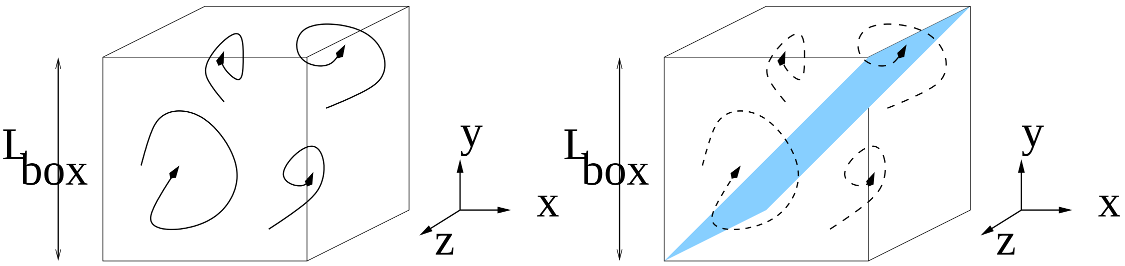

(a) Velocity (b) Substrate

Figure 3.1: DNS calculations configuration.

assimilation we chose a direct resolution for the Navier-Stokes equations and the substrate transport to perform a physical analysis of the different involved phenomena. By means of these analyses on a simple academic configuration, the development of models is envisaged at the cubic box scale. Finally the idea is to use the obtained models for RANS or LES simulations at the industrial scales. But this work does not considerer the industrial scale and remains focused on the microscopic (microorganisms) and mesoscopic (computational domain) scales.

Furthermore, we study a homogeneous isotropic forced turbulent flow with no mean velocity. The homogeneity of the flow corresponds to the invariance by translation of statistical properties of the flow field. If those statistical properties do not depend on the direction of computation, the flow field is isotropic and the correlations are invariant by rotation. A mathematical transcription of these assumptions is given in the statistical analysis paragraph. They are not realistic but they enable the development of theoretical models and the mathematical equations governing the flow.

But, the turbulent flows are dissipative by nature. Due to dissipation at the small scales, the turbulent properties of the velocity field will decrease in time, leading to an unsteady configuration for the simulations. This non-stationary nature of the flow increase the complexity of the study and the development of specific models. For that reason, we chose to consider a statistically steady Homogeneous Isotropic Turbulent (HIT) flow configuration. This statistically-steady state allows to obtain precise statistics and to focus on specific terms of interest.

The stationarity of the velocity field is maintained by addition of a forcing term f_i to the Navier-Stokes equations (3.2). Further details on the dynamic field forcing methods are given in the next section. Considering previous observations, a stationary configuration is chosen for the substrate concentration field as well. This does not mean that the substrate field is uniform at all times, but the statistic analysis is simplified but the steady configuration. In order to preserve a stationary substrate field, it is "forced" as well. The next paragraph is devoted to introduce the different forcing methods for both the velocity and substrate concentration fields.

3.1.3 Forcing method for the statistically-steady HIT

Dynamic field

As already introduced, the turbulent flows are dissipative by nature. In order to maintain a certain amount of turbulent kinetic energy, artificial input of energy is necessary. Different methods exist for forcing the turbulent energy.
The deterministic approach was developed by Overholt and Pope (1998). It consists of a linear

amplification of the lower-wave number modes (corresponding to the biggest scales) by relaxation over time toward a model energy spectrum function representing accurately a grid turbulence.

Another manner for injecting turbulent kinetic energy is to add a random force term, f, in the Navier-Stokes equation. This approach, called stochastic approach is used for the present work. The amplitude, frequency and wave-number range for the turbulent forcing have to be characterised. The forcing scheme proposed by Eswaran and Pope (1988) is chosen here. Several works were carried out with this forcing scheme for different studies: Overholt and Pope (1996) studied passive scalar transport with an imposed mean gradient in HIT, Sundaram and Collins (1997) evaluated the rate of inter-particle collisions as function of the turbulence parameters, or Boivin et al. (1998) used this technique to study the turbulence modulation by particles in isotropic turbulence.
Février and Simonin (2000) checked the validity of the forcing algorithm based on the formulation of Eswaran and Pope (1988). Further information can be found in Février and Simonin (2000) and Fede (2004). The forcing scheme parameters can be found in Appendix C for the different performed simulations.

$$\frac{\partial u_{f,i}}{\partial t} + u_{f,j}\frac{\partial u_{f,i}}{dx_j} = -\frac{1}{\rho_f}\frac{\partial p_f}{\partial x_i} + \nu_f \frac{\partial^2 u_{f,i}}{\partial x_j \partial x_j} + f_i. \tag{3.4}$$

Substrate concentration field

Different methods exist for the scalar forcing. The stochastic approach for forcing the scalar field can be used by applying an additional term f_S to the substrate transport equation (3.3). This method was chosen by Jaberi (1998) to study temperature fluctuations in a particle-laden turbulent flow.

An other method is chosen here, following the example of Overholt and Pope (1996), where a stochastic approach is used for the turbulence forcing and an imposed mean gradient is applied to force the scalar field.
The substrate concentration gradient is imposed in the y-direction and is constant in time:

$$\zeta = \frac{\partial S}{\partial y}. \tag{3.5}$$

Moreover, it is applied centred on the cubic box so that the mean applied substrate concentration by the imposed gradient is zero. Following this idea, the local substrate concentration can be written as:

$$S(\mathbf{x}) = S_0 + \tilde{s}(\mathbf{x}) + \zeta(y - \frac{L_{box}}{2}), \tag{3.6}$$

where S_0 is the total average concentration and $\tilde{s}$ is the substrate concentration deviation to the imposed substrate gradient.

In order to force fluctuations of substrate concentration, a mean concentration gradient $\underline{\zeta}$ is imposed and only the contribution in the second direction $x_2 = y$ is non-zero.

$$\underline{\zeta} = \begin{pmatrix} 0 \\ \zeta \\ 0 \end{pmatrix}. \tag{3.7}$$

Consequently, the concentration field is not isotropic and specific boundary conditions are required for the substrate field. In order to use similar boundary conditions for the velocity field and substrate field, the transport equation on fluctuating substrate concentration s' is considered and periodic boundary conditions can be applied in this case. This equation is given in paragraph 3.2. The instantaneous substrate concentration field can thus be reconstructed, at any point $\mathbf{x}$ of the domain, from the different contributions: imposed mean concentration S_0, fluctuating concentration s' and concentration gradient contribution:

$$S(\mathbf{x}) = S_0 + s'(\mathbf{x}) + \underline{\zeta}(\mathbf{x} - \frac{L_{box}}{2}). \tag{3.8}$$

By rewriting the transport equation (3.3) with the above decomposition for S we obtain:

$$\frac{\partial \tilde{s}}{\partial t} + v_f \frac{\partial S}{\partial y} + u_{f,j} \frac{\partial \tilde{s}}{\partial x_j} = \mathcal{D}_{S,f} \frac{\partial^2 \tilde{s}}{\partial x_j \partial x_j}, \tag{3.9}$$

where the second term can be written as $v_f \zeta$. Equation (3.9) is then equivalent to:

$$\frac{\partial \tilde{s}}{\partial t} + u_{f,j} \frac{\partial \tilde{s}}{\partial x_j} = \mathcal{D}_{S,f} \frac{\partial^2 \tilde{s}}{\partial x_j \partial x_j} + f_S, \tag{3.10}$$

where $f_S = -v_f \zeta$ can be seen as a production term by the mean gradient for the transport equation on $\tilde{s}$. By analogy with the momentum equations, the term f_S is the forcing term for the substrate concentration. The flow configuration for the substrate concentration field is shown in Figure 3.1b where the mean gradient is shown as an imposed layer in the y-direction.

3.1.4 Solved equations and boundary conditions

Considering the zero mean velocity field, and the HIT configuration for the dynamics, *periodic boundary conditions* are applied in the three directions for the velocity field. Moreover, any instantaneous variable is constituted from two terms: an average contribution and a fluctuating contribution. For example the fluid velocity $\mathbf{u}_f$ can be written as:

$$\mathbf{u}_f = \langle \mathbf{u}_f \rangle + \mathbf{u'}_f, \tag{3.11}$$

where $\langle \mathbf{u}_f \rangle$ is the mean part of $\mathbf{u}_f$ and $\mathbf{u'}_f$ the fluctuating part. From now on, the notations $\langle \cdot \rangle$ and $\cdot'$ will refer to averaged and fluctuating quantities respectively.

The definition of homogeneity and isotropy for the turbulence are then respectively:

$$\forall (i,j),\ \langle u'_{f,i}(\mathbf{x}_1,t) u'_{f,j}(\mathbf{x}_1,t) \rangle = \langle u'_{f,i}(\mathbf{x}_2,t) u'_{f,j}(\mathbf{x}_2,t) \rangle, \tag{3.12}$$

$$\forall (i,j),\ \langle u'_{f,i}(x,t) u'_{f,i}(\mathbf{x},t) \rangle = \langle u'_{f,j}(\mathbf{x},t) u'_{f,j}(\mathbf{x},t) \rangle. \tag{3.13}$$

Furthermore, according to the zero mean velocity field, the total fluid velocity $\mathbf{u}_f$ is equivalent to the fluctuating velocity $\mathbf{u'}_f$.

Concerning the substrate concentration field, due to the imposed gradient, the boundary conditions on S are tricky, Indeed the total substrate concentration is isotropic. But if we look at the substrate concentration decomposition (3.8), the deviation concentration to the gradient $\tilde{s}$ is homogeneous and isotropic by construction. Therefore it is easy to solve the transport equation on this substrate concentration $\tilde{s}$ with periodic boundary conditions[1].

---

[1] We may mention here that the periodic resolution for the substrate concentration field on the deviation concentration $\tilde{s}$ is one of the studied configurations. Indeed, in the last chapter, unsteady simulation for the substrate concentration requires the resolution of the total substrate concentration S. The precision on this resolution is given in chapter 5.

Finally, both the velocity and substrate field are handled periodically and the resolved equations are:

Mass balance equation:

$$\boxed{\frac{\partial u_{f,i}}{\partial x_i} = 0} \tag{3.14}$$

Forced Navier-Stokes equations:

$$\boxed{\frac{\partial u_{f,i}}{\partial t} + u_{f,j}\frac{\partial u_{f,i}}{\partial x_j} = -\frac{1}{\rho_f}\frac{\partial p_f}{\partial x_i} + \nu_f \frac{\partial^2 u_{f,i}}{\partial x_j \partial x_j} + f_i} \tag{3.15}$$

Forced substrate transport equation:

$$\boxed{\frac{\partial \tilde{s}}{\partial t} + u_{f,j}\frac{\partial \tilde{s}}{\partial x_j} = \mathcal{D}_{S,f}\frac{\partial^2 \tilde{s}}{\partial x_j \partial x_j} + f_S} \tag{3.16}$$

Finally, based on Reynolds decomposition, the substrate concentration field can be written as:

$$S(\mathbf{x}) = \langle S \rangle + s'(\mathbf{x}). \tag{3.17}$$

By analogy with the used decomposition in equation (3.8), the average concentration $\langle S \rangle$ can be seen as the contribution of both $S_0 + \langle \zeta y \rangle^2$ and the fluctuation s' as the deviation term $\tilde{s}$. Based on this analogy, the distinction between s' and $\tilde{s}$ is no longer made and the different statistics refer to the fluctuating concentration s'.

3.1.5 Limitations and Assumptions

Rheology

The present work focuses on the study of turbulent incompressible flows of Newtonian fluids. In biological reactors, it is known that the viscosity changes with the substrate feed or the biomass growth. For example, Thomson and Ollis (1980) describe the evolution of shear viscosities of xanthan batch fermentation broths and found out they obey a power-law relation, which parameters are the xanthan concentration. Thus, the broth rheology of this type of batch fermentation does not follow the Newton-law, and can affect the fluid flow. The expression of viscous term in bioreactor can, in consequence, be affected by the broth rheology and the Navier-Stokes equations are no longer suitable for the dynamic field resolution. But these situations will not be of interest here and the resolution of the equations (3.14) and (3.15) is a good approximation.

Incompressibility

Moreover, the incompressibility assumption can as well be discussed in bioreactors, where large concentrations of substrate are injected. The substrate, as dissolved species, can locally modify the density of the carrier phase, and compressibility effects can occur in the carrier flow. Nevertheless, these density modifications will not be investigated here and the flow is supposed to obey the mass balance for incompressible flow (equation (3.14)).

---

[2] where $\langle \zeta y \rangle = 0$ by definition of the imposed gradient.

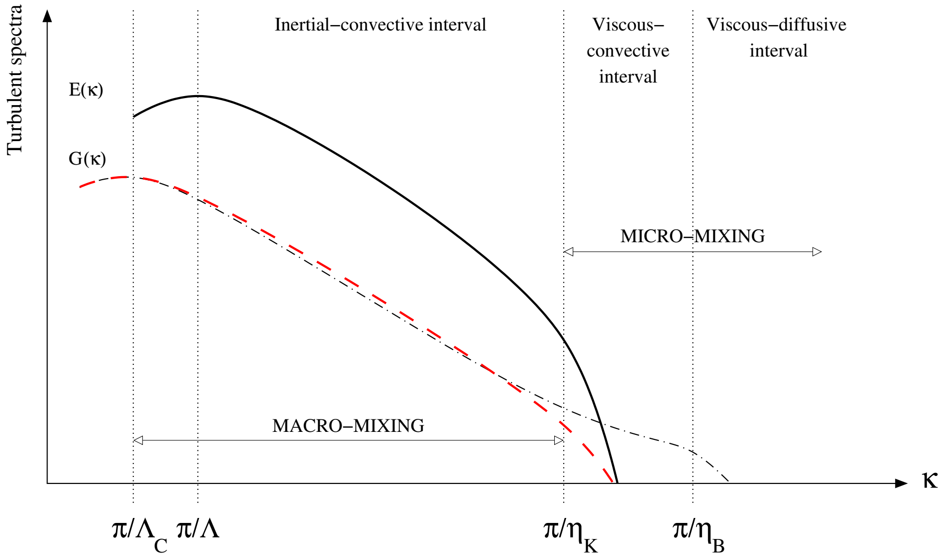

Figure 3.2: Turbulent energy spectra for the velocity (———) and scalar (-·-·-).

Numerical and computer limitations

We choose to simulate a fully turbulent flow by means of direct numerical simulations. As already explained, the Navier-Stokes equations are exactly solved with an appropriate numerical tool. Turbulent flows involve various scales that must entirely be solved in the DNS approach. Therefore the mesh size of the computational grid has to be smaller than the smallest scales of the turbulent flow.

If we look at Figure 3.2, representing the turbulent kinetic energy and the scalar energy spectra, we can see that the smallest scale for the flow dynamics is the Kolmogorov scale η_K. But for the scalar mixing, the Batchelor scale η_B is the smallest scale (Batchelor wavenumber κ_B much larger) where mixing is purely diffusive. The inertial convective subrange has to be solved as well and therefore, the resolution of the simulation must be increased in order to ensure $\Delta < \eta_B$ and the computational cost is increased. Moreover, the Batchelor scale increases with the Schmidt number of the flow. For large Schmidt-numbers flows involved in bioreactors (typically $Sc \equiv 1000$ for glucose in water), the Batchelor scale is 3 hundred times smaller than the Kolmogorov scale in a bioreactor. This implies a high-resolution grid that cannot be reached in the present work.

Nevertheless, because of numerical limitations (vectorial code), the present study focuses on smaller Schmidt-number simulations typically of order 0.7 to 1 in order to fully resolved all scales for the flow and mixing. Indeed, as studied by Batchelor et al. (1959), in the case of large diffusivity compared to the fluid viscosity, the scalar spectrum is less spread and the scalar fluctuations decrease faster than the universal-convective subrange (see figure 3.2, dashed line), so the smallest scales for the scalar mixing are close to the Kolmogorov scale.

We have in mind to study the impact of the flow dynamics on substrate mixing and then substrate assimilation by microorganisms. But we have seen that the simulation of liquid flow (high Schmidt number flow) is not reachable and therefore we rather chose to study small Schmidt number but large Reynolds numbers flow. But we must remind that the micro-mixing in the viscous-convective and viscous-diffusive intervals could have an impact on assimilation by the microorganisms. Indeed, the physics of the scalar mixing are modified by the Schmidt number. As shown by Yeung et al. (2002) the scalar mixing is weaker for small Schmidt numbers. Moreover, it has been shown that the scalar variance increases whereas the scalar dissipation rate remains constant for small turbulent Reynolds numbers $Re_\lambda = 8$ Yeung et al. (2004). Aware that the deviations below the Kolmogorov scale concerning the scalar mixing could have a direct impact on assimilation, those effects are not directly investigated in the present work.

After presenting the chosen configuration and the different limitations of the approach, the different tools for the statistical analysis are introduced in the next paragraph in order to explain the different turbulent quantities and to develop the different equations for the validation and analysis of the simulations.

3.2 Tools for statistical analysis

3.2.1 Averaging methods and definitions

The first average is the average over the time introduced in chapter 2. The *temporal average* for the signal $E(t)$, where T is a period of time, is:

$$\overline{E} = \frac{1}{T}\int_0^T E(t)dt. \tag{3.18}$$

This continuous definition for the temporal average can be discretised with $E_i = E(t_i)$ with $t = [t_i]_{i=1..n}$ and an ensemble average can be performed on the discretised samples E_i.

An other notation introduced in the precedent section $\langle\cdot\rangle$ is accounting for the *spatial average* over the spatial domain:

$$\langle E\rangle = \frac{1}{V}\int\int\int_0^V E(\mathbf{x})d\mathbf{x}. \tag{3.19}$$

For turbulent stationary flows, the random evolution of the variable $E(t)$ over a long period of time contains the same information as finite ensemble of realisations and the ergodic hypothesis applies. In the present case, the ensemble average is approached by the spatial average over the total number of nodes of the Eulerian grid. This quantity can as well be averaged in time. According to Février and Simonin (2000), the time period for averaging must be long enough to account for the different involved physical phenomena. So, for HIT, at least 10 integral time scale must be computed.

Finally, considering the Lagrangian tracking of particles, a last average is introduced and the average over the particle ensemble for the variable E is written:

$$\langle E\rangle_p = \frac{1}{N_p}\sum_{i=1}^{N_p} E_{i@p}, \tag{3.20}$$

where N_p is the particle number and the subscript $\cdot_p$ yields for "particles".

3.2.2 Average properties

For all average types, the same properties are found for the mathematical operator: it is linear and idempotent (3.21) and commutative (3.23). For the sake of convenience, the simple $\overline{\cdot}$ notation is chosen here for E and F and α, β are real constants.

$$\overline{\alpha E + \beta F} = \alpha\overline{E} + \beta\overline{F}, \tag{3.21}$$

$$\overline{EF} = \overline{E}\ \overline{F} + \overline{e'f'}, \tag{3.22}$$

$$\overline{\frac{\partial E}{\partial x}} = \frac{\partial \overline{E}}{\partial x}, \tag{3.23}$$

$$\overline{\overline{E}} = \overline{E}. \tag{3.24}$$

3.2.3 Averaged equations for the fluid phase

The Reynolds decomposition is applied to the fluid velocity and to the substrate concentration. Based on the solved equations for the velocity and substrate concentration, further equations are then derived for the transport of averaged and fluctuating quantities. By averaging equations (3.14) to (3.3) the average equations for velocity and substrate concentration are:

Mass balance for the mean velocity:

$$\frac{\partial\langle u_{f,i}\rangle}{\partial x_i} = 0. \tag{3.25}$$

Momentum equation for the mean velocity:

$$\frac{\partial\langle u_{f,i}\rangle}{\partial t} + \frac{\partial\langle u'_{f,i}u'_{f,j}\rangle}{\partial x_j} = -\frac{1}{\rho_f}\frac{\partial\langle P_f\rangle}{\partial x_i} + \nu_f\frac{\partial^2\langle u_{f,i}\rangle}{\partial x_j \partial x_j}. \tag{3.26}$$

Transport equation for the mean substrate concentration:

$$\frac{\partial\left\langle S\right\rangle}{\partial t} = \mathcal{D}_{S,f}\frac{\partial^2\left\langle S\right\rangle}{\partial x_j \partial x_j} - \frac{\partial\left\langle u'_{f,j}s'\right\rangle}{\partial x_j}. \tag{3.27}$$

We can see that second order terms appear in the average equation for the velocity and substrate concentration. The Reynolds stresses $\langle u'_{f,i}u'_{f,j}\rangle$ and scalar turbulent fluxes $\left\langle u'_{f,j}s'\right\rangle$ are unclosed terms in the averaged equations. Furthermore the average of the forcing force $\langle f_i\rangle$ is null and the fluctuating part of this force in the instantaneous force $f_i = f'_i$.

The equations for the fluctuating quantities are obtained by subtracting the averaged equations from the instantaneous equations.

Mass balance for the fluctuating velocity:

$$\frac{\partial u'_{f,i}}{\partial x_i} = 0. \tag{3.28}$$

Momentum equation for the fluctuating velocity:

$$\frac{\partial u'_{f,i}}{\partial t} + u'_{f,j}\frac{\partial u'_{f,i}}{\partial x_j} = -\frac{1}{\rho_f}\frac{\partial p'_f}{\partial x_i} + \nu_f\frac{\partial^2 u'_{f,i}}{\partial x_j \partial x_j} + f'_i. \tag{3.29}$$

Transport equation for the substrate fluctuating concentration:

$$\frac{\partial s'}{\partial t} + u'_{f,j}\frac{\partial\left\langle S\right\rangle}{\partial x_j} + u'_{f,j}\frac{\partial s'}{\partial x_j} = \mathcal{D}_{S,f}\frac{\partial^2 s'}{\partial x_j \partial x_j} + \frac{\partial\left\langle u'_{f,j}s'\right\rangle}{\partial x_j}. \tag{3.30}$$

We may remind here that there is no mean velocity for the HIT configuration, therefore the advection by the mean velocity terms have been removed from the above equations. Moreover the contribution of the imposed gradient in the y direction is in the second term of equation (3.30) reduces to:

$$u'_{f,j}\frac{\partial\left\langle S\right\rangle}{\partial x_j} = v'_f\zeta. \tag{3.31}$$

where v'_f is the fluctuating velocity component in the y direction $v'_f = u'_{f,2}$. Finally, the equation for the transport equation for the fluctuating substrate concentration is:

$$\frac{\partial s'}{\partial t} + u'_{f,j}\frac{\partial s'}{\partial x_j} = -v'_f\zeta + \mathcal{D}_{S,f}\frac{\partial^2 s'}{\partial x_j \partial x_j} + \frac{\partial\left\langle u'_{f,j}s'\right\rangle}{\partial x_j}. \tag{3.32}$$

This equation is solved by the numerical tool and periodic boundary conditions are applied for the fluctuating concentrations at the computational domain boundaries.

The equations for the transport of statistical properties for the fluctuating field can be derived, especially for the correlation of substrate concentrations variance $\langle s'^2 \rangle$. The following equations are simplified with the problem configuration (HIT and imposed mean gradient in y direction).

Transport equation for the substrate concentration variance:

$$\frac{\partial \left\langle {s'}^2 \right\rangle}{\partial t} = -2 \left\langle v'_f s' \right\rangle \zeta + \mathcal{D}_{S,f} \frac{\partial^2 \left\langle {s'}^2 \right\rangle}{\partial x_j \partial x_f} - 2\mathcal{D}_{S,f} \left\langle \frac{\partial s'}{\partial x_j} \frac{\partial s'}{\partial x_j} \right\rangle . \tag{3.33}$$

The temporal evolution of the substrate concentration variance is the balance between production by the mean concentration gradient and the concentration dissipation by molecular diffusivity. The production term is directly linked to the substrate concentration turbulent flux $\left\langle u'_{f,i} s' \right\rangle$.

Transport equation of the turbulent flux:

$$\begin{aligned} \frac{\partial \left\langle u'_{f,i} s' \right\rangle}{\partial t} \quad = & \quad - \left\langle u'_{f,i} u'_{f,j} \right\rangle \frac{\partial \langle S \rangle}{\partial x_j} \quad - \quad \frac{1}{\rho_f} \left\langle s' \frac{\partial p'}{\partial x_i} \right\rangle \\ & + \quad \mathcal{D}_{S,f} \left\langle u'_{f,i} \frac{\partial^2 s'}{\partial x_j \partial x_j} \right\rangle \quad + \quad \nu_f \left\langle s' \frac{\partial^2 u'_{f,i}}{\partial x_j \partial x_j} \right\rangle \quad + \quad \langle s' f'_i \rangle . \end{aligned} \tag{3.34}$$

At this time, the production term of substrate turbulent flux is controlled by the Reynolds stresses $\langle u'_{f,i} u'_{f,j} \rangle$.

Transport equation of the Reynolds stresses:

$$\begin{aligned} \frac{\partial \left\langle u'_{f,i} u'_{f,j} \right\rangle}{\partial t} \quad = & \quad -\frac{1}{\rho_f} \left\langle u'_{f,i} \frac{p'_f}{\partial x_j} \right\rangle \quad - \quad \frac{1}{\rho_f} \left\langle u'_{f,j} \frac{p'_f}{\partial x_i} \right\rangle \\ & + \quad \nu_f \frac{\partial^2 \left\langle u'_{f,i} u'_{f,j} \right\rangle}{\partial x_k \partial x_k} \quad - \quad 2\nu_f \left\langle \frac{\partial u'_{f,i}}{\partial x_k} \frac{\partial u'_{f,j}}{\partial x_k} \right\rangle \quad + \quad \langle u'_{f,i} f'_j \rangle + \langle u'_{f,j} f'_i \rangle . \end{aligned} \tag{3.35}$$

The equation evolution for the fluid turbulent kinetic energy is easily obtained from (3.35) by considering $i = j$.

The different introduced equations summarise the different equations after application of the Reynolds decomposition. The evolution of both mean velocity and concentration involve the second order moments such as the Reynolds stresses or turbulent flux in both equations (3.26) and (3.27). Moreover, the presented equations do consider the different assumptions of the flow configuration such as zero mean velocity and HIT. Further additional terms are found in the general equations. By considering those different equations and the different statistical correlations, different average quantities are extracted from the simulations at the box scale. For some variables, the results are known, but the calculation of statistical properties of the flow is a validation tool, for the simulations as well as for investigated models. These transport equations are used to validate the different simulations as we will see in the next paragraph.

3.3 Results of numerical simulations for the fluid flow

3.3.1 Fluid flows presentation

This part of the work is devoted to the analysis of the HIT with the imposed mean substrate concentration gradient. The performed simulations are classified in table 3.1. In the first set of

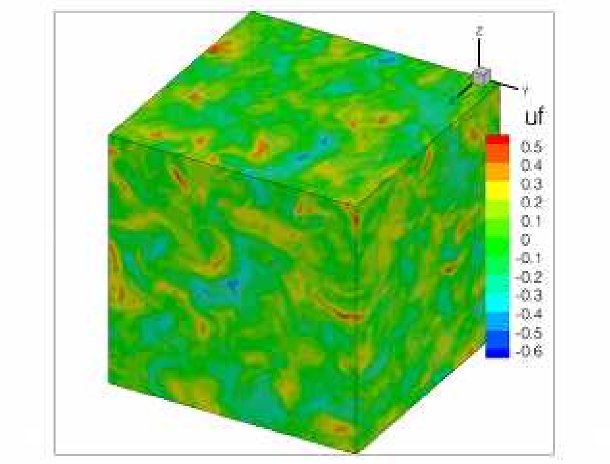

Figure 3.3: 3D view of the velocity field for simulation $R2$.

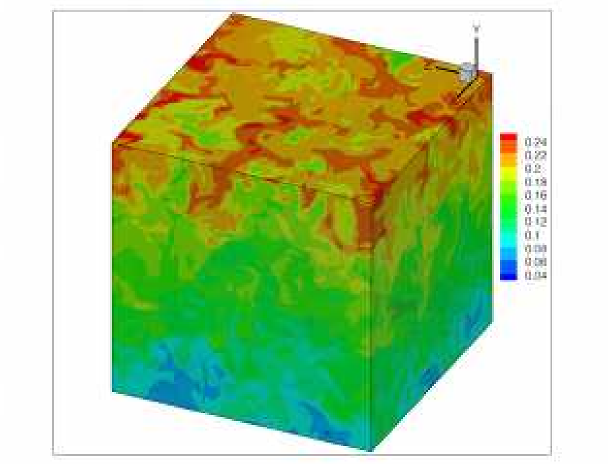

Figure 3.4: 3D view of the total substrate concentration field for simulation $R2$ with $S_0 = 0.15\ \mathrm{kg_S \cdot m^{-3}}$.

simulations P_i, the dynamics of the flow are constant and two values of the Schmidt number are considered. For a common velocity field, the substrate concentration fields will differ due to the different diffusivities.
Then, for $Sc = 0.7$, two simulations R_i are performed for two different turbulent Reynolds numbers (based on the integral length scale) of 68 and 110. The comparison between both simulations enlightens the effect of the flow dynamics on the substrate mixing for example.
Finally for the higher Reynolds number, different concentration gradients are set for the simulations $G1$ and $G2$. This will show the impact of mixing on the different statistics, especially for assimilation by microorganisms.
All simulations were performed on a $N^3 = 128^3$ grid and the box length is $L_{box} = 0.128$ m.

In order to visualise both the flow and substrate concentration field from the DNS, we propose a view of the computational box. Figure 3.3 shows the component u_f of the fluid velocity in the computational domain, and the total substrate concentration S field is shown in Figure 3.4 for the simulation $R2$ (see Table 3.1). Moreover, as seen in Figure 3.5, a slice at constant z allows a two-dimensional view of the substrate concentration field with the gradient contribution (figure 3.5a) and the resolved fluctuating substrate concentration (figure 3.5b). The latter figure illustrates the validity of the periodic boundary conditions handling for the fluctuating substrate concentration in the simulations.

The present section aims to present the validation of the simulations as well as to introduce the definitions of specific turbulence statistics. This chapter is also a data base for the one-phase simulations in this work. First the stationarity of the simulation is verified and the usual statistics and transport equations are validated. Then the different Eulerian statistics are briefly presented and the different spectra of the simulations are confronted. A brief introduction on the distribution of the velocity and scalar is proposed in order to validate the simulations with already existing work. Finally a paragraph is devoted to the definition and presentation of Lagrangian statistics.

Table 3.2 gives the different statistics of the investigated turbulent flows. The definition of the different eulerian length and temporal scales are given in paragraph 3.3.3. But, we will first focus on the statistics concerning the energy, dissipation and turbulent scales.

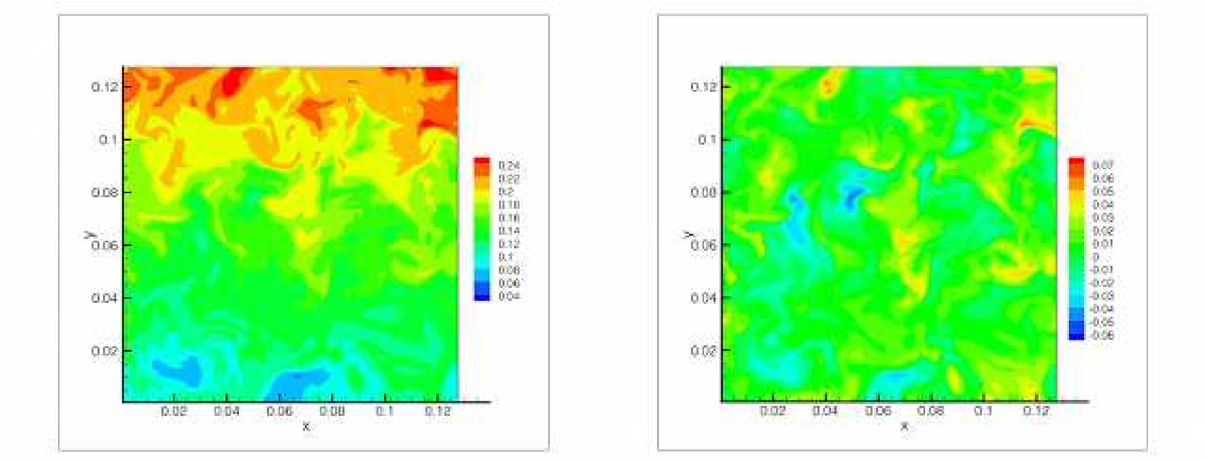

(a) $S(\mathbf{x}) = S_0 + \zeta(\mathbf{x} - \frac{L_{box}}{2}) + s'(\mathbf{x})$

(b) $s'(\mathbf{x})$

Figure 3.5: 2D view of the total substrate concentration field for simulation $R2$ with $S_0 = 0.15\ \mathrm{kg_S \cdot m^{-3}}$ (a) and the resolved fluctuating concentration $\tilde{s} = s'$ (b).

Table 3.1: Characteristics of the flow and physical properties of the fluid.

Run	Re_L	Re_λ	Sc	ζ	ρ_f	ν_f	$\mathcal{D}_{S,f}$
				$[\ \mathrm{kgS \cdot m^{-4}}\ ]$	$[\ \mathrm{kg \cdot m^{-3}}\ ]$	$[\ \mathrm{m^2 \cdot s^{-1}}\ ]$	$[\ \mathrm{m^2 \cdot s^{-1}}\ ]$
$P1$	68	37	0.7	1	1.17	$1.3 \cdot 10^{-5}$	$1.8 \cdot 10^{-5}$
$P2$			1				$1.3 \cdot 10^{-5}$
$R1$	68	37	0.7	1	1.17	$1.3 \cdot 10^{-5}$	$1.8 \cdot 10^{-5}$
$R2$	110	57					
$G1$	110	57	0.7	0.1	1.17	$1.3 \cdot 10^{-5}$	$1.8 \cdot 10^{-5}$
$G2$				5			

Table 3.2: Statistics of the different turbulent flow fields

Simulation		$P1$	$P2$	$R1$	$R2$	$G1$	$G2$
Mean concentration gradient	ζ [$\mathrm{kg_S \cdot m^{-4}}$]	1	1	1	1	0.1	5
Reynolds number	Re_Λ [$-$]	68	68	68	110	110	110
Reynolds number	Re_λ [$-$]	37	37	37	57	57	57
Schmidt number	Sc [$-$]	0.7	1	0.7	0.7	0.7	0.7
Kolmogorov time scale	τ_K [s]	$2.67 \cdot 10^{-2}$	$2.67 \cdot 10^{-2}$	$2.67 \cdot 10^{-2}$	$8.73 \cdot 10^{-3}$	$8.73 \cdot 10^{-3}$	$8.89 \cdot 10^{-3}$
Kolmogorov length scale	η_K/L_{box} [$-$]	$4.53 \cdot 10^{-3}$	$4.53 \cdot 10^{-3}$	$4.53 \cdot 10^{-3}$	$2.61 \cdot 10^{-3}$	$2.58 \cdot 10^{-3}$	$2.61 \cdot 10^{-3}$
Corrsin-Obukhov length-scale	η_C/L_{box} [$-$]	$5.9 \cdot 10^{-3}$	$4.53 \cdot 10^{-3}$	$5.9 \cdot 10^{-3}$	$3.41 \cdot 10^{-3}$	$3.38 \cdot 10^{-3}$	$3.41 \cdot 10^{-3}$
Corrsin-Obukhov time-scale	τ_C/τ_K [$-$]	1.2	1	1.2	1.2	1.2	1.2
Grid resolution	$\kappa_{max}\eta_K$ [$-$]	1.77	1.77	1.77	1.02	1.02	1.02
Fluid kinetic energy	q_f^2 [$\mathrm{m^2 \cdot s^{-2}}$]	$6.74 \cdot 10^{-3}$	$6.74 \cdot 10^{-3}$	$6.74 \cdot 10^{-3}$	$3.13 \cdot 10^{-2}$	$3.23 \cdot 10^{-3}$	$3.14 \cdot 10^{-2}$
Viscous dissipation rate	ε_f [$\mathrm{m^2 \cdot s^{-3}}$]	$1.78 \cdot 10^{-2}$	$1.76 \cdot 10^{-2}$	$1.78 \cdot 10^{-2}$	$1.61 \cdot 10^{-2}$	$1.66 \cdot 10^{-3}$	$1.56 \cdot 10^{-2}$
Substrate concentration variance	$q_{s_f}^2$ [$\mathrm{kg_S^2 \cdot m^{-9}}$]	$1.42 \cdot 10^{-4}$	$1.58 \cdot 10^{-4}$	$1.42 \cdot 10^{-4}$	$1.24 \cdot 10^{-4}$	$1.4 \cdot 10^{-6}$	$3.46 \cdot 10^{-3}$
Dissipation rate of concentration variance	ε_s [$\mathrm{kg_S^2 \cdot m^{-6} \cdot s^{-1}}$]	$6.46 \cdot 10^{-4}$	$6.58 \cdot 10^{-4}$	$6.46 \cdot 10^{-4}$	$1.22 \cdot 10^{-3}$	$1.32 \cdot 10^{-5}$	$3.29 \cdot 10^{-2}$
Dissipation time scale	τ_ε/τ_K [$-$]	14.2	14.3	14.2	22	22.3	22.6
Substrate dissipation time scale	$\tau_\varepsilon^s/\tau_K$ [$-$]	8.2	9	8.2	11.5	12.1	11.8
Integral longitudinal length scale	Λ_f/L_{box} [$-$]	$9.69 \cdot 10^{-2}$	$9.69 \cdot 10^{-2}$	$9.69 \cdot 10^{-2}$	$8.67 \cdot 10^{-2}$	$8.51 \cdot 10^{-2}$	$9.06 \cdot 10^{-2}$
Longitudinal to transversal integral length scale ratio	Λ_f/Λ_g	1.81	1.81	1.81	2.01	1.96	2.02
Taylor longitudinal length scale	λ_f/L_{box} [$-$]	$7.59 \cdot 10^{-2}$	$7.59 \cdot 10^{-2}$	$7.59 \cdot 10^{-2}$	$5.26 \cdot 10^{-2}$	$5.27 \cdot 10^{-2}$	$5.28 \cdot 10^{-2}$
Longitudinal to transversal Taylor length scale ratio	λ_f/λ_g [$-$]	1.41	1.41	1.41	1.41	1.41	1.41
Integral longitudinal concentration length scale	$\Lambda_{S,y}/L_{box}$ [$-$]	$9.92 \cdot 10^{-2}$	$9.22 \cdot 10^{-2}$	$9.92 \cdot 10^{-2}$	$1.03 \cdot 10^{-1}$	$1.10 \cdot 10^{-1}$	$1.01 \cdot 10^{-1}$
Longitudinal to transversal concentration length scale ratio	$\Lambda_{S,x,z}/\Lambda_{S,y}$ [$-$]	$7.2 \cdot 10^{-1}$	$7.3 \cdot 10^{-1}$	$7.2 \cdot 10^{-1}$	$6.4 \cdot 10^{-1}$	$6.9 \cdot 10^{-1}$	$6.6 \cdot 10^{-1}$
Taylor longitudinal length scale for the substrate	λ_s/L_{box} [$-$]	$2.69 \cdot 10^{-2}$	$2.35 \cdot 10^{-2}$	$2.69 \cdot 10^{-2}$	$1.83 \cdot 10^{-2}$	$1.86 \cdot 10^{-2}$	$1.86 \cdot 10^{-2}$
Eulerian integral time scale	T^E/τ_K [$-$]	8.35	8.35	8.35	8.74	8.83	8.89
Substrate Eulerian integral time scale	T_s^E/τ_K [$-$]	7.7	7.3	7.7	18.2	17.3	18.6

3.3.2 Statistical properties of the flow

The following part of the work aims to define the different statistics of the turbulent flow and for the substrate field. The flow is stationary, therefore, after a typical time of $t = 16T^{E3}$, statistical properties of the flow are constant. Both velocity and scalar field are statistically steady.

In consequence, the transport equation for turbulent kinetic energy derived from equation (3.35)[4] is a balance between production (by the forcing scheme) and dissipation where $q_f^2 = 1/2\langle u'_{f,i}u'_{f,i}\rangle$:

$$\frac{\partial q_f^2}{\partial t} = \underbrace{\langle u'_{f,i}f'_i\rangle}_{\text{Production}} \underbrace{+\nu_f \frac{\partial^2 q_f^2}{\partial x_k \partial x_k} - 2\nu_f \left\langle \frac{\partial u'_{f,i}}{\partial x_k}\frac{\partial u'_{f,i}}{\partial x_k}\right\rangle}_{\text{Dissipation}}. \tag{3.36}$$

The dissipation term ε_f is simplified in:

$$\varepsilon_f = \frac{\nu_f}{2}\left\langle\left(\frac{\partial u'_{f,i}}{\partial x_j} + \frac{\partial u'_{f,j}}{\partial x_i}\right)^2\right\rangle. \tag{3.37}$$

The temporal evolution of the energy kinetic balance is shown in figure 3.6d, where only the steady state is plotted. As observed, the kinetic energy balance is null and both the production by the stochastic forcing scheme and the dissipation compensate.

The same observations are appropriate for the concentration correlation balance from equation (3.33) that can be reduced to:

$$\frac{\partial q_{s,f}^2}{\partial t} = \underbrace{-\langle v'_f s'\rangle\zeta}_{\text{Scalar variance production}} \underbrace{- \mathcal{D}_{S,f}\left\langle \frac{\partial s'}{\partial x_j}\frac{\partial s'}{\partial x_j}\right\rangle}_{\text{Scalar dissipation rate}}, \tag{3.38}$$

where the substrate concentration variance and dissipation rate are respectively given by:

$$q_{s,f}^2 = \frac{1}{2}\left\langle s'^2\right\rangle, \tag{3.39}$$

$$\varepsilon_s = \mathcal{D}_{S,f}\left\langle \frac{\partial s'}{\partial x_j}\frac{\partial s'}{\partial x_j}\right\rangle. \tag{3.40}$$

In consequence, for the given flow configuration, the following results are expected:

- the kinetic energy q_f^2 and dissipation ε_f of the fluid are constant (Figure 3.6d),
- the velocity-concentration correlations are null expect in the y direction (Figure 3.6a),
- in the direction of the gradient this correlation $\langle v'_f s'\rangle$ is constant (Figure 3.6a),
- the scalar correlation $\langle s'^2\rangle$ is constant (Figure 3.6b),
- and the scalar variance equation results in a balance between production by the mean imposed concentration gradient and the substrate concentration dissipation (Figure 3.6e).

---

[3] T^E is the Eulerian time scale define later in the work.

[4] by contracting i and j indexes

Finally, according to the previous statistical results, the transport equations for the velocity-concentration correlation finally is on the y direction and yields:

$$\begin{aligned}\frac{\partial\left\langle v'_f s'\right\rangle}{\partial t} &= -\left\langle v'_f v'_f\right\rangle \zeta \;-\; \frac{1}{\rho_f}\left\langle s'\frac{\partial p'}{\partial y}\right\rangle \\ &\quad + \left(\mathcal{D}_{S,f}+\nu_f\right)\left\langle \frac{\partial s'}{\partial x_j}\frac{\partial v'_f}{\partial x_j}\right\rangle,\end{aligned} \tag{3.41}$$

where the first term $\partial\left\langle v'_f s'\right\rangle/\partial t$ is expected to be zero in view of the statistically steady configuration. As observed in Figure 3.6f, the expected evolution is observed and the three right terms compensate. These observations on the different correlations and mass balance evolutions allow the validation of the stationarity of the flow. The obtained statistics are, moreover, in total agreement with the configuration of the flow. Thus, further statistics can be found from these validated quantities.

Once the transport equations are validated, different statistical properties of the turbulent dynamic and substrate fields are defined. First, the Kolmogorov length scale, which expression is given hereafter, represents the smallest dynamic scales of the flow. The grid-space of the computational mesh must be smaller than the Kolmogorov scale for a good resolution of the direct numerical simulation. This condition is expressed as the product of the maximum wave-length and the Kolmogorov scale and is given by equation (3.44). The table 3.2 summarises this criterion for the different simulations that are fully resolved. The Kolmogorov characteristic time scale of the flow is also defined (3.43).

$$\eta_K = \left(\frac{\nu_f^3}{\varepsilon_f}\right)^{1/4}, \tag{3.42}$$

$$\tau_K = \left(\frac{\nu_f}{\varepsilon_f}\right)^{1/2}, \tag{3.43}$$

$$\kappa_{max}\eta_K > 1. \tag{3.44}$$

Our simulations are performed for small Schmidt numbers ($Sc \leqslant 1$), so that there is only purely diffusive mixing below the Kolmogorov scale. We may remind that the mixing mechanism differs for liquids where a viscous-convective subrange exists for the scalar mixing between the Kolmogorov scale η_K and the Batchelor scale η_B. For small Schmidt numbers, the effect of molecular diffusivity becomes important within the inertial subrange of the kinetic energy spectrum where the molecular viscosity does not play any role. Thus, for gases, the Corrsin's microscale (Corrsin, 1951) of turbulence is introduced as:

$$\eta_C = \left(\frac{\mathcal{D}_{S,f}^3}{\varepsilon_f}\right)^{1/4}, \tag{3.45}$$

and the corresponding time scale is given by:

$$\tau_C = \left(\frac{\mathcal{D}_{S,f}}{\varepsilon_f}\right)^{1/2}. \tag{3.46}$$

The different length scales and time-scales are given by table 3.2. The next section is devoted to the Eulerian description of the flow and mixing.

3.3.3 Eulerian correlations

Eulerian spatial autocorrelation function

In order to evaluate the correlation degree between two fluctuating concentrations at two distinct points from the Eulerian domain, we compute the Eulerian spatial autocorrelation functions. Their

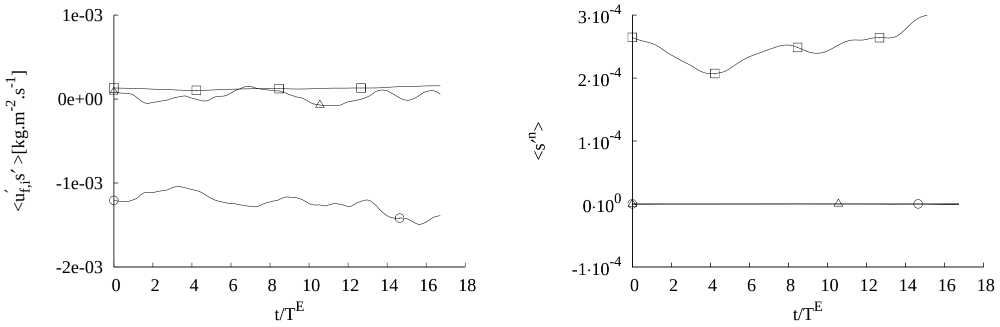

(a) Temporal evolution of the velocity-concentration correlations for the simulation $R2$. □: $\langle u'_f s'\rangle$, △: $\langle v'_f s'\rangle$, ○: $\langle w'_f s'\rangle$.

(b) Temporal evolution of the first moments of the substrate concentration for the simulation $R2$. □: substrate variance $\langle s'^2\rangle$ ([$\mathrm{kg}^2 \cdot \mathrm{m}^{-6}$]), △: $\langle s'^3\rangle$, ○: $\langle s'^4\rangle$.

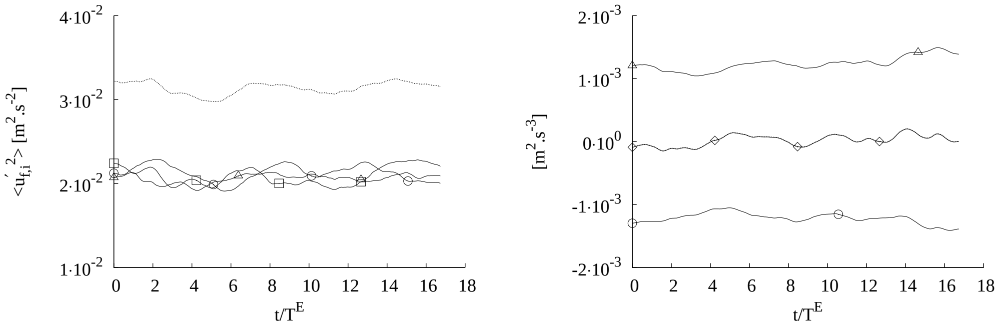

(c) Temporal evolution of the fluid kinetic energy in the steady state for the simulation $R2$. □: $\langle u'^2_f\rangle$, △: $\langle v'^2_f\rangle$, ○: $\langle w'^2_f\rangle$, and ········ : turbulent kinetic energy q_f^2.

(d) Temporal evolution for the fluid kinetic energy balance in the steady state for the simulation $R2$. ◇: $\frac{dq_f^2}{dt}$, △: Production, ○: dissipation, and ········ : sum of the production and dissipation contribution.

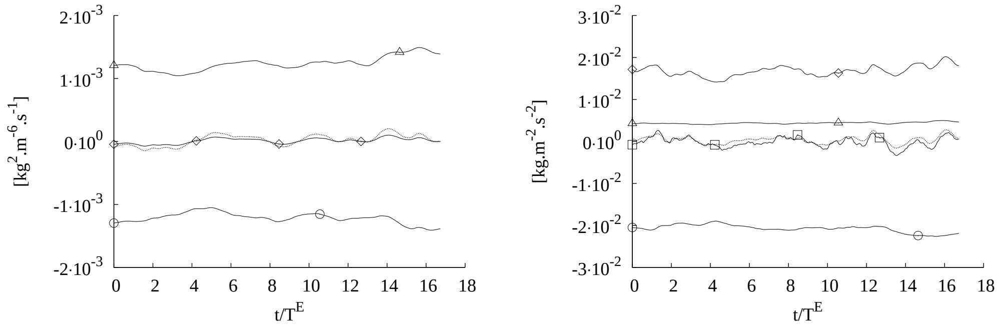

(e) Temporal evolution for the substrate energy balance in the steady state for the simulation $R2$. ◇: $\frac{dq^2_{s,f}}{dt}$, ○: $\langle v'_f s'\rangle \frac{d<S>}{dy}$ (production), △: ε_s, ········ : sum of the production and dissipation.

(f) Temporal evolution of the velocity-concentration correlations balance in y direction for the simulation $R2$. □: $\frac{d\langle <v'_f s'\rangle}{dt}$, △: $\langle v'_f s'\rangle \frac{d<S>}{dy}$ (production), ○: Pressure contribution, ◇: dissipation $\varepsilon_{v's'}$, and ········ : sum of the three contributions.

Figure 3.6: Temporal evolution of fluid statistics and equation balance for the fluid kinetic energy and substrate concentration energy for the simulation $R2$.

general definition is given by equation (3.47) and the longitudinal and transversal autocorrelation functions, depending on the distance r are defined by equations (3.48) and (3.49).

$$R_{ij}(\mathbf{r},t) = \langle u_{f,i}(\mathbf{x},t)u_{f,j}(\mathbf{x}+\mathbf{r},t)\rangle, \tag{3.47}$$

$$f(r) = \frac{\langle u_{f,i}(\mathbf{x},t)u_{f,i}(\mathbf{x}+r\mathbf{e}_i,t)\rangle}{2q_f^2}, \tag{3.48}$$

$$g(r) = \frac{\langle u_{f,i}(\mathbf{x},t)u_{f,i}(\mathbf{x}+r\mathbf{e}_j,t)\rangle}{2q_f^2}\ i \neq j, \tag{3.49}$$

where $\mathbf{e}_i$ is the unity vector in the i^{th} direction. The integral length scales (longitudinal and transversal respectively) correspond to the integral of $f(r)$ and $g(r)$:

$$\Lambda_f = \int_0^{+\infty} f(r)dr, \tag{3.50}$$

$$\Lambda_g = \int_0^{+\infty} g(r)dr, \tag{3.51}$$

$$g(r) = f(r) + \frac{r}{2}\frac{df(r)}{dr}. \tag{3.52}$$

Different authors have developed analytical expressions for both $f(r)$ and $g(r)$ (Kàrmàn and Howarth, 1938), (3.52). Because the usual exponential evolution for the longitudinal autocorrelation function is not appropriate, especially for the small distance r as seen in Figure 3.7 , Lavieville and Berlemont (1997) give an expression for $f(r)$ that depends on the integral length scales Λ_f and Λ_g (3.55), as well as the Taylor length scales, representing the slope at $r \to 0$ of the spatial autocorrelation functions. They yield:

$$\lambda_f = \left(-\frac{2}{\frac{d^2f}{dr^2}\|_{r=0}}\right)^{1/2}, \tag{3.53}$$

$$\lambda_g = \left(-\frac{2}{\frac{d^2g}{dr^2}\|_{r=0}}\right)^{1/2}, \tag{3.54}$$

$$f(r) = \frac{\lambda_g \exp\left(-r/\Lambda_f\right) - (\Lambda_f - \lambda_g)\exp\left(r/(\Lambda_f - \lambda_g)\right)}{2\lambda_g - \Lambda_f}. \tag{3.55}$$

Moreover, for isotropic turbulence, the dissipation term of the turbulent kinetic energy is found to be (Wiskind, 1962):

$$\varepsilon_f = 15\nu_f \frac{\langle u_f'^2\rangle}{\lambda_g}, \tag{3.56}$$

and the Taylor transversal scale is found from the turbulent velocity and the dissipation term. The two turbulent Reynolds numbers Re_Λ based on the integral length scale and Re_λ based on the Taylor length scale are thus defined by:

$$Re_\Lambda = \frac{u'\Lambda_f}{\nu_f}, \tag{3.57}$$

$$Re_\lambda = \frac{u'\lambda_f}{\nu_f}, \tag{3.58}$$

where $u' = \sqrt{\frac{2}{3}q_f^2}$. The eulerian spatial autocorrelation functions are plotted in figure 3.7 for the simulation $R2$. There are compared to the analytical expressions (3.52) and (3.55).

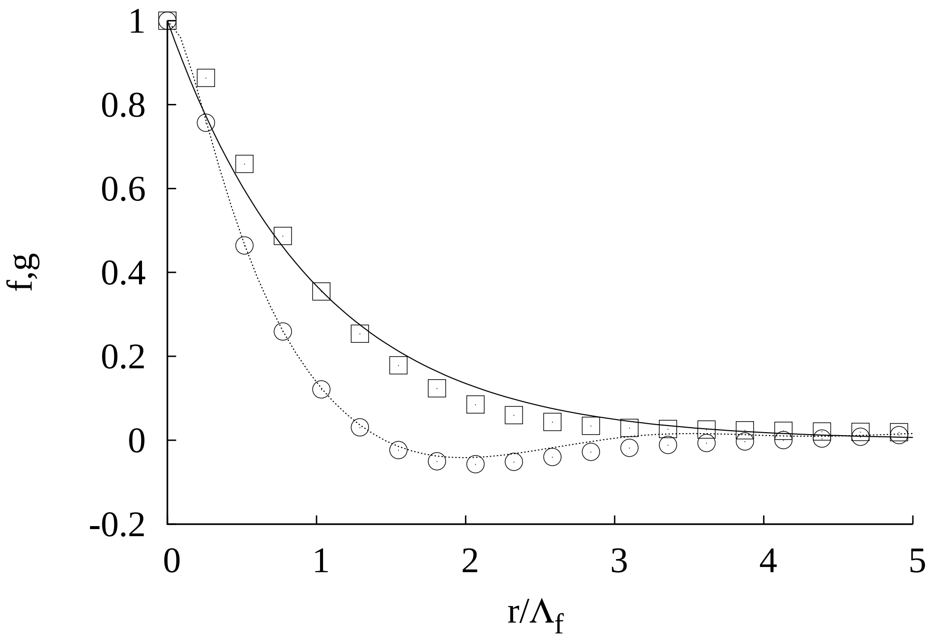

Figure 3.7: Eulerian spatial longitudinal $f(r)$ (□) and transversal $g(r)$ (○) correlation functions for the simulation $R2$. (········) line is for the Karmann and Howarth equation and (———) is the exponential law.

Eulerian properties can also be computed from the simulations for the scalar S. The eulerian spatial autocorrelation functions are then defined for any direction i by equation (3.59) and the corresponding integral length scales for the scalar are given by equation (3.60).

$$R^E_{S,i}(r) = \frac{\langle s'_f(\mathbf{x},t) s'_f(\mathbf{x}+r\mathbf{e}_i,t)\rangle}{2q^2_{s,f}}, \tag{3.59}$$

$$\Lambda_{s,i} = \int_0^{+\infty} R^E_{s,i}(r)dr. \tag{3.60}$$

In the steady-state with an imposed mean gradient for the scalar, Corrsin (1952) found the following expression for the scalar variance:

$$\langle s'^2\rangle = -\left(\frac{\lambda_s^2}{6\mathcal{D}_{s,f}}\right)\langle s'v'_f\rangle\frac{\partial S}{\partial y}, \tag{3.61}$$

where λ_s is the scalar Taylor length scale. According to equation (3.38), the term $-\langle s'v'_f\rangle\frac{\partial S}{\partial y}$ is exactly the scalar dissipation so that the Taylor length scale can be expressed as:

$$\lambda_s = \sqrt{6\mathcal{D}_{s,f}\frac{q^2_{s,f}}{\varepsilon_s}}. \tag{3.62}$$

The different eulerian length scales are reported in table 3.2 for the various simulations. Considering the configuration for the scalar field, the imposed gradient in the y direction influences the eulerian spatial autocorrelation functions. Figure 3.8 presents the evolution of the scalar autocorrelation functions for the three directions. The second function differs, especially for mid-range distance. Moreover the autocorrelation functions in the direction of isotropy (x and z) are equal and the corresponding scalar integral length scales are close to the integral length scale of the flow. Indeed, the large-scale scalar turbulent transport is only driven by the turbulent flow field. Therefore, for the simulation $P2$ with $Sc = 1$, meaning that diffusive and viscous contributions are equivalent, the scalar integral length scale is expected to be equal to the integral length scale of the flow.

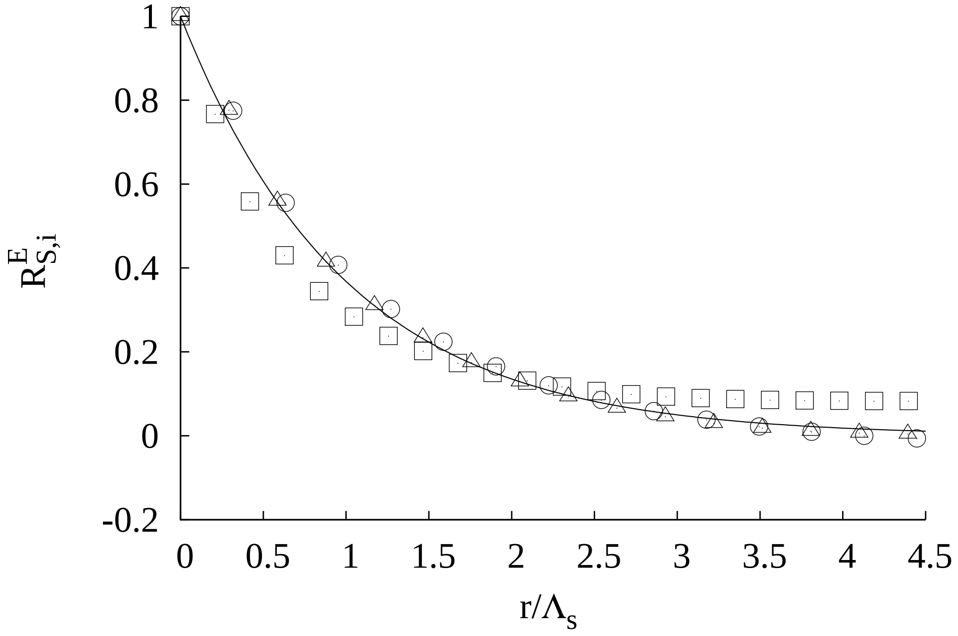

Figure 3.8: Scalar Eulerian autocorrelation functions for the simulation $G2$. □: R^E_{sy}, ○: R^E_{sx} and △: R^E_{sz}. The (——) line is the exponential law.

Eulerian temporal autocorrelation functions

The same way integral length scales are defined, Eulerian time scales can be derived from Eulerian temporal autocorrelation functions. They are defined in one point at different times. Their expression yields for the velocity and scalar respectively:

$$R^E(\tau) = \frac{\langle u'_{f,i}(\mathbf{x}(t),t)u'_{f,i}(\mathbf{x}(t),t+\tau)\rangle}{2q_f^2}, \tag{3.63}$$

$$R^E(\tau) = \frac{\langle s'_f(\mathbf{x}(t),t)s'_f(\mathbf{x}(t),t+\tau)\rangle}{2q_{s,f}^2}. \tag{3.64}$$

The Eulerian time scales are then:

$$T^E = \int_0^{+\infty} R^E(\tau)d\tau, \tag{3.65}$$

$$T^E_s = \int_0^{+\infty} R^E_s(\tau)d\tau. \tag{3.66}$$

The different Eulerian time scales for the simulations are given in table 3.2. As observed they are about 8 times bigger than the Kolmogorov time scales. These times are defined as the correlation degree between different times in one point and give a first idea on the required time for converged statistics on the turbulent flow. Moreover, they are further compared with the Lagrangian timescales in the section 3.4.2.

3.3.4 Spectral analysis - definition and modelling

Turbulent energy spectrum

In homogeneous turbulence, the turbulent energy spectrum $E(\kappa, t)$ is calculated from the velocity spectrum tensor by integrating in all directions (see equation (3.67)). The velocity spectrum is related to the spatial correlation function (3.47) and yields:

$$\mathbb{V}_{i,j}(\kappa, t) = \frac{1}{(2\pi)^3} \int\int\int_{\infty}^{+\infty} R_{ij}(\mathbf{r}, t) \mathrm{e}^{-i\kappa\cdot\mathbf{r}} d\mathbf{r}. \tag{3.67}$$

$$E(\kappa, t) = \int\int\int_{-\infty}^{+\infty} \frac{1}{2} \left(\mathbb{V}_{11}(\kappa, t) + \mathbb{V}_{22}(\kappa, t) + \mathbb{V}_{2}(\kappa, t)\right) \delta(\kappa - |\kappa|) d\kappa. \tag{3.68}$$

The turbulent kinetic energy can be found directly from the turbulent energy spectrum:

$$q_f^2 = \int_0^{+\infty} E(\kappa, t) d\kappa = \frac{1}{2} \left(\langle u_f'^2 + v_f'^2 + w_f'^2 \rangle\right), \tag{3.69}$$

and the kinetic energy dissipation can thus be expressed by:

$$\varepsilon_f = 2\nu_f \int_0^{+\infty} \kappa^2 E(\kappa, t) d\kappa. \tag{3.70}$$

The big eddies decrease in smallest eddies with an energy transfer form large scales to small scales. The cascade of energy, introduced by Kolmogorov, is universal in the inertial subrange where the energy spectrum is written:

$$E(\kappa) = K \varepsilon_f^{2/3} \kappa^{-5/3}, \tag{3.71}$$

where K is the Kolmogorov dimensionless constant experimentally and numerically estimated at $K \equiv 1.62$ by Sreenivasan (1995) and Yeung and Zhou (1997) for example. Pope (2000) developed a more general model that accounts for both large and small scales as well. Figure 3.9 shows the compensate kinetic energy spectra for both simulations $R1$ and $R2$ that relatively the $-5/3$ law plotted in dotted line, especially for simulation $R2$. For simulation $R1$ the turbulence intensity is smaller and the energy cascade is narrowed.

Scalar energy spectrum

For homogeneous scalar fields, the spectral analysis for the scalar similar to fluid velocity. Indeed, the scalar energy spectrum $E_s(\kappa, t)$ is defined in terms of the scalar spectrum $\mathbb{V}_s$ and yields:

$$E_s(\kappa, t) = \int\int\int_{-\infty}^{+\infty} \mathbb{V}_s(\kappa, t) \delta(\kappa - \|\kappa\|) d\kappa, \tag{3.72}$$

and the scalar variance and dissipation can be found from the scalar energy spectrum:

$$q_{s,f}^2 = \int_0^{+\infty} E_s(\kappa, t) d\kappa, \tag{3.73}$$

$$\varepsilon_s = 2\mathcal{D}_{s,f} \int_0^{+\infty} \kappa^2 E_s(\kappa, t) d\kappa. \tag{3.74}$$

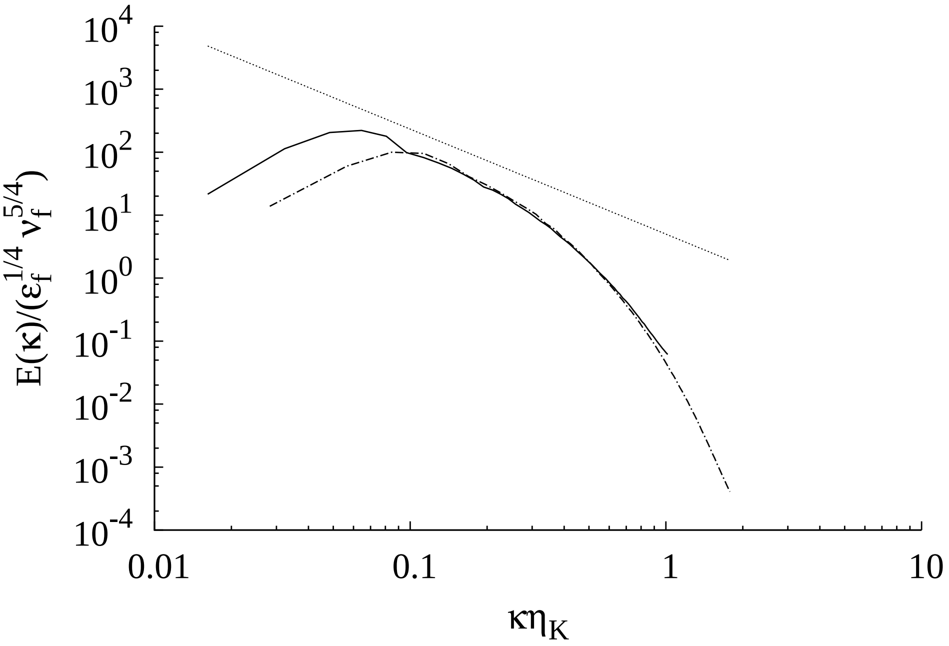

Figure 3.9: 3D fluid kinetic energy spectra for both simulations $R1$: (-·-·-) and $R2$: (——). (········) is the $-5/3$ power law.

For small Schmidt numbers, the smallest scales for the scalar are close to the Kolmogorov scale and the scalar energy spectrum follows the kinetic energy spectrum with the model for scalar energy spectrum in the inertial subrange:

$$E_s(\kappa) = C_{OC}\varepsilon_s\varepsilon_f^{-1/3}\kappa^{-5/3}, \tag{3.75}$$

where C_{OC} is the Obukhov-Corrsin constant and $C_{OC} \equiv 2/3$ according to different studies (Sreenivasan, 1996). For bigger Schmidt numbers, the viscous effects impact the scalar variance, with no effect of diffusivity in the viscous-convective subrange. In that case, the scalar energy spectrum is expressed as:

$$E_s(\kappa) = B\varepsilon_s\left(\frac{\nu_f}{\varepsilon_f}\right)^{1/2}\kappa^{-1}, \tag{3.76}$$

with B the Bachelor constant. Borgas et al. (2004) evaluated this constant ($B = 5$) with DNS of a passive scalar transport in steady homogeneous isotropic turbulent flow for higher Schmidt numbers. They found that contribution of the viscous-convective subrange is significant, and that micromixing is a major issue for reacting flows. We may remind here, that in the present work only small Schmidt numbers are investigated, but, considering the results of Borgas et al. (2004), performing higher Schmidt-number simulations for biological suspensions is an interesting perspective. Indeed, we perform simulations with favourable mixing, but the local non-homogeneity effects observed in the present work are minimised compared to the mixing phenomena in bioreactors.

Figure 3.10 presents the scalar energy spectrum for the simulation $P1$, $R1$; $R2$, $P2$ and $G1$, $G2$. The inertial zone is longer for higher Reynolds number as seen in Figure 3.10b but there is no effect of the imposed concentration mean gradient for the compensate scalar energy spectrum (see Figure 3.10).

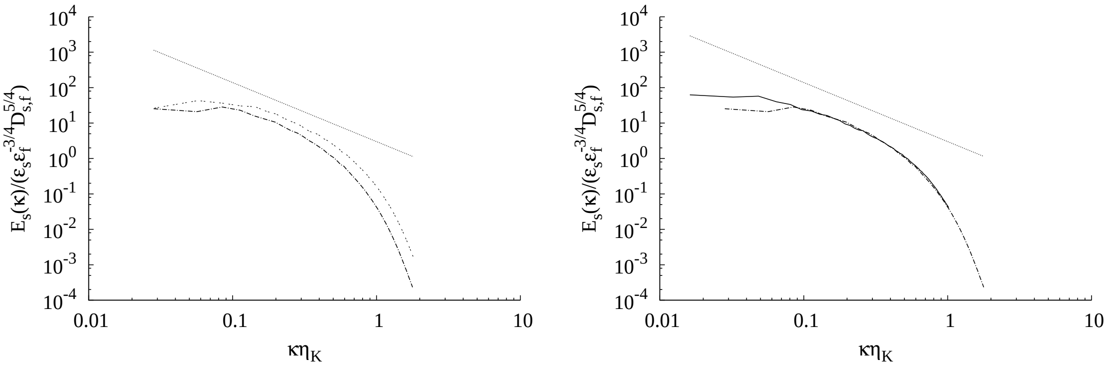

(a) Substrate concentration variance spectra for the simulations $P1$: (−·−·−) and $P2$: (−−−−)

(b) Substrate concentration variance spectra for the simulations $R1$: (−·−·−) and $R2$: (———)

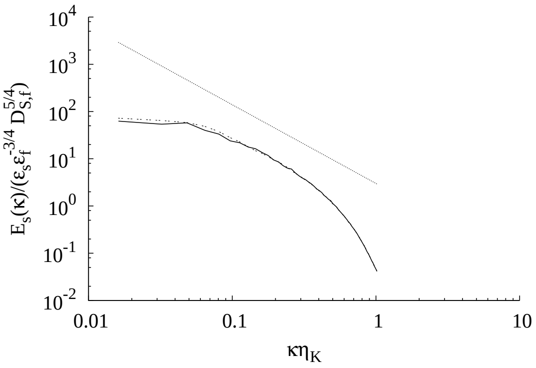

(c) Substrate concentration variance spectra for the simulations $R2$: (———) and $G1$ and $G2$: (········)

Figure 3.10: Substrate concentration energy spectra for all the simulations. (········) is the $-5/3$ power law.

3.3.5 Probability density functions

In this part of the work, we focus on the study of the substrate concentration fluctuations in the turbulent field. The spatial gradients of the fluctuations are also investigated in order to validate our case by comparison with experimental and numerical studies.

The normalised probability density function for the substrate concentration fluctuations are plotted in figure 3.11 for the simulations $R1$, $R2$ and $G2$. For the three simulations, the associated gaussian distribution (defined by equation (3.77)) is solid line.

$$P_g(s') = \frac{1}{\sqrt{2\pi\langle s'^2\rangle}}\exp(-\frac{1}{2}\frac{s'^2}{\langle s'^2\rangle}). \tag{3.77}$$

The scalar distribution function has been studied experimentally and numerically. By measurements of passive temperature spectra, Jayesh et al. (1994) found an exponential distribution for the scalar fluctuations in the case of decaying grid turbulence. Later, Overholt and Pope (1996) performed several numerical simulations of stationary HIT with an imposed mean gradient for the scalar and obtained a gaussian distribution for the scalar fluctuations over a large range of Reynolds numbers. Our results are then in agreement with Overholt and Pope (1996) results' for the same

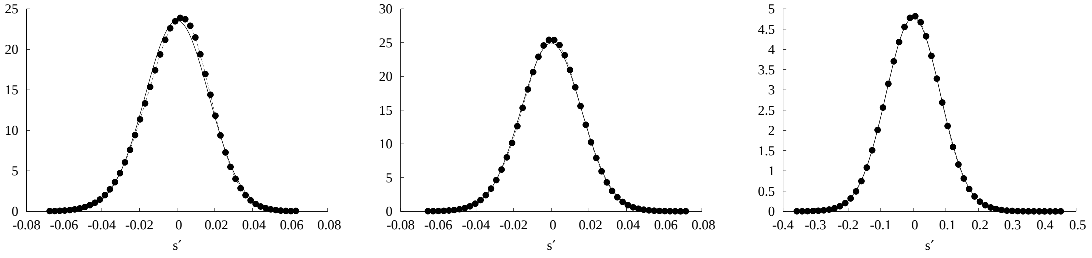

(a) $R1$ (b) $R2$ (c) $G2$

Figure 3.11: Normalised PDF of the substrate concentration fluctuations for different simulations. (——) is the corresponding gaussian distribution.

configuration. In order to characterise the different distributions, the skewness and kurtosis of the scalar were calculated. The general definition of the skewness and kurtosis (or flatness) are derived from the third and fourth standardised moments and yield (example for the scalar):

$$S^s = \frac{\langle s'^3 \rangle}{\langle s'^2 \rangle^{3/2}}, \tag{3.78}$$

$$K^s = \frac{\langle s'^4 \rangle}{\langle s'^2 \rangle^2}. \tag{3.79}$$

They are given in table 3.3 and are typical for gaussian distributions. Even if the scalar fluctuations distribution is gaussian, as for the velocity field, the spatial distributions of the scalar gradients do not follow the same distribution law. Pumir (1994) first studied the PDF of the scalar gradients parallel and perpendicular to the direction of the mean gradient in a 3D flow configuration then Overholt and Pope (1996) restated this study. As shown by figure 3.12, the substrate gradients perpendicular to the imposed gradient direction ($\partial_\perp s' = \frac{\partial s'}{\partial x}$ and $\frac{\partial s'}{\partial z}$) are similar and their distribution is not gaussian. Considering the flow configuration, the similar distribution expected for these perpendicular gradient is verified. An exponential form was proposed by Pumir (1994) where two parameters of the exponential distribution need to be fitted with the numerical results.

$$P(\partial_\perp s') = \mathcal{N} \exp(-\beta(|\partial_\perp s'|/\langle \partial_\perp^2 s' \rangle)^\alpha). \tag{3.80}$$

The PDF of substrate gradient in the y direction $\partial_y s' = \partial_\parallel s'$ differs from the perpendicular direction as shown by figure 3.13. They are not symmetric for the different investigated simulations and they are centred on the opposite of the imposed scalar gradient.

In order to characterise the different distributions, the skewness $S_\parallel^s$ and kurtosis in the parallel $K_\parallel^s$ and perpendicular direction $K_\perp^s$ of the gradient distributions are reported in table 3.3.

Table 3.3: Characteristics of the flow and physical properties of the fluid.

	S^s	K^s	$S^s_\parallel$	$S^s_{\perp x}$	$S^s_{\perp z}$	$K^s_\parallel$	$K^s_{\perp x}$	$K^s_{\perp z}$
$R1$	-0.1	3.13	1.513	-0.059	0.047	9.07	7.64	7.64
$R2$	-0.04	3.19	1.22	0.01	0.009	8.18	7.55	7.54
$G2$	0.2	3.12	12.28	-0.025	0.016	8.46	7.6	7.6

Finally, the distribution of the instantaneous scalar concentration S is given in figure 3.14 for different imposed concentrations S_0. We can see that, for a given substrate concentration variance,

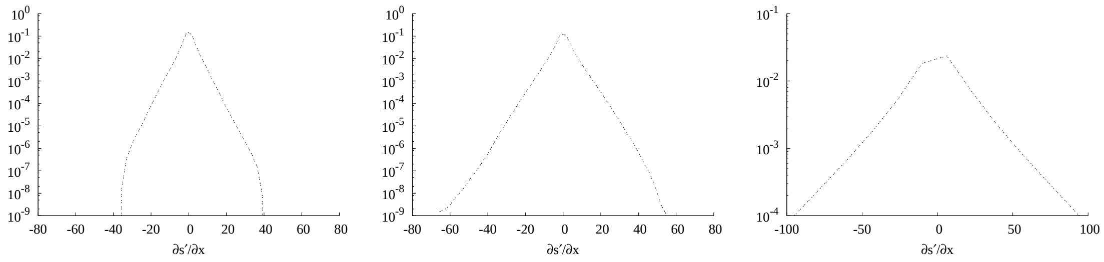

(a) $\partial_x s'$, $R1$ (b) $\partial_x s'$, $R2$ (c) $\partial_x s'$, $G2$

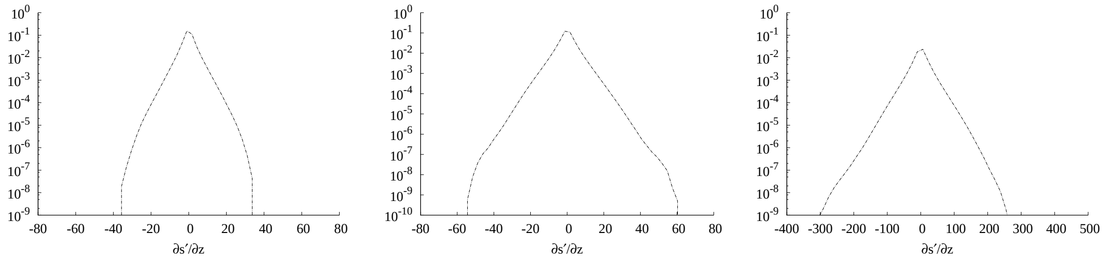

(d) $\partial_z s'$, $R1$ (e) $\partial_z s'$, $R2$ (f) $\partial_z s'$, $G2$

Figure 3.12: Normalised PDF of the substrate concentration fluctuations gradient in the x (----) in the upper part) and z (-·-·- at the bottom) directions for simulations $R1$, $R2$ and $G2$.

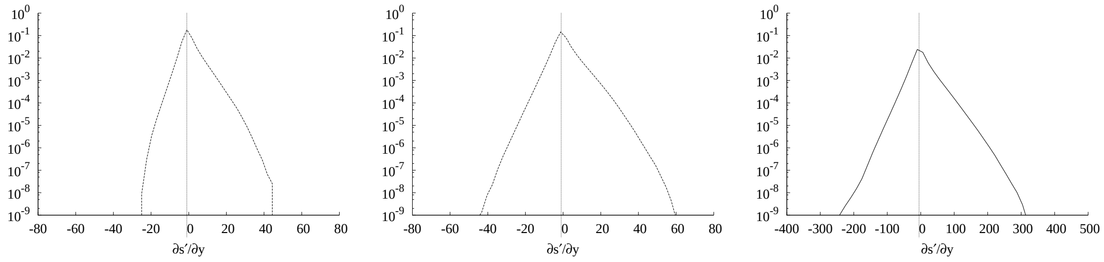

(a) $R1$ (b) $R2$ (c) $G2$

Figure 3.13: Normalised PDF of the substrate concentration fluctuations gradient in y direction for simulations $R1$, $R2$ and $G2$. (········) is the opposite of the imposed concentration gradient.

this distribution differs from one S_0 to another. It results from the combination of a gaussian (P(s')) and a uniform distribution and ($P(S_0 + \zeta(y - L_{box}/2))$).

This part of the work was devoted to the analyses of mono-phasic stationary turbulent flows. It has been verified that the velocity field is homogeneous and isotropic, whereas the substrate concentration field presents a non-isotropic property in the y direction as a consequence of the imposed gradient in that direction. Different successful validations were carried out by confrontation to already existing studies for the Eulerian characteristics and the different distribution functions for the scalar. The definition substrate energy spectra will be used in the last chapter of this work, whereas the different distributions are studied in the whole work. The next part of this chapter is devoted to the Lagrangian statistical analysis and Lagrangian stochastic modelling of the turbulence and the substrate transport.

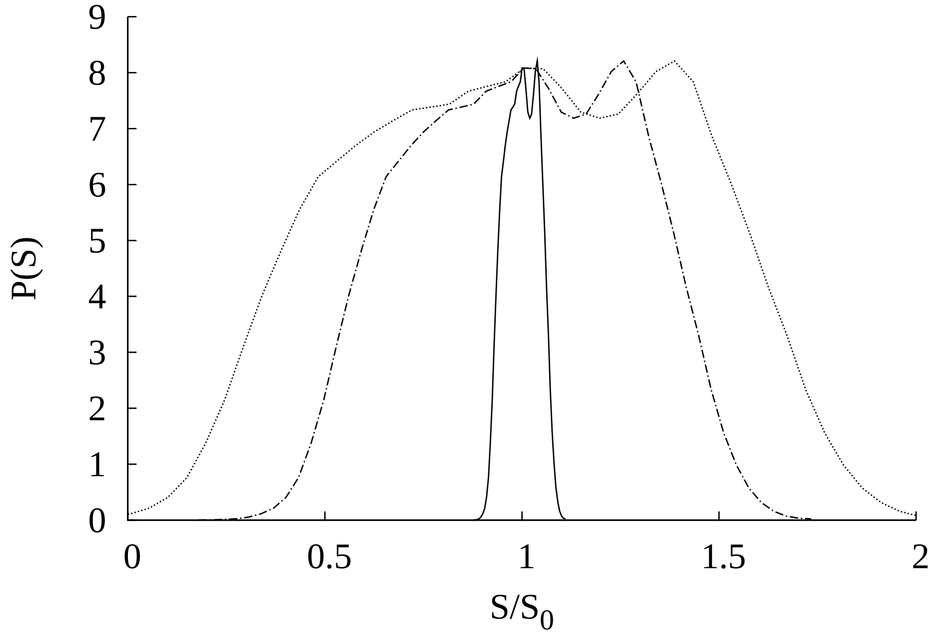

Figure 3.14: Normalised PDF of the substrate instantaneous concentrations for the simulation $R2$ for different S_0. (——): $S_0 = 1$ kg$_S \cdot$ m^{-3}, (-·-·-): $S_0 = 0.15$ kg$_S \cdot$ m^{-3} and (········): $S_0 = 0.1$ kg$_S \cdot$ m^{-3}.

3.4 Lagrangian properties of the substrate turbulent field

In many problems of turbulent mixing the dominant mechanism is advective transport, whereby the flow property being mixed is carried along with the motion described by the velocity fluctuations. This is the case for the substrate concentration. This description is also pertinent for the microorganism tracking, as we assumed that they are tracers of the fluid. Thus, it is particularly useful to adopt a Lagrangian viewpoint, with an observer following the motion of a collection of fluid particles that together constitute the fluid continuum. The determination of Lagrangian properties in turbulent flows has been promoted by the increase in computational power, indeed, their experimental determination remains complicated. Yeung and Pope (1989) present numerical simulations for Lagrangian determination of the velocity field and further study investigates the effect of the Reynolds number on Lagrangian statistics (Yeung et al., 2006). The Lagrangian characteristics of scalar transport have been studied by Yeung et al. (2000) in the case of stationary isotropic turbulence with uniform mean scalar gradient. The obtained results from our simulations will be confronted to the results of Yeung et al. (2000). The Lagrangian statistical properties for the velocity and the substrate fields are introduced in the next section.

Two approaches can be considered for the study of fluid flows. On the one hand, the Eulerian viewpoint where we observed the different properties of the flow field at one point over time. This matches the experimental probe in an experimental setup for example. On the other hand, the Lagrangian viewpoint consists in following a fluid particle and to observe the dynamics of the flow through its movement. This approach is more appropriate for the study of scalar turbulent transport, for example, and requires the definition of the fluid particle by its position $\mathbf{x}(t)$, velocity $\tilde{\mathbf{u}}_f(t) = \mathbf{u}_f(\mathbf{x}(t), t)$ and substrate concentration $\tilde{\mathbf{s}}(t) = s(\mathbf{x}(t), t)$. The two last quantities are obtained by interpolation from the Eulerian field. The position of the fluid particles are then derived from the particles trajectories equation where $\mathbf{x}_0$ is the initial position of the fluid particle at time t_0:

$$\frac{d\mathbf{x}(t)}{dt} = \tilde{\mathbf{u}}_f(t), \tag{3.81}$$

$$\mathbf{x}(t_0) = \mathbf{x}_0. \tag{3.82}$$

The Lagrangian statistical properties are defined from these Lagrangian quantities. Since each trajectory is an individual event, averages over a large amount of fluid particles is necessary therefore the coming results are obtained by following 200,000 fluid particles.

3.4.1 Lagrangian correlation functions

The temporal correlation degree of velocity or substrate concentration along a fluid particle trajectory can be calculated from the Lagrangian autocorrelations of velocity $R^L_{u_{f,i,j}}(\tau)$ and substrate concentration $R^L_s(\tau)$. From an initial time t_0 we compute the correlation degree between the considered quantity at the time t_0 and $t_0 + t$. Both functions yield:

$$R^L_{u_i u_j}(\tau) = \langle \tilde{u}'_{f,i}(t)\tilde{u}'_{f,j}(t+\tau)\rangle, \tag{3.83}$$

$$R^L_s(\tau) = \langle \tilde{s}'(t)\tilde{s}'(t+\tau)\rangle. \tag{3.84}$$

The average over different realisations of R^L_i are performed starting at different initial times t_0, typically, 5 autocorrelation functions were computed and averaged.

Two time scales are defined from these autocorrelations: the Lagrangian integral time scale T^L and the Lagrangian characteristic time-scale for the substrate T^L_s that characterises the time required by one fluid-particle to be de-correlated from its initial state.

$$T^L = \frac{1}{2q_f^2}\int_0^{+\infty} R^L_{u_i u_i}(\tau)d\tau, \tag{3.85}$$

$$T^L_s = \frac{1}{2q_s^2}\int_0^{+\infty} R^L_s(\tau)d\tau. \tag{3.86}$$

Figure 3.15 shows the non-dimensional[5] Lagrangian autocorrelations for the velocity for the simulation $R1$ and $R2$. We can see that the Lagrangian characteristic time-scale is bigger for the smaller Reynolds-number flow (see figure 3.15a), but if the time is non-dimensionalised by the corresponding Lagrangian time scale of the simulation (figure 3.15b), the velocity autocorrelation evolution is similar. Figure 3.16 presents the non-dimensionalised autocorrelations for both velocity and substrate in the case of simulation $R2$[6]. We can see that the Lagrangian time scale for the substrate is larger than the dynamic Lagrangian time scale. This result is reported in table 3.4.

The influence of the flow dynamics and of the forcing gradient on the Lagrangian autocorrelation for the substrate is shown in figure 3.17 where the substrate autocorrelations of simulations $R1$, $R2$, $P2$ and $G2$ are plotted. We can see that the value of the forcing gradient has an important influence on the Lagrangian time scale for the substrate, whereas there is no effect of the Schmidt number between the simulations $P1$ ($R1$) and $P2$ on R^L_s. This result is in agreement with Yeung et al. (2002) results in the range of investigated Schmidt numbers. The correlation degree between the velocity and the substrate concentration of a fluid element can also be defined with the Lagrangian velocity-scalar cross-correlations:

$$R^L_{sv}(\tau) = \langle s'(t)v'_f(t+\tau)\rangle, \tag{3.87}$$

---

[5] by $2/3q_f^2$.

[6] non-dimensionalisation by the substrate energy $2q_{s,f}^2$.

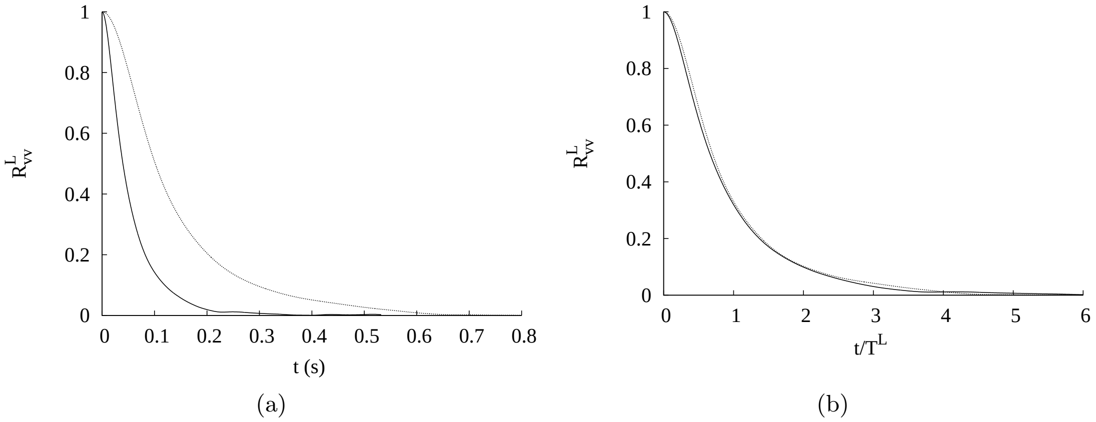

(a)

(b)

Figure 3.15: Velocity autocorrelation functions for the simulation $R1$: (········) and $R2$:(———). In figure 3.15b the time is non-dimensionalised by the Lagrangian dynamic time scale from the DNS.

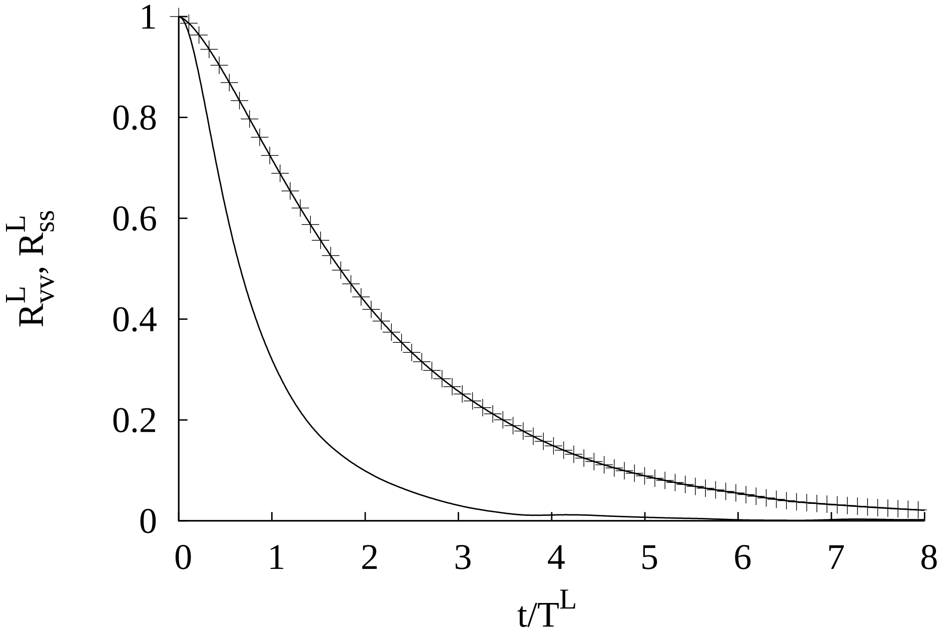

Figure 3.16: Velocity (———) and substrate concentration (—+ —) autocorrelation functions for the simulation $R2$.

$$R^L_{vs}(\tau) = \langle v'_f(t) s' f(t+\tau) \rangle, \tag{3.88}$$

These cross-correlation functions are plotted in figure 3.18 for the simulation $R2$. They are non-dimensionalised by the cross-correlation $\langle v'_f s' \rangle$. We can see that these two correlations are not similar, and R^L_{vs} increases at the beginning due to the scalar gradient. Yeung (2001) obtained similar results for the turbulent transport of a scalar with an imposed mean gradient.

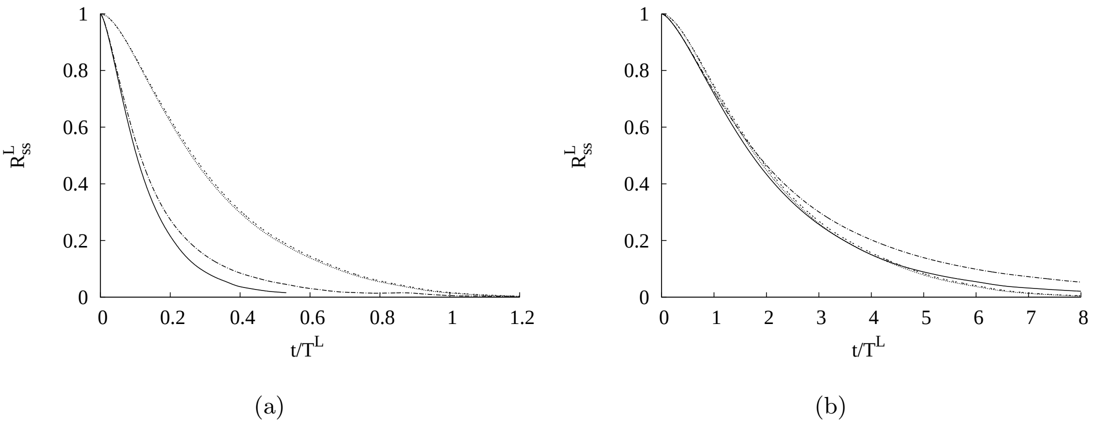

(a)

(b)

Figure 3.17: Substrate autocorrelation functions for the simulation $R1$: (········), $R2$:(——), $G2$: (-·-·-) and $P2$: (- - - -). In figure 3.17b the time is non-dimensionalised by the corresponding Lagrangian dynamic time scale from the DNS.

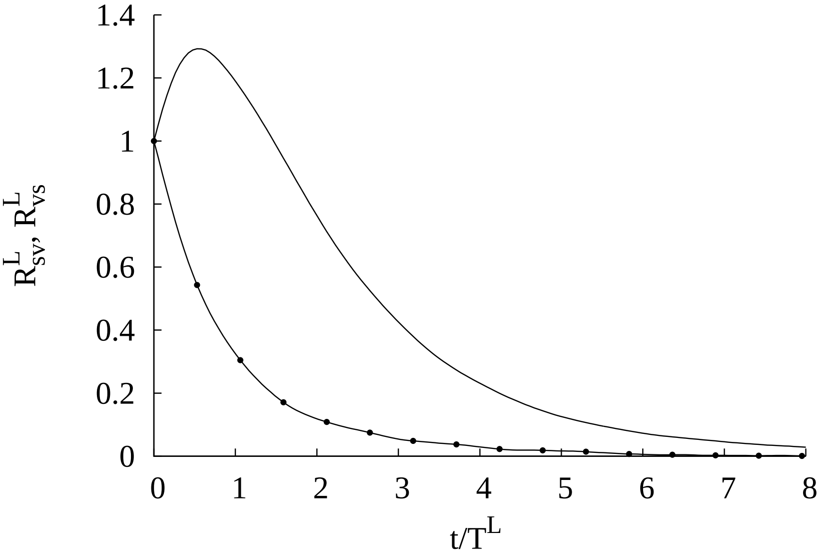

Figure 3.18: Velocity-substrate (——) and substrate-velocity (●) cross-correlation functions normalised by the cross-correlation $\langle v'_f s' \rangle$ for the simulation $R2$.

3.4.2 Analysis of the characteristic time-scales

The dynamic Lagrangian time scale T^L is generally compared to the Eulerian dynamic time scale T^E with the ratio R^E. Table 3.4 summarises the different values for this ratio and we can see that it ranges from 0.7 to 0.78 in our simulations. These results obtained for r_ε are in agreement with the obtained values of Yeung (2001) for different simulations with increasing Re_λ. The ratio of the two Lagrangian time scales defined from the autocorrelation functions is usually considered (Yeung, 2001):

$$r^L_S = \frac{T^L_S}{T^L}. \tag{3.89}$$

Table 3.4 summarises the different values for this ratio. According to Yeung (2001), this ratio is generally about 2. But an increase is observed by increasing both the Reynolds and the Schmidt numbers. We can see that the data from our simulations are higher than expected, especially for the simulation $G2$. Finally the mechanical-to-scalar time-scale ratio is often discussed in the literature on turbulent mixing, for example (Eswaran and Pope, 1988). Its definition is:

$$r_\varepsilon = \frac{q_f^2}{\varepsilon_f} / \frac{q_s^2}{\varepsilon_s}. \tag{3.90}$$

Table 3.4: Lagrangian time scales and comparison with Eulerian time scales.

		$P2$	$R1$	$R2$	$G1$	$G2$
Lagrangian integral time scale	T^L/τ_K	5.54	5.54	6.85	7.02	7.2
Substrate Lagrangian time scale	T_S^L/τ_K	11.9	11.8	17.5	17.6	19
Lagrangian time scale ratio	r_S^L	2.16	2.12	2.55	2.51	2.66
Lagrangian to Eulerian dynamic time scale ratio	T^L/T^E	0.65	0.66	0.78	0.8	0.81
Lagrangian to Eulerian scalar time scale ratio	T_S^L/T_S^E	1.65	1.52	1.02	0.98	1.03
Mechanical-to-scalar time-scale ratio	r_ε	1.59	1.73	1.62	1.83	1.9

3.4.3 Lagrangian Structure functions

From the work of Kolmogorov on the Eulerian structure functions (Kolmogorov, 1941), that later derives the famous 5/3 law for the kinetic energy spectra in the inertial subrange. In the Lagrangian framework, second-order structure functions are defined. They represent the square of the Lagrangian velocity (in the i^{th} direction) increment over a time interval τ:

$$D^L_{u_i u_j} = \langle [\tilde{u}'_{f,i}(t+\tau) - \tilde{u}'_{f,i}(t)]^2 \rangle. \tag{3.91}$$

From Kolmogorov (1962) hypothesis, the second-order Lagrangian structure function $D^L_{u_i u_i}$ are written in the inertial subrange:

$$D^L_{u_i u_j}(\tau) = C_0 \varepsilon_f \tau \delta_{ij}, \ (\tau_K \ll \tau \ll T^L), \tag{3.92}$$

where δ_{ij} is the Kronecker symbol and C_0 is the Lagrangian Kolmogorov constant.
The knowledge of C_0 is very important in Lagrangian modelling of the turbulence. The exact determination of C_0 requires a significant scaling range that appears as a plateau in a plot of $D^L_{uu}(\tau)/(\varepsilon_f \tau)$ (Lien and D'Asaro, 2002). But, for insufficiently high Reynolds numbers, the plateau may be short or exists only as bump with the maximum value C_0^* (Yeung et al., 2006). The constant C_0 has been measured in the $2-4$ range (Pope, 2000) and the dependance to the Reynolds number has first been studied by Sawford (1991). By mean of highly resolved DNS, Yeung et al. (2006) obtained bigger value for the maximum of the constant C_0^* and Fox and Yeung (2003) proposed an expression (from fitting data) for the constant C_0 that gives $C_0 = 6.5$ for very large Reynolds numbers:

$$C_0 = 6.5 \left[1 + \frac{8.1817}{Re_\lambda} \left(1 + \frac{110}{Re_\lambda} \right) \right]^{-1}. \tag{3.93}$$

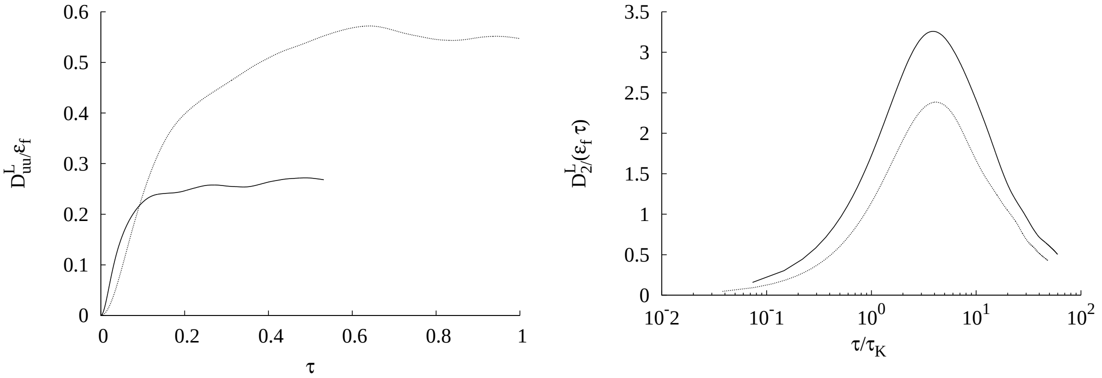

(a) D^L_{uu} non-dimensionalised by the flow dissipation rate ε_f of the correponding simulation.

(b) Temporal evolution of the C_0 constant.

Figure 3.19: Temporal evolution of the second-order Lagrangian structure function for the x component of the velocity and of the constant C_0 for the simulations $R1$: (········) and $R2$: (———).

In our work, we performed simulations with moderate Reynolds numbers. The constant C_0 is then expected to be in the order of 2 (Pope, 2000). The second-order Lagrangian structure functions D^L_{uu} for simulations $R1$ and $R2$ are plotted in figure 3.19a. The structure functions in the 2^{nd} and 3^{rd} directions are close from D^L_{uu}, therefore they are not presented here. We can see that the shape of those functions are similar, but the final values differ from one simulation to another. Figure 3.19b shows the peak of the constant C_0 for both simulations. We can see that the value of C_0 is smaller for the simulation $R1$ than for the simulation $R2$. This result is in agreement with Yeung et al. (2006) and shows the dependance of the Lagrangian Kolmogorov constant to the Reynolds number of the simulation. Moreover the maximum value of the peak for our simulations agrees with the results of Sawford (1991). Even if the determination of the peak of C_0^* is easy, it is more difficult to predict C_0. Table 3.5 gives the values for the two simulations resulting from averages in an interval containing the peak values higher than $\sqrt{2}C*_0$. The third column gives the constant C_0 from the equation (3.93). We can see that the obtained values from our simulation are smaller than the one obtained by Fox and Yeung (2003). Despite this results, the obtained evolution for increasing Reynolds number is observed.

Table 3.5: Values of the constants measured from the DNS for the Lagrangian structure functions of velocity, substrate concentration and mixed velocity-concentration.

	C_0	C_0 from Fox and Yeung (2003) (3.93)	C_1^S	C_2^S
$R1$	2.15	3.46	1.37	0.69
$R2$	2.87	4.58	1.81	0.69
$G2$	2.8	4.58	1.54	0.66
$P2$	2.13	3.46	1.43	0.65

Concerning the substrate, the scalar Lagrangian structure functions have not been studied theorically, but, as for the Lagrangian structure function, we assume that the function only depends on the scalar dissipation rate ε_s in the inertial range. This yields for the second-order structure function for substrate:

$$D^L_s(\tau) = \langle [\tilde{s}'(t+\tau) - \tilde{s}'(\tau)]^2 \rangle = C_1^S \varepsilon_s \tau, \ (\tau_K \ll \tau \ll T^L_S). \tag{3.94}$$

Similarly, the mixed Lagrangian structure function for the velocity-substrate concentration is defined

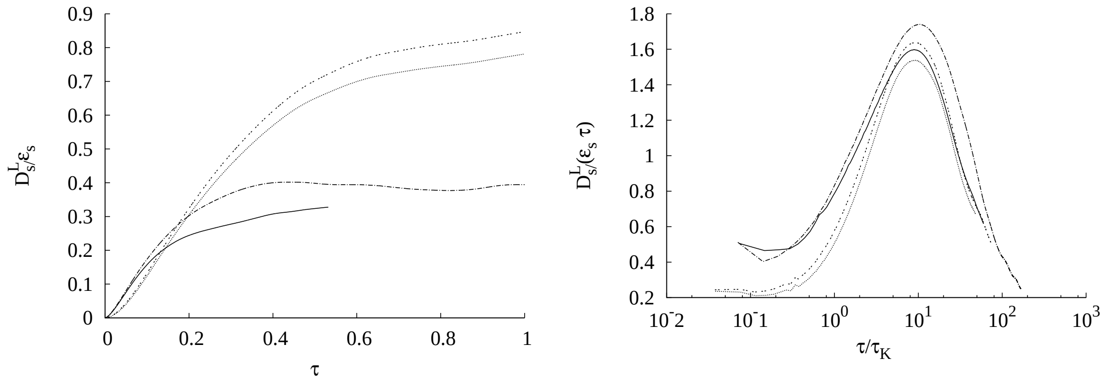

(a) D_S^L non-dimensionalised by the substrate dissipation rate ε_s of the corresponding simulation.

(b) Temporal evolution of the C_1^S constant.

Figure 3.20: Second-order Lagrangian structure functions for substrate concentration and constant C_1^S for the simulations $R1$: (········) and $R2$: (———), $G2$: (-·-·-) and $P2$: (- - - -).

and approached by:

$$D^L_{su_i}(\tau) = \langle[\tilde{s}'(t+\tau) - \tilde{s}'(\tau)][\tilde{u}'_{f,i}(t+\tau) - \tilde{u}'_{f,i}(\tau)]\rangle = C_2^S \varepsilon_{S,f}^{1/2}\varepsilon_f^{1/2}\tau, \ (\tau_K \ll \tau \ll T_S^L). \qquad (3.95)$$

The second-order Lagrangian structure functions for the simulations $R1$, $R2$, $G2$ and $P2$ are plotted in figure 3.20a. We can see that the presumed linear zone is observable for the four simulations. Figure 3.20b shows the peak of the constant (C_1^{S*}) for the different simulations and we can observe an effect of the flow dynamics on the value of C_1^{S*} The imposed concentration gradient also impacts the substrate Lagrangian structure function (for the simulation $G2$ in comparison with simulation $R2$) where the constant C_1^S decrease. Finally, increasing the Schmidt number increases the C_1^S constant. The different constants C_1^S for the simulations are summarised in table 3.5. We can remark in figure 3.21 that the linear zone is longer for the substrate second-order structure function than for the velocity. This can be explain by the fact that the Lagrangian time scale for the substrate mixing is around twice the dynamic time-scale.

Finally, the mixed Lagrangian structure functions for the four simulations are shown in figure 3.22a. A linear zone is observed, and the peak of the constant (C_2^{S*}) are shown in figure 3.22b.The constant C_2^S does not change from one simulation to another, as shown by table 3.5.

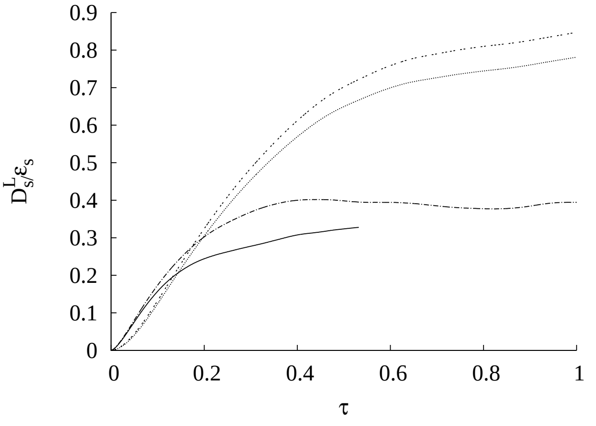

Figure 3.21: Second-order Lagrangian structure function for the velocity (———) and the substrate concentration (∘) for the simulation $R2$.

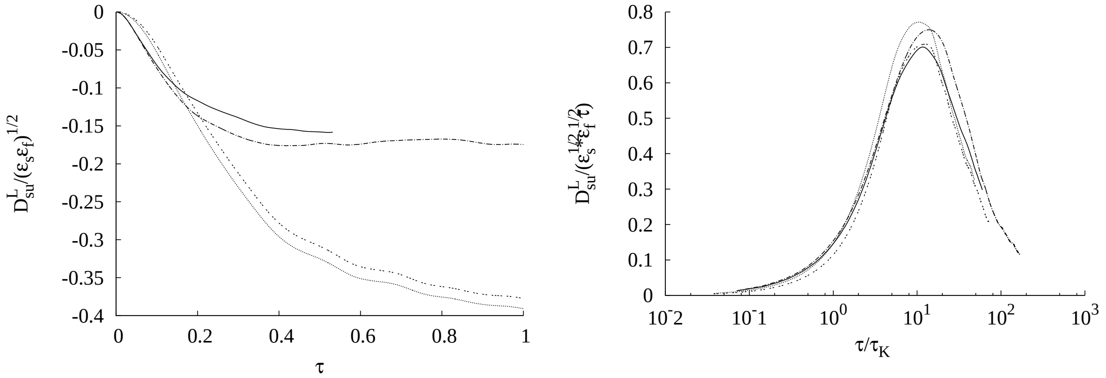

(a) D^L_{sv} non-dimensionalised by the root square of substrate dissipation rate ε_s and the energy dissipation rate ε_S of the corresponding simulation.

(b) Temporal evolution of the C^S_2 constant.

Figure 3.22: Temporal evolution of the mixed Lagrangian structure functions for the substrate and of the constant C^S_2 for the simulations $R1$: (········) and $R2$: (———), $G2$: (–·–·–) and $P2$: (– – – –).

3.5 Conclusion

This part of the work was devoted to the presentation of the DNS approach for the velocity and substrate concentration fields calculation. The numerical tool was introduced and the different resolved equations were enlightened. Further simplified transport equations necessary for the statistical analysis of flow dynamics and mixing were also presented.

The statistically-steady property of the different HIT allows a deep statistical analysis of the different flows. The main statistics are given in table 3.2 and the physical parameters of the simulation are summarised in table 3.1. The further chapters of this work will often refer to these tables.

In order to verify the results from simulations, different validations were performed. The different Eulerian correlations were introduced and the Eulerian statistics of the flows were collected. This validation part focuses more specifically on integral length scales. Their determination is important to characterise turbulent flows.

Then a short spectral analysis is proposed, where the turbulent kinetic energy and substrate energy spectra are presented for the different simulations. The obtained spectra in the steady configuration are the reference cases for the rest of the work.

An analysis on the different distributions is also proposed, where the study is emphasised on the scalar PDF. The different obtained results are confronted with already existing results of the literature (Pumir, 1994; Overholt and Pope, 1996) in order to validate our simulations.

Finally, a large presentation of the Lagrangian properties of the flows is provided. the different Lagrangian statistics are introduced and compared with the work of Yeung et al. (2000). The analysis of Lagrangian statistics is of prime importance in turbulence modelling. We will see in the next chapter how they are used to develop specific Lagrangian models.

Different flow fields were investigated. By changing the Reynolds number of the flow, two dynamic fields can then be compared. The effect on the substrate mixing is also investigated for these two dynamics. A study on the substrate mixing is also carried out by changing the substrate diffusivity in the fluid for the same flow dynamics. And the substrate mixing intensity was also studied for three different cases with the same flow dynamics. These five carrier flow configurations will be used in the next part of the work and allow a wide range of configurations to study the interaction between mixing and assimilation by the microorganisms.

Figures

Chapter 4

Substrate assimilation by a population of microorganisms in turbulent flows

With the aim of characterising the assimilation of one population of microorganisms, different two-phase numerical simulation are performed. In a first approach, the simulations are stationary for both the dynamic and scalar field. Based on the fluid-flow simulations introduced in the previous chapter, the following part of the work is a first step in the direct numerical simulation of biological flows. The different assumptions required for the forthcoming simulations as well as the discrete particle simulation principle are presented. By the mean of different fluid-flow and different biological parameters, the DNS+DPS simulations are presented.

Primary macroscopic results are obtained for various populations of microorganisms and first influence of the dynamic flow field are found. In the case of the Monod assimilation law applied at the microorganism scale, a wide study on the dispersed phase statistics is performed. First trends are extracted and the simulations are validated a posteriori. By imposing a microscopic assimilation, the deviations to the usual prescribed macroscopic law for assimilation are bigger for intermediate affinity constants. Moreover, the flow dynamics impacts the assimilation for microorganisms. A big impact of the substrate mixing is also found for the macroscopic assimilation, accounting for local effects of the substrate fluctuations.

Then, a presentation of the different PDF for the fluid and the microorganisms gives a first overview on the overall distribution at the individual scale. A discussion on these distributions is a first step in the explanation of the micro-mixing effect on the metabolite production for example. The latter is finally estimated from the simulations as well as the biomass growth from a metabolic model.

Résumé

Ce chapitre est dédié à l'étude de l'assimilation de substrat par une population de microorganismes dans un écoulement turbulent. Le fluide est résolu par simulation numérique directe, tandis que les microorganismes sont suivis par une approche Lagrangienne dans l'écoulement. Les microorganismes sont considérés comme des traceurs du fluide compte tenu de leur faible taille. Cette approche par suivi Lagrangien permet de pouvoir prendre en compte les hétérogénéités de concentration en substrat vues par les microorganismes.

Toujours dans l'idée de prendre en compte le caractère local de l'assimilation du substrat par les microorganismes, une loi d'assimilation microscopique est imposée à chaque microorganisme. Le choix de la loi d'assimilation locale est guidé par les différents résultats obtenus au second chapitre de ce travail. Les lois d'assimilation de Monod et de Blackman sont donc principalement utilisées et basées sur la concentration en substrat vue localement par les microorganismes, issues de l'interpolation du champ Eulérien de concentration. Le modèle d'assimilation bilinéaire est également brièvement étudié dans cette configuration, mais son utilisation reste restreinte en raison, principalement, des limitations numériques.

Les champs dynamique et scalaire sont totalement caractérisés par les différentes grandeurs statistiques introduites au chapitre 3, et on peut ainsi étudier l'effet de chacun d'eux sur la réaction biologique. Dans cette partie du travail, les différentes simulations sont statistiquement stationnaires et l'effet de la réaction biologique sur le champ de concentration du fluide n'est pas pris en compte. En d'autre terme, cette approche peut être assimilé à la modélisation à petite échelle d'un réacteur continu où le substrat serait injecté en continu, et le biomasse soutirée afin de conserver un volume utile constant.

Une analyse statistique sur ces simulations stationnaires est conduite sur la phase biologique et permet de trouver une loi d'assimilation macroscopique, à l'échelle de la population, intégrant les effets locaux pour chaque microorganisme. Les lois d'assimilations obtenues sont sensiblement équivalentes à la loi macroscopique basée sur la concentration moyenne en substrat dans le domaine, généralement utilisée dans la plupart des travaux sur la modélisation des bioréacteurs. Malgré la non-linéarité des réactions biologiques, ce résultat s'explique par le caractère bien macro-mélangé de notre configuration. En effet, même si un gradient de concentration en substrat est imposé, les concentrations sont relativement homogènes ce qui conduit à de faibles écarts par rapport à la loi macroscopique d'assimilation.

Cependant, si l'on regarde les différentes statistiques de la phase biologique en terme de fluctuations, nous observons des écarts assez significatifs entre les différentes populations de microorganismes étudiées. Ces populations diffèrent de par leur affinité au substrat. Lorsque la constante d'affinité au substrat est de l'ordre de la concentration moyenne, les corrélations statistiques sont maximales ainsi que l'écart par rapport à la loi d'assimilation à l'échelle de la population basée sur la concentration moyenne.

Ces écarts étant uniquement dus au effet de micro-mélange, nous nous sommes intéressés aux différentes distributions pour la phase biologique. Nous avons montré que pour une agitation plus importante, avec cependant un même champ de scalaire, les distributions en terme de concentrations vues et de flux assimilés par les microorganismes sont relativement identiques. Ce constat diffère dans le cas où le champ de concentration présente une variance plus importante, les distributions sont plus étalées.

L'intérêt de ce travail se situe plus particulièrement dans l'analyse de ces distributions de flux assimilés par les microorganismes. En effet, ce sont ces écarts autour du taux d'assimilation moyen

basé sur la concentration moyenne qui, pour une même population, vont conduire à des baisses du taux de croissance ou à la production de métabolites secondaire dans le mécanismes d'*overflow*.

Les observations sur les distributions obtenues par les simulations numériques directes ont permis de proposer une approche analytique pour la détermination de la distribution de flux de substrat assimilé par une population de microorganismes, compte-tenu de la dynamique de l'écoulement et plus particulièrement du mélange du substrat. La connaissance de l'état de micro-mélange de ce dernier permet en effet de prédire la répartition des taux d'assimilations locaux pour la populations de microorganismes. De manière plus générale, cette approche pourrait être utilisée pour des simulations de bioréacteurs à plus grande échelle, où les équations de transport du scalaire et de sa variance sont résolues. À l'aide des modèles de micro-mélange existants, la distribution des taux d'assimilations à l'intérieur d'une maille du calcul CFD pourrait être obtenue.

Enfin, à l'aide d'un modèle métabolique spécifique prenant en compte la contribution de trois fonctionnements simultanés pour une population de microorganismes, des résultats en terme de croissance de la biomasse et de production de métabolites secondaires sont proposés pour nos simulations. Ce modèle métabolique n'est considéré qu'en milieu purement oxydatif, c'est-à-dire que l'apport en oxygène sera toujours considéré comme non-limitant. Par la prise en compte des mécanismes de maintien énergétique et de croissance des cellules (anabolisme et catabolisme oxydatif), ainsi que de la production de métabolites secondaires par le mécanisme d'*overflow*, les résultats obtenus montrent une baisse de rendement de croissance dans le cas de population à faible affinité au substrat par rapport au rendement de croissance attendu. De plus, la baisse de rendement est d'autant plus importante que la variance de concentration en substrat est importante, s'accompagnant parallèlement d'une augmentation de la production de métabolites secondaires par le mécanisme *overflow*.

Ces derniers résultats en terme de croissance et productions de métabolites secondaires sont une première explication de l'impact du micro-mélange sur les cultures de populations de microorganismes. De plus, ces résultats sont en accords avec les observations expérimentales sur la production localisés de métabolites secondaires par exemple.

Contents

Introduction

We decide to study the assimilation of substrate by a population of microorganisms in a turbulent flow. This approach at the population scale will help in understanding the effect of local variations encountered by the microorganisms at the individual scale on population assimilation.

This chapter is devoted to study the assimilation of substrate by a population of microorganisms in a turbulent flow. Following the idea to model the assimilation at the microorganisms scale, this approach will help in understanding the effect of local variations encountered by the microorganisms along their trajectories at the population scale.

Based on the dynamic velocity and substrate concentration fields, obtained with DNS, characterised in the previous chapter, the calculation of microorganisms trajectories will be added to the simulations and the local assimilation rate is exactly known from the local substrate concentration with the prescribed assimilation law. The biological statistics are computed and analysed in detail in order to study the impact of microscopic effects at the population scale.

The different existing approaches for multiphase flow simulations and the chosen method for biological flows are presented hereafter.

4.1 About two-phase flows

Multiphase flows are found in many industrial applications and receive much attention from scientific communities in various application areas. As examples of applications we may mention chemical engineering, energy conversion, heat exchangers, fuel injection, pollutant transport in the atmosphere, biological engineering... These flows involve two or more phases (gas, liquid, solid) and various phenomena are observed for the dispersed phase such as droplets coalescence or break-up, particle-particle interactions, turbulent dispersion, fluid modulation by the dispersed phase and so on. The multiplicity of two-phase flows has lead to a rigorous categorisation of flow types over the years and different approaches have been developed for the numerical simulation of transport of a dispersed phase by a turbulent flow.

The resolution and modelling of two-phase flows is challenging, and the adaptation to biological flow is encouraged by the multiphase-nature of biological flows in bioreactors. Indeed, two or more phases, biomass included are transported by a turbulent flow and the interactions between the different phases are of prime importance. Different methods for modelling two-phase flows and their applicability to biological flows are summarised hereafter.

The Two-phase Direct Numerical Simulation solves the exact Navier-Stokes equations for turbulence in the whole domain, as well as around the inclusions. No hypothesis are needed, but the calculation cost is extremely prohibitive and therefore this method is restricted to dilute flows on a small-scale geometry. For biological flows, this approach can be relevant to extract local interaction laws between the substrate transport and the assimilation. The influence of one microorganism assimilation on one neighbouring could also be investigated. But due to the particle number restriction, this approach is only suitable for determination of microscopic models.

In the Euler-Lagrange approach, the equations for the fluid-flow are solved by Direct Numerical Simulations (DNS) or Large Eddy Simulations[1] (LES). The particle trajectories are then computed

---

[1] LES requires the use of a sub-grid model.

by the balance of forces acting on each inclusion. This method is called the Discrete Particle Simulation (DPS) and can be used for a large amount of particles. But, different laws accounting for fluid-inclusions transfers are required. Nevertheless, the number of inclusions is limited and statistical methods are developed for industrial configuration under some conditions. The DNS+DPS approach is chosen for the present study, because we decide to study the impact of the flow dynamics and mixing on substrate assimilation by microorganisms. The resolution of the different scales of the flow by DNS leads to fully determined velocity and substrate concentration fields and we only focus on biological assimilation. The Lagrangian tracking of microorganisms helps in understanding the fluctuations encountered by microorganisms in the reactor. Moreover, this DNP+DPS resolution presents the advantage of prescribing an assimilation law at the microorganisms scale.

Finally, the Euler-Euler approach or two fluids model, is also based on a statistical approach of the flow, but the transport equations of the first moments of the PDF are solved. This resolution requires turbulence models for the carrier phase as well as for the dispersed phase. The terms accounting for interaction between the phases must be handled carefully. This method is much more convenient for industrial applications. Indeed, the possibility of addressing complex geometries and the low calculation costs compared to other cited approaches is a real asset. Of course this approach remains one of the main objectives for the simulation of bioreactors, but the necessity of providing mass transfer and assimilation models requires a specific attention on this biological phenomenon.

Therefore, aiming at better understanding biological assimilation, we choose the DNS+DPS approach. Despite the fact that the geometry is unrealistic, this allows a full resolution of the substrate mixing, and its effect on assimilation by the biomass. Due to computer limitations, a finite number of microorganisms is tracked. A presentation of the two-phase simulations is given hereafter.

4.2 Lagrangian tracking of microorganisms and assimilation representation

In this work, the microorganism are considered as particles transported by the turbulent flow. The study of inclusions in different flows has been widely investigated over the years. Stokes (1851) studied the different forces acting on a spherical object in a laminar flow with no-slip boundary condition at the particle surface. Boussinesq (1885), Basset (1888) and Oseen (1927) further investigated this problem considering the streamlines around the sphere and deriving an equation of motion depending on the Reynolds number of the flow around the sphere. Later, Tchen (1947) addressed the more general problem of particles suspended in a turbulent fluid with gravity forces.

4.2.1 Discussion on forces acting on a microorganism

In the context of biological flows, microorganisms can be thought as particles transported in the bioreactor. Suspended in a turbulent flow, the microorganisms are subjected to shear forces that can modify their shape (Yim and Shamlou, 2000). As already introduced, in 1, the hydrodynamic strains directly affect microorganisms and result in their deformations. These deformations are not studied in the present work. As far as our objective is to model assimilation and since there is no evidence or model describing the relationship between deformation and assimilation, it is decided to represent microorganisms as solid spherical particle of constant diameter d_p. The diameters for yeast and bacteria range from 10^{-6} to 10^{-5} m (Yim and Shamlou, 2000). But it is necessary to compare those diameters with the characteristic length scales of the flow in bioreactors.

According to Vràbel et al. (2001), the specific dissipation rate obtained in three large-scale bioreactors ranges from 1.3 to 3.1 $\mathrm{m}^2 \cdot \mathrm{s}^{-1}$. Even if those values are an averaged dissipation rate over the vessel, the corresponding Kolmogorov length scales are about $3 \cdot 10^{-5}$ m. In conclusion, the microorganisms diameters are small compared to the Kolmogorov length scale in bioreactor:

$$d_p \ll \eta_K. \tag{4.1}$$

Microorganisms growth

As already introduced, the biomass growth is one of the preponderant objective in biological processes. One microorganism grows in size and two daughter cells are formed. The microorganisms radius increases and might be doubled. Nevertheless, the microorganisms diameter remains small compared to the Kolmogorov length scale. In this work, the biomass growth is not modelled, and the microorganisms diameter is kept constant. Moreover, no bacterial aggregates are considered in this work.

The microorganisms are supposed to be in a regime where the viscous effects are preponderant. This regime is called the Stokes regime and the associated particle Reynolds number is very small:

$$Re_p = d_p \frac{|\mathbf{u}_p - \mathbf{u}_{f@p}|}{\nu_f} \ll 1, \tag{4.2}$$

where $u_{f@p}$ is the fluid velocity at the particle position, undisturbed by the particle and $|\mathbf{u}_p - \mathbf{u}_{f@p}|$ is the relative velocity between the particle and the fluid.

It is then important to know if the microorganisms respond rapidly to the fluid velocity. Therefore, we calculate the Stokes number St as the ratio of the Stokes particle relaxation time τ_p and the fluid dissipation characteristic time scale τ_ε. The former is given by (4.3) for small particulate Reynolds numbers:

$$\tau_p = \frac{\rho_p d_p^2}{18\nu_f}. \tag{4.3}$$

The fluid dissipation time scale is computed from the direct numerical simulations and reported in table 3.2. The obtained Stokes number is then:

$$St = \frac{\tau_p}{\tau_\varepsilon} \simeq 10^{-5}. \tag{4.4}$$

Considering the small values for the Stokes number, the microorganisms rapidly respond to the fluid, and will be treated as tracers of the fluid, and the different forces are negligible. The trajectory equations for one microorganism n becomes:

$$\boxed{\left\{ \begin{array}{lcl} \frac{d\mathbf{x}_p^{(n)}(t)}{dt} & = & \mathbf{u}_{f@p}^{(n)}(t) \\ \frac{d\mathbf{u}_p^{(n)}(t)}{dt} & = 0 & \end{array} \right.} \tag{4.5}$$

The system of equations (4.5) is solved in time using an integrated Runge-Kutta method with the same time step as the fluid resolution.

The main difficulty for the resolution of the system equations (4.5) is to compute the fluid velocity at the particle position. In fact, the fluid equations are solved on an Eulerian grid, and the particles trajectories are Lagrangian. Therefore, the determination of $\mathbf{u}_{f@p}(t)$ requires the interpolation of the eulerian velocity field $\mathbf{u}_f(t)$ at the particle position. Balachandar and Maxey (1989) analysed different interpolation schemes and the Shape Function Method (SFM) is chosen here. A further discussion on interpolation schemes is proposed in chapter 5 and Annexe B presents the general method.

The same interpolation is employed for the calculation of the substrate concentration at the microorganism's position $S_{@p}$.

4.2.2 Representation of substrate assimilation by microorganisms

The assimilation rate is the amount of substrate assimilated by one microorganism during a given period. According to the previous consideration on assimilation, we chose to model the uptake rate at the microorganism scale. Therefore, the quantity Φ, introduced as the mass flux in the previous chapter on the substrate assimilation by one microorganism exposed to fluctuating concentration, is related to one microorganism and is written Φ_p (in $[\ \mathrm{kg_S \cdot s^{-1}}\ ]$). This mass flux directly depends on the substrate concentration at the microorganism position $S_{@p}$.

Three assimilation models are investigated in this part of the work. Two of then are standard models, whereas the last one is the bilinear model developed in chapter 2 accounting for substrate limitation.

Monod law
First, the Monod assimilation model is applied to any microorganism n. The corresponding uptake rate is then:

$$\Phi_p^M = \Phi_{max} \frac{S_{@p}}{k_S + S_{@p}}, \tag{4.6}$$

where k_S is the microscopic affinity constant to the substrate S. Thus, each microorganism is characterised by its assimilation rate Φ_p.

Blackman model
An other standard model for assimilation is the Blackman bilinear assimilation model (Koch and Houston Wang, 1982). The mass flux is obtained by comparison of the available substrate concentration compared to the constant affinity of the microorganism:

$$\Phi_p^{Bl} = \begin{cases} \Phi_{max} & if \quad S_{@p} > 2k_S \\ \Phi_{max} \frac{S_{@p}}{2k_S} & if \quad 0 \leqslant S_{@p} \leqslant 2k_S. \end{cases} \tag{4.7}$$

The limitation of both standard model remains in the determination of the local affinity constant k_S. Indeed, those models are generally integrated at the reactor scale with an a posteriori determination of the affinity constant. Therefore the last model presents the advantage to get rid of any assumption on the affinity to the substrate.

Bilinear model The bilinear model is based on the idea that each microorganism regulates its substrate assimilation by means of two distinct mechanisms. Either the assimilation rate is below the maximum capacity of the microorganism to assimilate substrate, and therefore no residual concentration is found in the direct vicinity of the microorganisms interface, or the maximum capacity is reached and there is a substrate accumulation around the microorganism. The second regime is observed when the biological reaction is the limiting process whereas the first regime corresponds to the physical regime where transport limits the assimilation. The two asymptotic cases are then summarised by the following expression for the bilinear assimilation model:

$$\Phi_p^{Bi} = \begin{cases} \Phi_{max} & if \quad S_{@p} > S^{sat} \\ \Phi_{max} \frac{\pi d_p \mathcal{D}_{S,f}}{2} S_{@p} (1 + \frac{d_p}{d_p + 2\eta_K}) & if \quad 0 \leqslant S_{@p} \leqslant S^{sat}. \end{cases} \tag{4.8}$$

where S^{sat} is the saturation concentration for which $\Phi_p^{Bi}(S^{sat}) = \Phi_{max}$ and its expression is:

$$\frac{2\Phi_{max}}{4\pi \mathcal{D}_{S,f} d_p \big(1 + \frac{d_p}{d_p + 2\eta_K}\big)^{-1}}. \tag{4.9}$$

The far-field concentration introduced for the one-dimensional case is approximated by the interpolated substrate concentration $S_{@p}$ and the diffusional length is the Kolmogorov scale of the

simulation, below which the substrate transport is purely diffusive[2].
But, the above definition of the bilinear model is considering the steady state for assimilation. Indeed, the substrate diffusional transport from the far-field towards the cell is unsteady and temporal analysis is required for the integration of the diffusive transport in the DNS. The next paragraph aims to evaluate the different characteristic times for the bilinear model and to compare them with the DNS time-step.

4.2.3 Discussion on the integration of the bilinear model in DNS calculations

As we did in the previous chapter, the radial diffusion equation for substrate transport from the far-field to the microorganism is solved. But the strong coupling of the resolution from this equation with the DNS time-advancement requires a time analyses in order to identify different possible regimes. Indeed, the far-field concentration is obtained from one time-step Δt_{DNS} of the DNS calculation whereas the interfacial concentration $S_{@p,int}$ requires several time steps of the diffusive transport Δt_{Diff}. The key parameter is the ratio between the time step from the DNS and the characteristic time for diffusion over the Kolmogorov scale: $\Delta t_{DNS}/\tau_{\mathcal{D}_S}$. Three asymptotic regimes for the diffusional transport below the Kolmogorov scale are then envisaged.

- $\Delta t_{DNS}/\tau_{\mathcal{D}_S} \gg 1$: corresponds to the case where the diffusional transport is stationary in one time-step of the DNS simulation and the steady interfacial concentration is reached. This results is shown in figure 4.1a.
- $\Delta t_{DNS}/\tau_{\mathcal{D}_S} \equiv 1$: in that case, we may think that the diffusional substrate transport is about to reach the steady-state in one time step of the DNS simulation. The resulting interfacial concentration thus corresponds to the steady-state interfacial concentration. The result from numerical simulation is shown in figure 4.1b and both the dynamic and steady resolutions are similar.
- $\Delta t_{DNS}/\tau_{\mathcal{D}_S} \ll 1$: in that case the characteristic diffusional time $\tau_{\mathcal{D}_S}$ is large compared to the DNS time-step. Thus, the interfacial concentration is obtained by solving the diffusional equation over several time steps of the DNS and requires the transport of the spherical domain around the micro-organism through the DNS, or intermediate iterations for the diffusional transport towards the microorganism in order to obtain the exact assimilation rate during the DNS time-step. The evolution of the interfacial concentration for a top-hat far-field concentration is illustrated in figure 4.1c with the solid and dashed lines for this configuration. A more general study can be found in Linkès et al. (2012). But, the dynamic resolution is not applicable in the following framework from numerical accuracy.

The temporal ratios for the different simulations performed in the previous chapter are found to be less than one. A dynamic resolution is required for the determination of the exact assimilation rate for one microorganism during one time-step of the DNS. Nevertheless, intermediate-iterations are not envisaged because of the high computational cost. Therefore, the steady-state resolution is chosen and the interfacial concentration is approximated by the value of the interfacial concentration calculated by the steady-state approach, solving the stationary diffusional equation. Figure 4.1c shows the obtained signals for the dynamic and steady approach. As observed, the steady approach given by the symbols underestimates the actual uptake rate. More specifically for this top-hat calculation, we underestimate the uptake rate by 72%, whereas the interfacial concentration is overestimated by 50%.

---

[2] Indeed the Schmidt number of the performed simulations is of order 1.

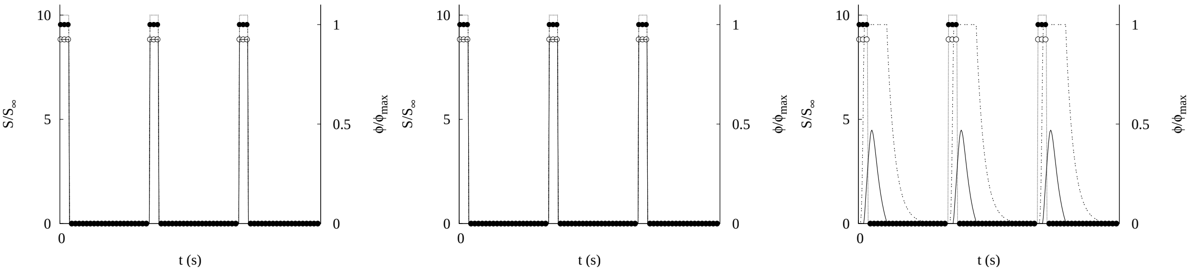

(a) $\Delta t_{DNS} \gg \tau_{\mathcal{D}_S}$ (b) $\Delta t_{DNS} \equiv \tau_{\mathcal{D}_S}$ (c) $\Delta t_{DNS} \ll \tau_{\mathcal{D}_S}$

Figure 4.1: Comparison of interfacial concentration and uptake rate temporal evolution for dynamic resolution of the diffusion equation (——) and (- - - -) respectively, and for the steady approximation: S_{int} : ○ and ϕ : ● with a top-hat far-field concentration evolution (········).

According to previous considerations, the bilinear assimilation model for one microorganism is then given by equation (4.8). Even if the resolution in the steady manner gives good results for the interfacial concentration, the interfacial uptake rate is more sensitive to this approach and might be overestimated. In fact, the uptake rate for one microorganisms will be either on the constant or linear slope of the bilinear model in one DNS time-step. Nevertheless, a time-average for the interfacial uptake for one microorganism will lead to a hyperbolic law, as we obtained in chapter 2. Moreover, the assimilation of one microorganism is not disturbed by a neighbouring microorganism since the assimilation has no repercussion on the fluid flow in this part of the work.

After presenting the framework for Lagrangian tracking of microorganisms and defining the different types of investigated assimilation models, we present the different stationary two-phase simulations in the next section.

4.3 Presentation of the simulations DNS+DPS

4.3.1 Numerical considerations

The trajectories of microorganisms are coupled with the fluid-field resolution by Direct Numerical Simulations. As earlier introduced, the microorganisms are tracers of the fluid. One can remind here that the microorganisms Stokes number is very small and corroborates the idea that the microorganisms are inertial-less.

In this part of the work, the influence of microorganisms on the fluid is not considered and the only effects of the flow dynamics, substrate mixing or local assimilation model are scrutinised.

The microorganisms are handled in a periodical manner at the boundaries of the domain, and in the case of the Bilinear model, the interfacial properties are modified in the y-direction in order to be consistent with the presence of the imposed gradient. For the other cases, no specific handling is necessary for the particles, because the assimilation rate only depends on the local concentration $S_{@p}$ which is built to take the gradient contribution into account.

We remind here that the velocity and substrate concentration at the particle positions are evaluated from interpolation of the Eulerian field by means of the Shape Function Method. The substrate concentration at the particle position is then be reconstructed from the interpolated resolved concentration $\tilde{s}_{@p}$, the gradient contribution and the imposed mean concentration such that for the particle n:

$$S_{@p} = S_0 + \tilde{s}_{@p} + \zeta(y_p - \frac{L_{box}}{2}). \tag{4.10}$$

In the manner of the eulerian fluid substrate concentration, the substrate concentration at the particle position can be decomposed in:

$$S_{@p} = \langle S_{@p} \rangle_p + s'_{@p}, \tag{4.11}$$

where $\langle . \rangle_p$ is the ensemble average over the microorganisms operator and $s'_{@p}$ is the fluctuating interpolated concentration. In order to be consistent with section 3.1.4, the average substrate concentration can be expressed as $\langle S_{@p} \rangle_p = S_0 + \langle \zeta(y_p - \frac{L_{box}}{2}) \rangle_p$, where the last term is zero and the fluctuation $s'_{@p}$ as the interpolated deviation substrate concentration $\tilde{s}_{@p}$. From now only the notation $s'_{@p}$ is kept. Moreover the notation $\langle ._{@p} \rangle_p$ and $\langle ._p \rangle_p$ are simplified into the following: $\langle . \rangle_p$. It is thus implicit that ensemble averages over the microorganisms are performed for particle related quantities.

It is important to notice here that the substrate concentration must be positive or zero at any point in time. Therefore, we paid careful attention to the value of the mean imposed concentration S_0 that must ensure this condition. As we can see in figure 3.14, for the simulation $R2$, the mean imposed concentration $S_0 = 0.15\ \mathrm{kg_S \cdot m^{-3}}$ does not obey this condition and will not be further investigated for biological suspensions.

4.3.2 Biological parameters

The different characteristics of the biological suspension are summarised in table 4.1. The microorganism density is set to be constant in the different numerical simulations, as well as the particle diameter d_p. In this part of the work, all microorganisms are supposed to be in the same physiological state. Therefore, we choose a constant value for the maximum specific uptake rate Φ_{max}. This supposition enables to consider the non-dimensionalised uptake rate, getting rid of Φ_{max} because we do not take the biological effect on the fluid.

Table 4.1: Microorganisms properties.

Density	ρ_p	[$\mathrm{kg_S \cdot m^{-3}}$]	10^3					
Diameter	d_p	[m]	$2 \cdot 10^{-6}$					
Maximum mass flux	Φ_{max}	[$\mathrm{kg_S \cdot s^{-1}}$]	$2.23 \cdot 10^{-11}$					
Affinity constants	k_S	[$\mathrm{kg_S \cdot m^{-3}}$]	10^{-3}	$5 \cdot 10^{-3}$	10^{-2}	$5 \cdot 10^{-2}$	10^{-1}	$5 \cdot 10^{-1}$
			1	5	10	$5 \cdot 10^{1}$	10^{2}	$5 \cdot 10^{2}$

Nevertheless, the microorganisms are categorised in terms of their affinity to the substrate k_S in the case of Monod or Blackman assimilation models. The affinity constant k_S account for the microscopic affinity at the microorganisms scale. In the following of the work, twelves classes of particles are scrutinised, accounting for affinity constants ranging from $10^{-3}\ \mathrm{kg_S \cdot m^{-3}}$ to $5 \cdot 10^{2}\ \mathrm{kg_S \cdot m^{-3}}$. Considering the area of variation for the mean concentrations in this work (ranging from $S_0 = 0.15\ \mathrm{kg_S \cdot m^{-3}}$ to $S_0 = 1\ \mathrm{kg_S \cdot m^{-3}}$, this range covers the 3 asymptotic cases where the microorganisms have a weak affinity for the substrate (big k_S), a high affinity (small k_S) and finally intermediate affinities.

4.3.3 Simulations presentations

This paragraph presents the different two-phase simulations performed for this work. They are based on the fluid flow simulations performed in the previous chapter. Typically, simulations $R1$, $R2$ and $G2$ will be used for two-phase simulations. For the flow field of simulation $R2$, two different mean concentrations ${S_0}^3$ will be scrutinised but the statistical properties of the substrate field will remain unchanged for the two simulations. Once the flow-field and the substrate-field are stationary, the microorganisms are injected randomly in the computational box. Their velocity matches the fluid velocity at the particle position and the substrate concentration is interpolated at the particle position to compute the assimilation rate. Each class is composed of $N_p = 2 \cdot 10^5$ microorganisms[4]. This configuration of two-phase flow corresponds to a continuously agitated bioreactor with constant substrate injection and where the biomass concentration remains constant by subtracting solution. By analysing the results for assimilation, this part of the work is devoted to scrutinise the mixing effect on the bioreactor performances. Table 4.2 summarises the different two-phase simulations.

Table 4.2: Summary of the two-phase simulations for the Monod and Blackman assimilation models.

Simulation	Fluid flow	$S_0[\ \mathrm{kg_S \cdot m^{-3}}\ ]$	Assimilation model
$R1M$	$R1$	0.15	Monod
$R2S_{0.15}M$	$R2$	0.15	Monod
$R2S_1M$	$R2$	1	Monod
$G2M$	$G2$	1	Monod
$R2S_{0.15}Bl$	$R2$	0.15	Blackman
$R2S_1Bl$	$R2$	1	Blackman

For the bilinear assimilation model, the simulations are quite different. The parameter k_S is no longer required and the saturation constant is the only parameter for one microorganisms class. According to equation (4.9), the saturation constant does not depend on the mean concentration but only on the dynamics of the flow (meaningly from $\mathcal{D}_{S,f}$ and η_K). Therefore for one flow-field, several mean concentrations S_0 are considered. Remembering that the instantaneous substrate concentration field must be either positive or zero everywhere in the domain, a particular attention must be paid to the value of S_0. Typically for the simulation $R2$, mean concentration under $0.15\ \mathrm{kg_S \cdot m^{-3}}$ is non-physical. From table 4.3 that summarises the simulations for the bilinear model we can see that the saturation constant is lower than $0.15\ \mathrm{kg_S \cdot m^{-3}}$. Therefore we performed simulations for larger S_0 and we chose to keep the flow dynamics and to consider lower substrate concentration fluctuations by decreasing the imposed gradient to $\zeta = 0.1\ \mathrm{kg_S \cdot m^{-4}}$. This matches the simulation $G1$ which characteristics are given in table 3.2. Considering the small concentration variance, small mean substrate concentrations S_0 are reachable with positive substrate field.

The next section presents the first results for assimilation in the steady configuration.

---

[3] the suffix S_1 and $S_{0.15}$ are added at the simulation name $R2$ accounting for $S_0 = 1\ \mathrm{kg_S \cdot m^{-3}}$ and $S_0 = 0.15\ \mathrm{kg_S \cdot m^{-3}}$ respectively.

[4] so that the corresponding volume ratio is: $\alpha_p = N_p \frac{V_p}{V_{box}} = 4 \cdot 10^{-10}$, with V_p a microorganism volume and V_{box} the gaseous volume. Giving this small value for α_p, the collisions between microorganisms are not considered in this work.

Table 4.3: Summary of the two-phase simulations for the Bilinear assimilation model.

Simulation	Fluid flow	Saturation concentration S_{R2}^{sat} [$\mathrm{kg_S \cdot m^{-3}}$]	Range of mean concentration S_0 [$\mathrm{kg_S \cdot m^{-3}}$]
$R2Bi$	$R2$	$9.53 \cdot 10^{-2}$	$0.15 \ \rightarrow \ 10$
$G1Bi$	$G1$	$9.53 \cdot 10^{-2}$	$10^{-2} \ \rightarrow \ 10$

4.4 Results for assimilation at the population scale

4.4.1 Macroscopic results

The results of the different two-phase simulations are given here for the biological phase, in terms of assimilation rate at the population scale. Meaningly, ensemble averages are performed over the microorganisms in order to extract a macroscopic assimilation law.

As introduced in section 3.2.1, the ensemble average over the particles is performed (3.20) for the concentration $S_{@p}$ and uptake rate Φ_p. All results for the uptake rate are non-dimensionalised by the maximum specific uptake rate Φ_{max}. The averaged assimilation rate $\langle \Phi_p(S_{@p}) \rangle_p = \langle \Phi \rangle_p$ is compared to the assimilation rate based on the average concentration $\Phi(\langle S \rangle)$ with respect to the ratio $< S > /k_S$. Indeed, the flow configuration gives similar results for $\langle S_{@p} \rangle_p$ and $\langle S \rangle$ so that we directly compare our macroscopic assimilation rate with a classical macroscopic determination of the assimilation rate based on the averaged fluid concentration $\langle S \rangle$. The latter yields for both Blackman and Monod assimilation rates:

$$\Phi^{Bl}(\langle S \rangle) = \begin{cases} \Phi_{max} & if \quad \langle S \rangle > 2k_S \\ \Phi_{max}\frac{\langle S \rangle}{2k_S} & if \quad 0 \leqslant \langle S \rangle \leqslant 2k_S, \end{cases} \tag{4.12}$$

$$\Phi^{M}(\langle S \rangle) = \Phi_{max}\frac{\langle S \rangle}{k_S + \langle S \rangle}. \tag{4.13}$$

The comparisons for both models with different mean substrate concentration are given in figure 4.2 for both Monod and Blackman assimilation law. We can see that for both simulations $R2S_1M$ and $R2S_1Bl$, the average uptake rate follows the macroscopic law based on the average substrate concentration. This advantageous result is explained by the small substrate concentration fluctuations compared to the average concentration S_0 in the domain. Indeed, if we look at the figure 3.14 we can see that for $S_0 = 1\ \mathrm{kg_S \cdot m^{-3}}$, the PDF of S is really narrowed, and the average uptake rate is weakly affected by the concentration distribution. On the opposite, for $S_0 = 0.15\ \mathrm{kg_S \cdot m^{-3}}$, the substrate concentration distribution is larger and affects the averaged uptake rate, especially for affinity close to the averaged substrate concentration, as we can see on both figures 4.7a and 4.7b. The deviations to the uptake rate based on the averaged substrate concentrations quantified by the ratio:

$$\xi = (\langle \Phi \rangle + p - \Phi(\langle S \rangle))/\Phi(\langle S \rangle), \tag{4.14}$$

are shown by figure 4.3 for the two assimilation model. The deviations are very similar for Monod assimilation model, but the amplitude is 100 times higher for simulation $R2S_{0.15}M$. Moreover, the maximum deviation is found for $\langle S \rangle / k_S \equiv 1$. Indeed the non-linearities are found in this specific range. Concerning Blackman assimilation, the differences are found in a narrow range at the discontinuity $\langle S \rangle / k_S \equiv 2$. In the other cases, the differences are far smaller and not shown. We can see that the bigger substrate concentration fluctuations, by comparison with the average concentration, the bigger the error to evaluate the uptake rate from macroscopic concentration.

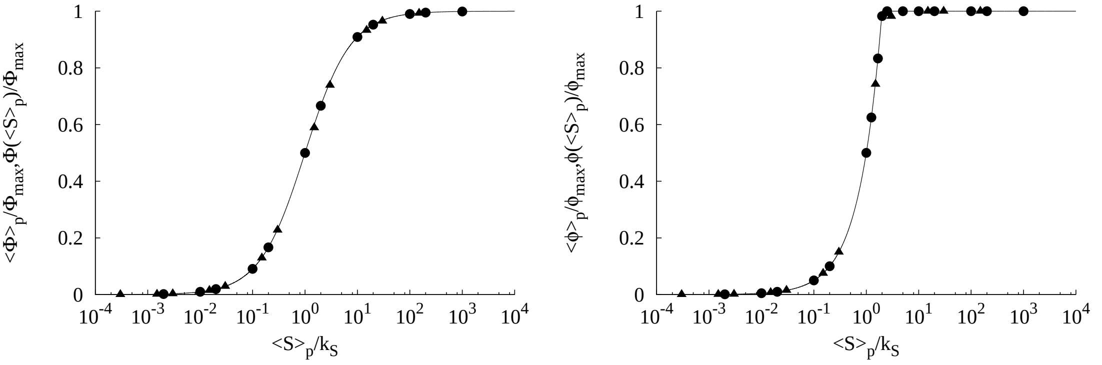

(a) Average uptake rate for simulations $R2S_1M$: • and $R2S_1M$: ▲.

(b) Average uptake rate for simulations $R2S_1Bl$: • and $R2S_1Bl$: ▲.

Figure 4.2: Non-dimensionalised average uptake rate $< \Phi >_p$ for Monod (left) and Blackman (right) assimilation models with respect to the dimensionless ratio $< S >_p /k_S$ for the dynamic flow $R2$. Symbols refer to mean concentrations $S_0 = 1$ $\mathrm{kg_S \cdot m^{-3}}$: • and $S_0 = 0.15$ $\mathrm{kg_S \cdot m^{-3}}$: ▲. (——) represents the non-dimensionalised uptake rate based on the average substrate concentration $\Phi(< S >_p)$.

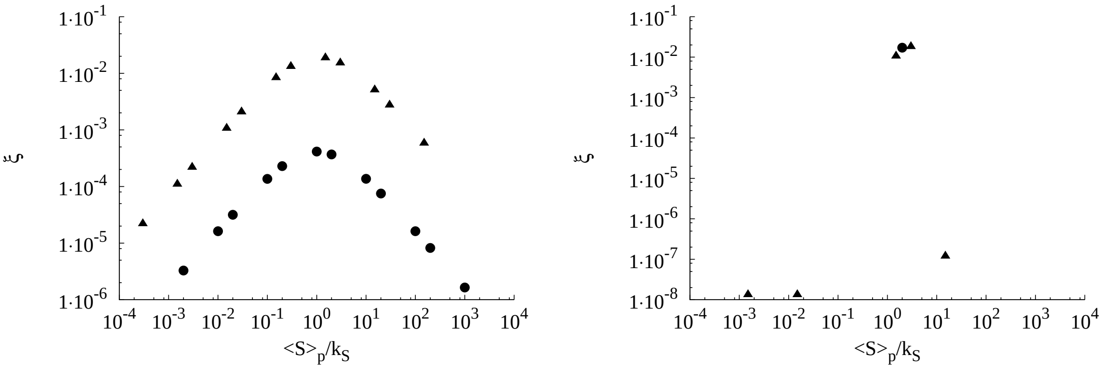

(a) Difference of the average uptake rate for simulations $R2S_1M$: • and $R2S_{0.15}M$: ▲.

(b) Difference of the average uptake rate for simulations $R2S_1Bl$: • and $R2S_{0.15}Bl$: ▲.

Figure 4.3: Deviation from the average uptake rate $< \Phi >_p$ to the uptake rate based on average substrate concentration for Monod (left) and Blackman (right) assimilation models with respect to the dimensionless ratio $< S >_p /k_S$ for the dynamic flow $R2$. Symbols refer to mean concentrations $S_0 = 1$ $\mathrm{kg_S \cdot m^{-3}}$: • and $S_0 = 0.15$ $\mathrm{kg_S \cdot m^{-3}}$: ▲.

This result depicts the non-linearity of biological reactions and the downside of assimilation model to predict assimilation at the scale of a whole population of microorganisms. Moreover, the concentration fluctuations are relatively small and non-linearity effects appear. Furthermore, these effects are expected to be stronger for higher substrate concentration fluctuations. Lapin et al. (2006) performed RANS numerical simulation of a bioreactor with $1.5 \cdot 10^5$ *E. coli* and a combined model for assimilation. The resulting substrate field presents a strong gradient between the feeding point ($S_f = 600$ $\mathrm{kg_S \cdot m^{-3}}$) and the bottom point of the reactor where there is no mean residual concentration. The fluctuations are very important and a big deviation is observed for the uptake rate compared to the expected distribution.

Moreover, in the case of simulations $R2S_{0.15}M$ and $R2S_{0.15}Bl$, the competition between substrate fluctuations and assimilation seems to result in a deviation to the expected macroscopic law by a modification in the affinity constant which results as an effective affinity constant. It is interesting to notice here that same conclusions arise for a population of microorganisms in a turbulent flow as for one isolated microorganism submitted to physical limitations for substrate transport as previously evoked in the second chapter of this work. This really encourages the necessity of microscopic modelling of the assimilation by microorganisms to develop macroscopic laws accounting for microscopic effects.

Bilinear assimilation model

We now present the results for the bilinear assimilation model where the transport of substrate from the smallest scale of the flow towards the microorganisms is modelled by a purely diffusive process. Previous considerations introduced for that case are applied to the resolution: steady resolution of the diffusion equation and the simulations are performed for various S_0, respecting a positive instantaneous concentration field.

For the Monod and Blackman assimilation models, the average interfacial uptake rate $\langle \Phi \rangle_p$ is compared to the assimilation rate based on the average concentration $\Phi(\langle S \rangle)$. Since there is no k_S in this model S^{sat} is used as reference and $\langle \Phi \rangle_p$ is plotted with respect to the ratio $\langle S \rangle / S^{sat}$. Figure 4.4 presents the average uptake rate for both fluid flows $R2Bi$ and $G1Bi$. The amplitude of fluctuations are weaker for simulation $G1Bi$, so that smaller mean concentration S_0 are possible to consider. Indeed, considering the value of S^{sat} and the limitations for S_0 the results are limited to $S_0 > 0.15$ $\mathrm{kg_S \cdot m^{-3}}$ in the case of simulations $R2Bi$. But for smaller imposed concentration gradient we can observe deviations, especially for value of S_0 close to the saturation concentration.

In conclusion, by investigating different assimilation laws at the microorganisms scale, the results for assimilation at the population scale present similar conclusions. First, when the microorganisms are subjected to small substrate concentration fluctuations the overall assimilation rate can be approached by the corresponding macroscopic assimilation law based on the averaged concentration at first sight. But despite this encouraging result, the microorganisms have different trajectories and the product formation can be impacted by these local discrepancies. Secondly, the fluctuation amplitude compared to the mean concentration is an important parameter to consider. Indeed, for the same substrate concentration variance, the macroscopic assimilation rate differs, especially for affinity constant close to the mean concentration. The same behaviour is observed for the bilinear model for S_0 close to the saturation concentration.

Finally, compared to the usual macroscopic law based on the average substrate concentration, the obtained assimilation rates at the population scale do not present strong deviations. But the small observed discrepancies are sufficient to alert on the local deviations at the microorganisms scales where the local amount of assimilated substrate can lead to the production of different products. In the next section, a deeper statistical analysis is proposed.

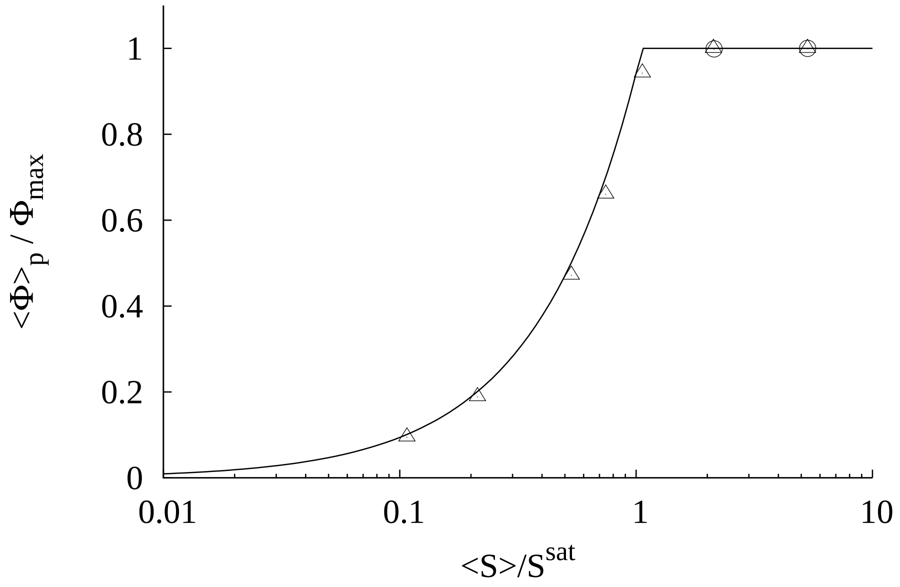

Figure 4.4: Non-dimensionalised averaged resulting uptake rate for the bilinear assimilation model with respect to the non-dimensionalised averaged concentration $< S > /S^{sat}$ for two different imposed mean gradients of concentration. ○: $\zeta = 1\ \mathrm{kg_S} \cdot \mathrm{m}^{-4}$ and △: $\zeta = 0.1\ \mathrm{kg_S} \cdot \mathrm{m}^{-4}$. The solid line represents the non-dimensionalised uptake rate based on the averaged substrate concentration $\Phi(< S >_p)$.

4.4.2 Statistic properties of the dispersed phase

Based on the average over the particles, the statistics for the biological phase are computed from the different simulations. As the microorganisms are tracers of the fluid, the microorganisms velocity is exactly the interpolated velocity at the particle position: $u'_{p,i} = u'_{f@p,i}$ and the values for Lagrangian quantities averaged over the particles for the fluid are very close to the Eulerian quantities as we can see in table 4.4. The small discrepancies are explained by the interpolation scheme. The Reynolds decomposition is then applied to the uptake rate and a statistical analysis is performed for the different two-phase simulations. The forthcoming results are given for the Monod assimilation model. Table 4.5 summarises the statistics for the different two-phase simulations. [5]

Table 4.4: Fluid statistics at the particle position - Dynamic properties of the dispersed phase.

	$R1$	$R2$	$G2$
$\frac{q^2_{f@p}}{q^2_f}$	0.999	0.996	0.996
$\frac{q^2_{s,f@p}}{q^2_{s,f}}$	0.998	0.993	0.994
$\frac{\langle u'_{f@p} s'_{@p} \rangle}{\langle u'_f s' \rangle}$	1.15	1.02	1.02
$\frac{\langle v'_{f@p} s'_{@p} \rangle}{\langle v'_f s' \rangle}$	1.00	0.96	1.00
$\frac{\langle w'_{f@p} s'_{@p} \rangle}{\langle w'_f s' \rangle}$	1.34	1.00	1.10

---

[5] The presented statistic all refer to the non-dimensionalised uptake rate $\Phi^* = \Phi/\Phi_{max}$. The averaged and fluctuating uptake rate are non-dimensionalised by Φ_{max} as well. These quantities are written with a $*$ superscript.

Table 4.5: Statistics of the biological suspension for assimilation.

k_S [$\mathrm{kg_S \cdot m^{-3}}$]	10^{-3}	$5 \cdot 10^{-3}$	10^{-2}	$5 \cdot 10^{-2}$	10^{-1}	$5 \cdot 10^{-1}$	1	5	10^{1}	$5 \cdot 10^{1}$	10^{2}	$5 \cdot 10^{2}$
R1M												
$\langle \phi'^{*2} \rangle_p$ [−]	$5.54 \cdot 10^{-6}$	$1.20 \cdot 10^{-4}$	$3.91 \cdot 10^{-4}$	$3.45 \cdot 10^{-3}$	$5.14 \cdot 10^{-3}$	$2.43 \cdot 10^{-3}$	$9.78 \cdot 10^{-4}$	$6.00 \cdot 10^{-5}$	$1.60 \cdot 10^{-5}$	$6.69 \cdot 10^{-5}$	$1.69 \cdot 10^{-7}$	$6.77 \cdot 10^{-9}$
$\langle \phi'^{*} s' \rangle_p$ [$\mathrm{kg_S \cdot m^{-3}}$]	$1.75 \cdot 10^{-5}$	$8.15 \cdot 10^{-5}$	$1.34 \cdot 10^{-4}$	$4.34 \cdot 10^{-4}$	$5.34 \cdot 10^{-4}$	$3.64 \cdot 10^{-4}$	$2.63 \cdot 10^{-4}$	$5.68 \cdot 10^{-5}$	$2.98 \cdot 10^{-5}$	$6.10 \cdot 10^{-6}$	$3.08 \cdot 10^{-6}$	$6.13 \cdot 10^{-7}$
$\langle \phi'^{*} v' \rangle_p$ [$\mathrm{m \cdot s^{-1}}$]	$-3.81 \cdot 10^{-5}$	$-1.76 \cdot 10^{-4}$	$-3.28 \cdot 10^{-4}$	$-9.46 \cdot 10^{-4}$	$-1.16 \cdot 10^{-3}$	$-7.94 \cdot 10^{-3}$	$-5.05 \cdot 10^{-4}$	$-1.24 \cdot 10^{-4}$	$-6.48 \cdot 10^{-5}$	$-1.33 \cdot 10^{-5}$	$-6.69 \cdot 10^{-6}$	$-1.33 \cdot 10^{-6}$
$R2S_{0.15}M$												
$\langle \phi'^{*2} \rangle_p$ [−]	$5.27 \cdot 10^{-6}$	$1.15 \cdot 10^{-4}$	$3.91 \cdot 10^{-4}$	$3.36 \cdot 10^{-3}$	$4.98 \cdot 10^{-3}$	$2.38 \cdot 10^{-3}$	$9.55 \cdot 10^{-4}$	$5.88 \cdot 10^{-5}$	$1.55 \cdot 10^{-5}$	$6.53 \cdot 10^{-7}$	$1.64 \cdot 10^{-7}$	$6.59 \cdot 10^{-9}$
$\langle \phi'^{*} s' \rangle_p$ [$\mathrm{kg_S \cdot m^{-3}}$]	$1.55 \cdot 10^{-5}$	$7.27 \cdot 10^{-5}$	$1.34 \cdot 10^{-4}$	$3.91 \cdot 10^{-4}$	$4.76 \cdot 10^{-4}$	$3.24 \cdot 10^{-4}$	$2.05 \cdot 10^{-4}$	$5.10 \cdot 10^{-5}$	$2.62 \cdot 10^{-5}$	$5.38 \cdot 10^{-5}$	$2.70 \cdot 10^{-6}$	$5.12 \cdot 10^{-7}$
$\langle \phi'^{*} v' \rangle_p$ [$\mathrm{m \cdot s^{-1}}$]	$-7.06 \cdot 10^{-5}$	$-3.30 \cdot 10^{-4}$	$-6.09 \cdot 10^{-4}$	$-1.78 \cdot 10^{-3}$	$-2.16 \cdot 10^{-3}$	$-1.49 \cdot 10^{-3}$	$-9.43 \cdot 10^{-4}$	$8.80 \cdot 10^{-6}$	$-1.21 \cdot 10^{-4}$	$-2.48 \cdot 10^{-4}$	$-1.25 \cdot 10^{-5}$	$-2.49 \cdot 10^{-6}$
$R2S_1M$												
$\langle \phi'^{*2} \rangle_p$ [−]	$1.66 \cdot 10^{-9}$	$4.09 \cdot 10^{-8}$	$1.60 \cdot 10^{-7}$	$3.43 \cdot 10^{-9}$	$1.14 \cdot 10^{-5}$	$8.22 \cdot 10^{-5}$	$1.04 \cdot 10^{-4}$	$3.20 \cdot 10^{-5}$	$1.13 \cdot 10^{-5}$	$6.10 \cdot 10^{-7}$	$1.59 \cdot 10^{-7}$	$6.55 \cdot 10^{-9}$
$\langle \phi'^{*} s' \rangle_p$ [$\mathrm{kg_S \cdot m^{-3}}$]	$2.67 \cdot 10^{-7}$	$1.33 \cdot 10^{-6}$	$2.34 \cdot 10^{-6}$	$1.22 \cdot 10^{-5}$	$2.24 \cdot 10^{-5}$	$6.00 \cdot 10^{-5}$	$6.76 \cdot 10^{-5}$	$3.75 \cdot 10^{-5}$	$2.23 \cdot 10^{-5}$	$5.20 \cdot 10^{-6}$	$2.66 \cdot 10^{-6}$	$5.40 \cdot 10^{-7}$
$\langle \phi'^{*} v' \rangle_p$ [$\mathrm{m \cdot s^{-1}}$]	$-1.23 \cdot 10^{-6}$	$-6.11 \cdot 10^{-6}$	$1.21 \cdot 10^{-5}$	$-5.61 \cdot 10^{-5}$	$-1.03 \cdot 10^{-4}$	$-2.76 \cdot 10^{-4}$	$-3.11 \cdot 10^{-4}$	$-1.72 \cdot 10^{-4}$	$-1.03 \cdot 10^{-4}$	$-2.40 \cdot 10^{-5}$	$1.22 \cdot 10^{-5}$	$-2.48 \cdot 10^{-6}$
G2M												
$\langle \phi'^{*2} \rangle_p$ [−]	$5.39 \cdot 10^{-8}$	$1.32 \cdot 10^{-6}$	$5.18 \cdot 10^{-6}$	$1.08 \cdot 10^{-4}$	$3.51 \cdot 10^{-4}$	$2.28 \cdot 10^{-3}$	$2.75 \cdot 10^{-3}$	$8.00 \cdot 10^{-4}$	$2.83 \cdot 10^{-4}$	$1.53 \cdot 10^{-5}$	$3.97 \cdot 10^{-6}$	$1.64 \cdot 10^{-7}$
$\langle \phi'^{*} s' \rangle_p$ [$\mathrm{kg_S \cdot m^{-3}}$]	$8.20 \cdot 10^{-6}$	$4.06 \cdot 10^{-5}$	$8.05 \cdot 10^{-5}$	$3.67 \cdot 10^{-4}$	$6.61 \cdot 10^{-4}$	$1.68 \cdot 10^{-3}$	$1.83 \cdot 10^{-3}$	$9.81 \cdot 10^{-4}$	$5.82 \cdot 10^{-4}$	$1.35 \cdot 10^{-4}$	$6.91 \cdot 10^{-5}$	$1.40 \cdot 10^{-5}$
$\langle \phi'^{*} v' \rangle_p$ [$\mathrm{m \cdot s^{-1}}$]	$7.50 \cdot 10^{-6}$	$-3.72 \cdot 10^{-5}$	$-7.39 \cdot 10^{-5}$	$-3.36 \cdot 10^{-4}$	$-6.03 \cdot 10^{-4}$	$-1.54 \cdot 10^{-3}$	$-1.69 \cdot 10^{-3}$	$-9.05 \cdot 10^{-4}$	$-5.33 \cdot 10^{-4}$	$-1.24 \cdot 10^{-4}$	$-6.34 \cdot 10^{-5}$	$-1.28 \cdot 10^{-5}$

Further simulations were performed with the Monod assimilation model in order to scrutinise the effects of dynamics and mixing on the assimilation for a population of microorganisms. On the one hand, the effect of the dynamics of the flow is obtained by comparison of simulations $R1M$ and $R2S_{0.15}M$, whereas the mixing effect is given by comparison of both $R2M$ and $G2M$. On the other hand, the results presented in section 4.4.1 show the influence of the ratio comparing the fluctuations amplitude to the average concentration for a given flow dynamic and mixing.

Figure 4.5 displays the averaged uptake rate for all simulations with Monod assimilation model compared to the uptake rate based on the average concentration. Even if the discrepancies are not striking, we can see an influence of the mixing for intermediate affinity constant, especially within the range of $< S >_p \simeq k_S$. Moreover by comparing both simulations $R1M$ and $R2S_{0.15}M$, we can see that flow dynamics do not seem to influence the assimilation rate. In order to quantify the differences between both $\langle \Phi \rangle_p$ and $\Phi(\langle S \rangle)$ the deviation ξ is shown by Figure 4.6. Indeed, the flow dynamics is found not to influence the assimilation rate for the chosen simulation parameters. An other striking result is the deviation evolution with respect to the affinity constant. The deviation is maximum for $\langle S \rangle \equiv k_S$. Besides, the smaller the mean substrate concentration, the higher the deviations to the Monod macroscopic assimilation law. A factor 10^3 is observed for the maximum deviation between both simulations $R2S_1M$ and $G2M$ accounting for the strong influence of mixing on assimilation at population scale.

Concerning the flow dynamics, we can see that both simulations $R1M$ and $R2S_{0.15}M$ give similar results, so that the flow dynamics do not seem to influence the assimilation. If we look at Table 3.2 we can see that the substrate concentration variance for both simulations $R1$ and $R2$ is similar, and confirms the effect of mixing on the uptake rate assimilation. Nevertheless, the scalar dissipation rate differs for the two simulations meaning that the uptake rate is not sensitive to the scalar dissipation.

The uptake rate variance $\langle \phi'^{*2} \rangle$ has been calculated for each class of particles and various affinity constants and figure 4.7 shows the dependencies of the uptake rate variance to the average concentration $\langle S \rangle_p$ and substrate variance $< s'^2 >$. The uptake rate variance presents a maximum for all simulations at $k_S = \langle S \rangle_p$. Moreover, if we look at figure 4.6, we can see that the results are similar for the different simulations. For simulation $R2S_1M$ the uptake rate variance is lower than for the other simulations. This result was expected considering the small discrepancies between $\langle \Phi \rangle_p$ and $\Phi(\langle S \rangle_p)$.

If we now look at figure 4.7b, it is interesting to remark that for large k_S, all the simulations present the same uptake rate variance evolution. The representation is given in log-log scale, therefore a power law of the form:

$$\langle \phi'^{*2} \rangle_p = b \left(\langle s'^2 \rangle^{1/2} / k_S \right)^a , \tag{4.15}$$

can be deduced where a and b are the power law parameters to be fitted. For small affinity constants, the uptake rate variance evolution seems to evolve in a similar manner for all simulations. And the peaks of uptake rate variance range from $k_S = 0.01 \langle s'^2 \rangle^{1/2}$ for simulation $R2S_1M$ to about $k_S = 0.5 \langle s'^2 \rangle^{1/2}$ for both simulations $R2S_{0.15}M$ and $R1M$. The decrease of $< \phi'^{*2} >_p$ could thus be determined from a power law (see equation (4.15), where the exponent a is negative and the constant b differs from one simulation to another.

The cross-correlation $\langle \phi'^{*} s' \rangle_p$ is then studied. We can see in figure 4.8 that for any class of particle, the non-dimensional[6] cross-correlations are almost constant for large constant affinity and fluctuate for smaller k_S. For the simulation $R1$, the evolution is the same than for all simulations, but the value is around 5% higher than for simulation $R2S_{0.15}M$. Surprisingly, the flow dynamics has an

---

[6] by $\sqrt{< s'^2 >_p < \phi'^{*2} >_p}$.

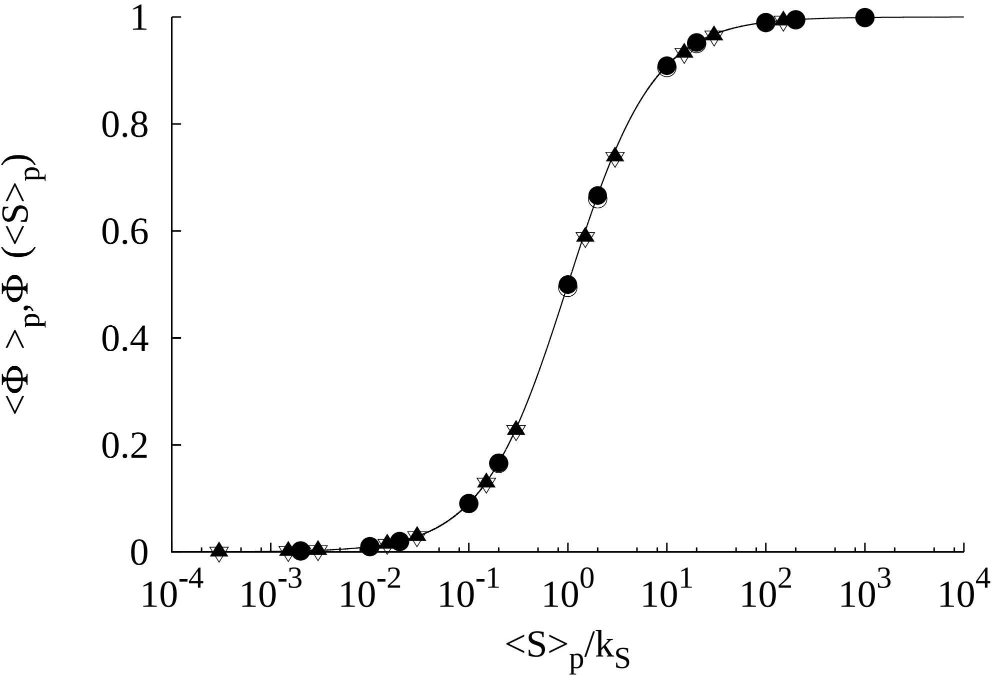

Figure 4.5: Non-dimensionalised average uptake rate $< \phi >_p$ for Monod assimilation model with respect to the dimensionless ratio $< S >_p /k_S$ for the simulations $R2S_1M$: • and $R2S_{0.15}M$: ▲, $R1M$: ▽, $G2M$: ○.

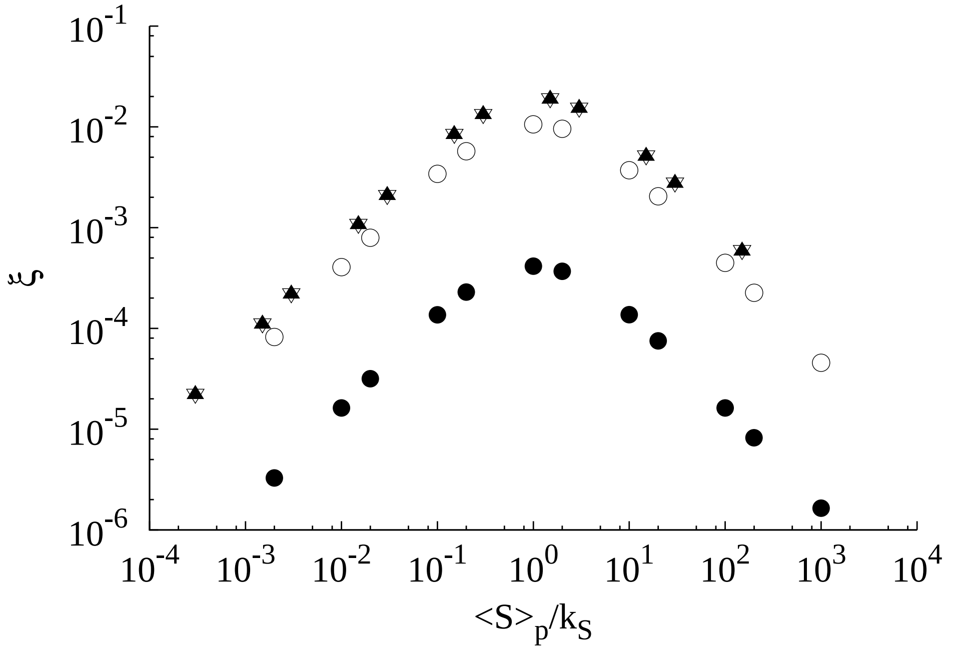

Figure 4.6: Deviation from the average uptake rate $< \phi >_p$ to the uptake rate based on average substrate concentration for Monod assimilation model with respect to the dimensionless ratio $< S >_p /k_S$ for the different simulations $R2S_1M$: • and $R2S_{0.15}M$: ▲, $R1M$: ▽, $G2M$: ○.

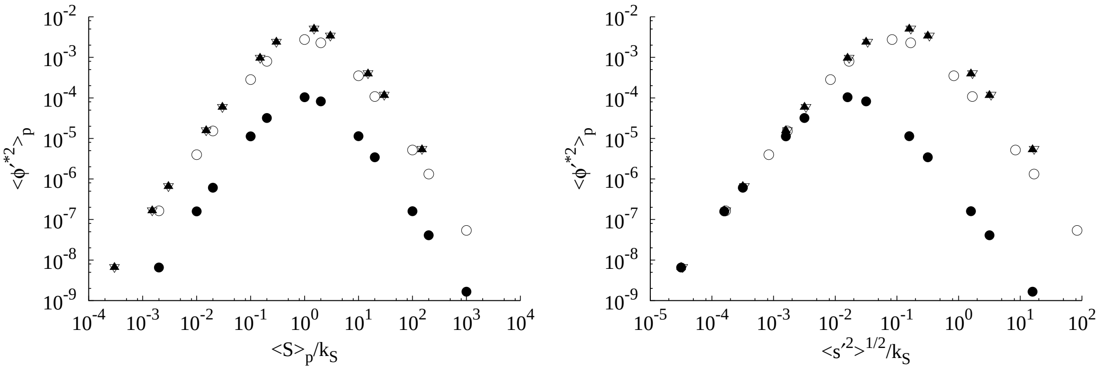

(a) Evolution of the uptake rate variance with respect to the ratio: $< S >_p / k_S$.

(b) Evolution of the uptake rate variance with respect to the ratio: $< s'^2 >^{1/2} / k_S$.

Figure 4.7: Uptake rate variance $< \phi'^{*2} >_p$ for Monod assimilation model with respect to the dimensionless ratio $< S >_p / k_S$ (left) and $< s'^2 >^{1/2} / k_S$ for the simulations $R2S_1M$: • and $R2S_{0.15}M$: ▲, $R1M$: ▽, $G2M$: ○.

effect on the substrate concentration-uptake rate correlation. It is also expected that the velocity-uptake rate correlations depends on the flow dynamics and thus on the Reynolds number of the flow. This result is discussed hereafter.

Firstly, as we can see in figure 4.9, the same conclusions arise for the velocity-uptake rate cross-correlation as for the velocity-scalar flux: the component in the y-direction is negative and its amplitude is around ten times bigger than for the other directions. Moreover, the above comment on the flow dynamics is verified by confronting the results between $R2S_{0.15}M$ (▲) and $R2S_1M$ (•). For the simulations with $Re_\Lambda = 110$, the results are almost identical, and no effect of the mean concentration is observed. By comparing simulations $R2S_{0.15}M$ (▲) and $R1M$ (▽), the Reynolds number effect is important and the amplitudes of the cross-correlations are bigger for a smaller Reynolds-number flow. If we look at the symbols from simulation $G2M$, we can see that for a same velocity field, the substrate concentration variance modifies the velocity-uptake cross-correlations, accounting for a direct effect of mixing.

4.4.3 A posteriori validation of simulations

Monod assimilation model

Using the Monod assimilation model, it is possible to find an analytical expression for the average uptake rate from its Reynolds decomposition. Indeed, from the Monod model definition at one particle position $\mathbf{x}_p$ we have (from equation (4.6)):

$$\Phi_p = \Phi_{max} \frac{S_{@p}}{k_S + S_{@p}}, \tag{4.16}$$

with $S_{@p} = S_0 + s'_{@p} + \underline{\zeta}(y_p - L_{box}/2)$ and $S_0 = \langle S \rangle_p$. By replacing $S_{@p}$ in equation (4.16) and by averaging over all the particles, the following expression is obtained for the average uptake rate:

$$\langle \Phi^* \rangle_p = \frac{\langle S \rangle_p}{\langle S \rangle_p + k_S} - \frac{\langle \phi' s' \rangle_p}{\langle S \rangle_p + k_S} - \zeta \frac{\langle \phi' y \rangle_p}{\langle S \rangle_p + k_S}, \tag{4.17}$$

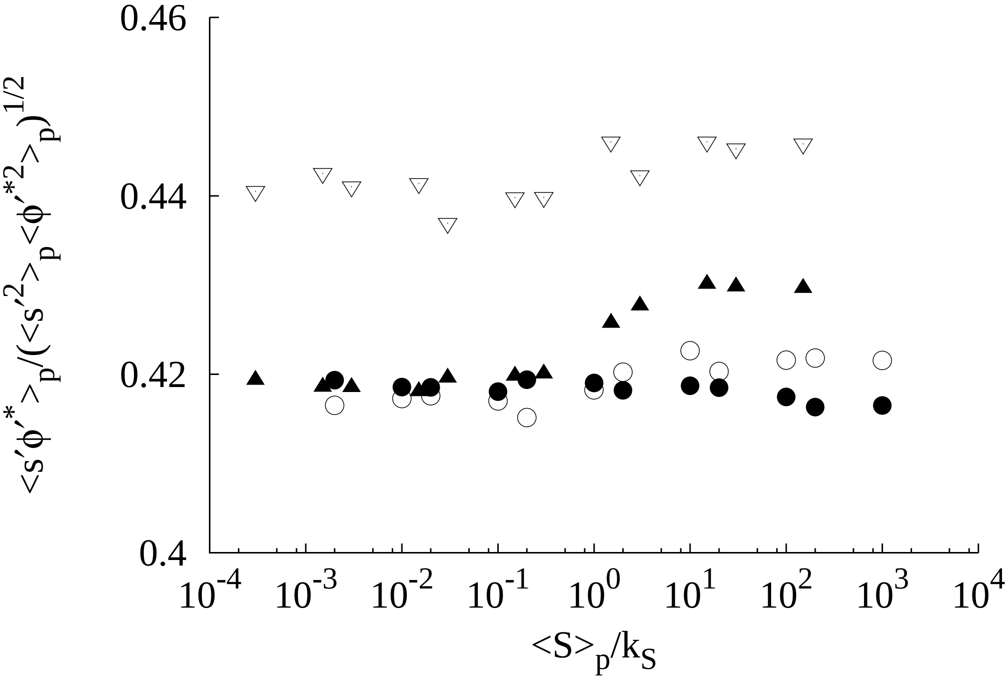

Figure 4.8: Evolution of the normalised cross-correlation $< \phi'^{*} s' >_p$ for Monod assimilation models with respect to the dimensionless ratio $< S >_p / k_S$ for the simulations $R2S_1M$: • and $R2S_{0.15}M$: ▲, $R1M$: ▽, $G2M$: ○.

where both ϕ' and y_p are correlated because of the configuration of the flow with the imposed substrate gradient.

The first part of equation (4.17) is the Monod uptake rate based on the average concentration, the middle term yields for the cross-correlation between substrate concentration and uptake rate and finally the last term accounts for the gradient contribution. The parameter ξ previously defined to evaluate the difference between $\langle\Phi\rangle$ and $\Phi(\langle S\rangle_p)$ must then be equal to:

$$\xi_{Monod} = -\frac{\langle\phi' s'\rangle_p + \zeta\langle\phi' y\rangle_p}{\langle S\rangle_p}. \tag{4.18}$$

Both ξ and ξ_{Monod} are shown by Figure 4.10, and they perfectly match for each simulation. This result validates the DNS calculations and shows the dependence of the average uptake rate to the concentration-uptake rate correlation.

Conclusion

Using the Monod assimilation model at the microscopic scale, different statistics for the microorganisms have been computed. The analysis shows that the determination of the macroscopic uptake rate based on the microscopic affinity constant is a good approximation in this configuration, but small deviations are observed, especially for intermediate affinity constants. The deviations are coming from the substrate concentration-uptake rate cross-correlation, which is intuitively non-zero. The imposed gradient also impacts the uptake rate at the microorganisms scale, but due to the non-linearity of biological assimilation, despite a zero mean contribution of the gradient, the

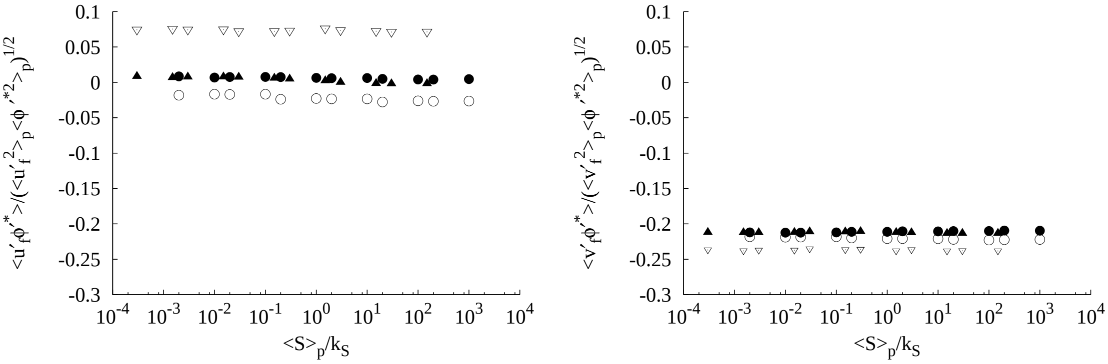

(a) $< \phi'^{*} u' >_p$

(b) $< \phi'^{*} v' >_p$

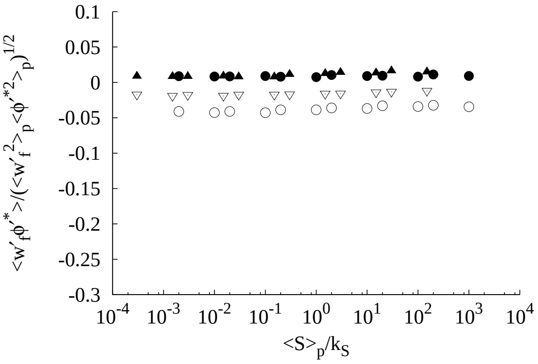

(c) $< \phi'^{*} w' >_p$

Figure 4.9: Evolution of the normalised cross-correlation $< \phi'^{*} u'_i >_p$ for Monod assimilation model with respect to the dimensionless ratio $< S >_p / k_S$ for the simulations $R2S_1M$: • and $R2S_{0.15}M$: ▲, $R1M$: ▽, $G2M$: ○.

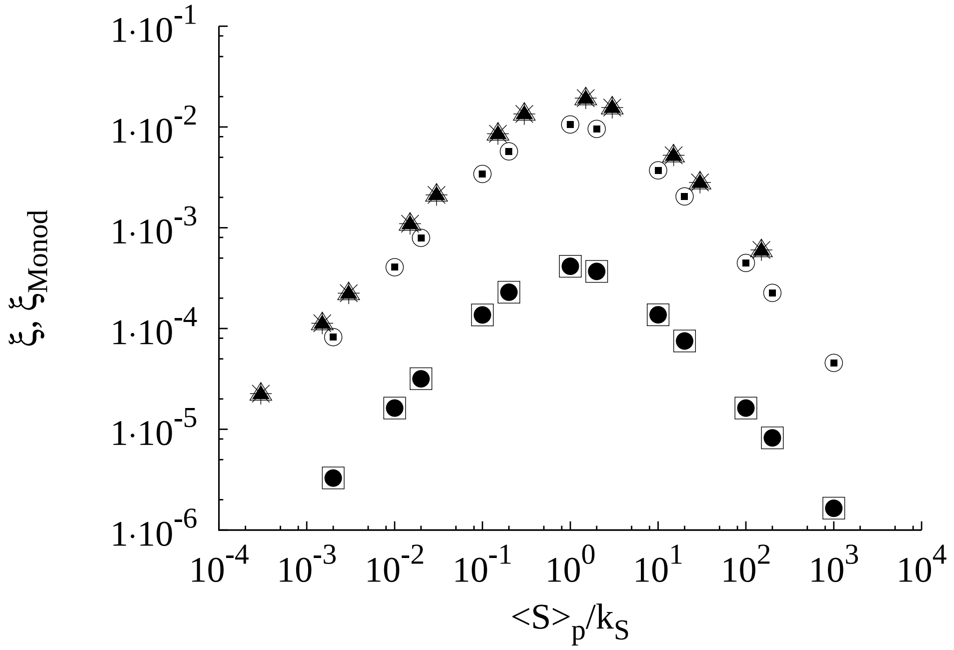

Figure 4.10: Comparison of the deviation from the DNS and the theoretical difference from the average for Monod assimilation model with respect to the dimensionless ratio $\langle S\rangle_p/k_S$ for the different two-phase simulations. The filled symbols and + are for ξ and the theoretical difference is given by the empty symbols and ×. $R2S_1M$: • and $R2S_{0.15}M$: ▲, $R1M$: + , $G2M$: ▫.

macroscopic effect on the overall assimilation can be non-negligible. This last result is of prime importance in the study of a bioreactor where the assimilation create substrate gradients (Bylund et al., 1998), but as shown in the present work, the substrate concentration gradients directly impact the assimilation even for a relatively well micro-mixed vessel. From this first conclusion, we decided to study the trajectory of one microorganism in the computational domain in order to investigate the influence of substrate concentration fluctuations on the assimilation rate of the microorganism.

4.4.4 Microscopic tracking of one microorganism

Previous results are given in terms of average over the microorganisms population. We show here the microscopic values of substrate concentration and uptake rate along one microorganism trajectory for different populations.

First the total and fluctuating substrate concentrations along the microorganism path are shown for different simulations in Figure 4.11. The total substrate concentration seen by one microorganism is given as a solid line and refers to the left axis, whereas the fluctuating concentration is represented as a dotted line on the right axis. As shown by both Figures 4.11a and 4.11b, the fluctuations have the same magnitude for both simulations $R2S_{0.15}M$ and $R2S_1M$ but, the total concentration is different. Indeed, the ratio s'/S is higher for simulation $R2S_{0.15}M$.

The instantaneous concentration seen by one microorganism along its trajectory is given in solid line by Figure 4.11a and 4.11b for simulations $R2S_{0.15}M$ and $R2S_1M$ respectively. We may remind that the total substrate concentration is written: $S_{@p} = S_0 + s'_{@p} + \zeta(y_p - L_{box}/2)$. For both simulations, the concentration fluctuations seen by the microorganism are of same order, but the ratio $s'_{@p}/S_{@p}$

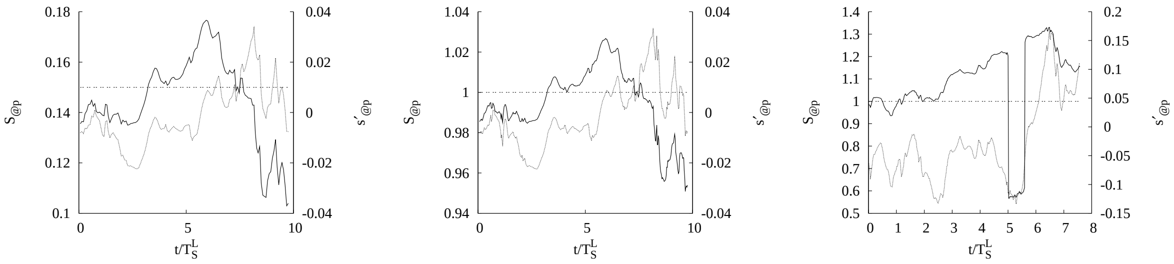

(a) $R2_S0.15M$.

(b) $R2_S1M$.

(c) $G2M$.

Figure 4.11: Fluctuating (········) and total substrate concentrations (———) along one microorganism trajectory for simulations $R2_S0.1M$ (a) and $R2S_1M$ (b) and $G2M$ (c). The mean substrate concentration $\langle S\rangle$ is represented by (- - - -).

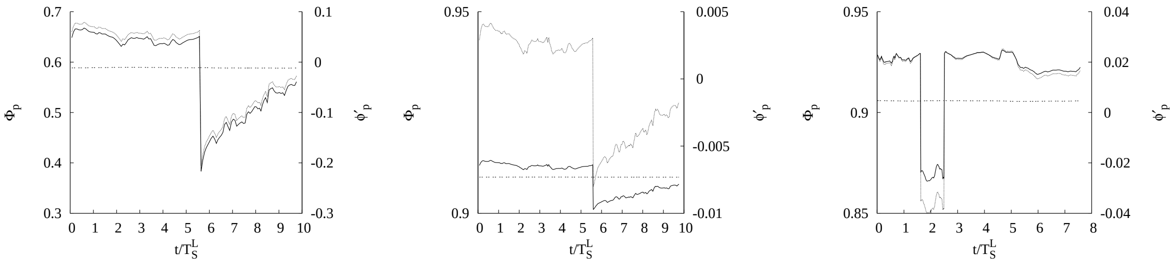

(a) $R2_S0.15M$.

(b) $R2_S1M$.

(c) $G2M$.

Figure 4.12: Fluctuating (········) and total (———) assimilation rate for one microorganism along its trajectory for simulations $R2_S0.1M$ (a) and $R2S_1M$ (b) and $G2M$ (c) with $k_S = 0.1\ \mathrm{kg_S \cdot m^{-3}}$. The averaged uptake rate over the population $\langle\Phi^*\rangle_p$ is represented by (- - - -).

is higher for simulation $R2S_{0.15}M$. The same representation is given for the simulation $G2M$ where the fluctuations are higher than for the simulations $R2$. The sudden change in $S_{@p}$ corresponds to the passage of the microorganism from the bottom to the top of the computational domain and the discontinuity is due to the imposed substrate gradient. We may check here that the fluctuating concentration is not affected by this change as periodic boundary conditions are used.

Then, the total Φ^*_p and fluctuating ϕ'^*_p uptake rate for one microorganism are represented by the solid and dotted line respectively in Figure 4.12 in the case of $k_S = 0.1\ \mathrm{kg_S \cdot m^{-3}}$. The fluctuation ϕ'^*_p is derived from the decomposition over the microorganisms population: $\phi'^*_p = \Phi^*_p = \langle\Phi'^*\rangle_p$. The averaged uptake rate is reported in dashed line. First, we can see that the microorganisms are sensitive to the boundary conditions in the simulation. Indeed, the uptake rate is based on $S_{@p}$, therefore, when one microorganism goes out of the domain at $y = L_{box}$ and is reinjected at $y = 0$, the gradient contribution influences both the total and fluctuating assimilation rate. Moreover, if we compare Figures 4.12a and 4.12b, the amplitude of fluctuations are higher for the lower averaged substrate concentration. In view of the macroscopic results, this observation was expected at the microscopic scale.

The same results are given for a larger affinity constant $k_S = 0.5\ \mathrm{kg_S \cdot m^{-3}}$ in Figure 4.13. This time, the fluctuations are stronger for the two simulations with $\langle S\rangle = 1\ \mathrm{kg_S \cdot m^{-3}}$. This shows the impact of the ratio $k_S/\langle S\rangle$ in the simulations. As we introduced in the previous section, deviations to the macroscopic assimilation law are observed for a population of microorganisms, especially for $\langle S\rangle = k_S = 1$. If we tackle the problem from microscopic point of view, we can see that the

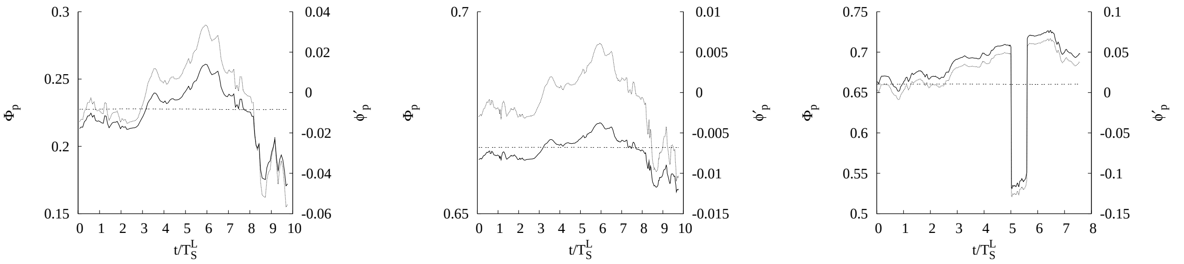

(a) $R2_S0.15M$.

(b) $R2_S1M$.

(c) $G2M$.

Figure 4.13: Fluctuating (········) and total (——) assimilation rate for one microorganism along its trajectory for simulations $R2_S0.1M$ (a) and $R2S_1M$ (b) and $G2M$ (c) with $k_S = 0.5\ \mathrm{kg_S \cdot m^{-3}}$. The averaged uptake rate over the population $\langle \Phi^* \rangle_p$ is represented by (----).

microorganisms encounter fluctuations in substrate concentration along their trajectories. As we pointed out in chapter 2, these fluctuations at the microorganism scale are of prime importance on the assimilation. Indeed, this statistical study at one microorganism scale, can also be envisaged in terms of temporal averages for the considered microorganism. With the ergodicity theorem, both ensemble and temporal averages are equivalent for sufficient large times or microorganisms number. Meaningly $\langle \Phi^* \rangle_p \equiv \overline{\Phi^*(t)}$ for the microorganism. In both cases the observed fluctuations to the average assimilation rate will directly impact the metabolite production. As previously observed, the general law for assimilation based on the average uptake rate $\langle S \rangle$ or $\overline{S}$ is almost verified, but, the microscopic effects lead to different metabolisms.

The next step in characterising the biological suspension is to look at the distributions at the individual scale and to analyse the different distributions. In so doing, the next section is devoted to the Probability Density Function (PDF) analysis for the uptake rate.

4.5 Probability density functions for uptake rate

4.5.1 Effect of substrate affinity on the uptake distribution

In the case of simulation $R2S_1M$, we present here the results for 3 classes of microorganisms with low, moderate and high affinity to the substrate. Namely, the results for the three populations with $k_S = 10^{-3}\ \mathrm{kg_S \cdot m^{-3}}$, $k_S = 10^{-1}\ \mathrm{kg_S \cdot m^{-3}}$ and $k_S = 10^{2}\ \mathrm{kg_S \cdot m^{-3}}$ will be investigated. Firstly, no effect of the flow dynamics nor mixing is considered. The substrate concentration PDF for the three populations are given in figure 4.14. As expected, the distributions are similar for each population and match the one-point PDF for substrate as seen in section 3.3.5. We will further analyse this result.

The normalised PDF of the uptake rate fluctuations is given by figure 4.15a for the three aforementionned affinity constants. We can see that for high affinity to the substrate ($k_S = 10^{-3}\ \mathrm{kg_S \cdot m^{-3}}$), the PDF is very narrow compared to the other affinity constants. In the case of intermediate affinity to the substrate, the PDF is very spread. The figure 4.15b presents the PDF normalised by the uptake rate variance root-square, in order to approach the shapes of the PDFs. We can see that the three shapes for the PDF are very similar and that the value of k_S is very important. Moreover, as we can see, the shapes of these PDF are very close to the distribution of $S_{@p}$, but the strongest deviation is for $k_S \gg \langle S \rangle$.

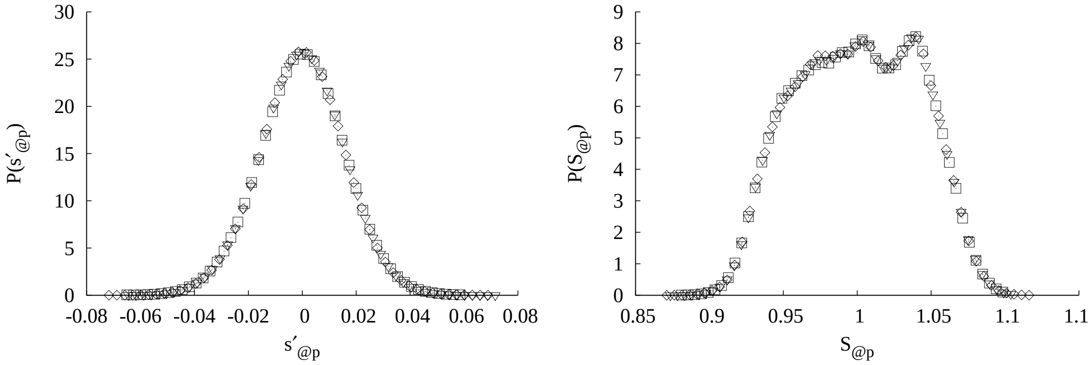

(a) Normalised PDF of the fluctuating substrate concentration.

(b) Normalised PDF of the total concentration.

Figure 4.14: PDF of the substrate concentration for different affinity constants. $k_S = 10^{-3}$ $\mathrm{kg_S \cdot m^{-3}}$: ◇, $k_S = 10^{-1}$ $\mathrm{kg_S \cdot m^{-3}}$: ▽ and $k_S = 10^2$ $\mathrm{kg_S \cdot m^{-3}}$: □.

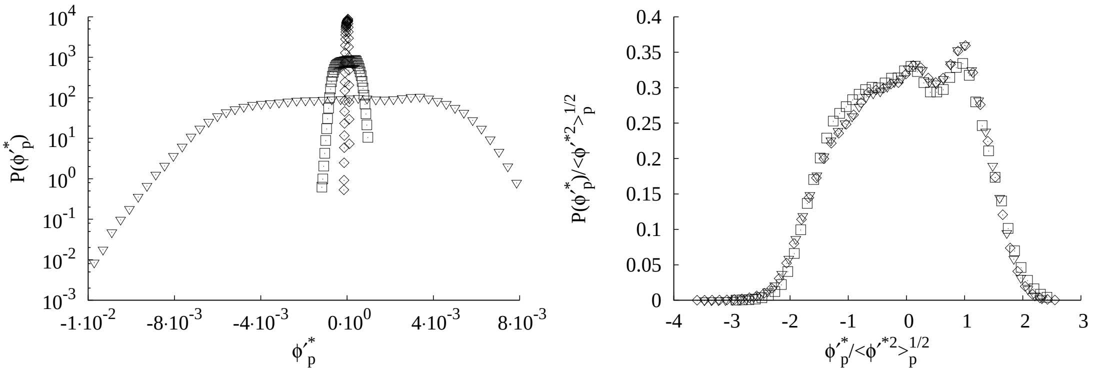

(a) Normalised PDF of the fluctuating part of the uptake rate.

(b) Normalised PDF of the fluctuating part of the uptake rate.

Figure 4.15: PDF of the uptake rate fluctuation for different affinity constants. $k_S = 10^{-3}$ $\mathrm{kg_S \cdot m^{-3}}$: ◇, $k_S = 10^{-1}$ $\mathrm{kg_S \cdot m^{-3}}$: ▽ and $k_S = 10^2$ $\mathrm{kg_S \cdot m^{-3}}$: □.

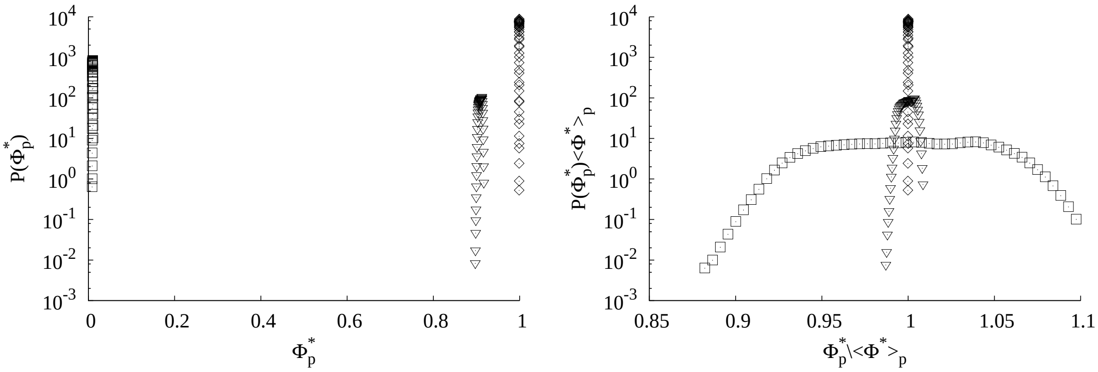

(a) Normalised PDF of the instantaneous uptake rate.

(b) Normalised PDF of the instantaneous uptake rate.

Figure 4.16: PDF of the uptake rate fluctuations for different affinity constants: $k_S = 10^{-3}$ $\mathrm{kg_S \cdot m^{-3}}$: ◇, $k_S = 10^{-1}$ $\mathrm{kg_S \cdot m^{-3}}$: ▽ and $k_S = 10^{2}$ $\mathrm{kg_S \cdot m^{-3}}$: □.

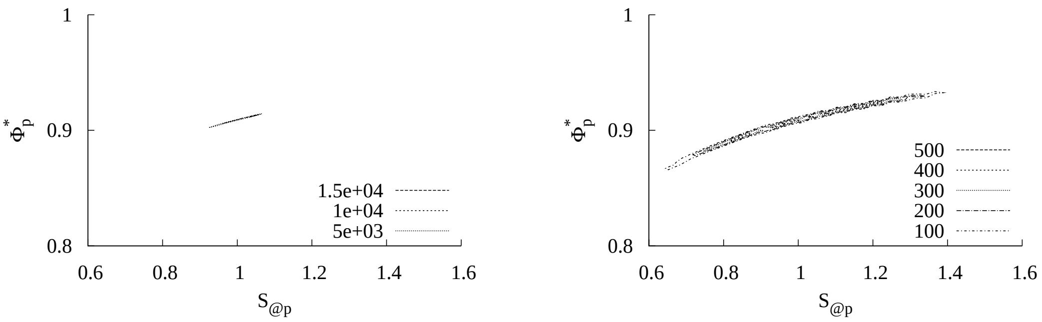

(a) $R2S_1M$

(b) $G2M$

Figure 4.17: Contours of the total substrate concentration-uptake rate joined -PDF for simulations $R2S_1M$ (a) and $G2M$ (b) for $k_S = 0.1 \mathrm{kg_S \cdot m^{-3}}$.

The distributions of the total uptake rate $\Phi_p = \Phi(S_{@p})$ are given by figure 4.16a in semi-log representation. Depending on the affinity to the substrate, the distributions are localised around the average uptake rate value. Figure 4.16b presents the normalised PDF, by the average mass flux, for the total uptake rate. The same conclusions are found than for the fluctuating uptake rate. The smaller k_S, the narrower distribution. Indeed, this result was expected because the fluctuations distribution is directly included in the total uptake rate distribution.

The joined substrate concentration-uptake rate PDFs for instantaneous and fluctuating variables $f_{S_{@p},\Phi_p^*}, f_{s'_p,\phi_p'^*}$ were computed from the DNS calculations. The contours of $f_{S_{@p},\Phi_p^*}$ are shown by Figure 4.17a and 4.17b respectively for the two simulations $R2S_1M$ and $G2M$ for the population with $k_S = 10^{-1}$ $\mathrm{kg_S \cdot m^{-3}}$. The obtained distribution is close to a hyperbolic evolution of Φ^* as a function of S with an offset of $\langle\Phi\rangle_p$ and a small spreading accounting for the concentration distribution of fluctuations. especially for the simulation $G2M$.

Concerning the joined PDF of fluctuating quantities, for $k_S \equiv \langle S \rangle$, they are ten times more spread in $\phi_p'^*$ than for high affinity constants. Whereas for small k_S the joined distribution is very narrow. It is also interesting to notice that the overall shape of the distribution is maintained for the different simulations, expect for the simulation $G2M$ with $k_S = 10^2\ \mathrm{kg_S \cdot m^{-3}}$ as seen in Figure 4.18f. This result might be explained by the direct dependency of Φ_p^* to $S_{@p}$ for large affinity constants. Therefore the stronger the fluctuations, the more spread the fluctuating assimilation rate distribution. We will now try to study the impact of flow dynamics and substrate concentration mixing on the uptake rate distribution for the biomass.

4.5.2 Effect of the flow dynamics and mixing properties on PDFs

First the PDF for the simulations $R1M$ and $R2S_{0.15}M$ are compared. Small discrepancies are observed for the fluctuating substrate concentration. In fact, the substrate variances of both simulations are very close leading to similar distributions for the substrate concentration fluctuations as seen in Figure 4.19a. Concerning the total substrate concentration distributions, we can see that both distributions present a peak. But the substrate concentration corresponding to the observed peaks are not similar for both simulations. The might be explained by the small observed deviation for the gaussian distribution of the fluctuating concentration. Nevertheless, considering the similar shape and maximum value, this distribution is totally acceptable and does not differ that much. Thus, considering these similarities for the first and second moment of substrate concentration, the flow dynamic effect can be characterised on the uptake rate distributions.

In Figures 4.19c to 4.19d it is interesting to notice that the distribution for the uptake rate fluctuations differs from one simulation to another, especially for $k_S \simeq \langle S \rangle$. Even if the shapes are similar, the maxima are not the same. Moreover, an asymmetric distribution is observed for the small and intermediate affinity constants. This asymmetric distribution is also observed for the distribution of the total uptake rate as seen in figures 4.19f and 4.19g. If we observed the former, a dirac-like distribution is obtained at the mean uptake rate $\langle \Phi^* \rangle$, and the asymmetry is observed on the left of the peak on a very small range. For large values of k_S, the obtained distribution is perfectly symmetric largely resembles the instantaneous concentration distributions. Finally, for $k_S \simeq \langle S \rangle$, the important non-symmetry for the uptake rate is at the origin of the macroscopic deviations of the mean uptake rate compared to the macroscopic assimilation law $\Phi^*(\langle S \rangle)$. Moreover, as observed in section 4.4.2, even if the effect of the flow dynamics is not directly observable, the fluctuating components for the biological phase are sensitive to the velocity field. In other words, the microorganisms see an uptake rate distribution along their trajectories. If we now consider the whole population, a mass flux distribution over the microorganisms is found. This result is shown in both Figures 4.19c and 4.19d, where the distributions of the fluctuating part of the uptake rate differ. This means that the microorganisms can be in different assimilation regimes. We will discuss this result later. Now, the effect of the concentration fluctuations and gradient contribution is scrutinised.

Now, we investigate the impact of mixing on the distribution for the microorganisms uptake rate. The results of the simulations $R2S_1M$ and $G2M$ are compared in figure 4.20. The normalised distributions of the fluctuating and total concentrations are given in figures 4.20a and 4.20b for both simulations. For the simulation $G2M$, the imposed mean gradient is larger and the fluctuations are more important than in simulation $R2S_1M$. This result can be seen on both figures where the gaussian distribution is more spread for simulation $G2M$, accounting for the bigger variance. This more spread distribution is also observable for the total substrate concentration distribution. As the uptake rate depends directly on the total concentration, more spread distributions for the uptake rate are expected.

If we look at the fluctuating part of uptake rate distributions, for different affinities to the substrate, the expected result in terms of spread distribution is not verified. Indeed, the normalised

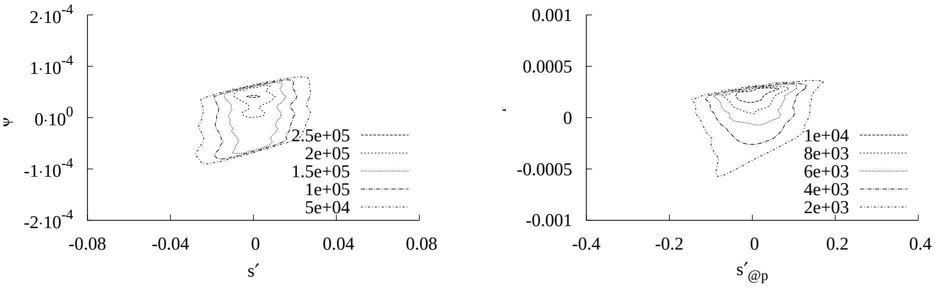

(a) $R2S_1M$, $k_S = 10^{-3} kg_S \cdot m^{-3}$

(b) $G2M$, $k_S = 10^{-3} kg_S \cdot m^{-3}$

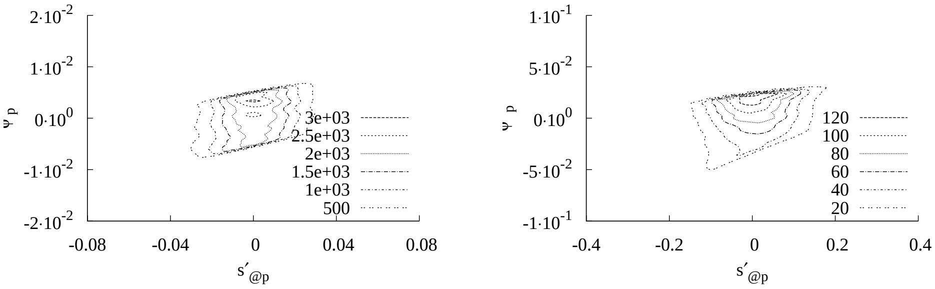

(c) $R2S_1M$, $k_S = 10^{-1} kg_S \cdot m^{-3}$

(d) $G2M$, $k_S = 10^{-1} kg_S \cdot m^{-3}$

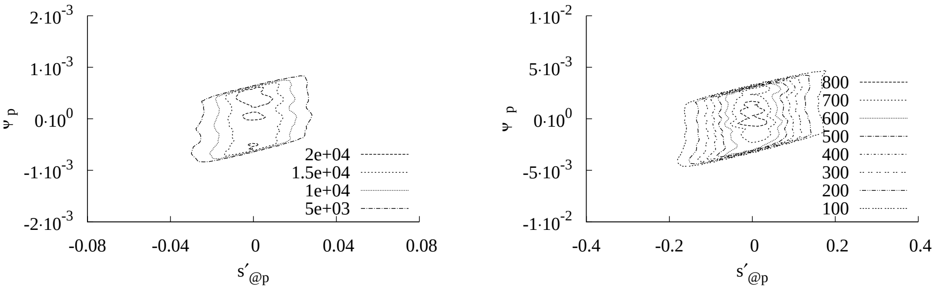

(e) $R2S_1M$, $k_S = 10^2 kg_S \cdot m^{-3}$

(f) $G2M$, $k_S = 10^2 kg_S \cdot m^{-3}$

Figure 4.18: Contours of the joined-PDF of the fluctuating variables for simulation $R2S_1M$ ((a), (c) and (e)) and for simulation $G2M$ ((b), (d)t and (f)) for different substrate affinities: $k_S = 10^{-3}$ $\mathrm{kg_S \cdot m^{-3}}$, $k_S = 10^{-1}$ $\mathrm{kg_S \cdot m^{-3}}$ and $k_S = 1 \cdot 10^2$ $\mathrm{kg_S \cdot m^{-3}}$ from top to bottom.

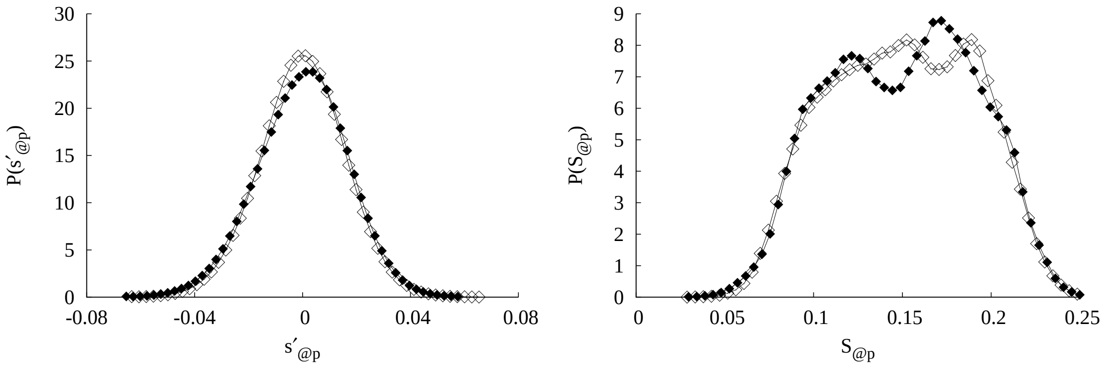

(a) $P(s'_{@p})$, $R1M$: ◆ and $R2S_{0.15}M$: ◇.

(b) $P(S_{@p})$, for simulation $R1M$: ◆ and $R2S_{0.15}M$: ◇.

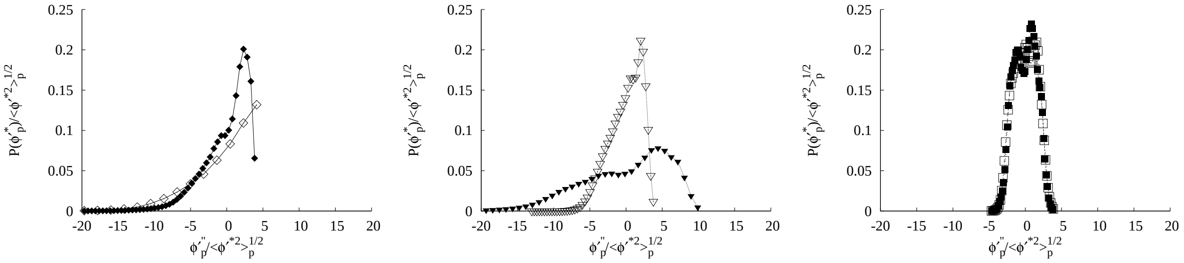

(c) Normalised $P(\phi_p'^*)/\langle\phi'^{*2}\rangle_p^{1/2}$, $k_S = 10^{-3}$ $\text{kg}_S\cdot\text{m}^{-3}$.

(d) Normalised $P(\phi_p'^*)/\langle\phi'^{*2}\rangle_p^{1/2}$, $k_S = 10^{-1}$ $\text{kg}_S\cdot\text{m}^{-3}$.

(e) Normalised $P(\phi_p'^*)/\langle\phi'^{*2}\rangle_p^{1/2}$, $k_S = 10^{2}$ $\text{kg}_S\cdot\text{m}^{-3}$.

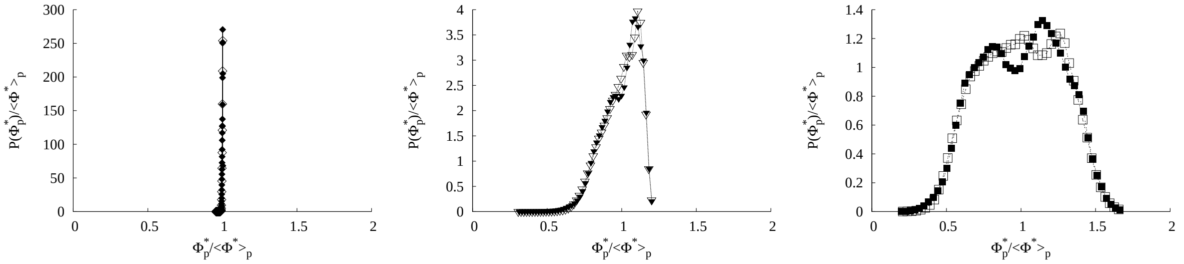

(f) Normalised $P(\Phi_p^*)/\langle\Phi^*\rangle_p$ for $k_S = 10^{-3}$ $\text{kg}_S\cdot\text{m}^{-3}$.

(g) Normalised $P(\Phi_p^*)/\langle\Phi^*\rangle_p$ for $k_S = 10^{-1}$ $\text{kg}_S\cdot\text{m}^{-3}$.

(h) Normalised $P(\Phi_p^*)/\langle\Phi^*\rangle_p$ for $k_S = 10^{2}$ $\text{kg}_S\cdot\text{m}^{-3}$.

Figure 4.19: PDF of the fluctuating (a) and instantaneous (b) concentrations seen by microorganisms for simulations $R1M$ and $R2S_{0.15}M$. Normalised distributions of uptake rate fluctuations (c) to (e) and instantaneous uptake rate (f) to (h) for different affinity constant: $k_S = 10^{-3}$ $\text{kg}_S\cdot\text{m}^{-3}$: ◇, $k_S = 10^{-1}$ $\text{kg}_S\cdot\text{m}^{-3}$: ▽ and $k_S = 10^{2}$ $\text{kg}_S\cdot\text{m}^{-3}$: ▫. The empty symbols refer to simulation $R2S_{0.15}M$ and filled symbols to simulation $R1M$.

distributions range approximately from $-5 \leqslant \phi_p'^*/\langle\phi'^{*2}\rangle_p^{1/2} \leqslant +5$ for the three populations. In the case of low affinity to the substrate ($k_S \gg \langle S\rangle$), both distributions are similar (Figure 4.20e). But, for higher affinity to the substrate, the distributions deviates from one simulation to another. Especially for the $G2M$ simulation, the distribution is non-symmetrical for the fluctuating uptake rate (Figure 4.20c). This conclusion arises again when looking at the distributions of the total uptake rate, except for $k_S \gg \langle S\rangle_p$. This non-symmetry is once again at the origin of the discrepancies on the macroscopic results for the uptake rate on both simulations. More fluctuations lead to non-symmetrical distribution of the microscopic uptake rate and decrease in the expected amount of

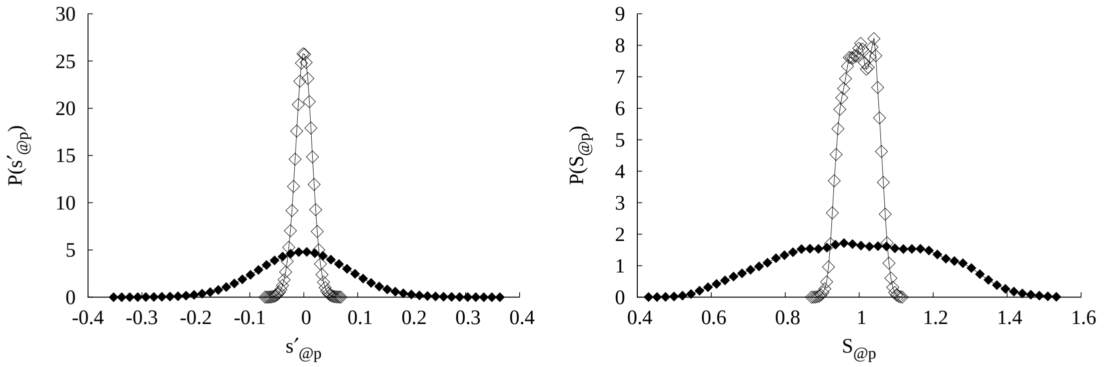

(a) $P(s')$, $G2M$: ◆ and $R2S_1M$: ◇.

(b) $P(S)$, $G2M$: ◆ and $R2S_1M$: ◇.

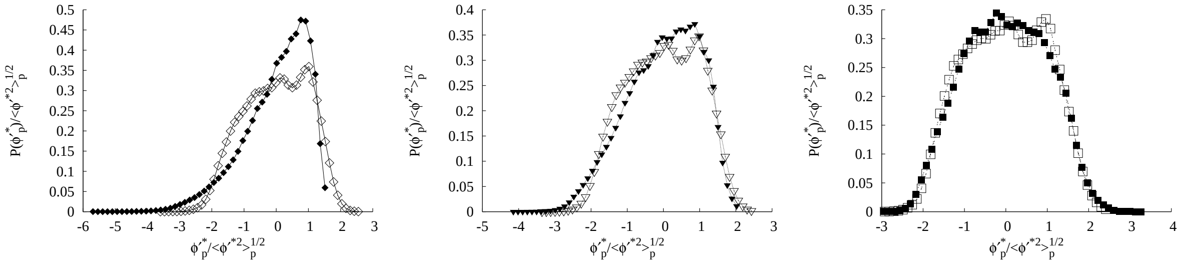

(c) Normalised $P(\phi'^*_p)/\langle\phi'^{*2}\rangle_p^{1/2}$, $k_S = 10^{-3}$ kgs · m^{-3}.

(d) Normalised $P(\phi'^*_p)/\langle\phi'^{*2}\rangle_p^{1/2}$, $k_S = 1$ kgs · m^{-3}.

(e) Normalised $P(\phi'^*_p)/\langle\phi'^{*2}\rangle_p^{1/2}$, $k_S = 10^2$ kgs · m^{-3}.

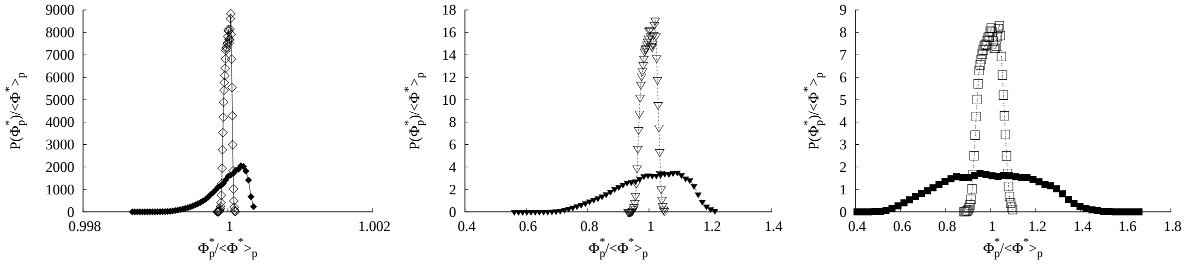

(f) Normalised $P(\Phi^*_p)/\langle\Phi^*\rangle_p$, $k_S = 10^{-3}$ kgs · m^{-3}.

(g) Normalised $P(\Phi^*_p)/\langle\Phi^*\rangle_p$, $k_S = 1$ kgs · m^{-3}.

(h) Normalised $P(\Phi^*_p)/\langle\Phi^*\rangle_p$, $k_S = 10^2$ kgs · m^{-3}.

Figure 4.20: PDF of the fluctuating (a) and total (b) concentrations seen by the microorganisms for simulations $G2M$ and $R2S_1M$. PDF of uptake rate fluctuations (c) to (e) and instantaneous uptake rate (f) to (h) for different affinity constant: $k_S = 10^{-3}$ kgs · m^{-3}: ◇, $k_S = 10^{-1}$ kgs · m^{-3}: ▽ and $k_S = 10^2$ kgs · m^{-3}: ▫. The empty symbols refer to simulation $R2S_{0.15}M$ and filled symbols to simulation $G2M$.

assimilated substrate.

Once again, the obtained distribution for the microscopic uptake rate accounts for the different state of microorganisms. Indeed, it is expected that the microorganisms with uptake rate lower than the mean uptake rate present a smaller growth than the other microorganisms. This distribution will thus directly impact the biomass growth. The same conclusions arise for the by-products formation. Indeed, due to the uptake rate distribution, the microorganisms are expected to produce different kind of by-products. The amount of by-products will also be influenced by the uptake rate distribution. For example, the microorganisms limited by the amount of substrate, will more likely be in the anabolic pathway (growth) rather than form by-products. Moreover, as observed, the

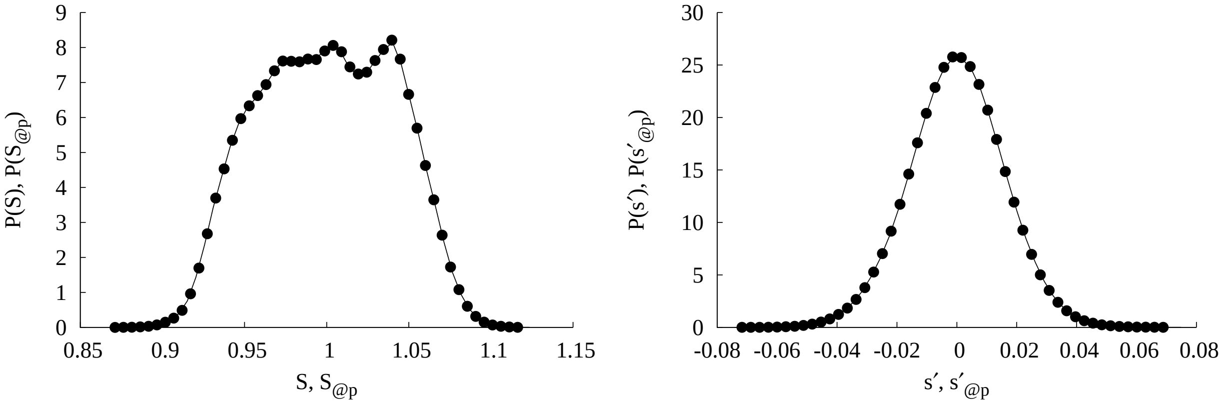

(a) Total substrate concentration

(b) Fluctuating substrate concentration

Figure 4.21: Comparison of the total substrate concentration distribution for fluid (———) and particles (•) for the simulation $R2S_1M$.

different distributions are not symmetric for the uptake rate, so that the effect of growth limitation or by-product formation will not be compensate.

Therefore, the knowledge of the uptake rate distribution for one population arises as the required parameter for the determination of biological growth for example. Moreover the uptake rate distribution will depend on the prescribed microscopic assimilation model, but, on the flow dynamics and substrate mixing as well. Furthermore, the resemblances between the total uptake rate distribution and the total substrate concentration for high affinity constants (by comparison of Figures 4.20b and 4.20h) encourages to find a relationship between both distributions. This means that from the knowledge of the substrate concentration distribution, the mass flux distribution over the microorganisms population could be derived. The further paragraphs of this work are devoted to find the analytical distributions for both S and Φ_p^*.

4.5.3 Relating PDF to fluctuating and instantaneous data

The usual approach for scalar transport in turbulent flows focuses on the scalar fluctuations PDF. The originality of this work is to consider the total substrate field because the reaction rate is based on this substrate concentration.

First, we will discuss the validity to approach the substrate concentration distribution seen by the microorganisms by the fluid substrate distribution. Indeed, we found that both distribution for the total substrate concentration are very close. Figure 4.21 shows that the distributions for the fluctuating substrate concentration are identical. This result is valid for a large number of microorganisms and because of the construction of the total substrate concentration.

The total substrate concentration is the sum of three contributions: the fluctuating concentration s', the gradient contribution and the imposed average concentration S_0 for the fluid substrate concentration. For the substrate concentration, the fluctuating concentration is interpolated at the particle position and the concentration at the particle position is obtained by summing this fluctuation and the averaged imposed concentration as well as the gradient contribution (at the particle position). The equations for both concentrations are given by:

$$S = S(\mathbf{x}, t) = S_0 + \zeta(\mathbf{x} - \frac{L_{box}}{2}) + s'(\mathbf{x}, t), \tag{4.19}$$

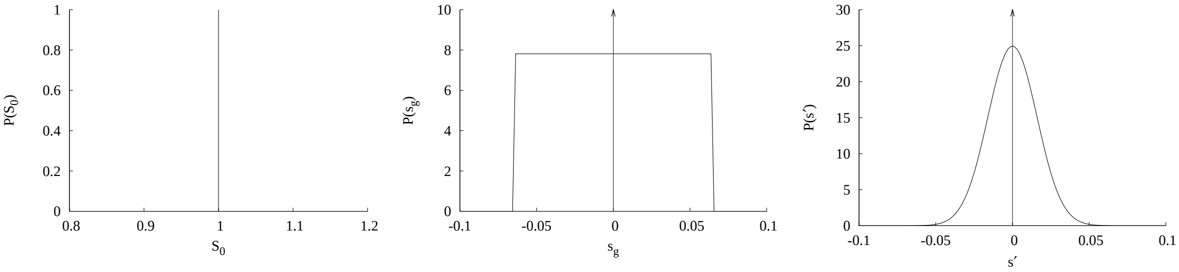

(a) $P(S_0)$: mean imposed concentration.

(b) $P(s_g)$: gradient contribution

(c) $P(s')$: fluctuation contribution

Figure 4.22: Distributions of the different substrate concentration contributions for simulation $R2S_1M$.

$$S_{@p} = S(\mathbf{x}_p, t) = S_0 + \zeta(\mathbf{x}_p - \frac{L_{box}}{2}) + s'_{@p}(\mathbf{x}_p, t). \tag{4.20}$$

The distribution of each term of both equations (4.19) and (4.20) are known. From now on, we focus on the substrate distribution of the fluid. Indeed, considering the large number of microorganisms, any discrepancies found its origin in numerical treatment error such as boundary condition or interpolation scheme. But the latter has been validated in the third chapter of this work. So, due to the statistically-steady character of the flow configuration without two-way coupling, we will now further distinguish different concentrations and just focus on the fluid substrate concentration S, s' and contribution gradient. The substrate concentration contribution from the imposed gradient is called $s_g = s_g(\mathbf{x}, t)$. The three distributions for the independent substrate concentration contribution distributions are:

Mean imposed concentration:

$$P_M(s) = \delta(s - S_0). \tag{4.21}$$

Fluctuating concentration

$$P_f(s') = \frac{1}{\sqrt{2\pi}\sqrt{\langle s'^2 \rangle}} \exp\left(-\frac{1}{2}\frac{s'^2}{\langle s'^2 \rangle}\right). \tag{4.22}$$

Gradient contribution

$$P_g(\zeta(y - \frac{L_{box}}{2})) = \begin{cases} \zeta(y - \frac{L_{box}}{2}) & \text{if } 0 \leqslant y \leqslant L_{box} \\ 0 & \text{otherwise.} \end{cases} \tag{4.23}$$

In other words, the last distribution can be written only in term of s_g:

$$P_g(s_g) = \begin{cases} \frac{1}{\zeta L_{box}} & \text{if } -\zeta\frac{L_{box}}{2} \leqslant s_g \leqslant \zeta\frac{L_{box}}{2} \\ 0 & \text{otherwise.} \end{cases} \tag{4.24}$$

The normalised distributions for the three contributions are shown in Figure 4.22 for the case of simulation $R2S_1M$. It is important to notice that the three distributions are independent. Indeed, the correlation between s' and s_g is null by construction of s'.

The fluctuation distribution is gaussian and a null mean is expected. But, as observed in Figure 3.11, the maximum of the distribution can slightly deviate from the zero mean, especially for simulations $R1$ and $R2$. The distribution of the gradient contribution is uniform and the concentration range from $-0.5\zeta L_{box}$ to $0.5\zeta L_{box}$. And finally, the imposed average concentration distribution matches a dirac at S_0.

The distribution of the total concentration is a combination of the three individual distributions. More specifically, it is defined as the convolution of the three distributions and yields:

$$P(S = S_0 + s' + s_g) = (P_M * P_f * P_g)(S). \tag{4.25}$$

This general definition will help us in the determination of the total substrate concentration S.

Let us first consider the "intermediate" substrate concentration S_1 being the contribution of S_0 and s', getting rid of the substrate concentration gradient contribution:

$$S_1 = S_0 + s'. \tag{4.26}$$

The precedent result on the distribution is applied to the substrate concentration $S1$. The obtained distribution for the substrate concentration $S1$ is thus the gaussian distribution function centred on S_0 with the same variance $\langle s' \rangle^2$:

$$\boxed{P_{S_1}(S_1) = \frac{1}{\sqrt{2\pi}\sqrt{\langle s'^2 \rangle}} \exp\left(-\frac{1}{2}\frac{(S_1 - S_0)^2}{\langle s'^2 \rangle}\right).} \tag{4.27}$$

We now consider the total concentration $S = S_0 + s' + s_g = S_1 + s_g$. Both distributions P_{S1} and P_g are convoluted in order to obtain the total concentration distribution:

$$P_S(S) = \int_{-\infty}^{+\infty} P_{S1}(S - s_g) P_g(s_g) ds_g = \frac{1}{\zeta L_{box}} \int_{-\zeta \frac{L_{box}}{2}}^{+\zeta \frac{L_{box}}{2}} P_{S_1}(S - s_g) ds_g. \tag{4.28}$$

By the mean of a variable change, the obtained expression for the total substrate concentration is:

$$\boxed{P_S(S) = \frac{1}{2\zeta L_{box}} \left[\mathrm{erf}\left(\frac{S - S_0 + \zeta L_{box}/2}{\sqrt{2\langle s'^2 \rangle}} \right) - \mathrm{erf}\left(\frac{S - S_0 - \zeta L_{box}/2}{\sqrt{2\langle s'^2 \rangle}} \right) \right]} \tag{4.29}$$

where $\mathrm{erf}(x)$ is the error function defined by:

$$\mathrm{erf}(x) = \frac{2}{\sqrt{\pi}} \int_0^x \mathrm{e}^{\frac{t^2}{2}} dt. \tag{4.30}$$

The distribution function P_S is shown by Figure 4.23 in solid lines for the parameters of simulations $R2S_1M$ and $G2M$ and they are compared with the obtained PDF for the total substrate concentration in the DNS calculation. The peak observed for the DNS calculations is not found for the analytical distribution. The origin of this peak is found in the discrete character of the computed distributions.

In conclusion, the obtained analytical distribution for the total substrate concentration is a general form that depends on the imposed gradient, the length of the domain, the mean imposed concentration and the substrate concentration variance. In other words, all information on the mixing state is included in this distribution.

Finally the knowledge of this substrate concentration distribution allows the determination of different biological properties in terms of assimilation. These results are discussed in the next paragraph.

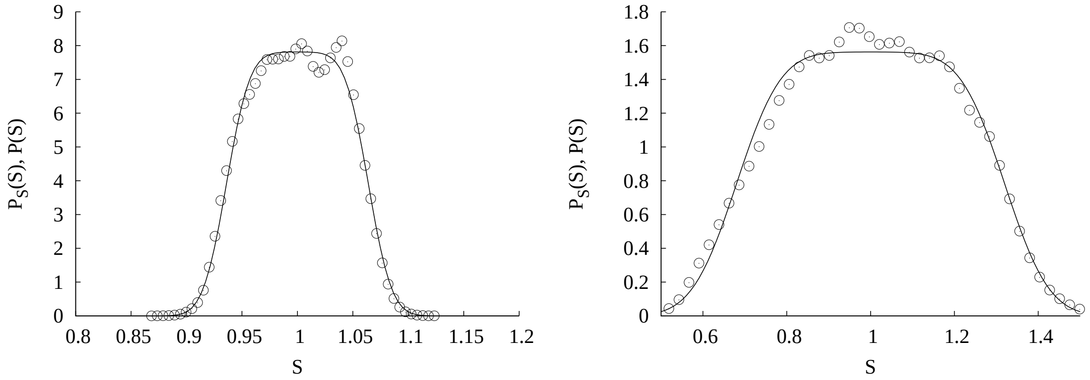

(a) $P_S(S)$ and $P(S)$ from DNS calculations for simulation $R2S_1M$.

(b) $P_S(S)$ and $P(S)$ from DNS calculations for simulation $G2M$.

Figure 4.23: Comparison of the analytical distribution for the total concentration S (———) with the distribution from DNS simulations (○) for simulations $R2S_1M$ (a) and (b).

Determination of the biological macroscopic properties from the substrate concentration distribution

For turbulent reacting flow, one of the most important statistics is the mean "chemical" source term. In our biological configuration, this term is the assimilation uptake rate Φ. The mean chemical source term is defined in terms of the one-point PDF of the scalar (equation (3.24) from Fox (2003)). In our case, it is then expected that the average uptake rate over the microorganisms yields:

$$\langle \Phi \rangle_{p,pdf} = \int_{-\infty}^{+\infty} \Phi(\varsigma) P_S(\varsigma; \mathbf{x}, t) d\varsigma, \tag{4.31}$$

where the particle uptake rate is multiplied by the PDF of the total concentration S and integrated over all values of S. The distribution of the total substrate concentration is known and the uptake rate is only dependent on S so that the averaged uptake rate can be analytically derived and thus its analytical expression yields:

$$\langle \Phi^* \rangle_{p,pdf} = \int_{-\infty}^{+\infty} \frac{S}{S+k_S} P_S(S) = \frac{1}{2\zeta L_{box}} \left[\mathrm{erf}\left(\frac{S - S_0 + \zeta L_{box}/2}{\sqrt{2\langle s'^2 \rangle}} \right) - \mathrm{erf}\left(\frac{S - S_0 - \zeta L_{box}/2}{\sqrt{2\langle s'^2 \rangle}} \right) \right]. \tag{4.32}$$

An analytical solution is not proposed here, but a numerical approximation of the integral (4.32) is possible with the knowledge of $P_S(S)$. The obtained uptake rate based on the theoretical distribution of the total substrate concentration are compared in terms of the deviation ξ_{pdf} to the total uptake rate based on the average concentration and the deviation is given in Figure 4.24.

$$\xi_{PDF} = \frac{\langle \Phi \rangle_{pdf} - \Phi \langle S \rangle_p}{\Phi \langle S \rangle_p}. \tag{4.33}$$

As observed, both figures 4.6 and 4.24 are identical. This result enlightens the validity of the determination of the average uptake rate from the substrate concentration distribution. Moreover, this property is also suitable to approach the value of the cross-correlation $\langle s' \phi'^* \rangle_p$ for the different steady-simulations. Indeed, based on equation (4.17), if we consider a gaussian distribution for the substrate concentration (see equation (4.27)), the following relationship is found for the uptake rate-substrate concentration cross-correlation:

$$\langle s' \phi'^* \rangle_p = \langle S \rangle - \langle \Phi^* \rangle_p (\langle S \rangle + k_S). \tag{4.34}$$

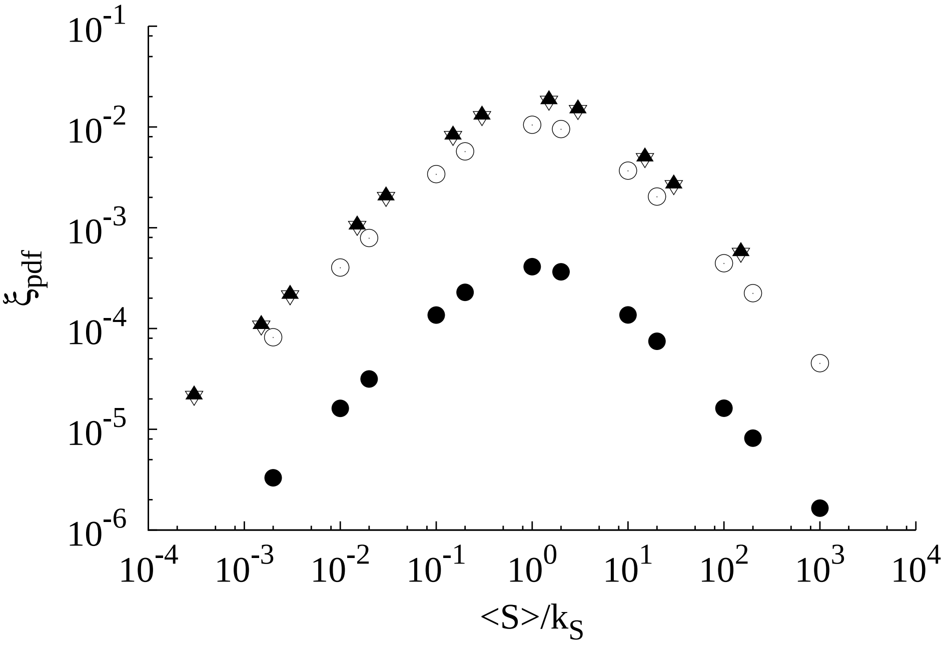

Figure 4.24: Deviation from the average uptake rate $\langle\Phi^*\rangle_{pdf}$ to the uptake rate based on average substrate concentration for Monod assimilation model with respect to the dimensionless ratio $\langle S\rangle_p/k_S$ for the different simulations $R2S_1M$: • and $R2S_{0.15}M$: ▲, $R1M$: ▽, $G2M$: ○.

We can also see that the normalised cross-correlation $\langle s'\phi'^*\rangle_p/(\langle s'^2\rangle\langle\phi'^{*2}\rangle_p)^{1/2}$ is a constant for the different simulations, so that the uptake rate variance can be derived as well from the substrate concentration distribution. And the gradient contribution in the averaged uptake rate deviation is found using equation (4.17).

Finally, we just show that the knowledge of the exact substrate concentration distribution helps in determining the average uptake rate for the microorganisms population. As seen in our simulations, the obtained averaged uptake rate is not that different from the uptake rate based on the averaged concentration. Indeed, the difference is always lower than 5%. This results was actually expected because of the well macro-mixed state of the simulated "bioreactor". This result is observed with the contribution of the imposed substrate gradient that increases the deviation ξ. So, at the scale of the considered domain, the macroscopic heterogeneities are relatively weak and the macroscopic law is verified. But, if the reactor is not well macro-mixed and blob of substrate are transported in the flow, the population is more likely to observe variations of the mean concentration. In that case, the averaged uptake rate will probably be affected by the macroscopic heterogeneities and largely differ from the macroscopic law based on the mean substrate concentration in the whole reactor. But, this macro-mixing effect was not the point in the present study and we rather focused on the micro-mixing.

Indeed, if we now look at the uptake rate distributions over the microorganisms population, it is clear that the population is found to be in a heterogeneous assimilation state. Despite the microscopic biologic parameters are unchanged for the microorganisms, the assimilation rate differs in the population. This mass flux distribution might be at the origin of the decreased growth obtained in large-scale bioreactors compared to the laboratory scale for example. This remark will be discussed in the last part of this chapter. The obtained distribution for the assimilation rate in the population is then important to describe. Based on the observation that for high affinity constant to the substrate, the distributions of the mass flux present similar shape compared to the total substrate concentration distribution, we propose hereafter an analytical study for the determination of the assimilation rate distributions.

4.5.4 Determination of the mass flux distributions

Based on the previous obtained distributions for the substrate concentration, we decide to determine the different distributions for the uptake rate. The general definition for the mass flux distribution function can be obtained from the already introduced joined substrate concentration-uptake rate PDF $f_{S@p,\Phi_p^*}$. We keep the idea that both substrate concentration distributions are identical for the fluid and microorganisms so that we write: $P(\Phi_p^*, S) = f_{S@p,\Phi_p^*}$. The general definition for the mass flux distribution is given by:

$$P(\Phi_p^*) = \int_{-\infty}^{+\infty} P(\Phi_p^*, S) dS. \tag{4.35}$$

This joined PDF is also linked to the substrate concentration distribution:

$$P(\Phi_p^*, S) = P(\Phi_p^* | S) P_S(S), \tag{4.36}$$

where $P(\Phi_p^*|S)$ is the PDF of the uptake rate conditioned by the substrate concentration. In the present work, the mass flux directly depends on the total substrate concentration so that a theoretical solution exists for the determination of the mass flux distribution. The latter is obtained by considering the distribution of the total substrate concentration P_S and the expression of the mass flux with respect to the total substrate concentration ($\Phi_p^* = g(S) = \frac{S}{S+k_S}$ in the case of the Monod assimilation model.). The distribution of the mass flux is given by:

$$P_\Phi(\Phi_p^*) = \frac{1}{g'[g^{-1}(S)]} P_S(g^{-1}(S)), \tag{4.37}$$

where g' is the first derivative of g and g^{-1} is the inverse of g so that $g[g^{-1} = x]$. The inverse function g^{-1} is thus given by $g^{-1}(x) = \frac{k_S x}{1-x}$ if $x \neq 1$. By definition of the Monod assimilation model, the curve $y = 1$ is the asymptote of Φ_p^* so that the previous inverse function is defined for all Φ_p^*. In the case of Monod assimilation law the distribution function for the non-dimensionalised mass flux is thus:

$$\boxed{P_{\mathrm{M}}(\Phi_p^*) = \frac{k_S}{(1-\Phi_p^*)^2} P_S\Big(\frac{k_S \Phi_p^*}{1-\Phi_p^*}\Big).} \tag{4.38}$$

Validation in the gaussian case

In order to validate this result, the simple gaussian distribution for the substrate concentration S_1 is studied. The corresponding distribution is P_{S_1} given by equation (4.27). According to previous considerations, the following equation is found for the mass flux distribution:

$$P_{\mathrm{M}}(\Phi_p^*(S_1)) = \frac{k_s}{(1-\Phi_p^*)^2} \frac{1}{\sqrt{2\pi\langle s'^2\rangle}} \exp\Big(\frac{k_S^2}{2\langle s'^2\rangle}\big(\frac{\Phi_p^*}{1-\Phi_p^*} - \frac{S_0}{k_S}\big)^2\Big). \tag{4.39}$$

In order to verify the analytical expression, the obtained distribution function is compared to numerical results in the case of a simulation where the gradient contribution is not taken into account for the uptake rate calculation. Meaningly $\Phi_p^* = \frac{S_0+s'}{S_0+s'+k_S}$. The results are presented in Figure 4.25 for the simulations $R2$, with $S_0 = 0.15\ \mathrm{kg_S \cdot m^{-3}}$ for different affinity constants.

Firstly, in the case where the gradient contribution is not taken into account for the uptake rate, the obtained distributions seem nearly gaussian. Nevertheless an asymmetric evolution is observed at both extremities of the distribution. Moreover, the calculated distribution and the analytical evolution for the uptake rate distribution perfectly match.

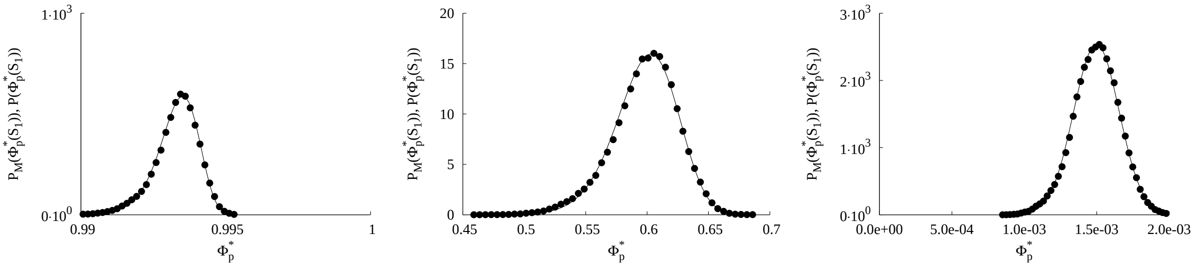

(a) $k_S = 10^{-3}$ kg$_S \cdot$ m^{-3} (b) $k_S = 10^{-1}$ kg$_S \cdot$ m^{-3} (c) $k_S = 10^{2}$ kg$_S \cdot$ m^{-3}

Figure 4.25: Comparison of the analytical distribution for the assimilated mass flux Φ_p^* by the microorganisms (——) with the distributions obtained from DNS (∘) for simulation $R2S_{0.15}M$ with no contribution of the substrate gradient for the assimilation rate for different affinity to the substrate.

Validation in a more general case

Then, we consider the general case of our simulations where the substrate gradient affects the assimilation rate. The corresponding substrate concentration distribution $P_S(S)$ is given by equation (4.29). Using the Monod assimilation model, the resulting distribution for the mass flux for the microorganisms is thus given by:

$$\boxed{P_{\mathrm{M}}(\Phi_p^*(S)) = \frac{k_s}{(1-\Phi_p^*)^2}\frac{1}{2\zeta L_{box}}\left[\mathrm{erf}\Big(\frac{\frac{k_S\Phi_p^*}{1-\Phi_p^*} - S_0 + \zeta L_{box}/2}{\sqrt{2\langle s'^2\rangle}}\Big) - \mathrm{erf}\Big(\frac{\frac{k_S\Phi_p^*}{1-\Phi_p^*} - S_0 - \zeta L_{box}/2}{\sqrt{2\langle s'^2\rangle}}\Big)\right]} \tag{4.40}$$

The obtained analytical expression is compared with the results of the different performed simulations. We focused on simulations $R2S_{0.15}M$, $R2S_1M$ and $G2M$. The distributions for three different affinity constants are given by Figure 4.26. In all cases, both distributions are in agreement and we observed that for small affinity to the substrate $k_S = 10^2$ kg$_S \cdot$ m^{-3}, the obtained distribution is closed to the substrate concentration distribution. The asymptotic behaviour $\Phi_p^* \simeq \S/k_S$ is verified for large k_S. For the large and moderate affinity to the substrate, the obtained distribution for the flux is not easily predictable because the effects of the different parameters (substrate concentration variance, affinity constant, mean substrate concentration, gradient contribution) directly affect the mass flux distribution.

By an analytic approach, the local heterogeneities seen by microorganisms of a given population can be integrated at the population scale when regarding the substrate concentration distribution. This result is obtained when an assimilation law is prescribed at the microorganisms scale and when the assimilation does not influence the substrate concentration field. Moreover, even if we did not consider the biomass growth in our simulations, we will see that it is possible to predict a specific growth rate from the mass flux seen by microorganisms.

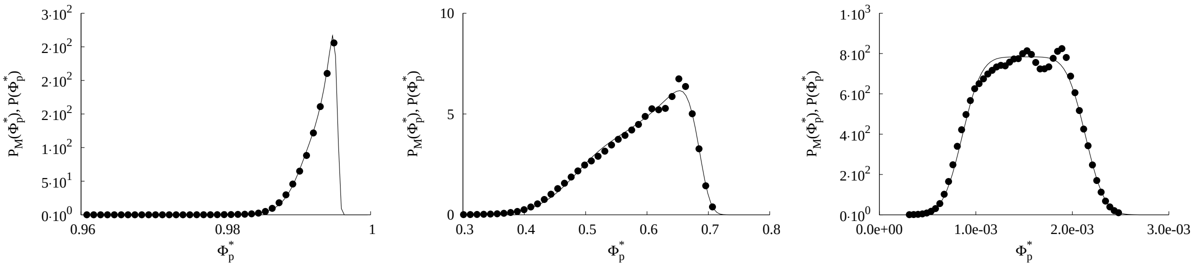

(a) $R2S_{0.15}M$, $k_S = 10^{-3}$ $\mathrm{kg_S \cdot m^{-3}}$ (b) $R2S_{0.15}M$, $k_S = 10^{-1}$ $\mathrm{kg_S \cdot m^{-3}}$ (c) $R2S_{0.15}M$, $k_S = 10^{2}$ $\mathrm{kg_S \cdot m^{-3}}$

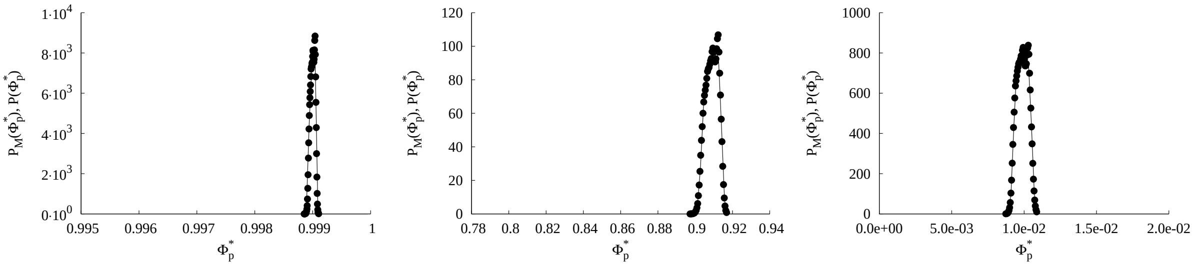

(d) $R2S_1M$, $k_S = 10^{-3}$ $\mathrm{kg_S \cdot m^{-3}}$ (e) $R2S_1M$, $k_S = 10^{-1}$ $\mathrm{kg_S \cdot m^{-3}}$ (f) $R2S_1M$, $k_S = 10^{2}$ $\mathrm{kg_S \cdot m^{-3}}$

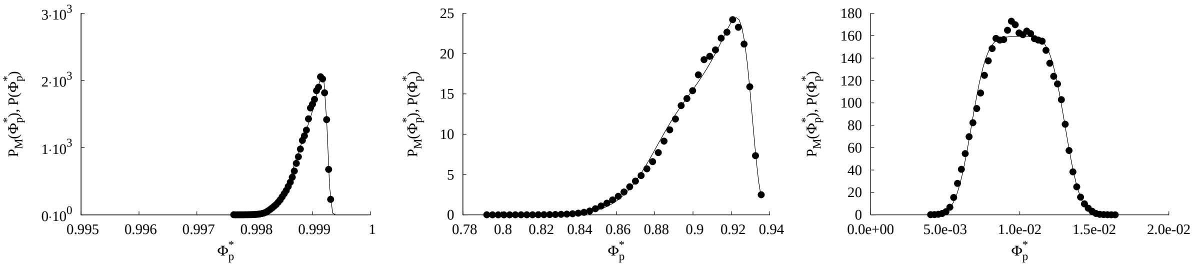

(g) $G2M$, $k_S = 10^{-3}$ $\mathrm{kg_S \cdot m^{-3}}$ (h) $G2M$, $k_S = 10^{-1}$ $\mathrm{kg_S \cdot m^{-3}}$ (i) $G2M$, $k_S = 10^{2}$ $\mathrm{kg_S \cdot m^{-3}}$

Figure 4.26: Comparison of the analytical distribution for the assimilated mass flux Φ_p^* by the microorganisms (——) with the distributions obtained from DNS (∘) of simulations $R2S_{0.15}M$, $R2S_1M$ and $G2M$ for different affinity to the substrate.

4.6 Effect of concentration heterogeneities on the biological reactions

4.6.1 Presentation of biological reaction and biomass growth balances

4.6.1.1 Metabolic model

The metabolic model we use here is a adapted from the metabolic model published by Xu et al. (1999) for *Escherichia coli* in batch or fed-batch cultivations under fully aerobic conditions. It is based on a limited number of key internal processes (or reactions) as well as mass and energy balances.

$$\begin{array}{cclll}
S + Y_{SE}ATP & \xrightarrow{q_{ana}} & Y_{SX}X & & \text{Anabolism} \\
S + Y_{SO}O_2 & \xrightarrow{q_{oxy}} & Y^o_{SE}ATP & & \text{Oxidative Catabolism} \\
S & \xrightarrow{q_{ferm}} & Y_{SP}P + Y^f_{SE}ATP & & \text{Fermentative Catabolism} \\
S + ATP & \xrightarrow{q_{over}} & Y_{SBP}BP & & \text{Dissimilation} \\
ATP & \xrightarrow{q_{main}} & 0 & & \text{Maintenance}
\end{array}$$

q are the specific rates of intracellular reactions in $[\ \mathrm{mol_S.g_X^{-1}.h^{-1}}\ ]$,

Y_{ij} are the stoichiometric coefficients in $[\ \mathrm{mol_j \cdot mol_i^{-1}}\ ]$[7].

In the case of facultative aerobes, energy can be obtained from an oxidative pathway or by fermentation when oxygen is absent or in default. The two metabolic pathways do not have the same energetic yield and fermentative catabolism leads to the formation of a product P. It is assumed that *overflow* metabolism leads to the excretion of another by-product named BP. The production of new cellular material (anabolism), the withdrawal of carbon in excess (dissimilation or *overflow* metabolism) and maintenance are energy consuming.

4.6.1.2 Specific bioreaction rates

The specific reaction rates r_i are expressed in $[\ \mathrm{g_i \cdot g_X^{-1} \cdot h^{-1}}\ ]$ are given by the following set of equations:

$$r_X = q_{ana}.Y_{SX}.M_X \tag{4.41}$$

$$r_{O2} = -q_{oxy}.Y_{SO}.M_{O2} \tag{4.42}$$

$$r_S = -(q_{ana} + q_{oxy} + q_{ferm} + q_{over}).M_S \tag{4.43}$$

$$r_P = q_{ferm}.Y_{SP}.M_P \tag{4.44}$$

$$r_{BP} = q_{over}.Y_{SBP}.M_{BP} \tag{4.45}$$

where M_i are the molar masses of the different species. In order to get the source or sink term in the conservation of a given species, these rates have to be calculated for each value of the uptake rate considering the actual distribution. This is done in section 4.6.2.

The table 4.6 gathers the different parameter values of the metabolic model.

Table 4.6: Parameter values of the metabolic model of *Escherichia coli*.

Name	Symbol	Value	Unit
Anabolism (ATP)	Y_{SE}	12.05	$[\ \mathrm{mol_{ATP} \cdot mol_S^{-1}}\ ]$
Anabolism (biomass)	$Y_{XS}M_X$	136.6	$[\ \mathrm{g_X \cdot mol_S^{-1}}\ ]$
Oxidative Catabolism (oxygen)	Y_{SO}	6	$[\ \mathrm{mol_{O2} \cdot mol_S^{-1}}\ ]$
Oxidative Catabolism (ATP)	Y^o_{SE}	20	$[\ \mathrm{mol_{ATP} \cdot mol_S^{-1}}\ ]$
Fermentative Catabolism (product)	Y_{SP}	6	$[\ \mathrm{mol_P \cdot mol_S^{-1}}\ ]$
Fermentative Catabolism (ATP)	Y^f_{SE}	20	$[\ \mathrm{mol_{ATP} \cdot mol_S^{-1}}\ ]$
Dissimilation (biopolymer)	Y_{SBP}	1	$[\ \mathrm{mol_{BP} \cdot mol_S^{-1}}\ ]$

---

[7] superscripts stand for oxidative or fermentative catabolism.

4.6.1.3 Calculation of the metabolic fluxes - Hypothesis

In order to make this calculation feasible some assumptions have to be made and some constraints added:

1. **No accumulation**: assuming that neither energy nor mass accumulate inside the microorganisms the following conservation equation for energy (namely ATP) over the cell can be written:
$$q_{oxy}Y_{SE}^{o} + q_{ferm}Y_{SE}^{f} - q_{ana}Y_{SE} - q_{over} - q_{main} = 0. \tag{4.46}$$
A conservation equation for the substrate can be obtained by equating the total specific molar flux through the cell membrane $q_{mol,S}$ [$\mathrm{mol_S.g_X^{-1}.h^{-1}}$] to the sum of all substrate consumptions rates:
$$q_{S,mol} = q_{ana} + q_{oxy} + q_{over} + q_{ferm}. \tag{4.47}$$

2. **Preferential catabolism**: the bacteria are supposed to favour the production of energy through the oxidative pathway and they only make use of the fermentation pathway when the amount of energy produced by oxidation does not fulfil the energetic demand.

3. ***Overflow* metabolism**: the excretion of carbon in excess is triggered when the rate of substrate assimilation is greater than the rate of consumption due to anabolism and catabolism. The amount of energy consumed by the dissimilation is supposed to be negligible which results in the elimination of q_{over} in (4.46).

4. **Maintenance**: the energetic cost of maintenance is supposed to be negligible which also leads to a simplification of equation (4.46)

5. **Oxygen consumption rate**: the oxygen consumption rate is a function of the local dissolved oxygen concentration in the liquid phase. In the following, it is assumed that the dissolved oxygen concentration is non-limiting, such that only oxidative catabolism is active. This simplification allows a direct calculation of all metabolic fluxes, since the mass balance for the substrate can be simplified into:
$$q_{S,mol} = q_{ana} + q_{oxy} + q_{over}, \tag{4.48}$$
and the energy balance now reduces to:
$$q_{ana}Y_{SE} = q_{oxy}Y_{SE}^{o}. \tag{4.49}$$
Note: It would be also possible to proceed to the resolution of the metabolic model in case of oxygen limitation. In the context of this work it would necessitate the joined-PDF for the substrate and oxygen fluxes. Since this information is not available at the moment, oxygen non-limiting conditions are assumed.

6. **Relation between fluxes and internal reaction rates**: dividing equation (4.48) by $q_{S,max}$ one forms a non-dimensional variable q^* which is simply related to the non-dimensional flux through:
$$q^* = \frac{q_{S,mol}}{q_{S,max}} = \frac{<S>}{k_s + <S>} = \frac{\Phi}{\Phi_{max}} = \Phi^*. \tag{4.50}$$

The normalised value of the assimilation rate only depends on the concentration and on the type of microorganisms considered (identified by the value of k_S), so does the normalised internal reaction rate.

4.6.1.4 Balanced growth

In the original model of Xu et al. (1999), the overflow metabolism starts under fully aerobic conditions when the rate of oxygen consumption required for glucose oxidation exceeds the maximum respiration rate. In that case, the uptaken substrate flux exceeds the maximum oxidative capacity of the cell. In the present work, a slightly different approach is used. It is assumed here that overflow metabolism is triggered when the instantaneous substrate uptake rate exceeds the rate of substrate consumption (through anabolism and oxidative catabolism) which mainly depends on the substrate concentrations experienced by the population in the past. This substrate consumption rate is determined by assuming that microorganisms transported in a medium, characterised by the averaged concentration $\langle S \rangle$, are adapted to this concentration. In other words, the metabolism is balanced (without overflow) when the consumption rate equals the assimilation rate corresponding to the mean concentration $\langle S \rangle$. In the following, this balanced state is marked by the superscript ^{0}.

$$\Phi^0 = \Phi_{max} \frac{< S >}{k_s + < S >}. \tag{4.51}$$

In the balanced growth state, the assimilation rate exactly meets the sum of utilisation rates through the anabolic and oxidative catabolic pathways, which leads with non-dimensional variables:

$$\Phi^{*0} = q^{*0}_{ana} + q^{*0}_{oxy}. \tag{4.52}$$

The simplified energy balance presented in the previous section gives:

$$q^*_{oxy} = \frac{Y_{SE}}{Y^o_{SE}} q^*_{ana} = \alpha q^*_{ana}, \tag{4.53}$$

which is also valid in the balanced growth state; therefore we get

$$q^{*0}_{ana} = \frac{\Phi^{*0}}{1+\alpha}, \tag{4.54}$$

$$q^{*0}_{oxy} = \frac{\alpha \Phi^{*0}}{1+\alpha}. \tag{4.55}$$

4.6.1.5 Unbalanced growth

The determination of the actual metabolism in the general case, named unbalanced growth, is based on the comparison between the normalised uptake rate Φ^* and the normalised utilisation rate in the balanced growth state Φ^{*0}.

Limited growth

On the one hand, microorganisms receiving a substrate flux Φ^* smaller than Φ^{*0} are facing a nutrient limitation. However all cells are accustomed to an average flux Φ^{*0} meaning that the *cell factory* would be able to metabolise higher amounts of substrate. As a consequence the totality of the substrate assimilated is directed to the anabolic and oxidative catabolic pathways. Equations (4.54) and (4.55) remain valid since the proportionality between q_{oxy} and q_{ana} is maintained. The only difference is that the superscript ^{0} falls indicating that the actual uptake rate is sub-optimal.

$$q^*_{ana} = \frac{\Phi^*}{1+\alpha}, \tag{4.56}$$

$$q^*_{oxy} = \frac{\alpha\Phi^*}{1+\alpha}. \tag{4.57}$$

On the other hand, microorganisms receiving a substrate flux Φ^* greater than Φ^{*0} are facing a nutrient excess. The anabolic capacity of those cells is saturated which also limits the growth rate. The anabolic and oxidative rates are identical for all cells in that situation :

$$q^*_{ana} = \frac{\Phi^{*0}}{1+\alpha}, \tag{4.58}$$

$$q^*_{oxy} = \frac{\alpha\Phi^{*0}}{1+\alpha}. \tag{4.59}$$

Overflow

The fraction of the population exposed to substrate concentration higher than $\langle S\rangle$ internalise a substrate flux higher than Φ^{*0} and they have to cope with an excess of nutrient. In standard approaches, the uptake rate never exceeds that defined by the average concentration. In our approach it is on the contrary admitted that some cells can internalise more substrate than the whole population does on average. However, the amount of substrate directed in the anabolic and oxidative catabolic pathways is limited to that defined by the balanced growth state. As a consequence, the difference between the effective uptake rate and the utilisation rate due to balanced metabolism represents an extra-assimilation which has to be diverted into by-products since accumulation is not allowed in the metabolic model. The number of moles of by-product formed depends on the stoichiometry of the reaction converting internal substrate into by-products. For convenience it will be assumed here that the stoichiometric coefficient Y_{SBP} is equal to unity [8] and we will analyse the results in terms of q^*_{over} defined as:

$$q^*_{over} = \frac{q_{over}}{q_{S,max}} = \Phi^* - \Phi^{*0}. \tag{4.60}$$

Note that whatever the value of Φ the definition of the variables implies that:

$$q^*_{ana} + q^*_{oxy} + q^*_{over} = \Phi^*. \tag{4.61}$$

4.6.2 Population averaged bioreaction rates

The previous calculations start with the knowledge of the assimilated mass flux. In the simulations presented earlier in this chapter, a distribution of flux $P(\Phi^*)$ was computed for different parameters of the flow, such as the Reynolds number, mean concentrations and concentration gradients. Therefore, the overall uptake rates at the scale of the entire volume of the HIT box have to be calculated by taking into account the distribution obtained in each case.

4.6.2.1 Substrate assimilation

By definition the mean substrate consumption rate (averaged over the population of microorganisms) is the first moment of the distribution $P(\Phi)$. Since we indeed start from the normalised distribution $P(\Phi^*)$, we actually calculate the normalised value of the mean substrate consumption rate (the mean divided by Φ_{max}).

$$\langle\Phi^*\rangle = \int_0^\infty P(\Phi^*)\Phi^* d\Phi^*. \tag{4.62}$$

---

[8] This also implies $M_S = M_{BP}$.

It was found in section 4.4.1 that the averaged flux over all the particles is very close ti the flux computed from the mean concentration $\langle S \rangle$. Equation (4.50) shows that:

$$\langle \Phi^* \rangle = \Phi^{*0}. \tag{4.63}$$

The real value depends on the values of Φ_{max}, $\langle S \rangle$ and k_S.

4.6.2.2 Growth

The population averaged, or mean specific growth rate is related to the mean anabolic rate through equation (4.41). This leads to the following expression for the mean normalised specific growth rate:

$$\langle \mu^* \rangle = \frac{\langle \mu \rangle}{\mu_{max}} = \int_0^\infty P(\Phi^*) q^*_{ana}(\Phi^*) d\Phi^*. \tag{4.64}$$

The relative specific growth rate $\langle \mu^* \rangle$ can be compared to the relative specific growth rate $\langle \mu^{*0} \rangle$ that would be obtained if the same flux was assimilated by each particle in the box (perfectly mixed hypothesis), and the relative specific growth rate would be:

$$\langle \mu^{*0} \rangle = \int_0^\infty P(\Phi^*) \frac{\Phi^{*0}}{1+\alpha} d\Phi^* = \frac{\Phi^{*0}}{1+\alpha}. \tag{4.65}$$

The integration interval of equation (4.64) must be split into two subintervals because the definition of $q^*_{ana}(\Phi^*)$ actually depends on the value of Φ^* with respect to Φ^{*0} as explained in section 4.6.1.5.

$$\frac{\langle \mu^* \rangle}{\langle \mu^{*0} \rangle} = \frac{1+\alpha}{\Phi^{*0}} \Big(\int_0^{\Phi^{*0}} P(\Phi^*) \frac{\Phi^*}{1+\alpha} d\Phi^* + \int_{\Phi^{*0}}^\infty P(\Phi^*) \frac{\Phi^{*0}}{1+\alpha} d\Phi^* \Big). \tag{4.66}$$

The first term on the right hand side corresponds to the growth limited by the incoming flux (physical limitation) and the second term corresponds to the growth limited by the cell capacities (biological limitation). Recall that the mean anabolic flux is the same for all cells and defined by $\langle S \rangle$. The ratio therefore quantifies the specific growth rate reduction due to imperfect micro-mixing.

4.6.2.3 By-product formation

Following the same approach, the mean normalised production rate of by-product due to overflow metabolism is obtained through:

$$\langle q^*_{over} \rangle = \frac{1}{\Phi^{*0}} \int_{\Phi^{*0}}^\infty P(\Phi^*) \big(\Phi^* - \Phi^{*0} \big) d\Phi^*. \tag{4.67}$$

It corresponds to the ratio between the mean by-product formation rate and the mean substrate consumption rate. It can also be interpreted as the fraction of the total substrate influx that is diverted towards overflow metabolism.

4.6.3 Results

Normalised probability density functions of the normalised flux Φ^* are obtained from numerical simulations. As already explained, simulations are performed with the same average concentration $\langle S \rangle$ for various type of particles (or microorganisms) distinguished by their own affinity constant k_S. Different values for k_S were investigated, which implies that the values of Φ^{*0} is also different.

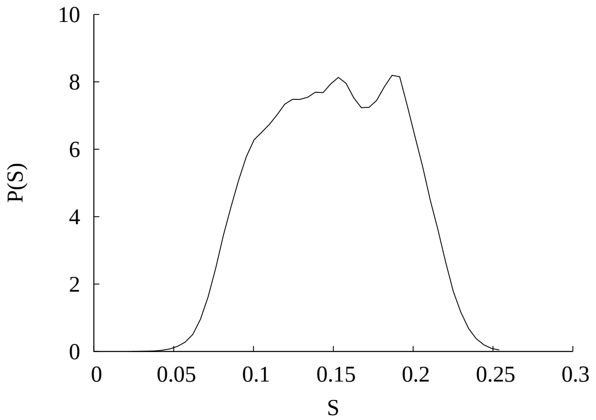

Figure 4.27: Substrate concentration distribution for simulation $R2S_{0.15}M$.

4.6.3.1 Calculation of the normalised internal reaction rates

In this first part of the results, calculations have been performed for an averaged concentration $\langle S\rangle = 0.15\ \mathrm{kg_S \cdot m^{-3}}$ which corresponds to the simulation $R2S_{0.15}M$. The typical concentration distribution computed in that case is presented in Figure 4.27 and the corresponding distribution $P(\Phi^*)$ is shown in figure 4.28. A value of $k_S = 0.1\ \mathrm{kg_S \cdot m^{-3}}$ is chosen to illustrate the results of metabolic rates calculations. The mean value $\langle\Phi^*\rangle = \Phi^{*0}$ is equal to 0.6 under these conditions. Thus, it can be observed that the rates of anabolism and oxidative catabolism are proportional, both increasing with Φ^*, as long as $\Phi^* \leqslant \Phi^{*0}$. Beyond this limit, the rates of anabolism and oxidative catabolism remain constants while the rate of overflow metabolism progressively increases. It can be noticed that these calculations only depend on the value of Φ^* and Φ^{*0} that defines the limit between limited growth and over-flow metabolism. The overall consequences in terms of specific growth rate reduction and amount of by-product formed for the entire population actually result from the combination of the two graphs presented in Figure 4.28. Therefore, it is expected that, for the same average concentration, these results will be dependent on the degree of mixing in the HIT box, namely the variance of the substrate concentration distribution. The quantification of these aspects, overall consequences and mixing effects, are treated in the next part.

4.6.3.2 Effect of k_S on the mean specific growth and by-product rates

First, the calculations of integrals corresponding to equation (4.67) and (4.66) have been performed using the same scalar field for different values of k_S. The results are presented in Figure 4.29a in terms of specific growth rate reduction and fraction of the incoming substrate flux diverted into by-product for different values of the ratio $\langle S\rangle/k_S$. On the right part of the graphs, the affinity constant for the substrate is much smaller than the average concentration, the uptake rate is maximum and consequently the presence of concentration gradients has almost no effect on the mean population growth rate (which is indeed equal to μ_{max}). In fact, the distribution $P(\Phi^*)$ is also very narrow and since $\Phi^{0*} \rightarrow 1$, no by-product is formed. On the left part of the graphs, the distribution of S results in a distribution of $P(\Phi^*)$ such that $\Phi^{0*} << 1$ so the whole population is growing at $\mu < \mu_{max}$. Among this population some individuals are facing limiting conditions, those for which $\Phi^* < \Phi^{0*}$, some other individuals have to cope with an excess of substrate $\Phi^* > \Phi^{0*}$. Thus, we concomitantly observe a reduced growth rate and a by-product formation at the population scale.

Then, the effect of substrate heterogeneities is investigated. In Figure 4.30, the specific growth rate reduction is presented as a function of the ratio $\langle S\rangle/k_S$ for the different flow configurations. For all

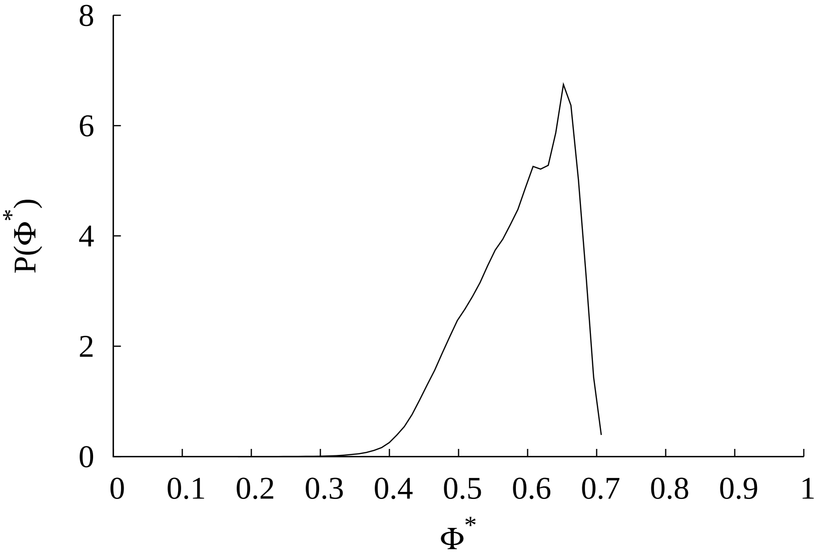

(a) $P(\Phi^*)$

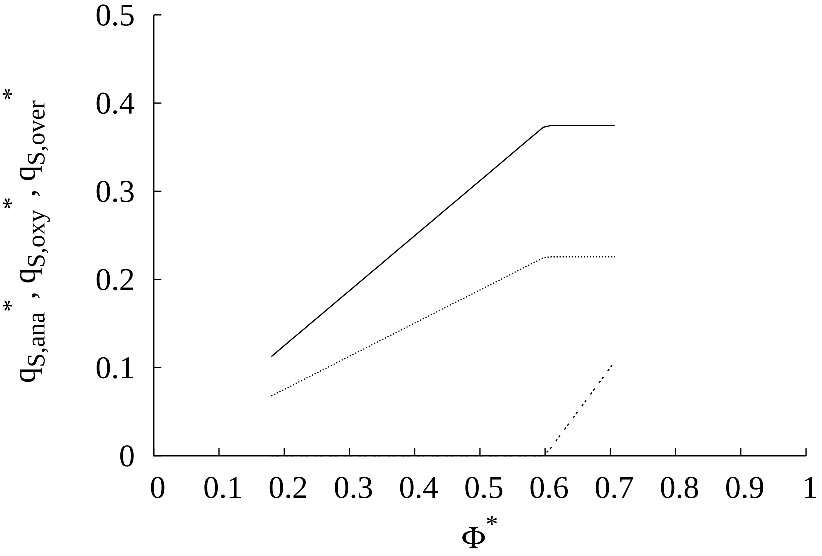

(b) Anabolism (———), Oxidative (········) and overflow (- - - -) fluxes.
(bottom)

Figure 4.28: Normalized uptake rate distribution (top) and corresponding anabolism, oxidative catabolism and overflow rates with respect to the normalised uptake rate for simulation $R2S_{0.15}M$ and $k_S = 0.1\ \mathrm{kg_S \cdot m^{-1}}$.

flow configurations, the same trend is observed: a growth rate reduction is present for small values of the ratio $\langle S \rangle / k_S$ (i.e. under substrate limiting conditions). The magnitude of this phenomenon is dependent on the heterogeneity of the substrate concentration field. Simulation $R2S1M$ leads to a narrow distribution (presented in chapter 3) and consequently, there is almost no drop in the specific growth rate. Increasing the magnitude of the concentration gradient while preserving the same average concentration and velocity fields ($G2M$) produces a more heterogeneous concentration field. As a result, the fraction of cells facing sub-optimal concentrations increases and the actual

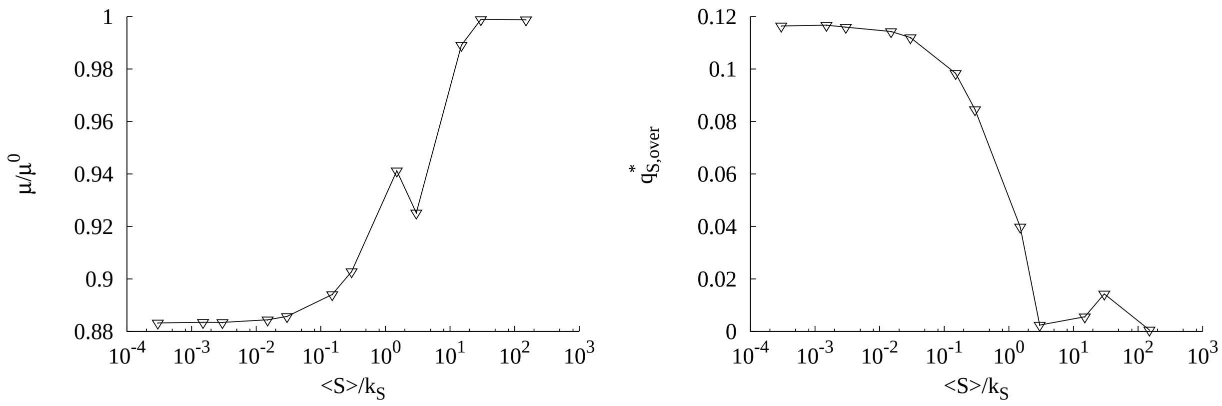

(a) Specific growth rate reduction.

(b) Overflow production.

Figure 4.29: Specific growth rate reduction and by-products formation with respect to the ratio $\langle S\rangle/k_S$ for the simulation $R2S_{0.15}M$.

specific growth rate is lower than what it would be in a prefectly mixed environment. In the end, simulations $R2S_{0.15}M$ and $R1M$ produce wide distributions because of small average concentration combined with a strong gradient. In these cases, the specific growth rate reduction, when it takes place, is more pronounced. A general observation is that a specific growth rate reduction of less than a few percent is probably impossible to detect through experimental measurements. In pratice, one would measure the same average substrate concentration but different specific growth rates (affected by the actual micro-mixing efficiency). In order to fit these data, with a Monod law, it would be necessary to adjust μ_{max} or k_S or both.

In figure 4.31, the rate of by-product formation is presented as a function of the ratio $\langle S\rangle/k_S$ for the different flow configurations simulated. It can be seen that using the proposed model, some by-product is formed as soon as the mean substrate concentration becomes smaller than $10k_S$. In the region of moderate limitation $\langle S\rangle/k_S \approx 1$, overflow metabolism can represent around 5% of the total carbon flux. This may not be sufficient to be detected, in particular if this by-product can be further re-assimilated, but it can explain the observed reduction of both the specific growth rate and the conversion yield of substrate into biomass.

The main conclusion is that the heterogeneity of the substrate concentration field is responsible for a decrease in the apparent specific growth rate at the HIT box scale. This conclusion can only be drawn through the use of a metabolic model. However, it is remarkable that using a metabolic model assuming homogeneity in the HIT box, i.e. without considering the actual distribution would lead to erroneous results: an overestimation of the specific growth rate and an under estimation of the amount of by-product formed. The assumption that the mesh cell is homogeneous is generally made in CFD simulations of bioreactors and it can explain at least partly the inaccuracy of these modelling approaches. Beyond the reference to a metabolic model, the use of a subgrid model to account for the substrate concentration distribution below the resolved scale of the CFD model is certainly a major way for improving simulations.

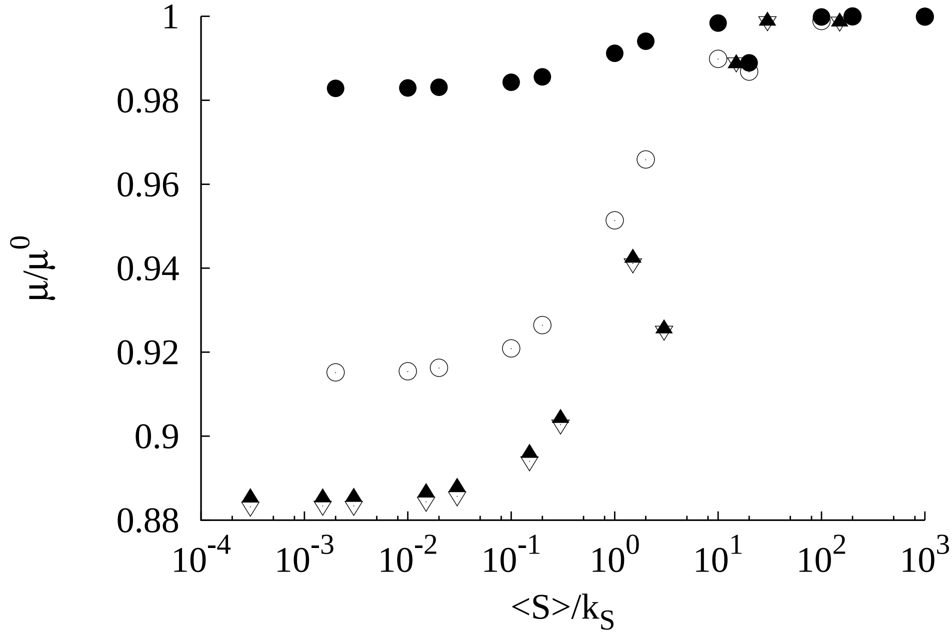

Figure 4.30: Specific growth rate reduction with respect to the ratio $\langle S \rangle / k_S$ for the different simulations. $R1M$: ▲, $R2S_{0.15}M$: ▽, $R2S_1M$: •, and $G2M$: ○.

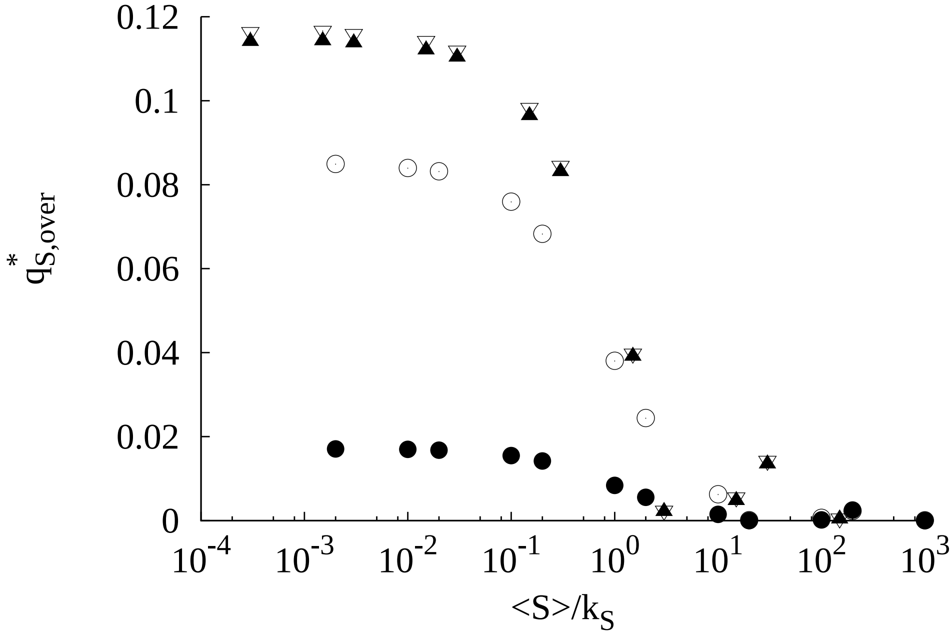

Figure 4.31: Specific growth rate reduction with respect to the ratio $\langle S \rangle / k_S$ for the different simulations. $R1M$: ▲, $R2S_{0.15}M$: ▽, $R2S_1M$: •, and $G2M$: ○.

Conclusion

In this chapter, we performed a detailed statistical analysis of biological assimilation for a population of microorganisms in a fully turbulent flow. The exact knowledge of the different turbulent parameters of the fluid velocity and substrate mixing helps in understanding the macroscopic results for biological assimilation. With the prescription of a microscopic assimilation law at the microorganism scale, an overall assimilation law is found at the population scale. This obtained macroscopic law is found to be very similar to the usually prescribed assimilation law at the population scale based on the averaged substrate concentration. Indeed, the discrepancies at the population scale remain relatively small, except for affinity constants of order the of the mean substrate concentration. Nevertheless, those deviations are smaller than 5% and the determination of the assimilation rate based on the averaged substrate concentration seems to be a good approximation in the present configuration and with the given range of turbulent parameters. The studied configuration aimed to represent a perfectly macro-mixed reactor. But in more realistic industrial configuration, due to localised substrate feeding for example, zones of highly concentration liquid are likely to appear and influence the biological assimilation for the microorganisms experiencing this high substrate concentration. Indeed, the microorganisms assimilation regime is expected to be in the biological regime where the biological reaction is the limiting process and the production of extra-cellular metabolites, whereas low-concentrated zone in the bioreactor exist and the assimilation rate in these zones is expected to be limited by the substrate transport. The physical limitation will result in a decrease of biomass growth in these areas.

Aware of this remark on the effect of macro-mixing on the overall assimilation rate, we rather focused on the micro-mixing effect for substrate assimilation. The micro-mixing effect is found to impact the assimilation of individual microorganisms along their trajectories, and regarding the assimilation rate distribution of the microorganisms population. The different distributions for the microorganisms are studied, and the impact of the flow dynamics and substrate mixing is scrutinised on the total uptake rate distribution.

An analytical approach is proposed that aims to link the uptake rate distribution to the substrate concentration distribution. Namely, the distribution of the total substrate concentration is a combination of the different concentration contributions: the mean imposed substrate concentration, the substrate fluctuations, whom distribution is gaussian, and the gradient contribution. The obtained distribution is thus function of the substrate variance and the substrate difference between the height and bottom of the computational box.

This approach can be used to consider the micro-mixing state inside a computational cell of a RANS calculation for example. Indeed in most computational approach, the substrate transport is solved, as well as the substrate variance transport equation, but the mixing inside the computational cell is assumed to be perfectly homogeneous. The latter assumption is not valid and the microorganisms actually see a concentration distribution. Based on the value of the transported variance, considering a homogeneous isotropic mixing in order to account for micro-mixing, the substrate concentration distributions can be approached by the analytical formula. The resulting distribution for the assimilation rate of microorganisms can thus be derived analytically if the assimilation law is prescribed at the microorganisms scale.

Finally an analysis of the biological growth in purely oxidative catabolism is performed. The metabolism is balanced for an assimilation rate corresponding to the mean concentration $\langle S \rangle$. The deviation around this balanced condition is then studied by considering the mass flux distributions obtained from the DNS simulations. The results on biomass growth and metabolites production are obtained for various cultures. The biomass growth is observed to decrease when the ratio $\langle S \rangle / k_S$

takes values below or of order unity. This case matches the case where the non-linear nature of the assimilation law (for Monod assimilation model) is found to be in the zone of distribution of the substrate concentration. Therefore the microorganisms of the same population are exposed to various substrate concentrations, which corresponding mass flux differs from the balance state. Indeed, while a proportion of microorganisms is limited in growth, the other proportion is in the overflow metabolism because of the large assimilation of substrate.

This simple statistically-steady approach is a first step to account for the microscopic effect of biological assimilation at the scale of the whole population. The results have been characterised in term of statistics and distributions of the biological phase. But, the unsteady approach introduced in the second chapter of this work remains one of the main perspective of the work. Indeed, the competition between substrate transport and assimilation at the microorganisms scale has not exactly been taken into account in the sense of chapter 2. We approached the substrate concentration at the particle position by the interpolated concentration from the fluid. But due to assimilation, a gradient between the substrate concentration at the cell-liquid interface exists, that is not taken into account in the proposed statistically-steady study. Furthermore, the moderate studied Schmidt numbers limits the analyses due to numerical limitations, but the physics of mixing is influenced by increasing the Schmidt number as shown by Yeung et al. (2002). They found, that the scalar statistics are modified, and show the spreading of the fluctuating scalar gradient in the direction of the imposed scalar gradient. Unfortunately, the distributions of the scalar fluctuations are not reported. In their work, Yeung et al. (2004) also showed that the scalar variance in the steady state increases for increasing Schmidt numbers. The latter observation helps in understanding that the presented results probably underestimate the distribution for assimilation at the microorganisms scale.

Despite the different limitations, the performed study proposes first explanations at the microscopic scale for the often observed decrease of biomass growth and by product formation by passing from laboratory to large scale bioreactors.

Figures

Chapter 5

Biological Two-Way Coupling

After analysing the different statistics for the biological phase in a one-way stationary turbulence for the velocity and substrate concentration fields in the previous chapter, the present part of the work is devoted to the analysis of the biological two-way coupling and substrate decay in a stationary turbulence. First the analysis of the substrate decay in a one-way coupling configuration with a stationary turbulence is proposed. The different statistics and PDF are analysed and this part introduces the non-stationarity of the substrate concentration field. Then the numerical modification required to handle the biological two-way coupling are presented. The different set of equations in the biological two-way coupling are introduced and a step-by-step validation is proposed. The substrate concentration decay is studied and the weight of the assimilation term is characterised for the different balance equations. The different statistics for the substrate concentration field and the microorganisms are scrutinised. Then, the influence of the fluid flow and substrate mixing on the biological assimilation is characterised for different cases. Then a parametric study on the biological parameters is performed and the effects of microorganisms initial conditions on the substrate assimilation are enlightened.

Résumé

Ce chapitre s'inscrit dans la continuité de la modélisation des bioréacteurs avec une approche locale pour l'assimilation du substrat. À l'inverse des simulations diphasiques effectuées au chapitre précédent, nous nous trouvons dans cette partie dans une configuration instationnaire pour le champ de concentration du substrat, alors que la stationnarité du champ dynamique est assurée par le forçage de la turbulence. En d'autre terme, d'un point de vue numérique, le forçage du scalaire est supprimé dans cette partie et la résolution du scalaire se fait sur la concentration en substrat totale.

Dans un premier temps, la concentration moyenne en substrat est maintenue constante et nous étudions la décroissance des fluctuations de concentration au cours du temps ainsi que les effets de cette tendance à l'uniformisation sur l'assimilation de substrat par les microorganismes. Cette étape intermédiaire du travail permet de caractériser la dépendance directe des statistiques pour la phase dispersée et la phase continue. De plus, le modèle IEM (Villermaux and Devillon, 1972) convient parfaitement dans ce cas particulier et on peut donc connaître l'évolution temporelle exacte de la variance de concentration du substrat. Les distributions spatiales de concentration totale peuvent donc être déterminées à chaque instant et par suite les distributions des vitesses d'assimilation par les microorganismes selon la méthode proposée dans le chapitre 4.

Ensuite, une étude sur le couplage inverse biologique est proposée. On entend par couplage inverse la prise en compte de l'assimilation du substrat par les microorganismes sur le champ de concentration du fluide environnant. On se place donc dans le cadre de simulations instationnaires avec décroissance de la concentration moyenne en substrat au cours du temps. L'agitation du domaine est maintenue dans le but de s'approcher de la modélisation d'un réacteur batch où l'on fait croître une population de microorganismes sans alimenter le réacteur au cours du temps mais tout en maintenant l'agitation.

La mise en place numérique du couplage inverse biologique est présentée avec notamment le schéma de projection utilisé, mais aussi l'adaptation du schéma d'interpolation de la concentration adapté à la simulation de réacteurs biologiques. En effet, la positivité de la concentration en substrat doit être assurée au cours des simulations. Des configurations simples sont testées pour permettre la validation de l'implémentation du couplage inverse. Ces validations sont faites en utilisant deux lois d'assimilations : Blackman et Monod.

Les premiers résultats sur les hétérogénéités de concentration provoquées par l'assimilation des microorganismes sont obtenus dans le cas d'un champ de vitesse nulle. Le champ de concentration initial est uniforme, et les microorganismes répartis de manière équidistante ou aléatoire dans le domaine. Les hétérogénéités de concentrations locales en microorganismes créent des hétérogénéités de concentration en substrat importante dans le domaine. Du fait de l'absence d'homogénéisation par un écoulement, les hétérogénéités induites par la consommation perdurent et s'accentuent au cours du temps. Cette situation artificielle permet néanmoins d'apprécier l'effet de la répartition spatiale des microorganismes en l'absence mélange turbulent.

L'évolution temporelle de la variance de concentration du fluide présente une importante augmentation dans les premiers instants de la simulation puis décroît doucement tandis que la variance du flux assimilé est maximale au début de la simulation, puis décroît au cours du temps. De plus, les hétérogénéités locales influencent directement le flux total assimilé à l'échelle de la population de microorganismes, car on observe une baisse de celui-ci par rapport au cas où chaque microorganisme voit la même concentration en substrat. Cette diminution est donc expliquée par l'augmentation de la variance de concentration en substrat du fluide vue par les microorganismes.

L'analyse du couplage inverse se poursuit ensuite dans le cas d'une turbulence homogène isotrope stationnaire pour le champ de vitesse, et l'on observe la décroissance du champ de concentration

en substrat. Les premiers résultats sur l'évolution des statistiques du fluide pour la concentration en substrat montrent une sensible augmentation de la variance de concentration au cours du temps tandis que la concentration moyenne en sucre diminue de manière quasi-linéaire (en fonction des paramètres de la simulation). Puis un second régime d'assimilation apparaît où la décroissance est exponentielle pour la concentration moyenne et s'accompagne d'une diminution de la variance de concentration. Dans la perspective de modélisation des écoulements biologique dans les bioréacteurs avec couplage inverse biologique, un premier essai pour modéliser les termes d'assimilation dans les équations de transport de la concentration moyenne et de la variance du fluide est proposé. Les statistiques pour l'ensemble de la population de microorganismes sont ensuite étudiées et, à l'inverse des situations où l'assimilation n'influence pas le champ de concentration du fluide, on observe des écarts entre l'évolution des corrélations du fluide et des particules au cours du temps.

On analyse ensuite d'un peu plus près les distributions de concentrations fluctuantes et totales pour le fluide et les microorganismes. Compte-tenu du chargement volumique en microorganismes, on remarque bien que les distributions de concentration en substrat ne sont plus confondues pour les microorganismes et le fluide. On peut également observer que les fluctuations de concentration dans le fluide n'obéissent plus à une loi gaussienne et l'on observe même des dissymétries dans la distribution. La détermination de cette distribution au cours du temps est donc inscrite comme l'une des premières perspectives au travail sur le couplage inverse afin de pouvoir en déterminer la distribution des taux d'assimilation par les microorganismes.

Par la suite, une analyse des effets de l'agitation et du mélange initial est proposée pour caractériser l'assimilation par une population de microorganismes dans un réacteur de type *batch*. Pour les paramètres de simulations choisis, si l'on regarde l' évolution temporelle des grandeurs moyennes, on trouve que la diminution de la concentration moyenne en substrat est plus lente dans le cas d'une agitation plus faible. L'évolution des taux d'assimilation moyens est, quant à elle, quasiment inchangée. Si l'on étudie ces résultats en termes d'approche classique où l'on modélise l'assimilation à l'échelle de la population par une loi d'assimilation macroscopique basée sur la concentration moyenne dans le substrat, cela revient à obtenir un taux d'assimilation moins élevé dans le cas d'une agitation moins importante. Ce résultat éclaire le rôle que peut avoir le micro-mélange sur l'identification des paramètres globaux d'une loi d'assimilation établie à partir des seules grandeurs macroscopiques.

L'impact de l'état de mélange initial sur l'assimilation est également étudié pour un même champ de vitesse mais différents champs de concentration initiaux. Pour les paramètres de simulation choisis, l'influence des fluctuations initiales de concentrations autour de la valeur moyenne n'est pas visible sur l'évolution des moments du premier ordre de la concentration et du flux assimilé. Cependant, une légère tendance concernant la variance de concentration du fluide et variance de flux assimilé par les microorganismes laisse à penser que l'écart à la loi d'assimilation macroscopique augmente avec l'hétérogénéité initiale. Plus le champ initial est hétérogène, moins la prédiction de la consommation basée sur la concentration moyenne s'avère pertinente.

L'influence des paramètres biologiques est caractérisée en termes d'assimilation moyenne, et, comme observé dans le quatrième chapitre de ce travail, les écarts sont d'autant plus importants que la concentration moyenne est de l'ordre de la constante d'affinité à l'échelle microscopique. D'autre part, le rapport entre les concentrations initiales en substrat et en microorganismes influence l'assimilation par l'ensemble de la population. Ce résultat avait également été abordé lors de l'approche 1D pour un microorganisme soumis à des fluctuations de concentration.

Enfin il est mis en évidence que, quel que soit le cas, le flux assimilé moyen est sous-estimé par rapport à la loi macroscopique d'assimilation que l'on peut facilement déterminer. Cependant la loi hyperbolique obtenue laisse à penser qu'il est possible d'obtenir effectivement une loi macroscopique à condition de prendre en compte les effets de transport et de limitation en substrat à l'échelle des microorganismes. À l'instar des résultats obtenus dans le second chapitre de ce travail pour un microorganisme isolé, une constante d'affinité macroscopique intégrant l'ensemble des phénomènes à l'échelle microscopique peut être identifiée. La détermination d'une telle constante en fonction des caractéristiques des microorganismes, de l'écoulement et du mélange représente l'une des principales perspectives pour la continuité de ce travail.

Contents

Introduction

In the second chapter, we investigated the competition between substrate transport and substrate assimilation for an academic configuration. The boundary condition at the microorganism interface (either null concentration or constant flux) accounts for the substrate assimilation by the microorganism and the substrate disappearance from the computational domain. But, the domain was fed at the far-field by an imposed substrate concentration, therefore we characterised the equilibrium between assimilation and feeding in the domain for the microorganism.

In the fourth chapter, we investigated the effect of dynamics and mixing on a population of microorganisms from a macroscopic point of view. The study is carried out in the statistically steady state. The stationarity for the substrate is ensured by imposing a substrate gradient. The microorganisms are tracked and their assimilation is studied in a steady manner. Meaningly, the obtained averages for biological statistics were computed from averaging over the microorganisms and afterwards by time-averaging of the ensemble averages. The substrate feed is continuous in time and the volume of the bioreactor remains constant. This can be related to a continuous culture of microorganisms where substrate is continuously injected whereas the culture is partly removed in order to maintain a constant volume of the reactor. Nevertheless, the numerical limitation requires a substrate feeding that is not locally injected, therefore our configuration can be seen as a part of the continuous bioreactor where the imposed substrate gradient is accounting for the macro-mixing.

But in the previous approach, the effect of biological assimilation of substrate is not considered on the substrate mixing. This phenomenon will be called "biological two-way coupling" and is investigated in this part of the work. Indeed, due to assimilation by the microorganisms, the substrate concentration in the vicinity of the bacteria decreases and transport limitations can arise at the microscopic scale if the substrate feeding is not sufficient, and we will try to characterise the effect of assimilation on substrate mixing and biological performances.

The configuration for this part of the work matches a batch bioreactor where the substrate feeding is not renewed in time and, the substrate concentration decreases during the fermentation. Indeed, from the simulations performed in chapter 3, we keep the flow dynamics, corresponding to the agitation of the bioreactor, and the imposed substrate concentration gradient is removed.

Firstly, we study the biological assimilation with no biological two-way coupling for a decaying turbulence for the substrate in order to introduce the physics of such configuration. Secondly, the numerical setup for the biological two-way coupling are presented and the validation of the biological two-way coupling is briefly introduced. Then, a discussion on the statistics of the fluid flow in term of mixing is proposed and a final section offers a parametric study for the biological phase.

5.1 Decaying turbulence for the substrate

As explained in the introduction of this chapter, an adaptation of the biological two-way coupling to our numerical simulation requires an unsteady configuration of the substrate field. Meaningly, the "bioreactor" is still agitated but, the mixing is no longer forced by substrate injection. When the effects of biological assimilation on the substrate field are not considered, the substrate field will tend to homogenisation and the final state is a perfectly mixed bioreactor. The corresponding equations are presented hereafter, and the balance for substrate concentration are given, as well as temporal evolution of the biological statistics.

5.1.1 Decay of substrate concentration field

The initial substrate concentration field is extracted from the single-phase simulations where the imposed substrate gradient is removed from the total concentration field, whereas no modifications are brought to the velocity field. The instantaneous substrate concentration becomes:

$$S(\mathbf{x}, t) = \langle S \rangle + s'(\mathbf{x}, t). \tag{5.1}$$

The different equations for the substrate concentration evolution are then modified compared to the stationary case and equations (3.32), (3.33) and (3.34) change to the following set of equations:

$$\frac{\partial s'}{\partial t} + u'_{f,j} \frac{\partial s'}{\partial x_j} = \mathcal{D}_{S,f} \frac{\partial^2 s'}{\partial x_j \partial x_j} + \frac{\partial \left\langle u'_{f,j} s' \right\rangle}{\partial x_j}, \tag{5.2}$$

$$\frac{\partial \left\langle {s'}^2 \right\rangle}{\partial t} = \mathcal{D}_{S,f} \frac{\partial^2 \left\langle {s'}^2 \right\rangle}{\partial x_j \partial x_f} - 2\mathcal{D}_{S,f} \left\langle \frac{\partial s'}{\partial x_j} \frac{\partial s'}{\partial x_j} \right\rangle, \tag{5.3}$$

$$\begin{aligned} \frac{\partial \left\langle u'_{f,i} s' \right\rangle}{\partial t} &= -\frac{1}{\rho_f} \left\langle s' \frac{\partial p'}{\partial x_i} \right\rangle \\ &+ \mathcal{D}_{S,f} \left\langle u'_{f,i} \frac{\partial^2 s'}{\partial x_j \partial x_j} \right\rangle \\ &+ \nu_f \left\langle s' \frac{\partial^2 u'_{f,i}}{\partial x_j \partial x_j} \right\rangle. \end{aligned} \tag{5.4}$$

According to equation (5.3) the substrate concentration variance will decrease in time as the substrate dissipation rate. We can also remark here, that the resolution of the fluctuating part of the substrate field is no longer necessary, and the total substrate concentration transport equation (5.5) is solved. In fact, the periodic boundary conditions are applicable for this variable, because the gradient contribution is removed.

$$\frac{\partial S}{\partial t} = \mathcal{D}_{S,f} \frac{\partial^2 S}{\partial x_j \partial x_j}. \tag{5.5}$$

Figure 5.1 presents the different statistics for the fluid flow. The evolution of the substrate-velocity cross correlations is given by figure 5.1a where the component $\langle v'_f s' \rangle$ increases to a null value. This evolution towards zero yields for the decrease of concentration fluctuations until a perfectly homogeneous substrate field. This decrease is also observed for the first moments of the substrate fluctuations as shown by Figure 5.1b, except for the mean concentration that remains constant. The different terms of the equation balance for substrate concentration variance and turbulent flux are also given by Figures 5.1c and 5.1d respectively. For the variance, the balance equation given by equation (5.3) is obtained as well as for the turbulent substrate flux with equation (5.4). We remind here that the statistics for the velocity field remain unchanged. Nevertheless, the effect of the flow dynamics on the substrate concentration field decay is given for the substrate variance in Figure 5.2. Figure 5.2a compares the substrate energy decrease for both simulations $R2$ and $R1$. For a similar initial substrate field, the decay is faster for the higher Reynolds turbulent flow. In Figure 5.2b, the substrate energy decay is compared for simulations $R2$ and $G2$. The evolutions are plotted versus time in order to show the different evolutions. For the same flow dynamics, the bigger the initial substrate energy, the longer the dissipation.

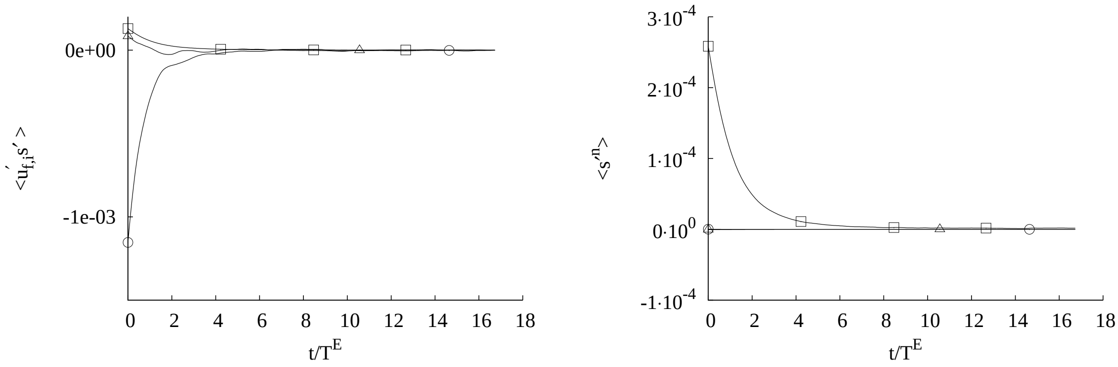

(a) Temporal evolution of the velocity-concentration correlations for the decaying simulation $R2$. □: $\langle u'_f s' \rangle$, △: $\langle v'_f s' \rangle$, ○: $\langle w'_f s' \rangle$ in [kg $\cdot$ m^{-2} $\cdot$ s^{-1}].

(b) Temporal evolution of the first moments of the substrate concentration for the decaying simulation $R2$. □: substrate variance $\langle s'^2 \rangle$ ([kg^2 $\cdot$ m^{-6}]), △: $\langle s'^3 \rangle$, ○: $\langle s'^4 \rangle$.

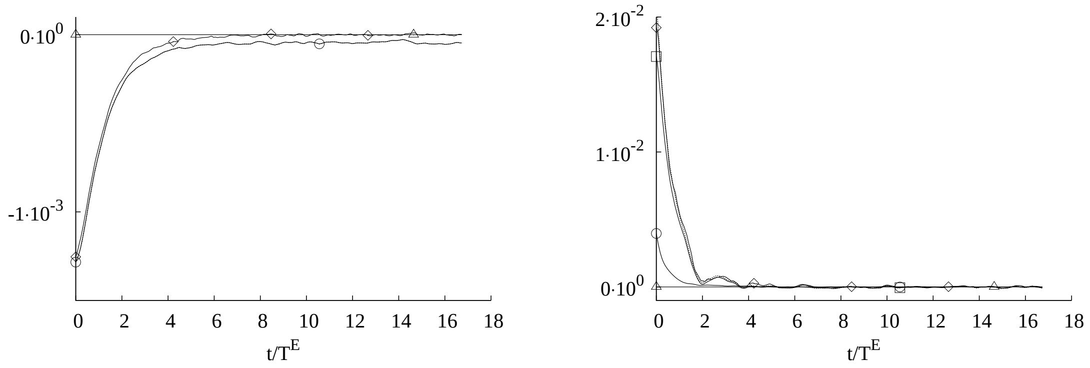

(c) Temporal evolution for the substrate energy balance in the steady state for the decaying simulation $R2$. ◇: $\frac{dq^2_{s,f}}{dt}$, △: $\langle v'_f s' \rangle \frac{d<S>}{dy}$ (production), ○: $\varepsilon_{s,f}$, ········ : sum of the production and dissipation, all in [kg^2 $\cdot$ m^{-6} $\cdot$ s^{-1}].

(d) Temporal evolution of the velocity-concentration correlations balance in y direction for the decaying simulation $R2$. ◇: $\frac{d\langle <v'_f s'\rangle}{dt}$, △: $\langle v'_f s' \rangle \frac{d<S>}{dy}$ (production), □: Pressure contribution, ○: dissipation $\varepsilon_{v's'}$, and ········ : sum of the three contributions, all in [kg $\cdot$ m^{-2} $\cdot$ s^{-2}].

Figure 5.1: Temporal evolution of fluid statistics and equation balance for the fluid kinetic energy and susbstrate concentration energy for the simulation $R2$ in decaying turbulence for the substrate, where T^E is the Eulerian time-scale of the simulation.

The IEM model for an inert scalar in a poorly micro-mixed environment can be applied to the studied configuration. It reduces to (Fox, 2003):

$$\frac{dS}{dt} = -\frac{1}{\tau_s}(S(t) - \langle S \rangle), \tag{5.6}$$

where τ_s is the characteristic time of the model. If we applied this model to the substrate concentration variance, we obtain the corresponding equation for the substrate variance:

$$\frac{d\langle s'^2 \rangle}{dt} = -\frac{2}{\tau_S \langle s'^2 \rangle}. \tag{5.7}$$

The right-hand-side of equation (5.7) is exactly the negative scalar dissipation rate $-\varepsilon_s$. The scalar

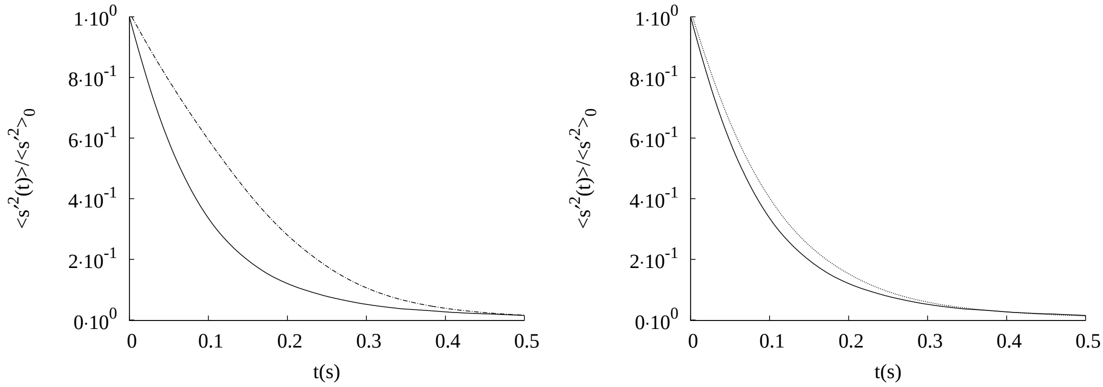

(a) Comparison of simulations $R2$ and $R1$. (b) Comparison of simulations $R2$ and $G2$.

Figure 5.2: Evolution of the substrate variance for decaying simulations $R2$: (———), $G2$: (········) and $R1$: (–·–·–).

Figure 5.3: Substrate variance decrease for simulation $R2$ (———) and comparison with the analytical solution of the IEM model: $\langle s'^2(t)\rangle = \langle s'^2(t)\rangle_0 \exp\big(-\frac{2t}{\tau_\varepsilon}\big)$: (········).

time-scale τ_s is usually linked to the dissipation time scale τ_ε:

$$\tau_s = \frac{2}{r_\varepsilon}\tau_\varepsilon, \tag{5.8}$$

where the mechanical-to-scalar time scale ratio r_ε is usually of order 2 (Pope, 2000).

Thus, the evolution of the substrate concentration variance is known at every time of the simulation and the distribution of the total concentration S is given as a function of the substrate variance. So following the method proposed in chapter 4 for the determination of the uptake rate distribution, the biomass growth and by-product formation can be derived for the decaying substrate concentration configuration.

Then, the substrate concentration spectrum is shown by Figure 5.4 at different times for the simulation $R2$. The fluctuations decay is observed for the small scales and the substrate kinetic energy decreases. By comparison with the steady spectra, the large scale of the substrate field are affected by the substrate fluctuations decrease, and the total amount of energy decreases in time.

The statistics of the biological phase for this decaying configuration are given here after for the cases of simulations $R2$ and $G2$.

5.1.2 Statistics of the biological phase

As for chapter 4, microorganisms are injected in the turbulent field with decaying substrate concentration and the statistics of the particle phase are computed. We chose here to present only the simulation with Monod assimilation law for intermediate affinity to the substrate where the effects were more significant in the previous chapter.

As the substrate concentration fields tends to homogeneity, the deviation of the averaged uptake rate from the macroscopic Monod law is expected to decrease in time. Meaningly, when the substrate

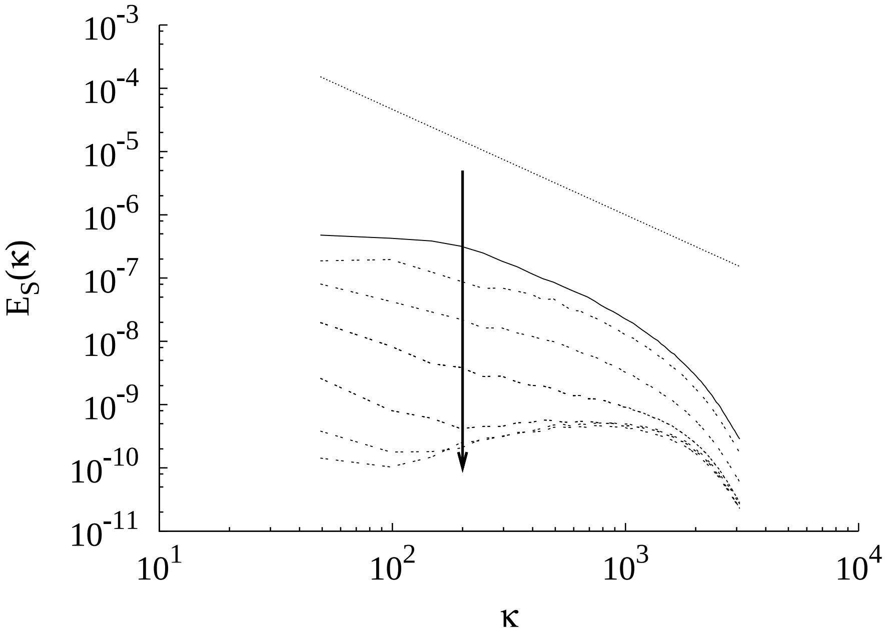

Figure 5.4: Substrate concentration energy spectra for the decaying simulations $R2$. (········) is the $-5/3$ power law.

field is uniform, that is to say perfectly micromixed,the average uptake rate matches the macroscopic Monod law. If we look at Figure 5.5 the ratio $\langle\Phi^*\rangle_p/\Phi^*(\langle S\rangle_p)$ is plotted with respect to the time for the different decaying simulations $R1M$, $R2S_{0.1}M$, $R2S_1M$ and $G2M$. For all simulations, this ratio tends to 1 for long times, meaning that a uniform assimilation is reached in the domain. The initial values of the ratio are in agreement with the observed deviations to the assimilation law based on the averaged concentration. For the simulation $R2S_1M$ with $S_0 = 1\ \mathrm{kg_S \cdot m^{-3}}$ and $k_S = 1\ \mathrm{kg_S \cdot m^{-3}}$ the effect of initial substrate fluctutations is not significant because the initial substrate fluctuations are weak compared to the average concentration. But for simulation $G2M$ where the initial fluctuations are stronger, the average uptake rate increases in time and reaches the macroscopic Monod law.

The equation (4.18) introduced in the previous chapter for the theoretical expression of the average uptake rate reduces to:

$$\langle\Phi^*\rangle_p = \frac{\langle S\rangle_p}{\langle S\rangle_p + k_S} - \frac{\langle\phi'^* s'\rangle_p}{\langle S\rangle_p + k_S}. \tag{5.9}$$

The last term for the gradient contribution is null in the present configuration. The ratio $\langle\Phi^*\rangle_p/\Phi^*(\langle S\rangle_p)$ is expected to evolve in time as $\langle\Phi^*\rangle_p/\Phi^*(\langle S\rangle_p)|_{th} = 1 - \langle s'\phi'^*\rangle_p/\langle S\rangle_p$. This result is verified in Figure 5.6 for the simulation $G2M$ for different affinity constants where the symbols, corresponding to the theoretical ratio, perfectly match the uptake rate ratio.

Further statistics on the biological phase are briefly presented hereafter. The temporal evolution of the cross-correlations and uptake rate variance are shown by Figure 5.7 for the simulation $G2M$ with $k_S = 1\ \mathrm{kg_S \cdot m^{-3}}$. We can see that all statistics decrease in time to reach null values that matches a perfectly mixed bioreactor. As we can see in Figure 5.7a, the decrease of both $\langle\phi'^{2*}\rangle_p$ and $\langle s'\phi'^*\rangle_p$ follow the exact decrease of the variance of substrate concentration of the fluid. This similar evolution is also observed for the velocity-uptake rate cross correlation in figure 5.7b where the symbols are representing the temporal evolution of $\langle v_f' s'\rangle/\langle v_f' s'\rangle_0$ for the fluid. This means that if a model for the substrate decay is developed, the model can be applied to the biological statistics

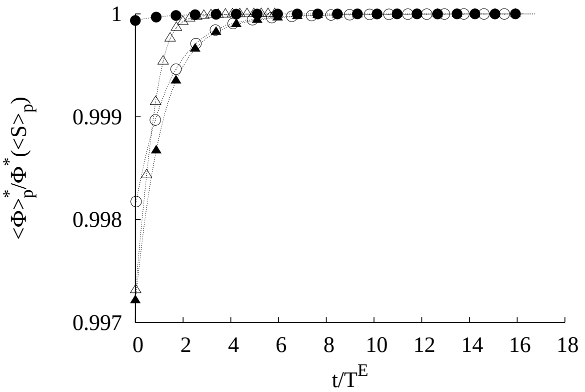

Figure 5.5: Temporal evolution of the ratio $\langle \Phi^* \rangle_p / \Phi^*(\langle S \rangle_p)$ with Monod assimilation model for the simulations $R2S_{0.1}M$: ▲, $R1M$: △ both with $k_S = 0.1\ \mathrm{kg_S \cdot m^{-3}}$, $R2S_1M$: • and $G2M$: ○ both with $k_S = 1\ \mathrm{kg_S \cdot m^{-3}}$ in the decreasing configuration.

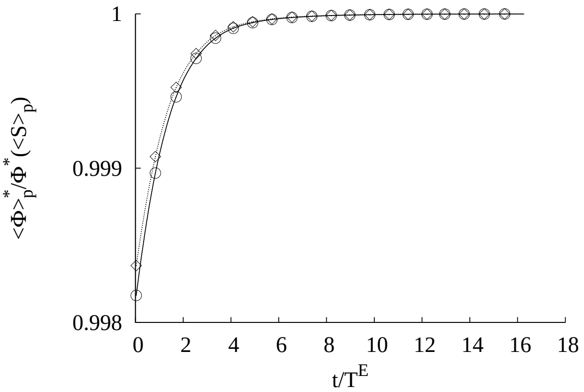

Figure 5.6: Comparison of $\langle \Phi^* \rangle_p / \Phi^*(\langle S \rangle_p)$ (lines) with (symbols) the theoretical ratio $\langle \Phi^* \rangle_p / \Phi^*(\langle S \rangle_p)|_{th}$ for ⋄: $k_S = 0.5\ \mathrm{kg_S \cdot m^{-3}}$ and ○: $k_S = 1\ \mathrm{kg_S \cdot m^{-3}}$.

in the one-way coupling configuration. The cross-correlations in the two other directions are not shown here, but they are two orders smaller than in the y-direction.

Finally, a short overview on the different distributions is proposed. The distributions for the substrate fluctuating concentrations spread in time with gaussian distribution but the variance is decreasing (see Figure 5.8b). In this part of the work, no mean gradient is imposed and the instantaneous substrate concentration distribution is exactly the substrate fluctuation distribution but centred on $\langle S \rangle$. Moreover, for $\langle S \rangle / k_S = 1$, the instantaneous PDF of the fluctuating uptake rate is close to a gaussian with zero mean, for which the variance is smaller than for the fluctuating substrate concentration, and tends to a dirac distribution for large times as shown in Figure 5.8c The distributions of assimilation rate narrows to a dirac distribution as well as the gaussian distribution of the instantaneous concentration. Finally, the distribution of the instantaneous uptake rate gets narrower while the maximum of the distribution is increasing with time.

5.1.3 Conclusion on the decaying turbulence of the substrate

This section was devoted to the study of a decaying configuration for substrate concentration fluctuations, while the flow dynamics remains steady. This approach is a first step in unsteady analysis of biological assimilation. The decaying statistics for the substrate variance, cross-correlations on the fluid pilot the biological statistics for assimilation. This interesting results will be under consideration for first modelling of assimilation. From this point, the biological assimilation will affect the substrate concentration field, namely, the biological two-way coupling is applied.

5.2 Presentation of the biological two-way coupling

5.2.1 Introduction

Over the years, the particle-laden flows have been extensively studied. Most of the theoretical studies are based on the Lagrangian statistical approach. Therefore this approach was chosen

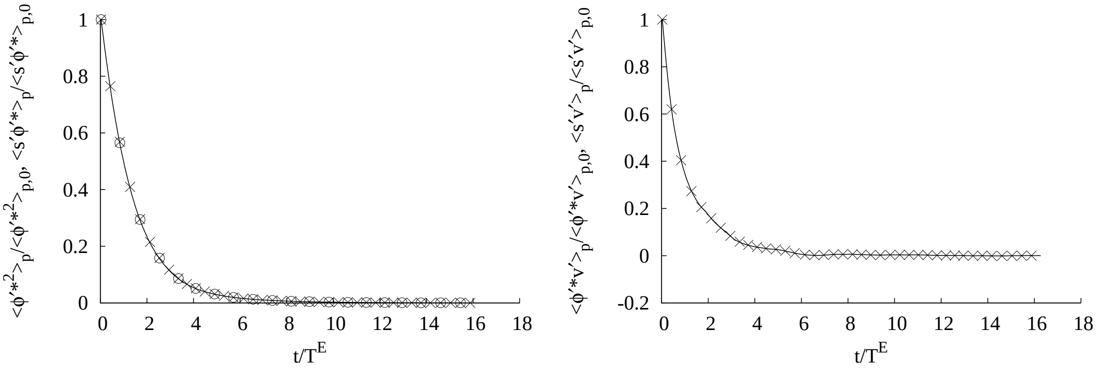

(a) Uptake rate variance (———), uptake rate-substrate concentration correlation ○ and the substrate variance $\langle s'^2 \rangle / \langle s'^2 \rangle_0$ decrease of the fluid ×.

(b) Uptake rate-velocity cross correlation in the y-direction (———) and substrate-velocity cross-correlation $\langle s' v'_f \rangle / \langle s' v'_f \rangle_p$ decrease for the fluid ×.

Figure 5.7: Temporal evolution of biological particle statistics for the simulation $G2M$ with $k_S = 1$ kg$_S \cdot$ m^{-3}.

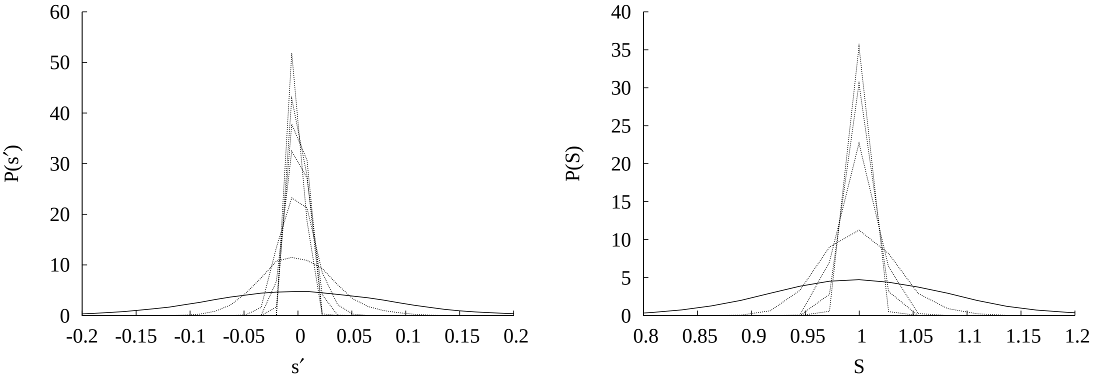

(a) $P(s')$

(b) $P(S)$

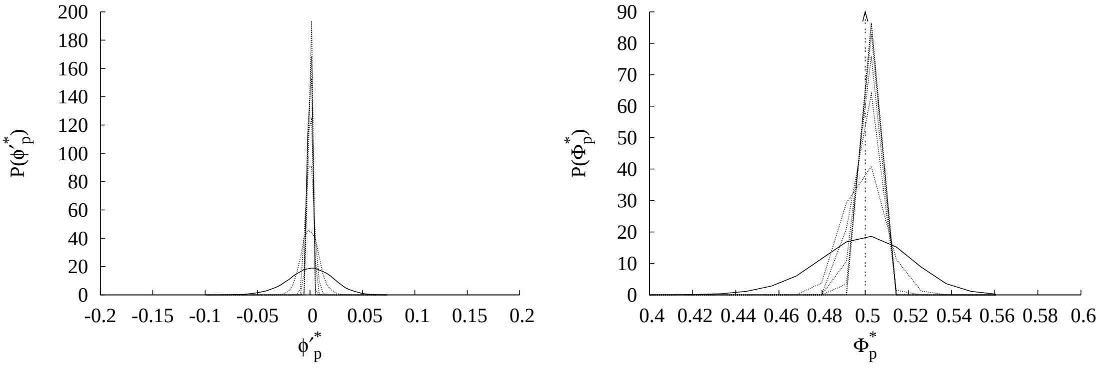

(c) $P(\phi')$

(d) $P(\Phi)$

Figure 5.8: Evolution of PDF distributions for the substrate concentration and uptake rate at different times of the simulation. (———) is the distribution at the beginning of the simulation.

to study biological suspensions. Some authors recently applied this Euler-Lagrange approach for biological suspensions (Lapin et al., 2006). But the present work is more theoretical from the mixing point of view as different existing work on the numerical simulation of bioreactor (Schmalzriedt et al., 2003; Enfors et al., 2001).

By using Direct Numerical Simulation, the constraints involved in the numerical analysis of particle-laden flow and of passive scalar transport are avoided. The full resolution of all scales of the flow is a serious advantage for further modelling of turbulent two-phase flow. Usually the main analysis is focused on the effect of the flow on the particles but recent studies have pointed out the effect of heavy particles (inertial particles) on the carrier fluid in forced turbulence (Squires and Eaton, 1990). Further studies on the dynamic two-way coupling were performed over the years (Elghobashi and Truesdell, 1993a) but heat or mass transfer are not considered. With the aim of better understanding important two-phase turbulent flows with heat or mass transfer, such as evaporation of a spray, combustion, few investigations were proposed, which studied the temperature variations in two-phase turbulent flows (Yarin and Hetsroni, 1994). Later, Mashayek (1998) proposed a numerical study on evaporating droplet dispersion in low-Mach number turbulence, where a two-way coupling is considered. Except for the last cited work, the temperature variations are considered most of the time. Jaberi (1998) proposes a study on the response of particle temperature to the variations in fluid temperature in a four-way coupled flow (meaningly, the inertial particles impacts the carrier velocity field and as well as the particles temperature). By forcing both velocity and temperature field he obtained statistics for homogeneous flow. We can compare this work to the chosen configuration in the present work where both velocity and substrate field were forced. Nevertheless, the inertialess property of microorganisms simplifies the problem in two-way coupling with mass transfer in our simulations.

The forcing method for the scalar differs in Jaberi (1998) from our imposed gradient, therefore it is more appropriate to confront our results with a later work proposed by Jaberi and Mashayek (2000) where the temperature decay is studied in two-phase turbulent flows for one-way and two-way coupling.

In our case the substrate concentration is studied but the same approach is employed for the temperature decay. Moreover, in our biological approach, we do not consider a concentration for the microorganisms, but we focus on the assimilation rate of substrate concentration proper to one microorganism. These considerations are presented in the following part of the work once the computational methodology is introduced. Finally, the validation of the biological two-way coupling is proposed before we present the effect of both the fluid and biological phase properties on assimilation and substrate concentration decrease.

5.2.2 Computational methodology and numerical set-up

In this section, the different numerical tools and the equations of two-way coupling are presented.

5.2.2.1 PSIC method

In chapter 4, the mass flux of one microorganism n, $\Phi_p(S_{@p})$, does not affect the substrate concentration field (one-way coupling). But in the biological two-way coupling, the effect of microorganisms assimilation on the substrate concentration field has to be considered. The mass flux for the microorganism n is expressed as function of the substrate concentration $S_{@p}$ see equation (4.6) for Monod assimilation model for example.

But the microorganism can be everywhere in the computational domain, and not only on the nodes of the Eulerian mesh for the substrate concentration resolution. Therefore the effect of biological assimilation must be divided between the Eulerian mesh. This numerical step is called Projection. Different projection methods exist and the most employed projection methods have initially been developed by Crowe et al. (1977) for gas droplet flows. The Particle Source In Cell (P.S.I.C.) methods divides the source term due to one particle to the mesh-cell in which the particle is located. The source term is projected to the eight nodes surrounding the particle.
Moreover, the repartition on the eight nodes is weighted by the distance between the particle and each of the eight nodes. Indeed, if the particle is close to one node, it is a priori expected that the particle influence is stronger for that node than for the seven others. Some authors proposed different weight methods (Elghobashi and Truesdell, 1993b; Truesdell and Elghobashi, 1994). The weight scheme proposed by Truesdell (1993) is used here. Squires and Eaton (1990) obtained results with this projection scheme for particle response and turbulence modification due to the dynamic two-way coupling (the particles affect the fluid velocity field by the mean of the drag term in the particles trajectory equations due to their inertia). In their work, Jaberi and Mashayek (2000), evaluate the sources terms in fluid momentum and heat equations based on the PSIC method as well.

As mentionned by Boivin et al. (1998), using a projection scheme in the frame of the PSIC method can be seen as a filtering operation for any variable. This filtering operation can be written for the mass flux as:

$$\hat{\Phi}(\mathbf{x},t) = \int_{\Delta} \Phi_p(\mathbf{x}_p,t) H_{\Delta}(\mathbf{x}-\mathbf{x}_p) d\mathbf{x}, \tag{5.10}$$

where H_{Δ} is a top-hat spatial filter. Its characteristic length scale is of order of the size of the mesh-cell. The projection scheme operator H_{Δ} is written:

$$H_{\Delta}(\mathbf{x}-\mathbf{x}_p) = \begin{cases} \prod_{i=1}^{3}(1-\gamma_i) & \text{if} \qquad (x_i - x_{p,i}) < \Delta_i \\ 0 & \text{otherwise} \end{cases} \tag{5.11}$$

where Δ_i is the mesh-cell size in the i^{th} direction and γ_i is the ratio in the i^{th} direction:

$$\gamma_i = \frac{|x_i - x_{p,i}|}{\Delta_i}. \tag{5.12}$$

This projection method will be applied to each microorganism in the biological two-way coupling simulations in order to account for the substrate assimilation effect on the substrate concentration field. In the present configuration for the biological two-way coupling, another numerical tool has to be adapted in order to fulfil the positivity of the substrate concentration field. Further details are given in the next paragraph.

5.2.2.2 Mixed interpolation

As already introduced, the interpolation scheme is very important in the determination of Lagrangian quantities from Eulerian field. Balachandar and Maxey (1989) present different interpolation schemes from the linear method to high order scheme. The Shape Interpolation Method or SFM interpolation has been chosen for the previous simulations. Other interpolation methods give higher accuracy such as the cubic spline method as shown by Fede (2004). This last method has a really high cost, and therefore the SFM is preferred.

The SFM method uses 32 nodes around the particle and this method is almost of second order. The scalar at the particle position is evaluated from the scalar value, and the scalar first derivative at the

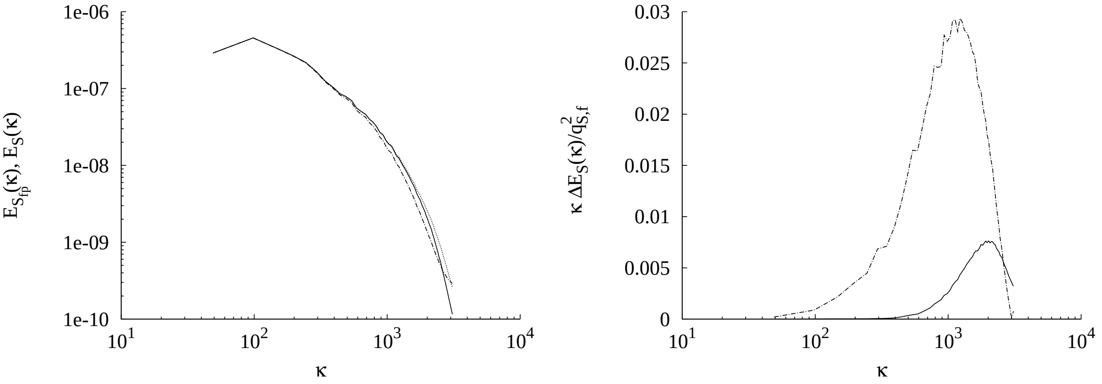

(a) Substrate kinetic energy spectrum.

(b) Relative error.

Figure 5.9: Comparison of Eulerian (········) and interpolated substrate energy spectrum for the SFM (———) and linear interpolation (-·-·-) for the fluid field $R2$.

eight points of the mesh-cell containing the particle. The exact expression for the scalar evaluation is given in Appendix B. In order to validate the interpolation of the substrate concentration at the particle position, the substrate concentration spectra are computed for the Eulerian and Lagrangian grid. The Lagrangian grid is obtained by randomly placing one particle per cell-mesh of the Eulerian grid. The substrate variance obtained from equation (3.73) for both Eulerian ($q^2_{s,f}$) and Lagrangian ($q^2_{s,f@p}$) quantities. Figure 5.9a presents both substrate concentration spectra $E_S(\kappa)$ and $E_{S@p}(\kappa)$ for the simulation $R2$. As we can see, some discrepancies appear for high wave number meaning that the interpolation scheme is not accurate for the small scales, but the errors remain relatively small for the SFM interpolation scheme that is rather chosen.

In the case of the biological two-way coupling, microorganisms eat the surrounding substrate. Therefore, the nodes around one microorganism will carry decreasing substrate concentration. Moreover, the substrate assimilation by microorganisms will create microscopic gradients of concentration between the microorganism and the far-field. This phenomenon is represented by Figure 5.10 in a 1D configuration. If we now discretise the 1D domain, the grid is given by $\times$, the microorganism represented by $\circ$ is located between to nodes $\times$. From a constant substrate concentration field (solid line), the substrate assimilation by the microorganism influences the substrate field and the substrate concentration at the closest nodes decreases (large dashed line in Figure 5.10a). The SFM interpolation in this simple configuration is represented by the different dashed line in Figure 5.10b. If the substrate concentration gradient is important between the nodes of the mesh, negative values of substrate concentration will be obtained at the particle position, as we can see in red (or smaller dashed line). This problematic issue, specific to the biological two-way coupling has been corrected by using a lower order interpolation scheme. Indeed, the linear interpolation bounds the interpolated value between the Eulerian data. Using this method, the interpolated concentration remains positive. This feature is shown in figure 5.10c where the interpolated concentration remains positive (in green or smaller dashed line).

Nevertheless, the linear interpolation scheme is less accurate than the SFM scheme. Indeed, if we compare Figures 5.10b and 5.10c, the interpolated substrate concentration is higher in the case of the linear interpolation. If we now come back to the 3D substrate concentration field, the corresponding substrate concentration spectrum and relative error is given by the dotted-dashed line. As we can see on Figure 5.9b the relative error is 3 times bigger than for the SFM scheme, and more scales are affected by the interpolation. Thus, it is not accurate to use the linear scheme for the different interpolations. Therefore, an alternative solution for the simulation of biological two-way coupling

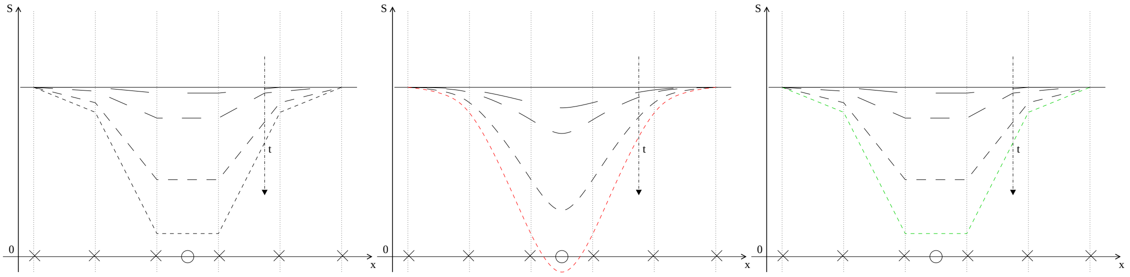

(a) Substrate evolution on the Eulerian grid.
(b) Substrate evolution at the microorganism position using SFM interpolation.
(c) Substrate evolution at the microorganism position using Linear interpolation.

Figure 5.10: 1D representation of substrate assimilation by the microorganism represented by ○. The nodes of the Eulerian grid are represented by ×. (——): initial substrate concentration. (- - - -) substrate profiles from large to narrow dashed.

is to keep the SFM interpolation for velocity interpolation. Concerning the substrate concentration interpolation, the SFM scheme is kept while the interpolated concentration is bounded between the minimum and maximum Eulerian substrate field. If this bounding condition is not locally satisfied, the linear method replaces the SFM method for the given particle. This configuration is shown by Figure 5.11 where the SFM interpolation is used until the red small dashed line is reached and the SFM interpolation no longer suitable. The linear interpolation is then preferred resulting in the green bold-solid line, and further iterations are possible as shown by the dotted line.

Figure 5.12 shows the relative error for different rates of "linear" particles in the domain. Intuitively, the more "linear" particles the bigger the relative error. In order to quantify the error, the relative error between the Eulerian and Lagrangian substrate variance $e_{q^2_{s_{f,f@p}}}$ given by (5.13) is plotted in figure 5.13 against the "linear" rate of particles.

$$e_{q^2_{s_{f,f@p}}} = \frac{q^2_{s,f@p} - q^2_{s,f}}{q^2_{s,f}}. \tag{5.13}$$

As we can see, the relative error on the substrate concentration variance is relatively small and remains constant if the percentage of particle with the linear interpolation scheme is less than 10%. In the different simulations, we paid attention to the evolution of this percentage. But, even if it reaches values higher than 10%, the error will remain less than 5%.

5.2.3 Governing equations

The presented numerical methods are used for the biological two-way coupling. The forthcoming simulations will represent an agitated vessel with an initial substrate concentration field that will decrease due to the local assimilation of microorganisms. The vessel is continuously agitated and is no longer fed with substrate. Thus, the fluid dynamics is unchanged and the statistics on the velocity field introduced in the previous chapter are unchanged. The different assumptions on the biological phase are unchanged as well: the microorganisms are tracers of the fluid and we do not take the biological growth into account.

As the microorganism locally assimilate the substrate, the whole substrate concentration will decrease in the computational domain. As for section 5.1, the simulations are stationary for the

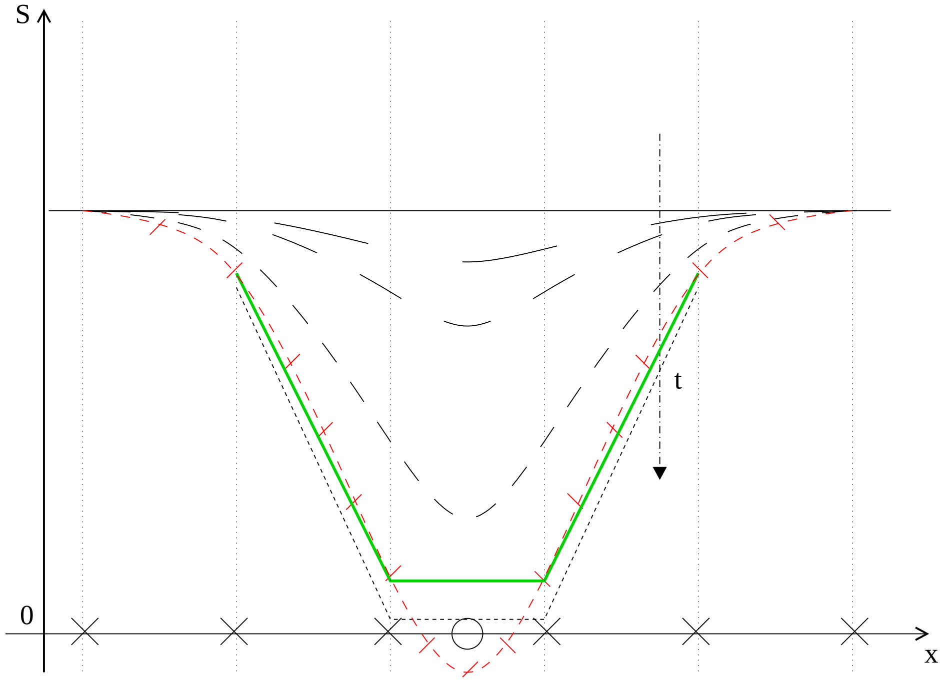

Figure 5.11: Schematic 1D representation of the mixed interpolation principle with SFM interpolation (dashed) and the linear interpolation (———), (········). ▬ is the linear interpolation at the switch with the SFM method.

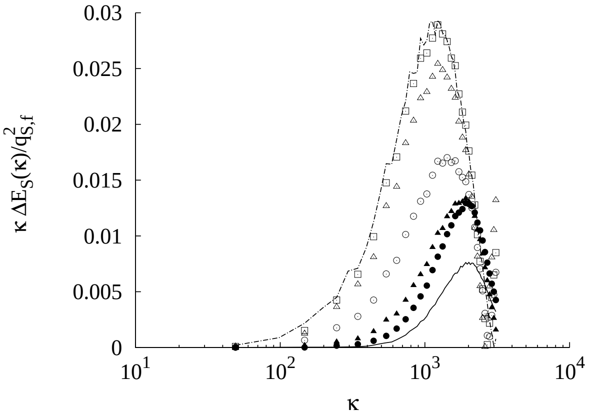

Figure 5.12: Comparison of the relative error for the mixed interpolation for different rates of particles with linear interpolation (in percentage of the total number of particles). Relative error for SFM (———) and linear interpolation (–·–·–) for the fluid field $R2$. •: 1%, ▲: 5%, ○: 20%, △: 50%, ▫: 75%.

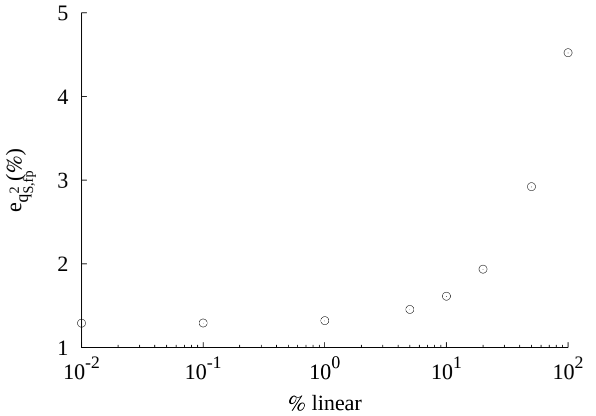

Figure 5.13: Comparison of the relative error for the mixed interpolation for different rates of particles with linear interpolation (in percentage of the total number of particles).

dynamics of the flow, whereas they are unsteady for the scalar. But, an additional term is found for the different Eulerian equations for the substrate concentration. In fact, the total substrate concentration S will decrease in time and the set of equations (5.1) to (5.5) will be modified. Firstly, the averaged concentration $\langle S\rangle$ is now time-dependent (5.14) and an additional term is introduced accounting for the effect of biological assimilation. This last term is written Π_* where the subscript $_*$ refers to the assimilation term in the different transport equations. The different equations involving the substrate concentration are then from the instantaneous evolution of S to the turbulent flux $u'_{f,i}s'$:

$$S(\mathbf{x},t) = \langle S(t)\rangle + s'(\mathbf{x},t). \tag{5.14}$$

$$\frac{\partial S}{\partial t} + u_{f,j}\frac{\partial S}{\partial x_j} = \mathcal{D}\frac{\partial^2 S}{\partial x_j x_j} + \Pi_S, \tag{5.15}$$

$$\frac{\partial s'}{\partial t} + u'_{f,j}\frac{\partial s'}{\partial x_j} = \mathcal{D}_{S,f}\frac{\partial^2 s'}{\partial x_j \partial x_j} + \frac{\partial\left\langle u'_{f,j}s'\right\rangle}{\partial x_j} + \Pi_{s'}, \tag{5.16}$$

$$\frac{\partial\langle S\rangle}{\partial t} = \mathcal{D}_{S,f}\frac{\partial^2\langle S\rangle}{\partial x_j \partial x_j} - \frac{\partial\left\langle u'_{f,j}s'\right\rangle}{\partial x_j} + \Pi_{\langle S\rangle}, \tag{5.17}$$

$$\frac{\partial\left\langle s'^2\right\rangle}{\partial t} = \mathcal{D}_{S,f}\frac{\partial^2\left\langle s'^2\right\rangle}{\partial x_j \partial x_f} - 2\mathcal{D}_{S,f}\left\langle\frac{\partial s'}{\partial x_j}\frac{\partial s'}{\partial x_j}\right\rangle + \Pi_{s'^2}, \tag{5.18}$$

$$\begin{aligned}
\frac{\partial\left\langle u'_{f,i}s'\right\rangle}{\partial t} &= -\frac{1}{\rho_f}\left\langle s'\frac{\partial p'}{\partial x_i}\right\rangle \\
&+ \mathcal{D}_{S,f}\left\langle u'_{f,i}\frac{\partial^2 s'}{\partial x_j \partial x_j}\right\rangle \\
&+ \nu_f\left\langle s'\frac{\partial^2 u'_{f,i}}{\partial x_j \partial x_j}\right\rangle \\
&+ \Pi_{u'_{f,i}s'}.
\end{aligned} \tag{5.19}$$

The assimilation term in the equation of the instantaneous concentration evolution (5.15) is actually a Lagrangian term that accounts for the local effect of microorganisms uptake rate. It is written as:

$$\Pi_S = \sum_{n=1}^{N_p}\Phi_p^{(n)}\delta(\mathbf{x} - \mathbf{x}_p^{(n)}), \tag{5.20}$$

where N_p is the total number of microorganisms, δ is the dirac function and $\Phi_p^{(n)}$ is the local assimilation rate at the microorganism position. As the substrate concentration S is an Eulerian quantity, it is more accurate to consider the term Π_S as a filtered term. The applied filter is the projection scheme as mentionned by Boivin et al. (1998) (see equation (5.10)).

The overall assimilation term is time-dependent. Actually, it depends on the instantaneous local substrate concentration at the microorganisms position $S_{@p}$ and thus evolves in time. Finally, the local assimilation is given by the chosen assimilation law. In the following of the work, only the Monod assimilation law will be investigated, except for the validation of the biological two-way coupling where the Blackman bilinear model was used as we will see in the next section.

5.2.4 Validation of two-way coupling with Blackman assimilation law

Academic configuration

Considering previous equations, the difficulty lies in the determination of the exact assimilation term at the box scale. In order to conduct the validation in a simple manner, an academic configuration was chosen. The cubic box is uniformly filled with substrate and no velocity field is applied. The microorganisms are injected with no inertia. A concentration of one microorganism per cell of the Eulerian mesh is chosen and an equidistant repartition of each microorganism is imposed. Considering the static fluid velocity field in the cubic box, a 64^3 grid was chosen in order to simplify the different calculations. Thus, the total number of microorganisms is $N_p = 64^3$. They all have the same biological properties given in table 5.1. In this configuration, the assimilation is uniform in the computational domain and the substrate concentration should also decrease uniformly.

In the present academic configuration, a 0D balance on the total mass of substrate m_S in the cubic box can be made, and the variation of this quantity due to the assimilation by microorganisms is:

$$\frac{dm_S}{dt} = -\sum_{n=1}^{N_p} m_c r_S, \tag{5.21}$$

where m_c is the mass of one microorganism and r_S is the specific uptake rate for substrate in $[\ \mathrm{kg_S \cdot kg_X^{-1} \cdot s^{-1}}\ ]$. The specific uptake rate for substrate is linked to substrate mass flux by the following equation:

$$\Phi_p = m_c r_S, \tag{5.22}$$

where the mass flux is function of the maximum specific uptake rate, the affinity constant and the instantaneous interpolated concentration at the particle (n) position. Moreover, the substrate concentration is linked to the mass of substrate in the cubic box by:

$$S = \frac{m_S}{V_{box}}. \tag{5.23}$$

So, the general term for the decrease of the substrate mass is:

$$\frac{dm_S}{dt} = -\sum_{n=1}^{N_p} m_c r_S = -\sum_{n=1}^{N_p} \Phi_p, \tag{5.24}$$

and the substrate concentration evolution in the computational domain can be related to the mass decrease by the following equation:

$$\frac{dS}{dt} = -\frac{1}{V_{box}} \sum_{n=1}^{N_p} m_c r_S = -\frac{1}{V_{box}} \sum_{n=1}^{N_p} \Phi_p^{(n)}, \tag{5.25}$$

where $\Phi_p^{(n)}$ is the local mass flux for particle (n) based on the interpolated substrate concentration $S_{@p}$ at the particle position. This equation is valid for any case study. If the specific uptake rate is identical for each microorganism, then equation (5.25) is simplified:

$$\frac{dS}{dt} = -\frac{1}{V_{box}} \sum_{n=1}^{N_p} m_c r_S = -X r_S, \tag{5.26}$$

where $X = N_p m_c / V_{box}$ is the microorganisms concentration in the computational domain.

Table 5.1: Fluid and particle properties for the biological two-way coupling validation.

Domain length	L_{box}	$[\ \mathrm{m}\ ]$	0.128
Nodes	N	$[\ -\ ]$	64^3
Box volume	$Vbox$	$[\ \mathrm{m}^3\ ]$	$2.097152 \cdot 10^{-3}$
Fluid density	ρ_f	$[\ \mathrm{kg} \cdot \mathrm{m}^{-3}\ ]$	1.17
Fluid dynamic viscosity	μ_f	$[\ \mathrm{kg} \cdot \mathrm{m}^{-1} \cdot \mathrm{s}^{-1}\ ]$	$1.52 \cdot 10^{-5}$
Fluid kinematic viscosity	ν_f	$[\ \mathrm{m}^2 \cdot \mathrm{s}^{-1}\ ]$	$1.3 \cdot 10^{-5}$
Particle number	N_p	-	64^3
Particles density	ρ_p	$[\ \mathrm{kg} \cdot \mathrm{m}^{-3}\ ]$	1000
Particles diameter	d_p	$[\ \mathrm{m}\ ]$	$2 \cdot 10^{-6}$
Maximum mass flux	Φ_{max}	$[\ \mathrm{kg_S} \cdot \mathrm{s}^{-1}\ ]$	$1.4\ 10^{-5}$

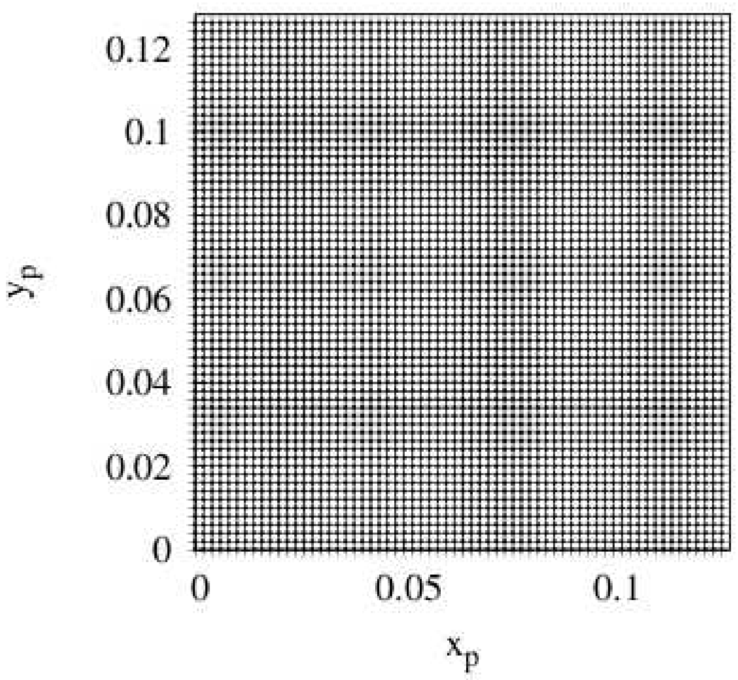

Figure 5.14: 2D view of the Eulerian (•) and Lagrangian (——) grids for the biological two-way coupling validation.

First validation

The microorganisms are fixed points and the microorganisms are located on the nodes of the Eulerian grid. Therefore both Lagrangian and Eulerian grids are identical for the substrate concentration resolution (see Figure 5.14).

In the chosen configuration, there is no distinction between the interpolated and local substrate concentrations, and the assimilation rate at the particle position can be exactly given on the Eulerian mesh with no projection so that the following equalities are validated:

$$S(\mathbf{x},t) = S_{@p} = \langle S \rangle = S, \tag{5.27}$$

$$\Phi_p(S_{@p}) = \Phi_p(S(\mathbf{x},t)) = \langle \Phi \rangle_p = \Phi_p(\langle S \rangle) = \Phi(S). \tag{5.28}$$

The writing S and Φ is then chosen for the validation paragraph. The exact equation for the substrate concentration decrease at one point of the computational grid is:

$$\frac{dS(\mathbf{x},t)}{dt} = -\frac{1}{V_{box}}\Phi(S(\mathbf{x},t)). \tag{5.29}$$

More specifically, as the substrate field is uniform and the microorganisms are equidistant, the total substrate concentration evolution in the computational field is given by the following equation:

$$\frac{dS}{dt} = -\frac{N_p}{V_{box}}\Phi(S(t)). \tag{5.30}$$

Theoretical background

The differential equation (5.30) can be analytically solved and the theoretical expression of the mean substrate concentration evolution is obtained. We chose here to study the Blackman assimilation model for local substrate assimilation by microorganisms:

$$\Phi(S) = \begin{cases} \Phi_{max} & if \quad S > 2k_S \\ \Phi_{max}\frac{S}{2k_S} & if \quad 0 \leqslant S \leqslant 2k_S. \end{cases} \tag{5.31}$$

At this specific part of the work, the Lagrangian and Eulerian quantities are identical. Compared to equation (4.7), no specifications for the particle n or for the interpolated substrate concentration are written here. Given all previous assumptions, the differential equation for the substrate concentration is:

$$\frac{d\langle S\rangle}{dt} = -\frac{N_p}{V_{box}}\begin{cases} \Phi_{max} & if \quad S > 2k_S \\ \Phi_{max}\frac{S}{2k_S} & if \quad 0 \leqslant S \leqslant 2k_S. \end{cases} \tag{5.32}$$

This linear first order differential equation can easily be solved, and the obtained solution requires to categorises different cases depending on the ratio S/k_S. The initial substrate concentration is written $S_0 = S(t=0)$. For a first validation of the biological two-way coupling, the asymptotic cases $S_0 \gg k_S$ and $S_0 \ll k_S$.

- $S_0 \gg k_S$

  If the initial substrate concentration is significantly bigger than the affinity constant for the substrate, the solution of equation (5.32) is linear in time and yields:

  $$S(t) = S_0 - \frac{N_p}{V_{box}}\Phi_{max} t. \tag{5.33}$$

  The temporal evolution of the non-dimensional average substrate concentration and averaged assimilation rate Φ from numerical simulations (symbols) are plotted in Figure 5.15a as well as the analytical solutions. The assimilation rate is constant at its maximal value whereas the substrate concentration decreases linearly in time. While the substrate concentration is bigger than $2k_S$, the linear evolution is observed.

- $S_0 \ll k_S$

  In the case where the initial substrate concentration is smaller than the affinity constant, the solution of equation (5.32) gives an exponential decrease for the substrate concentration:

  $$S(t) = S_0 \exp\big(-\frac{N_p\Phi_{max}}{2k_S V_{box}}t\big). \tag{5.34}$$

  As for the "linear" decrease, the temporal evolution of the non-dimensional average substrate concentration and averaged assimilation rate Φ from numerical simulations (symbols) are shown by Figure 5.15b[1].

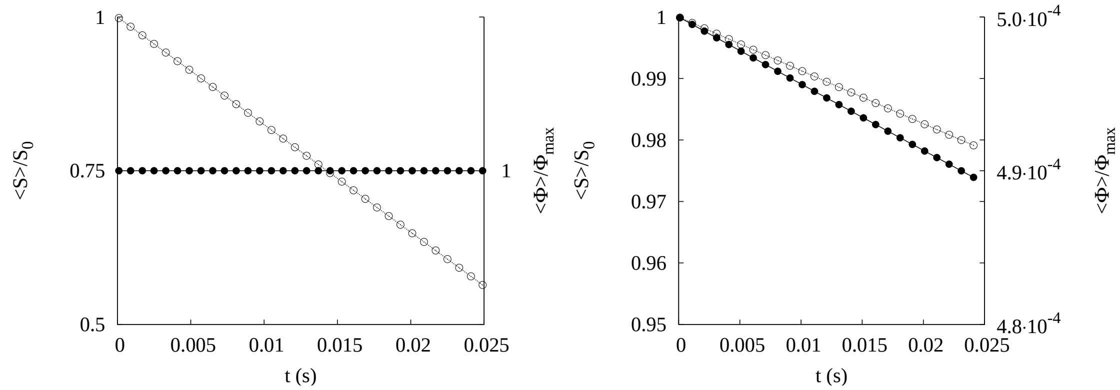

(a) $S_0 = 100$ kg$_{\mathrm{S}} \cdot$ m^{-3} $\gg k_S = 10^{-4}$ kg$_{\mathrm{S}} \cdot$ m^{-3} (b) $S_0 = 1$ kg$_{\mathrm{S}} \cdot$ m^{-3} $\ll k_S = 10^{3}$ kg$_{\mathrm{S}} \cdot$ m^{-3}

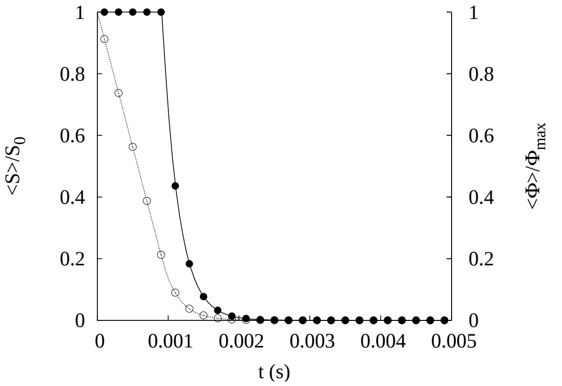

(c) $S_0 = 2$ kg$_{\mathrm{S}} \cdot$ m^{-3} $\simeq k_S = 0.2$ kg$_{\mathrm{S}} \cdot$ m^{-3}

Figure 5.15: Temporal evolution of the non-dimensional averaged substrate concentration ○ and uptake rate • obtained from the numerical simulation. (——) and (········) are the analytical solutions for $S(t)/S_0$ and Φ/Φ_{max} respectively.

Finally, in the case where the substrate affinity and the initial concentration are close the analytical resolution of equation (5.32) is given by the following set of equations, where the time t_1 is the time where $S(t_1) = 2k_S$.

$$\left\{ \begin{array}{lll} S(t) = S_0 - \frac{N_p}{V_{box}} \Phi_{max} t & \text{while} & S(t) > 2k_S \;\Leftrightarrow\; t < (S_0 - 2k_S)\frac{V_{box}}{N_p \Phi_{max}} \\ S(t_1) = S_0 - \frac{N_p}{V_{box}} \Phi_{max} t_1 & \text{if} & S(t_1) = 2k_S \;\Leftrightarrow\; t_1 = (S_0 - 2k_S)\frac{V_{box}}{N_p \Phi_{max}} \\ S(t > t_1) = 2k_S \exp\big(- \frac{N_p \Phi_{max}}{2k_S V_{box}} (t - t_1)\big) & \text{if} & S(t) < 2k_S \;\Leftrightarrow\; t > (S_0 - 2k_S)\frac{V_{box}}{N_p \Phi_{max}} \end{array} \right. \tag{5.35}$$

The corresponding evolution is given by Figure 5.15c. For small times, the concentration remains higher than $2k_S$ with a constant assimilation rate. Then further followed by an exponential decrease.

As we can observed on figure 5.15, the numerical results match the theoretical evolution in all the different cases. This observation is a first step in the validation of the biological two-way coupling implementation.

Projection validation

The next step of validation for the biological two-way coupling implementation, is the projection scheme. Indeed, in the previous case, the microorganisms are located on the Eulerian grid for the scalar resolution. In order to validate the projection scheme, the microorganisms are staggered from the Eulerian grid. Nevertheless, there are still equidistant from each other. The advantage of this configuration, shown in Figure 5.16, is to allow the same uniform decrease of substrate concentration as previously obtained. Different cases were investigated (different grids of microorganisms position). In all cases, the obtained results were in agreement with the analytical solutions and thus the projection scheme was validated.

Assimilation limitation for small concentrations

In some specific cases, the calculated assimilation rate by one microorganism can be too high compared to the available substrate concentration in the domain. Indeed, if we write rudely the substrate decrease due to assimilation at one point of the computational domain for one time-step of the numerical simulation we have:

$$\frac{\Delta S}{\Delta t} = \frac{\Phi}{V}. \tag{5.36}$$

where V is the volume of the computational cell around the particle. If the time step of the simulation (given by the dynamics of the flow) is high compared to the biological assimilation time that can be defined as $\Delta t_{bio} = SV/\Phi$, then some situations appear where $\Phi/V\Delta t \geqslant S$, meaning that the microorganisms assimilate more substrate than the available substrate with resulting negative substrate concentrations. This numerical issue is addressed by adding a limiting substrate concentration for the assimilation. Meaningly, a limiting value of substrate concentration S_{lim} is locally applied to the cases where the assimilation is higher than the assimilation prescribed by the available substrate concentration:

$$\Phi/V\Delta t = S + S_{lim}. \tag{5.37}$$

A study on the effect of this substrate limitation concentration is briefly presented for the validation case. Different simulations were performed for various S_{lim} for the Blackman assimilation model. The assimilation is uniform in the whole computational domain, and the results for the substrate

---

[1] The evolution is plotted for small times therefore the exponential decrease is not observed for the given times.

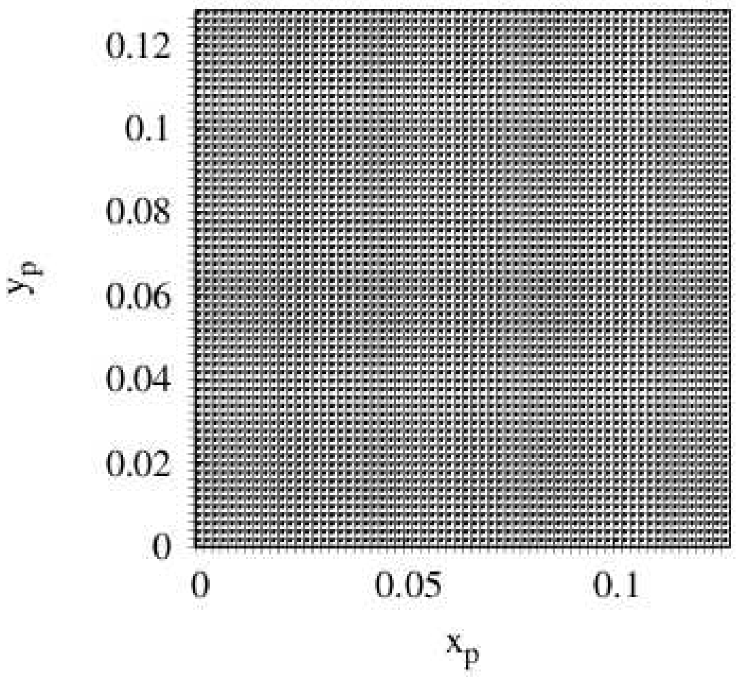

Figure 5.16: 2D view of the Eulerian (•) and staggered Lagrangian (——) grids for the biological two-way coupling validation.

concentration decrease and assimilation rate are given by Figure 5.17. In all simulations, the critical assimilation concentration is reached at the same time $t \simeq 45$ ms where the value of the substrate concentration is approaching the numerical error of the computer, and a plateau at the imposed limiting concentration is reached for the substrate concentration when the limitation is applied. The same conclusions are found for the assimilation rate. Moreover, the smaller the limiting concentration S_{lim}, the smaller the error for both the concentration and assimilation rate. Therefore, the limiting concentration will be set at $S_{lim} = 10^{-16}$ $\mathrm{kg_S \cdot m^{-3}}$ in the further simulations, so the calculations remain exact as long as $S > 10^{-16}$ $\mathrm{kg_S \cdot m^{-3}}$

5.2.5 Validation with Monod assimilation model

The biological two-way coupling was also investigated using the Monod assimilation model for the same validation configuration, so that[2]:

$$\frac{dS}{dt} = -\frac{N_p}{V_{box}}\Phi(S(t)), \tag{5.38}$$

where Φ_p is the Monod assimilation rate for one microorganism:

$$\Phi = \Phi_{max}\frac{S}{k_S + S}. \tag{5.39}$$

The temporal evolutions of the fluid substrate concentration $S = \langle S \rangle$ and the normalised flux[3] $\Phi^* = \langle \Phi^* \rangle$ are given by Figure 5.18 for two different affinity constants k_S. The first configuration

---

[2] in this configuration the notations (5.27) and (5.28) are still equivalent.

[3] where the * superscript corresponds to the non-dimensionalisation of the mass flux by the maximum mass flux Φ_{max}.

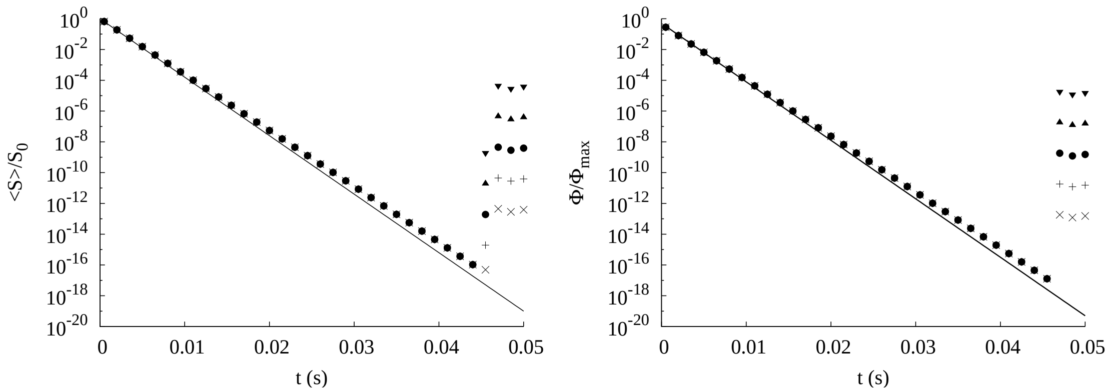

(a) Substrate concentration decrease

(b) Uptake rate evolution

Figure 5.17: Effect of the limiting substrate application on the substrate concentration and uptake rate evolution for $S_0 = 1\ \mathrm{kg_S \cdot m^{-3}}$ and $k_S = 1\ \mathrm{kg_S \cdot m^{-3}}$. ×: $S_{lim} = 10^{-12}$, +: $S_{lim} = 10^{-10}$, •: $S_{lim} = 10^{-8}$, ▴: $S_{lim} = 10^{-6}$, ▾: $S_{lim} = 10^{-4}$ in $[\ \mathrm{kg_S \cdot m^{-3}}\ ]$. (———) is the analytical evolution.

with large k_S is unphysical but yields as a validation case. The biological parameters and fluid properties are unchanged and can be found in table 5.1. As for the Blackman assimilation model, the influence of the substrate affinity constant is important, and for large k_S both evolution are linear-like, whereas for small k_S, two regimes are observed as for the Blackman assimilation model.

The analytical resolution of equation (5.38) involves the LambertW function and will not be presented here. But, the continuous nature of the Monod assimilation model is a property that we take advantage of by deriving equation (5.38) to obtain:

$$\frac{d^2S}{dt^2} = -\frac{N_p}{V_{box}}\frac{d\Phi}{dt} = -\frac{N_p}{V_{box}}\frac{\Phi_{max}}{S + k_S}\frac{dS}{dt}(1 - \frac{\Phi}{\Phi_{max}}). \tag{5.40}$$

In order to fullly validate the biological two-way coupling implementation, the evolution of the first and second derivative of $S = \langle S \rangle$ and the first derivative of Φ are compared in Figure 5.19. As we can see in Figure 5.19a, the substrate concentration first derivative and the weighted particle uptake rate are exactly similar. But, if we look at the evolution based on the substrate concentration, the evolution is not similar. This error is explained by the fact that the obtained substrate concentration $S_{@p} = S$ is estimated after consumption by the microorganisms. But the uptake rate is computed from the initial substrate concentration, at the beginning of the time-step. In Figure 5.19b, the second derivative of the substrate concentration presents a peak and the first derivative of the uptake rate is equivalent. The discrepancies are still observed when the evaluation is based on the fluid substrate concentration. Nevertheless, considering previous considerations, the biological two-way coupling has been validated for Monod assimilation model.

Biological two-way coupling implementation and validation

This part of the work was devoted to the definition of the two-way coupling and to the introduction of different numerical setup required. The biological two-way coupling was validated for an academic configuration with the Blackman bilinear assimilation model, that presents advantages for analytic study. First results on biological two-way coupling are proposed in the following paragraph accounting for a more realistic configuration where microorganisms are randomly located.

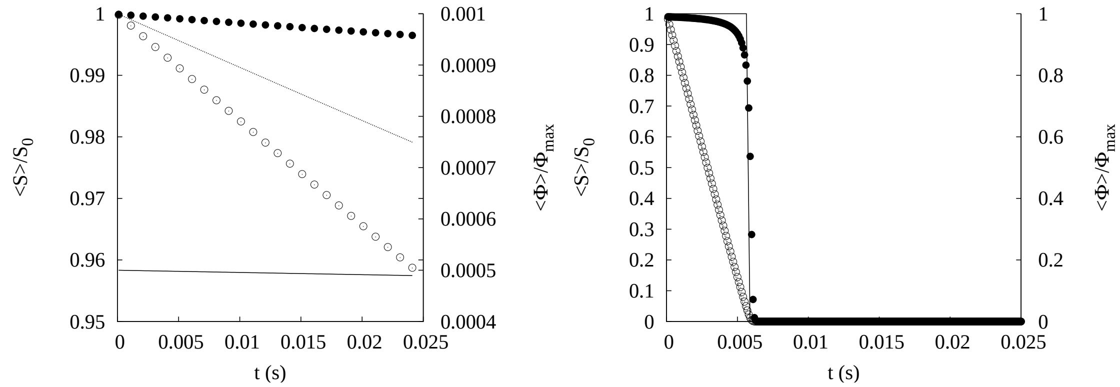

(a) $S_0 = 1$, $k_S = 10^3$ in $[\ \mathrm{kgs} \cdot \mathrm{m}^{-3}\ ]$ (b) $S_0 = 10$, $k_S = 10^{-3}$ in $[\ \mathrm{kgs} \cdot \mathrm{m}^{-3}\ ]$

Figure 5.18: Temporal evolution of the non-dimensional averaged substrate concentration ○ and uptake rate • obtained from the numerical simulation for Monod assimilation model. (———) and (········) are the analytical solutions for $S(t)/S_0$ and Φ/Φ_{max} for the corresponding parameter with Blackman assimilation model.

Table 5.2: Biological parameters for the inhomogeneous assimilation configuration.

Assimilation model			Blackman	Monod
Microorganism diameter	d_p	[m]	$2 \cdot 10^{-6}$	$2 \cdot 10^{-6}$
Maximum uptake rate	Φ_{max}	$[\ \mathrm{kgs} \cdot \mathrm{s}^{-1}\ ]$	$1.4 \cdot 10^{-5}$	$1.4 \cdot 10^{-5}$
Affinity constant	k_S	$[\ \mathrm{kgs} \cdot \mathrm{m}^{-3}\ ]$	10^{-1}	10^{-1}
Initial substrate concentration	S_0	$[\ \mathrm{kgs} \cdot \mathrm{m}^{-3}\ ]$	1	1
Microorganisms concentration	$\langle X\rangle/S_0$	-	$5.2 \cdot 10^{-7}$	$5.2 \cdot 10^{-7}$
Variance ratio	$\sigma_X/\langle X\rangle^2$	-	0	0
Variance ratio	$\sigma_X/\langle X\rangle^2$	-	$7.62 \cdot 10^{-2}$	$7.62 \cdot 10^{-2}$
Variance ratio	$\sigma_X/\langle X\rangle^2$	-	$2.98 \cdot 10^{-1}$	$2.98 \cdot 10^{-1}$

5.2.6 Inhomogeneous assimilation

The different results for validation were obtained for a 64^3 grid ($\Delta x = 2 \cdot 10^{-3}$m) and a total number of $N_p = 64^3$ microorganisms. The corresponding microorganisms concentration $\langle X\rangle = N_p \rho_p V_p / V_{box}$ is given in Table 5.2 as well as the different parameters of the calculations.

The equidistant position of microorganism with no variance for the microorganisms concentration is not realistic. Therefore we study two additional repartitions of microorganisms in the domain, keeping the total concentration $\langle X\rangle$ constant. By projection of the microorganisms Lagrangian field on the Eulerian field, the microorganisms non-homogeneities are characterised by the microorganisms variance given by $\sigma_X = \langle x'x'\rangle$, with the decomposition $X = \langle X\rangle + x'$ where X is the local concentration at node $\mathbf{x}$, $\langle X\rangle$ is the averaged microorganism concentration and x' is the fluctuating part of the microorganisms concentration field. The three studied repartitions of microorganisms are presented by Figures 5.20, where the microorganisms concentration variance σ_X increases.

The evolution of the averaged assimilation rate with respect to the averaged substrate concentration for different microorganisms concentration variances is shown by Figure 5.21 for both Blackman and Monod assimilation models. Important deviations are observed for the averaged assimilation rate compared to the case of equidistant microorganisms $\sigma_X = 0$ (solid lines). The microscopic law is not longer observable at the macroscopic scale due to microorganisms heterogeneities. Meaning

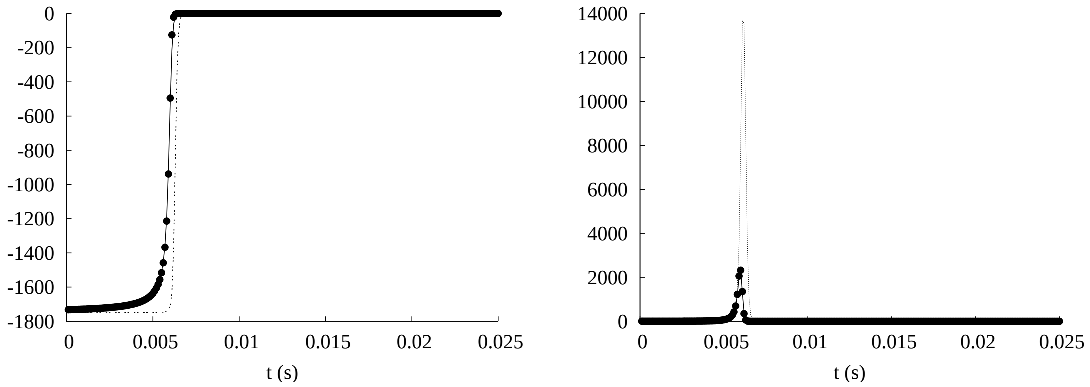

(a) $\frac{dS}{dt}$ (b) $\frac{V_b}{N_p \Phi_{max}} \frac{d^2 S}{dt^2}$

Figure 5.19: Temporal evolution of the first (a) and second derivative (b) of the substrate concentration (———). The uptake rate Φ is given by •. (········) line is the evolution based on the substrate concentration in equations (5.39) and (5.40). Both results for $S_0 = 10$, $k_S = 10^{-3}$ in [$\mathrm{kg_S \cdot m^{-3}}$].

that without mixing, the heterogeneities of substrate concentration increase, leading to a decrease in the total amount of assimilated substrate. The fact that no velocity field is applied increases the heterogeneities for the substrate concentration field. Even if this configuration is not realistic, this first result in a static cases shows the direct impact of the initial position of microorganism. In other words, if the biomass repartition is not uniform in the bioreactor, the assimilation of substrate will be much more important in zones where the biomass is highly concentrated, and the slight decrease of substrate concentration in the same zone will affect the assimilation rate in turn. We will now study the effect of agitation and mixing on the substrate decrease for a population of microorganisms.

Figure 5.22 presents a 2D view for the particle field and the substrate field concentration in the case of randomly located particle with $\sigma_X/\langle X \rangle^2 = 2.98 \cdot 10^{-1}$ for the Blackman assimilation model. The biological parameters are given in the caption of Figure 5.22. The particles have no velocity and the more particles at one point, the more substrate is assimilated, the smaller the residual substrate concentration. It can be seen that as already explained the concentration is lower where the local concentration of cells is high. This correlation between the substrate and microorganisms fields is due to the fact that particles are immobile in this case.

5.3 Study of the substrate concentration decay

Following the idea to model a batch reactor, we will now focus on a more realistic configuration, where the microorganisms are transported by a turbulent carrier flow. The initial substrate concentration field is obtained from the steady simulations and the imposed gradient is removed. The microorganisms will thus locally assimilate substrate, and the overall substrate concentration in the fluid decreases due to the consumption by the microorganisms. Simultaneously, the agitation is maintained: so that the turbulent mixing also impacts the substrate scalar field.

The main results on substrate concentration decay from an initial turbulent will be presented here. By forcing the velocity field, the dynamics of the flow are stationary. The different results are obtained from the initial substrate turbulent field $R2$ with $S_0 = 1\ \mathrm{kg_S \cdot m^{-3}}$ with no contribution of the mean gradient. The time-evolution of the different statistics of the flow are presented hereafter

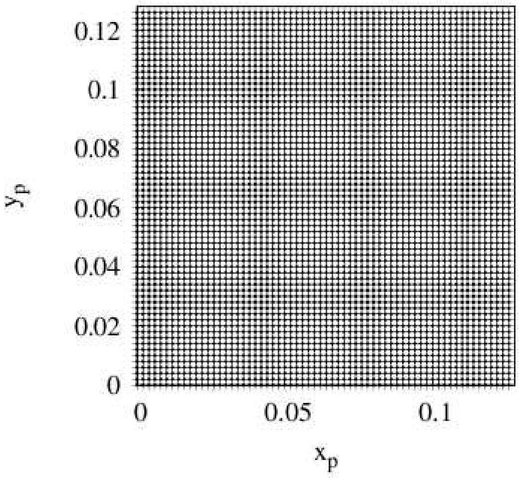

(a) $\sigma_X/\langle X\rangle^2 = 0$

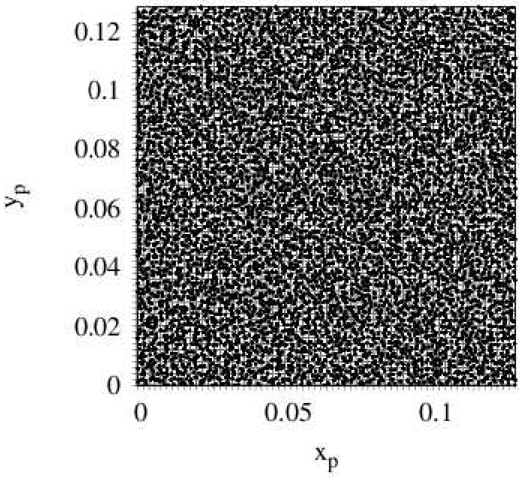

(b) $\sigma_X/\langle X\rangle^2 = 7.62 \cdot 10^{-2}$

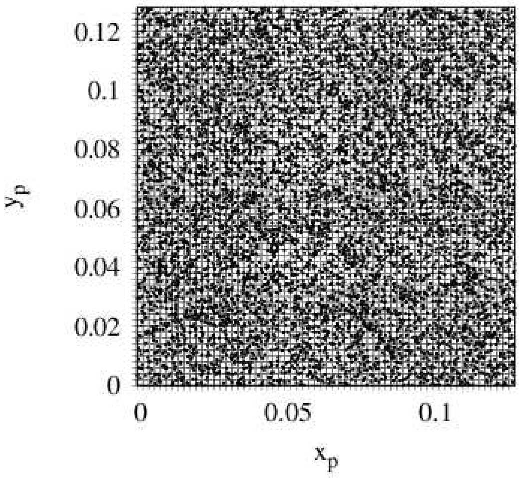

(c) $\sigma_X/\langle X\rangle^2 = 2.98 \cdot 10^{-1}$

Figure 5.20: Different initial positions for the particle field.

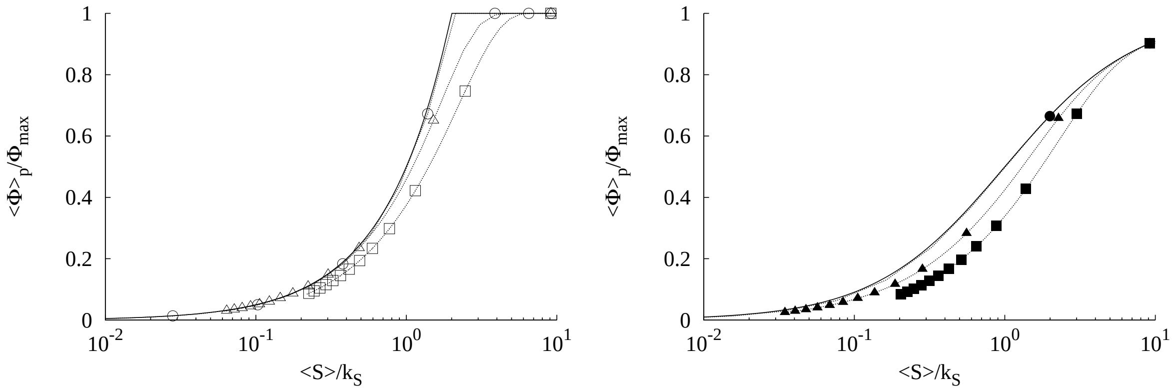

(a) Blackman

(b) Monod

Figure 5.21: Non-dimensional averaged resulting uptake rate for Blackman (a) and Monod (b) assimilation model with respect to the non-dimensional averaged concentration $\langle S \rangle / k_S$. ○, ●: $\sigma_X / \langle X \rangle^2 = 0$, △, ▲: $\sigma_X / \langle X \rangle^2 = 7.62 \cdot 10^{-2}$ and ▫, ■: $\sigma_X / \langle X \rangle^2 = 2.98 \cdot 10^{-1}$. (———) is the theoretical evolution for Blackman assimilation model.

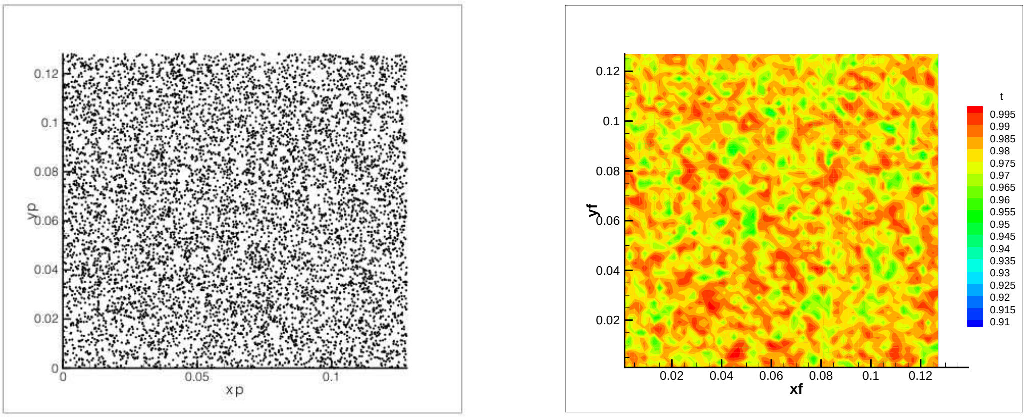

(a) Particle field

(b) Substrate concentration field

Figure 5.22: 2D view of particle (a) and substrate concentration field (b) for Blackman assimilation model with $S_0 = 1$, $k_S = 10^3$ (in [$\mathrm{kg_S \cdot m^{-3}}$]) at $t = 2.5 \cdot 10^{-2}$ s.

with respect to the time. The numerical parameters and the different initial parameters for the flow field and biological phase are given in Table 5.3.

5.3.1 Fluid statistics evolution

Firstly, the mean concentration temporal evolution is given in Figure 5.23. At first glance, the evolution give the impression to be divided in two parts. For $t/T^E \leqslant 1.5$, the decrease seems to be linear, then an exponential decrease could be observed. Moreover, the change in the slope is observed for the ratio $\langle S(t) \rangle / k_S \simeq 1$. This result has already been observed in the validation section for both Blackman and Monod assimilation law. In other terms, the substrate concentration seen by the microorganisms is limiting when it is less than k_S and the assimilation regime is in the "linear" zone for $\langle S \rangle > k_S$.

The statistics of the fluid are shown by Figures 5.24 and 5.25 for the simulation $R2$ with $S_0 =$

Table 5.3: Fluid and particle initial properties for substrate decrease.

Domain length	L_{box}	[m]	0.128
Nodes	N	[−]	128^3
Fluid density	ρ_f	[$\mathrm{kg \cdot m^{-3}}$]	1.17
Fluid dynamic viscosity	μ_f	[$\mathrm{kg \cdot m^{-1} \cdot s^{-1}}$]	$1.52 \cdot 10^{-5}$
Fluid kinematic viscosity	ν_f	[$\mathrm{m^2 \cdot s^{-1}}$]	$1.3 \cdot 10^{-5}$
Initial substrate variance	$\langle s'^2 \rangle_0$	[$\mathrm{kg_S^2 \cdot m^{-6}}$]	$1.4 \cdot 10^{-4}$
Initial substrate average concentration	$\langle S \rangle_0 = S_0$	[$\mathrm{kg_S \cdot m^{-3}}$]	1
Particle number	N_p	-	$2 \cdot 10^5$
Particles density	ρ_p	[$\mathrm{kg \cdot m^{-3}}$]	1000
Particles diameter	d_p	[m]	$2 \cdot 10^{-6}$
Particle total concentration	X	[$\mathrm{kg \cdot m^{-3}}$]	$3.99 \cdot 10^{-7}$
Maximum mass flux	Φ_{max}	[$\mathrm{kg_S \cdot s^{-1}}$]	10^{-7}
Affinity constant	k_S	[$\mathrm{kg_S \cdot m^{-3}}$]	0.1

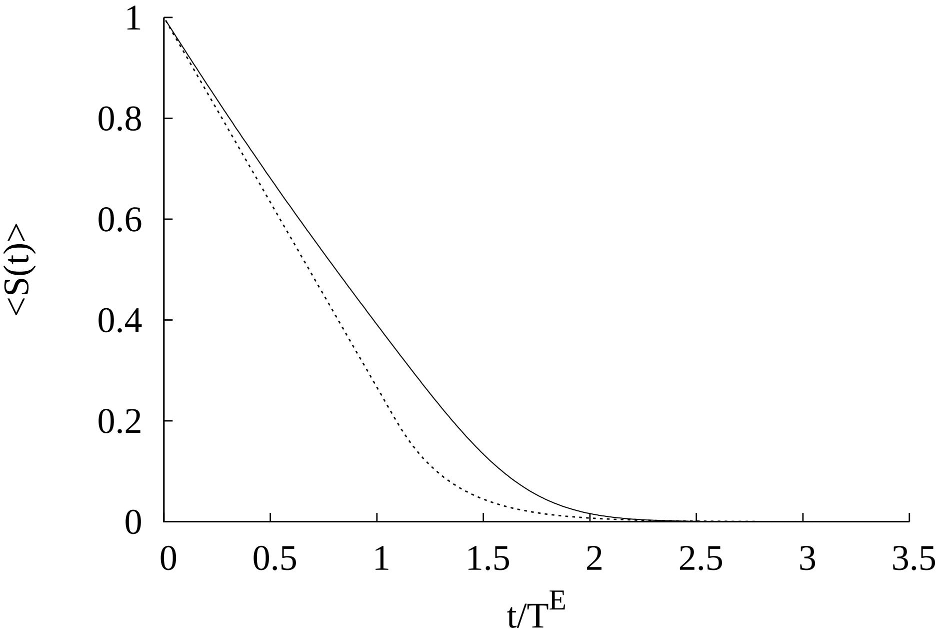

Figure 5.23: Temporal evolution of the mean substrate decrease with Monod model (——) for simulation $R2$. (········) corresponds to the analytical expression for the substrate decrease for Blackman assimilation law (5.35).

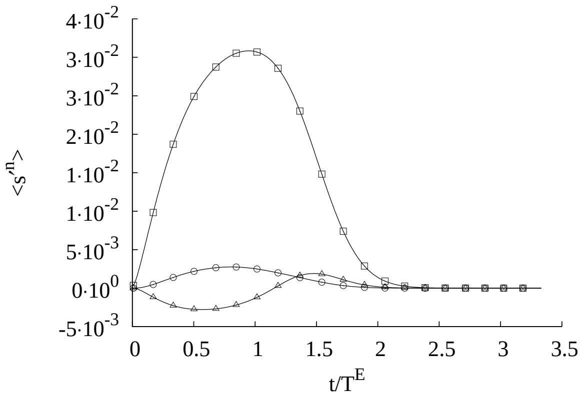

Figure 5.24: Temporal evolution of the first moments of the substrate concentration fluctuations.$\langle s'^2\rangle$: ▫, $\langle s'^3\rangle$: △, $\langle s'^4\rangle$: ○.

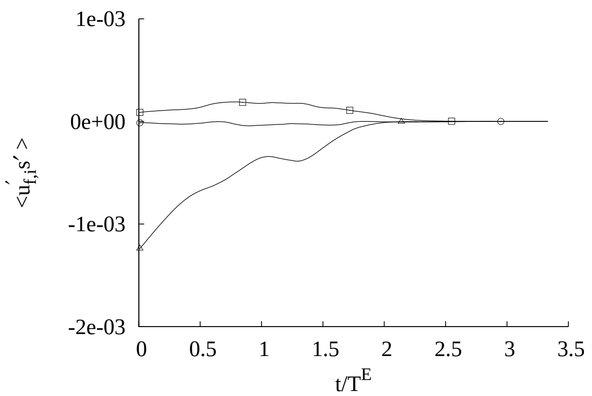

Figure 5.25: Temporal evolution of the velocity-substrate cross-correlations. ▫: $\langle u'_f s'\rangle$, △: $\langle v'_f s'\rangle$, ○: $\langle w'_f s'\rangle$.

1 $\text{kg}_\text{S} \cdot \text{m}^{-3}$. As we can see on Figure 5.24, the substrate concentration variance does not decrease in time. By comparison with the results obtained in section 5.1, we can confirm that the substrate assimilation by microorganisms increases the substrate fluctuations in the domain. The variance initial overshoot has also been observed by Jaberi and Mashayek (2000) for the temperature variance with two-way coupling. But as we perform non-stationary simulations, there is no stationary state for the substrate concentration field and the substrate concentration variance vanishes to zero.

Concerning the third order moment $\langle s'^3\rangle$: △, we can see that it first decreases and then becomes positive. This non-zero value for this moment is showing the non-gaussian nature of the substrate fluctuations distribution in time. This results will be discussed in section 5.3.5. Indeed, the odd-numbers moments are zero for gaussian distribution. The evolution of the substrate concentration-velocity cross correlations is more or less similar to the decay with no biological two-way coupling. But, in the x-direction, a small increase is observed whereas a change in the slope is observed in the y-direction at $t/T^E \simeq 1$. In order to approach the effect of substrate assimilation in time, the different terms of the balance equations are scrutinised in the following paragraph.

5.3.2 Fluid Balances evolution

The different terms of equations (5.17) to (5.19) are known from the DNS simulations, except the last term of each equation that accounts for the biological two-way coupling. The following part is devoted to evaluate the weight of the different assimilation terms in the different balance equations. The determination of this term can be of prime interest in modelling the substrate concentration distributions for example. First steps to model those term are also proposed.

Firstly, the different terms of the balance equation (5.17) are plotted in Figure 5.26. In Figure 5.26b, the diffusional term and the cross-correlation derivative are plotted at a smaller scale. The latter are verified to be negligible. Indeed, by construction they are null and do not affect the substrate concentration transport equation. This results is verified here and the averaged term for biological substrate assimilation $\Pi_{\langle S\rangle}$ from equation 5.17 is then equal to the mean concentration derivative.
As observed in the previous chapter, the well macro-mixed state of the substrate field, gives good results for the extrapolated macroscopic assimilation law based on the mean substrate concentration. Therefore, based on the results of the validation part, we propose a first approximation for the mean assimilation term. It corresponds to the opposite of the assimilation term based on the average

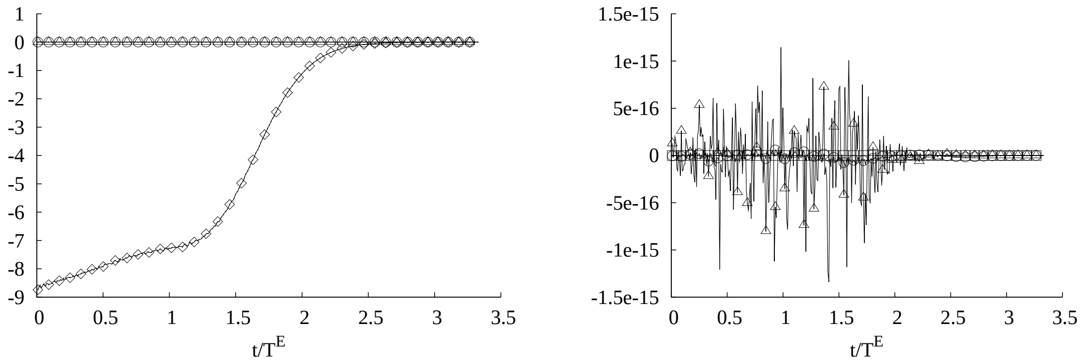

(a) Terms of the balance equation on average substrate concentration.

(b) Focus on the right-hand-side of equation (5.17) except for the assimilation term.

Figure 5.26: Temporal evolution of the different terms of equation (5.17) for the simulation $R2$ and the parameters of Table 5.25. $\diamond$: $\frac{d\langle S\rangle}{dt}$, $\circ$: $\mathcal{D}_{S,f}\frac{\partial^2\langle S\rangle}{\partial x_j \partial x_j}$, $\triangle$: $-\frac{\partial\langle u'_{f,j}s'\rangle}{\partial x_j}$.

concentration with Monod model:

$$\Pi_{\langle S\rangle}(\langle S\rangle) = \frac{N_p}{V_{box}}\Phi_{max}\frac{\langle S\rangle}{\langle S\rangle + k_S}. \tag{5.41}$$

We present in Figure 5.27 both modelled assimilation term and the mean substrate derivative. As we can observe, the approached term is in good agreement with the evolution of the first derivative of the mean substrate concentration, except at the beginning of the assimilation process. This result can be explained by analysing the substrate concentration fluctuations. Indeed, local substrate concentration gradients appear due to assimilation. The fluctuation concentration distribution for the fluid widens in the first instants. Thus, the wider the substrate concentration distribution, the higher the deviation from the macroscopic assimilation law based on the mean concentration. This observation is encouraged by the slightly increase of the substrate concentration variance as observed on Figure 5.24.

Now we examine the different terms of equation (5.18). As expected the variance derivative remains positive since the variance increases for $t/T^E < 1$, then the derivative becomes negative and the variance diminishes. The substrate variance dissipation term ε_s presents an unexpected evolution in time. Indeed after an important increase of this term, a smoother increase leads to a final decrease of the dissipation. If we look at the values reached by the dissipation term, it is important to notice that they are extremely high compared to the observed ranges when there is no two-way coupling (by comparison with Figure 5.1c). Moreover the term accounting for assimilation can be obtained by summing both contributions (variance derivative and substrate dissipation) and is represented by the dotted line in Figure 5.28.

Therefore we further analyse the different terms of the substrate concentration variance balance equation. In chapter 3 we introduced the mechanical-to-scalar ratio r_ε that compares both characteristic dissipation times for the flow dynamics and the scalar. This ratio is found to be constant in stationary simulations and takes values around 2 (Yeung, 2001). So we plot the evolution of the ratio $r_\varepsilon = 2(q_f^2/\varepsilon_f)(\langle s'^2\rangle/\varepsilon_s)$ in Figure 5.29. Even if the dissipation time-scale τ_ε remains constant in the simulation, the mechanical-to-scalar ratio is not constant in time. Moreover the values are more than ten times higher than the usual one. It is then complex to link both quantities $\langle s'^2\rangle$ and ε_s. In order to approach the assimilation term $\Pi_{\langle s'^2\rangle}$, we propose the following expression, based

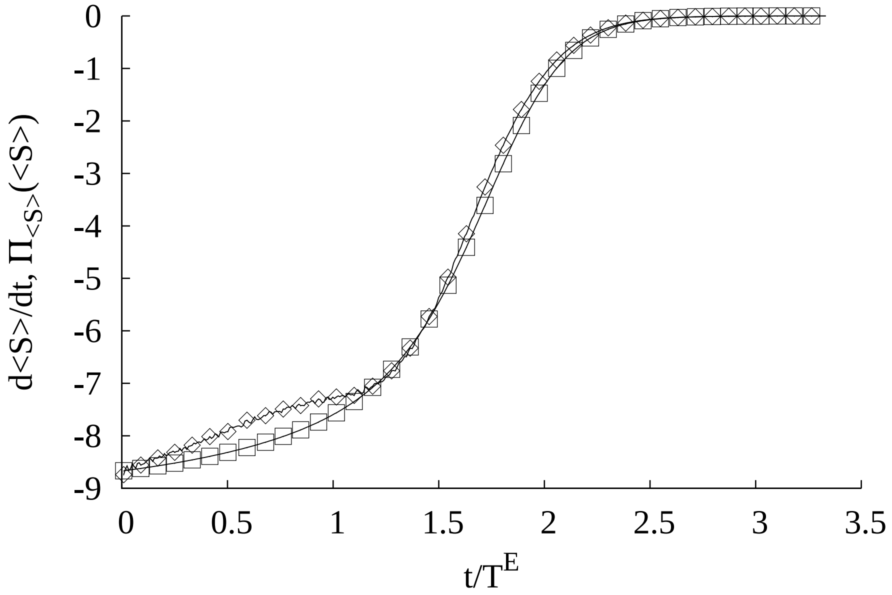

Figure 5.27: Temporal evolution of the first derivative of $\langle S\rangle$ ($\diamond$) and the assimilation term based on the average concentration: $\Pi_{\langle S\rangle}(\langle S\rangle) = \frac{N_p}{V_{box}}\Phi_{max}\frac{\langle S\rangle}{\langle S\rangle+k_S}$ ($\square$).

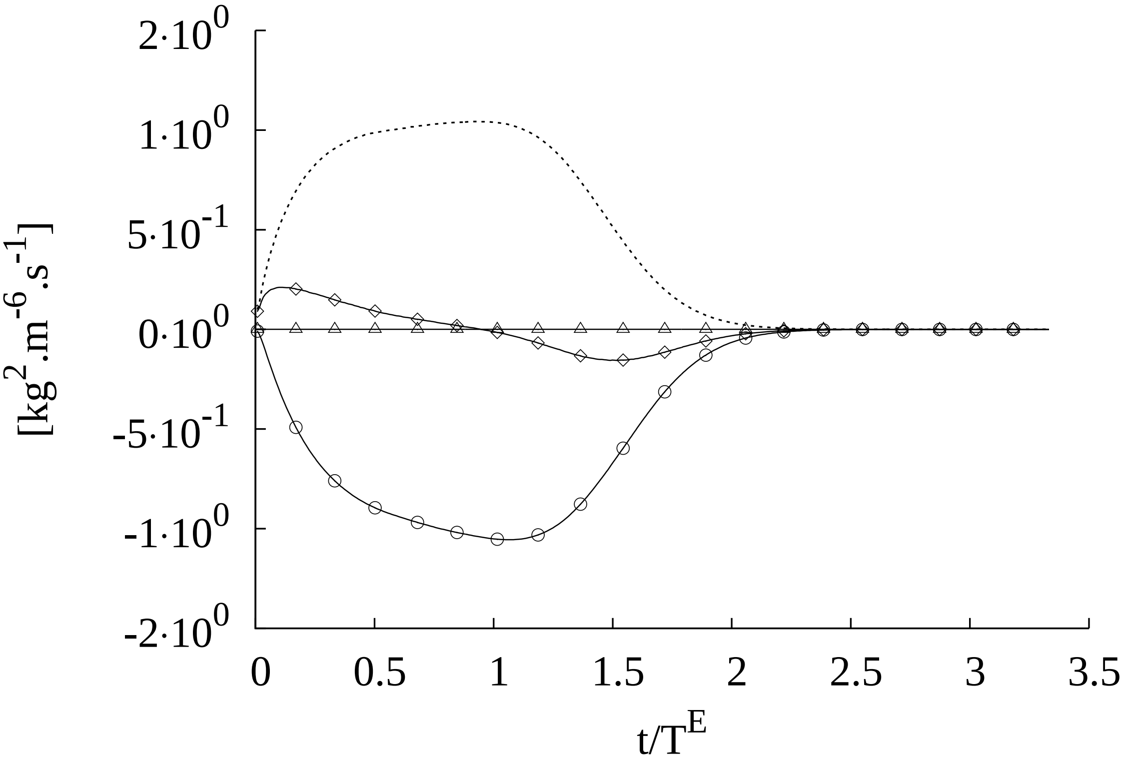

Figure 5.28: Temporal evolution of the terms of the variance transport equation (5.18) for simulation $R2$. $\diamond$: $\frac{d\langle s'^2\rangle}{dt}$, $\circ$: $-\varepsilon_{\langle s'^2\rangle}$, $\triangle$: production term. ($\cdots\cdots$) is the obtained assimilation term for variance $\Pi_{s'2}$ by summation.

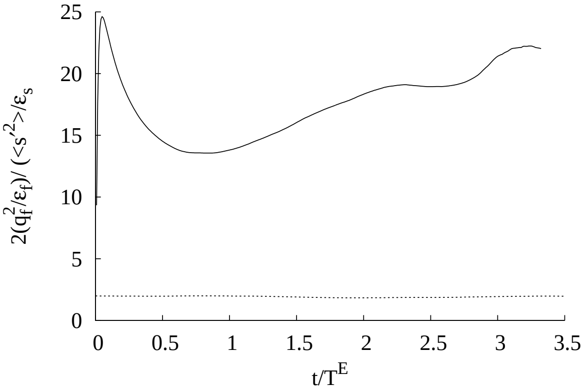

Figure 5.29: Temporal evolution of the mechanical to scalar time-scale ratio for the biological two-way simulation (———). The ratio for the statistically steady simulation is given by (········).

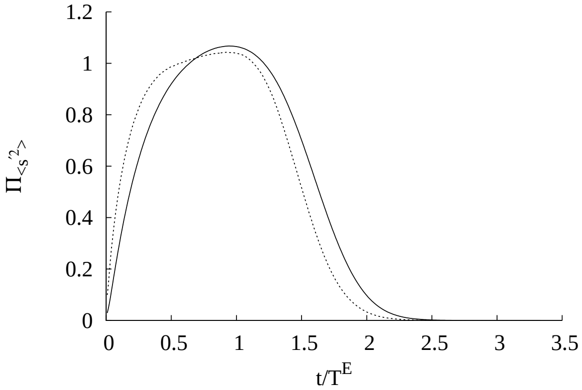

Figure 5.30: Temporal evolution of the assimilation term of the substrate variance transport equation from the DNS (········) and based on the substrate concentration variance: $\Pi_{\langle s'^2\rangle}(\langle s'^2\rangle) = \frac{N_p\Phi_{max}}{V_{box}}\frac{\langle s'^2\rangle}{\sqrt{\langle s'^2\rangle}+k_S}$: (———).

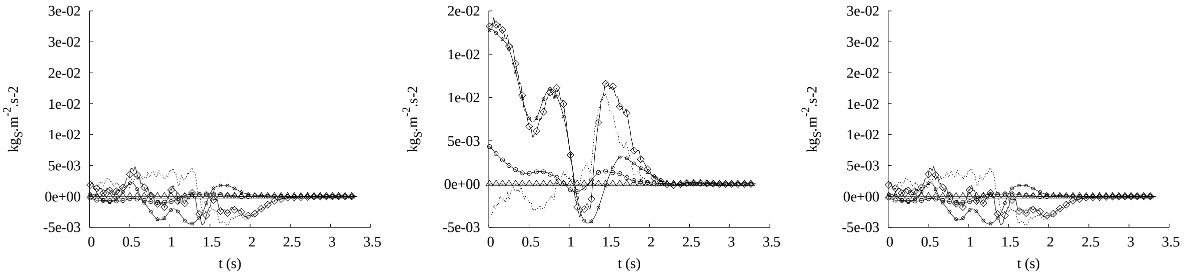

(a) $\langle u'_f s'\rangle$ (b) $\langle v'_f s'\rangle$ (c) $\langle w'_f s'\rangle$

Figure 5.31: Temporal evolution for the terms of the turbulent flux (a): $\langle u'_f s'\rangle$, (b): $\langle v'_f s'\rangle$, (c): $\langle w'_f s'\rangle$ transport equation (5.19) for simulation $R2$. ◇: $\frac{d\langle u'_{f,i}s'\rangle}{dt}$, ○: $-\varepsilon_{\langle u'_{f,i}s'\rangle}$, □: $-\frac{1}{\rho_f}\left\langle s'\frac{\partial p'}{\partial x_i}\right\rangle$. (········) is the obtained assimilation term for turbulent flux $\Pi_{u'_{f,i}s'}$ by summation.

on the substrate concentration variance:

$$\Pi_{\langle s'^2\rangle}(\langle s'^2\rangle) = \frac{N_p\Phi_{max}}{V_{box}}\frac{\langle s'^2\rangle}{\sqrt{\langle s'^2\rangle}+k_S}. \tag{5.42}$$

As shown by Figure 5.30 the proposed assimilation term is compared with the assimilation term obtained in the different simulations. In first approximation, the obtained evolution is correct, even if some discrepancies are observed.

The different terms of the equation for the cross-correlations $\langle u'_{f,i}s'\rangle$ (5.19) are plotted on Figure 5.31 for the three directions. The similar scale for the ordinates of the three plots shows that the terms of the turbulent flux remains higher in the direction of the initial imposed gradient y. The pressure contribution remains the most important term in the balance equation, for small times, and an important increase of the turbulent flux derivative at $t/T^E = 1$ is caused by the assimilation term. By summation of all "dynamic" terms, the latter is given in dotted lines for the simulation. It seems to impact the evolution after $t/T^E = 1$ For the turbulent fluxes in x and z directions, the evolutions is quite similar and no specific conclusions can be drawn. Nevertheless, it might be expected that

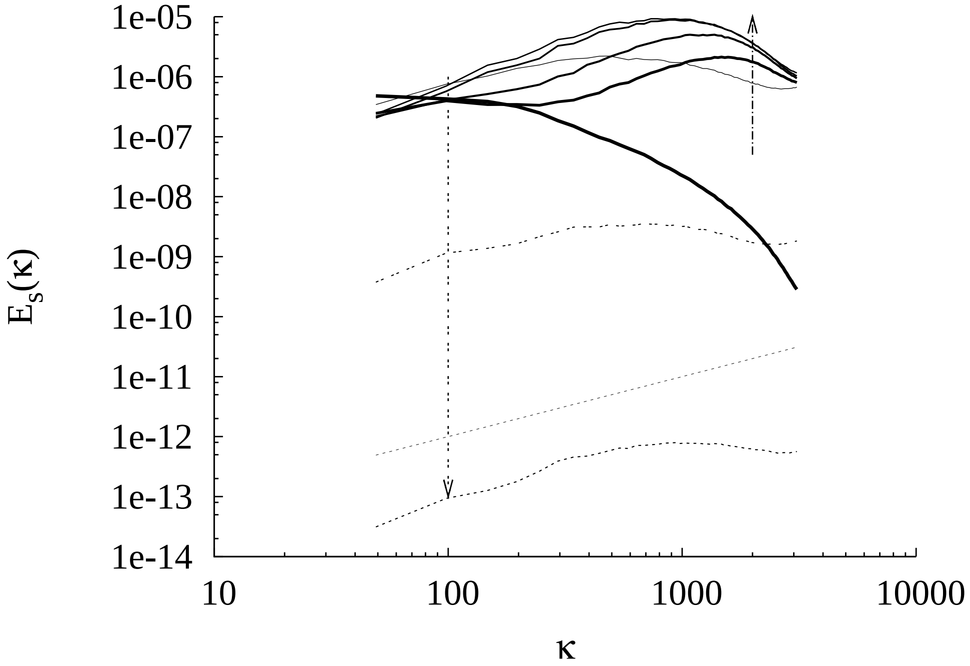

Figure 5.32: Substrate energy spectra for different times of the substrate decay. The bolder line correspond to the initial state. The thicker the line, the bigger the time. The arrow -·-·- shows the initial evolution whereas the ······· arrow presents the second phase evolution.

from a isotropic initial condition for the fluid statistics, the assimilation by microorganisms can create anisotropy in the substrate concentration field as observed in the validation section 5.2.6.

5.3.3 Spectral analysis

If we now look at the effect of assimilation on the decay of the carrier fluid substrate concentration, we can presume that the spectral density will be modified compared with the decay in the one-way coupled configuration. The evolution of the 3d spectral density for the substrate concentration for different times of the simulation is shown in Figure 5.32, where the initial spectrum in given by the bolder line. It is interesting to remark that in a first time, the higher wave-numbers are highly affected by the substrate assimilation. Indeed, the microorganisms locally assimilate the substrate and the small scales are directly impacted and the energy for the substrate grows for the small scales of the flow, while the energy contained in the large scales remain unchanged. This result was observed by (Jaberi and Mashayek, 2000), but the effects were less striking. Then a second phase for the decay is observed where the slope of the spectrum remains barely constant and the "amount of energy" decreases in time.

5.3.4 Biological statistics

The evolution of the different biological statistics are presented here. First, the averaged uptake rate is presented by Figure 5.33. Second, the non-dimensional (by the initial cross-correlation) uptake rate variance and uptake rate-substrate concentration correlations are given in Figure 5.34a and 5.34b respectively. The former increases largely to reach its maximal value for $t/T^E \simeq 1.5$ and

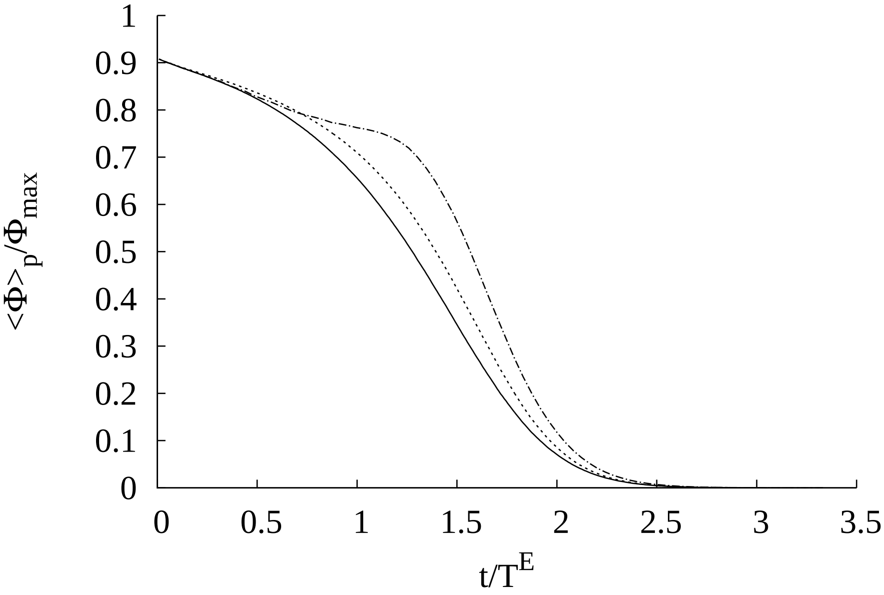

Figure 5.33: Temporal evolution of the averaged uptake rate by microorganisms $\langle \Phi \rangle_p / \Phi_{max}$ (———), and comparison with $\Phi(\langle S \rangle_p)/\Phi_{max}$ (········). (–·–·–) corresponds to the approached term for the Eulerian substrate field: $-\frac{V_{box}}{N_p}\frac{d\langle S\rangle}{dt}$.

then decreases to zero where there is no more substrate in the domain. The maximum value is about 3500 times bigger than the initial variance meaning that the biological assimilation creates fluctuations for the uptake rate. Concerning the cross-correlation $\langle \phi'^* s' \rangle_p$, it follows the same evolution, but the increase is weaker and the peak is found for smaller $t/T^E \simeq 1$. It is shown in Figure 5.34b that it does not vary as the substrate concentration variance for the fluid $\langle s'^2 \rangle / \langle s'^2 \rangle_0$. In the case of the one-way coupled decaying simulation, a similar evolution was observed.

Finally, the evolution of the uptake rate-velocity cross-correlations are plotted in Figure 5.34c. The component $\langle \phi'^* u'_f \rangle_p$ is not negligible in time compared with $\langle \phi'^* v'_f \rangle_p$. But the fact that $\langle \phi'^* v'_f \rangle_p$ remains smaller is not explained. Figure 5.34d gives the non-dimensional evolution of $\langle \phi'^* v'_f \rangle_p$. The typical evolution obtained for all statistic with an increase followed by a decrease is observed, but the evolution is smaller than for the other biological statistics.

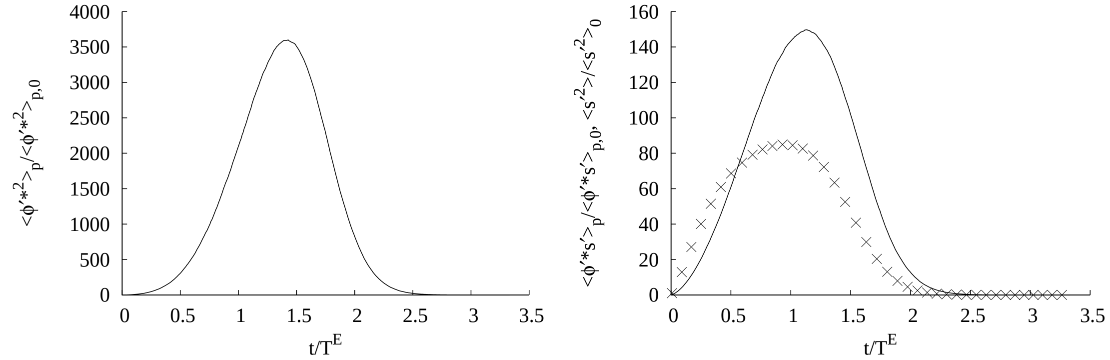

(a) $\langle \phi'^{*2}\rangle_p / \langle \phi'^{*2}\rangle_{p,0}$

(b) $\langle \phi'^{*} s'\rangle_p / \langle \phi'^{*} s'\rangle_{p,0}$

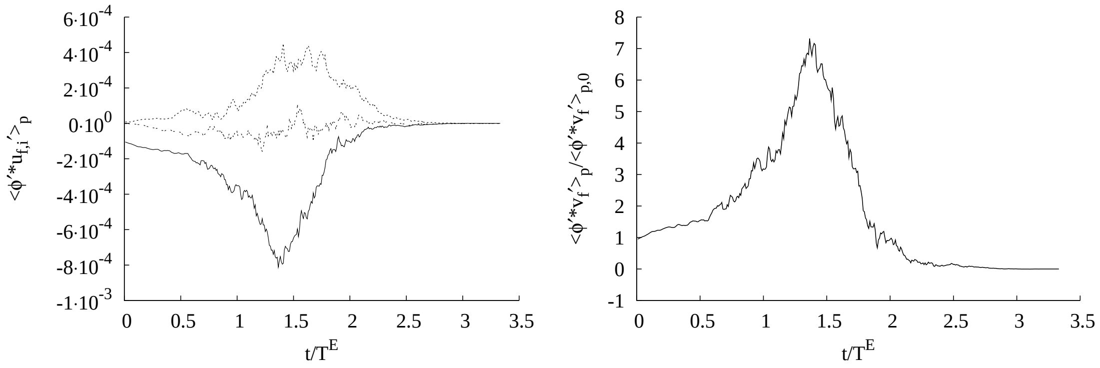

(c) $\langle \phi'^{*} u'_{f,i}\rangle_p$

(d) $\langle \phi'^{*} v'_f\rangle_p / \langle \phi'^{*} v'_f\rangle_{p,0}$

Figure 5.34: Temporal evolution for the biological statistics for assimilation. × corresponds to the non-dimensional fluid substrate variance $\langle s'^2\rangle^*$. For Figure (c), (········): $\langle \phi'^{*} u'_f\rangle_p$, (———): $\langle \phi'^{*} u'_f\rangle_p$, (- - - -): $\langle \phi'^{*} w'_f\rangle_p$.

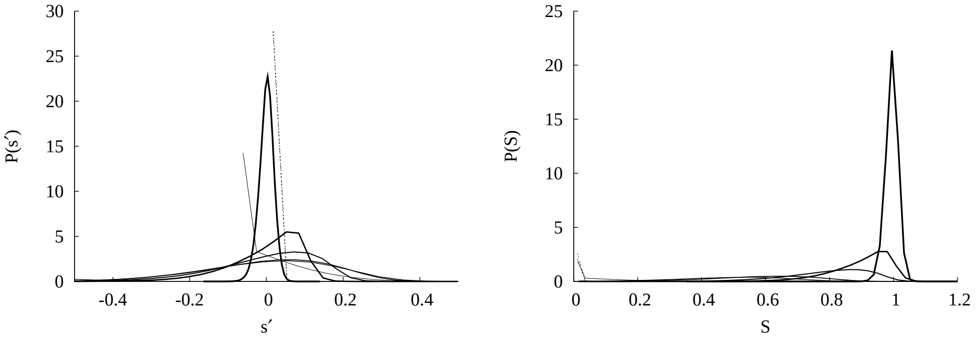

(a) $P(s')$ (b) $P(S)$

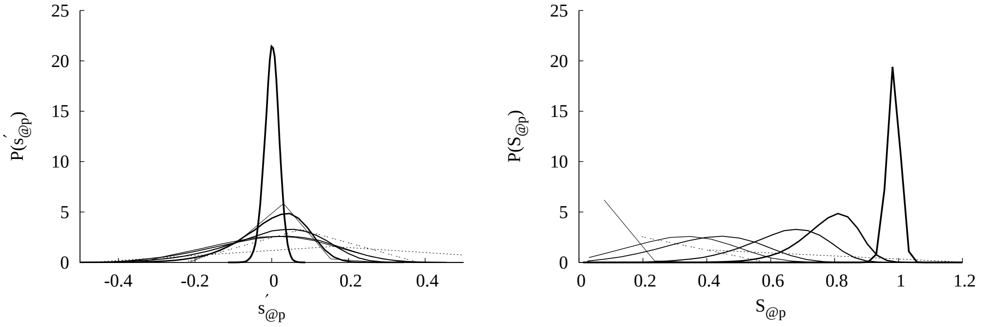

(c) $P(s'_{@p})$ (d) $P(S_{@p})$

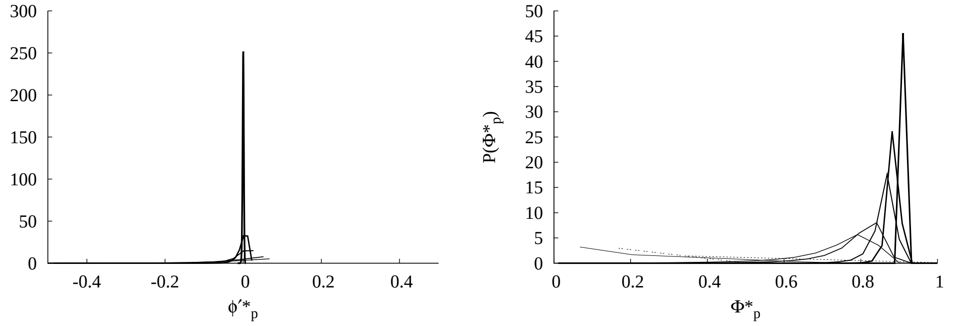

(e) $P(\phi_p'^*)$ (f) $P(\Phi_p^*)$

Figure 5.35: Normalised PDF evolution for the fluid and microorganisms in the biological two-way configuration at different times for the dynamic field and initial turbulent substrate field from simulation $R2$ with $S_0 = 1$ and $k_S = 0.1\ \mathrm{kg_S \cdot m^{-3}}$. The bolder line is for the initial PDF. The lines thickness decreases for increasing time.

5.3.5 PDF Analysis

The distributions of the fluid substrate concentration as well as the different distributions for the microorganisms are shown in this paragraph. As the simulation is unsteady for the scalar, the different PDF are computed independently at different time-steps of the simulation.

First, the PDF of the fluctuating and total concentration for the fluid are given in Figures 5.35a and 5.35b respectively. The initial gaussian distribution for the substrate concentration fluctuations is not preserved for the biological two-way coupling configuration. This first results was expected considering the third order moment of s' that is no longer zero. The distribution is asymmetric and the maximum is found for positive fluctuations. This means that the local concentration S is bigger than the mean concentration in an important proportion on the Eulerian mesh. The distribution of the instantaneous concentration decreases in time from S_0 to zero. The distribution is wider for bigger times accounting for more fluctuations as observed as well in Figure 5.35a. This results is in agreement with Figure 5.24 where the substrate variance concentration presents a strong increase. For the longer times, the distribution tends to a dirac at $S = 0$ meaning that all the substrate has been assimilated by the microorganisms.

The distributions of the fluctuating substrate concentration at the particle position differ from the distributions of s'. Indeed, due to assimilation, the concentration at the microorganism is modified, therefore the Lagrangian and Eulerian distribution are not similar anymore. Moreover, even if a perfect gaussian is not verified, the distribution of $s'_{@p}$ is more symmetric than the distribution of s'.
Concerning the distribution of assimilation rate over the microorganisms, the initial gaussian distribution with small variance of the fluctuating part of the uptake rate spreads in time and the gaussian distribution is no longer observed, as shown in Figure 5.35e. The total uptake rate distribution decreases slightly in time where the averaged value falls down, and the distribution spreads. For longer times, the distribution increases for the small values of Φ_p^* until the final state is reached where there is no residual substrate concentration and the distribution presents a dirac at $\Phi_p^* = 0$.

The analytical study of the distributions evolutions has not been performed in this part of the work. Nevertheless, the distributions obtained from the DNS could be used to predict the biomass growth and by-product formation in the domain for the overall simulations as it was done in chapter 4. After a first overview of the effect of biological assimilation on the fluid and biological statistics, the next section will focus on the effect of the fluid initial field on the substrate assimilation.

5.4 Fluid flow and mixing influence on the substrate assimilation

Indeed, as shown by (Warhaft and Lumley, 1978) and later by (Jaberi et al., 1996), the statistical evolution of a decaying temperature field is dependent on the initial condition. This result has been verified in section 5.1 where both the dynamic and substrate initial field impact the substrate decay. As for section 5.1, this suggest that the biological statistics in two-way coupled flows might also be dependent on the initial flow field or microorganisms conditions. The forthcoming work will present different results on fluid statistics, especially variance and biological assimilation for different cases.

5.4.1 Influence of the microscopic agitation in a batch-reactor

First of all, it has been experimentally shown that the fluid dissipation may control the susbtrate uptake rate (Al-Homoud and Hondzo, 2008). Considering the different simulations performed in chapter 3, it is possible to evaluate the effect of different turbulent dissipation rates on the biological assimilation. In practice this could correspond to a change in the agitation speed for example.

5.4.1.1 Initially perfectly mixed

The case of a uniform substrate concentration field at $S_0 = 0.15\ \mathrm{kg_S \cdot m^{-3}}$ is considered; the initial substrate variance is nul $\langle s'^2 \rangle_0 = 0$. The microorganisms are randomly placed in the reactor at the beginning of the simulation. The turbulent characteristics for the velocity can be found in Table 3.2. this can be regarded as the numerical simulation of a batch reactor.

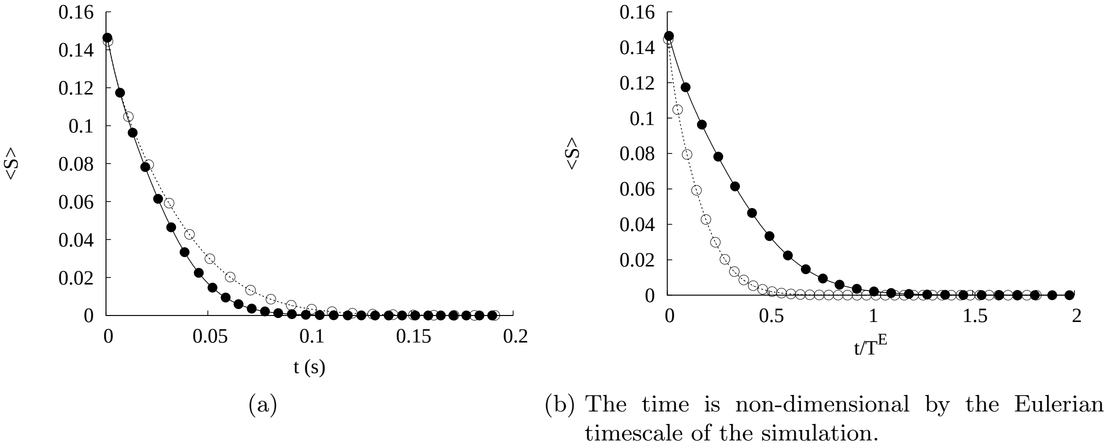

(a)

(b) The time is non-dimensional by the Eulerian timescale of the simulation.

Figure 5.36: Effect of the flow dynamics on the temporal evolution of the average substrate concentration for two different Reynolds numbers. The dynamic fields of simulations $R2$ (———) and $R1$ (········) with $S_0 = 0.15$ $\mathrm{kg_S \cdot m^{-3}}$ and $\langle s'^2 \rangle = 0$ are considered. The symbols refer to simulations $R2$ (•) and $R1$ (○) with $S_0 = 0.15$ $\mathrm{kg_S \cdot m^{-3}}$ and $\langle s'^2 \rangle = 2.6 \cdot 10^{-4}$ $\mathrm{kg_S \cdot m^{-3}}$.

The two simulations $R2$ and $R1$ for the dynamic flow field are compared in terms of assimilation characteristics. The biological parameters are unchanged and can be found in Table 5.3. The averaged concentration evolution is given in Figure 5.36 with the solid and dotted lines for the two simulations respectively. For the moment, symbols are not considered. They correspond to other cases that will be detailled afterwards. As first conclusion is that the concentration decrease is significantly accelerated at high Reynolds number. Namely, better mixing favour homogeneous (and fast) assimilation within the population.

On Figure 5.36b, the time is non-dimensional by the corresponding Eulerian time for the dynamic field. Is it important to remark that for the higher Reynolds-number simulation, the substrate decrease is fast and requires less than 0.5 Eulerian time for the fluid to reach small concentrations. On the opposite, 1 Eulerian time is required for the entire consumption of substrate in the case of simulation $R1$ with the prescribed parameters. This is a clear indication on how micro-mixing can affect assimilation at the local scale.

Beyond the changes in the average concentration the substrate variance evolution presented in Figure 5.37, shows that the production of variance in the first instants is identical for the two simulations. It is associated to the high initial uptake rate which is not counterbalanced by agitation. After $0.025s$, the average concentration has been divided by a factor 2 and the uptake rate is now much smaller and the effect of mixing intensity can be appreciated : due to a better agitation, the variance decreases earlier in simulation $R2$. Indeed, the fluid dynamics enhanced the mixing and the microorganisms see higher concentrations leading to a higher assimilation rate.

If we now look at the biological statistics shown in Figure 5.38, a striking result is that the averaged assimilation rates are very close. Some differences only appear after $t = 0.05s$ when the variances are the most different. This means that the assimilation rate decreases has a strong influence on $\langle S \rangle$ but that residual substrate concentrations are found for lower agitation even if the average uptake rate is not that different. So, for a given initial amount of substrate, the assimilation can be longer in time depending on the agitation.

Finally, the statistics of the biological phase are presented by Figure 5.38. The evolution of both the uptake rate variance and substrate concentration/uptake rate cross-correlation are very close

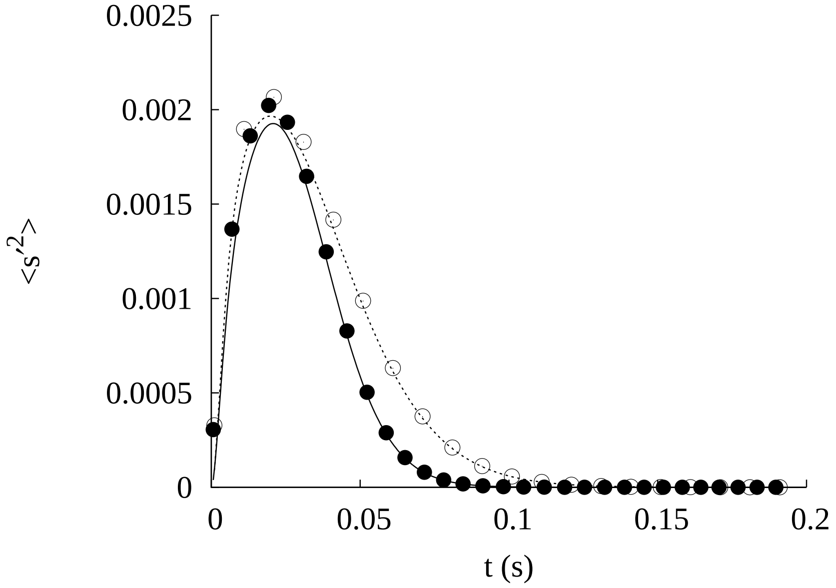

Figure 5.37: Effect of the flow dynamics on the temporal evolution of the substrate concentration variance for two different Reynolds numbers. The studied dynamic fields are simulations $R2$ (———) and $R1$ (········) with $S_0 = 0.15$ kg$_S \cdot$ m^{-3} and $\langle s'^2 \rangle = 0$. The symbols refer to simulations $R2$ (●) and $R1$ (○) respectively with $S_0 = 0.15$ kg$_S \cdot$ m^{-3} and $\langle s'^2 \rangle = 2.6 \cdot 10^{-4}$ kg$_S \cdot$ m^{-3}. The lines thus correspond to the perfectly mixed initial state, and the symbols refer to the imperfectly mixed initial states.

meaning that no sensitive effect of the fluid dynamics is found on the biological phase for the parameters of the simulations.

5.4.1.2 Initially imperfectly mixed

The former results are obtained for an initially uniform substrate field. But this perfectly mixed state is ideal but rarely possible and we will now observe the effect of an initial mixing state on the substrate decrease. The substrate concentration field is obtained from simulations $R1$ and $R2$ by removing the imposed gradient contribution. The substrate variance of both fields are very close and the ratio $\langle s'^2 \rangle_0 / S_0$ is almost equal for both simulations. The evolution of the averaged concentration is given with symbols in Figure 5.36 for both cases. As we can see, there are no significant differences between the initial perfectly mixed and the present results. This result can be explained by the fact that the production of variance due to the microorganisms assimilation is extremely important and thus the initial substrate concentration fluctuations become insignificant after a few time steps. However, it is most probable that higher heterogeneities (at $t = 0$) can have a stronger impact on the assimilation rate of microorganisms. The presence of an injection point in the reactor could lead to such heterogeneities and impact the biological assimilation. This interesting results is of prime importance in fed-batch bioreactors for example.

The different results for both simulations with an initial mixing-state are given by the symbols in Figures 5.37 and 5.38. By comparison with the simulations with a perfect initial mixing state (given with lines), we can see that the different statistics are somewhat higher, accounting for the initial fluctuations, but the mean substrate concentration and uptake rate are not influenced by the initial fluctuations. Nevertheless, the latter conclusion is drawn for relatively small substrate variance,

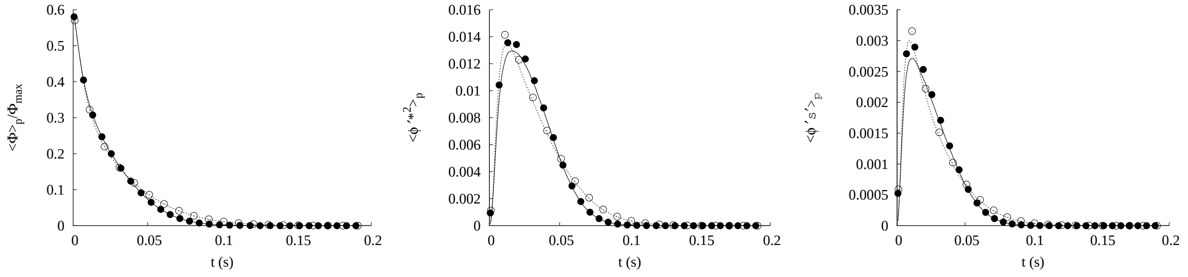

(a) $\langle\Phi\rangle_p/\Phi_{max}$ (b) $\langle\phi'^{*2}\rangle$ (c) $\langle\phi'^{*}s'\rangle_p$

Figure 5.38: Effect of the flow dynamics on the temporal evolution of the biological statistics for two different Reynolds numbers. The studied dynamic fields are simulations $R2$ (———) and $R1$ (········) with $S_0 = 0.15$ kg$_S \cdot$ m^{-3} and $\langle s'^2\rangle = 0$. The symbols refer to simulations $R2$ (•) and $R1$ (○) respectively with $S_0 = 0.15$ kg$_S \cdot$ m^{-3} and $\langle s'^2\rangle = 2.6 \cdot 10^{-4}$ kg$_S \cdot$ m^{-3}. The lines thus correspond to the perfectly mixed initial state, and the symbols refer to the imperfectly mixed initial states.

so the next paragraph will further analyse the effect of the initial substrate field on the substrate assimilation by microorganisms.

5.4.2 Influence of substrate initial field

5.4.2.1 Substrate concentration

It is expected that, for a given number of microorganisms characterised by their affinity constant k_S, the smaller the available substrate concentration, the fastest the assimilation in time. This result is shown by Figure 5.39a for the evolution of the substrate concentration in the case of the dynamic flow field $R2$ with two different uniform substrate concentration fields $S_0 = 0.15$ and $S_0 = 1$ kg$_S \cdot$ m^{-3}. As expected, the mean concentration decreases faster for the lower initial concentration with a given microscopic affinity constant. This is consistent with the definition of the charateristic time scale for assimilation which is related to the ratio S/X. It is also observed that the substrate variance evolution is less spread for smaller initial concentration. One can also remark that the variance increase is much smaller for smaller initial substrate concentration.

Concerning the biological statistics proposed in Figure 5.39, the assimilation rate by microorganisms presents totally different shapes for the two considered initial substrate concentrations. The observed regime for $S_0 = 0.15$ kg$_S \cdot$ m^{-3} is close to the exponential regime obtained in the case of Blackman assimilation model in the validation section. Moreover, the lower the initial substrate amount, the lower the assimilation rate, and the less the biomass growth. Concerning the uptake rate variance, we can remark that for the simulation with $S_0 = 1$ kg$_S \cdot$ m^{-3}, the peak is more or less symmetric whereas the evolution for $S_0 = 0.15$ kg$_S \cdot$ m^{-3} is asymmetric.

5.4.2.2 Influence of initial mixing

In section 5.4.1 a brief study on the effect of the initial mixing state on assimilation was performed. It was shown that the initial fluctuations of the substrate field only influence the biological statistics, but no specific effect was found for the averaged uptake rate compared to a uniform substrate concentration field. We may remind here that the considered fluctuations were relatively small.

We propose here to investigate the results for an initial substrate concentration field with stronger fluctuations. The chosen dynamic flow field is given by simulation $R2$. The initial mean substrate concentration is $S_0 = 1\text{kg}_\text{S} \cdot \text{m}^{-3}$. The three investigated cases correspond to a perfectly mixed batch reactor distribution, and to initially mixed reactors where the initial substrate concentration field and variance are given by simulations $R2$ and $G2$, with no contribution of the imposed gradient on the substrate field.

Figure 5.39a shows that, as observed in section 5.4.1, no differences on the mean concentration decrease are obtained. But as shown in Figure 5.39b, the substrate concentration variance for the fluid is influenced by the initial mixing state. Indeed, for important initial fluctuations, the maximum variance is bigger than for small initial fluctuations. Moreover, the variance is similar for a perfectly mixed bioreactor and an initial homogeneous mixing with small fluctuations. If we scrutinise the evolution of the substrate variance compared to the initial variance $\langle s'^2 \rangle_0$ an interesting result arises.[4]. On the one hand, the substrate variance is up to 100 times bigger than the initial substrate variance in the case of the initially mixed substrate field from simulation $R2$. On the other hand, the ratio $\langle s'^2 \rangle / \langle s'^2 \rangle_0$ remains less than 10 for the initial substrate field from simulation $G2$. This means that the substrate fluctuations created by the microorganism assimilation have a weaker impact on the fluid when the initial substrate field present strong fluctuations. This results should be observable on the substrate energy spectrum evolution. Indeed, as observed in Figure 5.41, the initial energy is bigger for the substrate field from simulation $G2$. After 20 iterations, the energy at the small scale increases and is similar for both simulations. The energy at the big scales decreases slowly. But if we look at the intermediate scales, the energy spectra differ a lot for small times. The energy transfer from the small scales to the intermediate scales is more important for small initial substrate fluctuations. At large times, when the residual substrate concentration is very small, the substrate energy is higher for the case with initial large concentration fluctuations.

Concerning the biological statistics, there is no significant effect of the initial substrate fluctuations on the total assimilation rate $\langle \Phi \rangle_p$. But, as observed in section 5.4.1, the uptake rate variance $\langle \phi'^{*2} \rangle_p$ and the cross-correlation $\langle s' \phi'^{*} \rangle_p$ are slighlty bigger for the bigger initial variance. The non-dimensional evolution of $\langle s' \phi'^{*} \rangle_p$ not shown here presents the same conclusions as for the non-dimensional substrate variance.

5.4.3 Characterisation of the flow and mixing on the substrate assimilation

The study carried out in the previous sections is devoted to characterise the effects of the flow dynamics and mixing on the substrate assimilation by microorganisms in a stationary turbulent velocity field. The substrate concentration decrease is analysed and the different deviations on macroscopic data are partly explained by the local fluctuations. The flow dynamics play a role on the substrate decrease that is weaker for a smaller Reynolds-number velocity field, for a given initial concentration.

The substrate decrease evolution differs for different initial amount of substrate and the initial mixing state has been found to impact the different biological statistics for important initial substrate variance. Moreover, the energy transfer from the small scales to the larger scales is characteristic of biological two-way coupling with substrate concentration decay. The transfer from small to intermediate scales is lowered in the case of strong initial fluctuations. Meaningly the more initial fluctuations, the less impact of the substrate fluctuations created by the microorganisms assimilation on the overall assimilation process.

---

[4] The non-dimensionalisation for the initial uniform substrate field (——— and ········) in 5.39c is performed by using $\langle s'^2 \rangle = 2.78 \cdot 10^{-4}\ \text{kg}_\text{S} \cdot \text{m}^{-3}$.

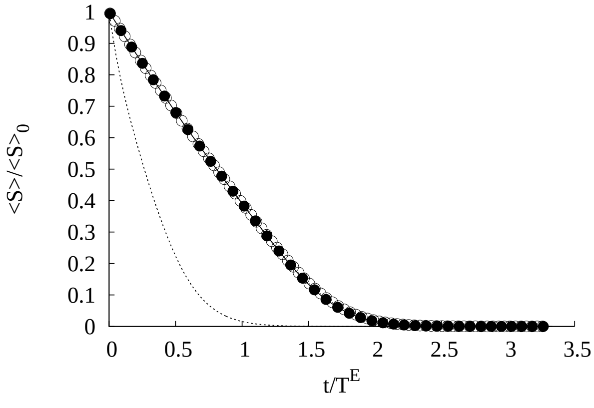

(a) $\langle S\rangle$

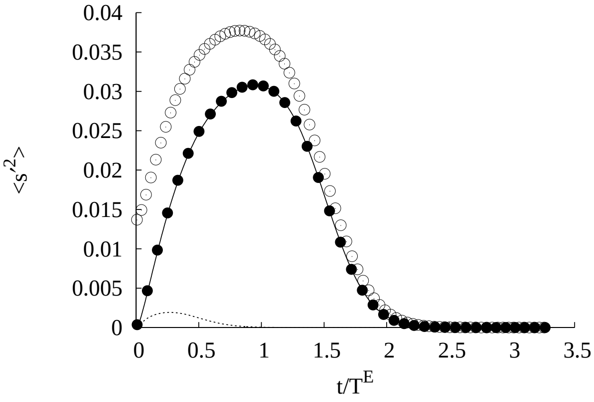

(b) $\langle s'^2\rangle$

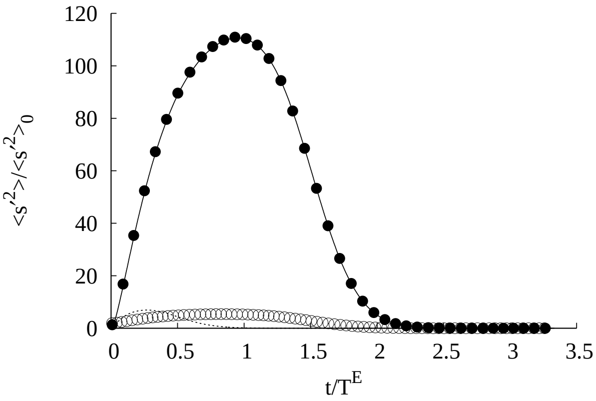

(c) Normalised variance: $\langle s'^2\rangle/\langle s'^2\rangle_0$

Figure 5.39: Effect of the initial substrate field on the temporal evolution of the mean substrate concentration and substrate variance for different initial substrate variances. (——) corresponds to the dynamic fields of simulations $R2$ with a uniform concentration $S_0 = 1\ \mathrm{kg_S\cdot m^{-3}}$ corresponding to $\langle s'^2\rangle = 0$. The symbols refer to simulations $R2$ (•) and $G2$ (○) respectively with $S_0 = 1\ \mathrm{kg_S\cdot m^{-3}}$ and the initial substrate concentration variance $\langle s'^2\rangle = 2.78\cdot10^{-4}\ \mathrm{kg_S\cdot m^{-3}}$ and $\langle s'^2\rangle = 7.02\cdot10^{-3}\ \mathrm{kg_S\cdot m^{-3}}$ respectively. The (········) line refers to simulation $R2$ with a uniform initial concentration $S_0 = 0.15\ \mathrm{kg_S\cdot m^{-3}}$

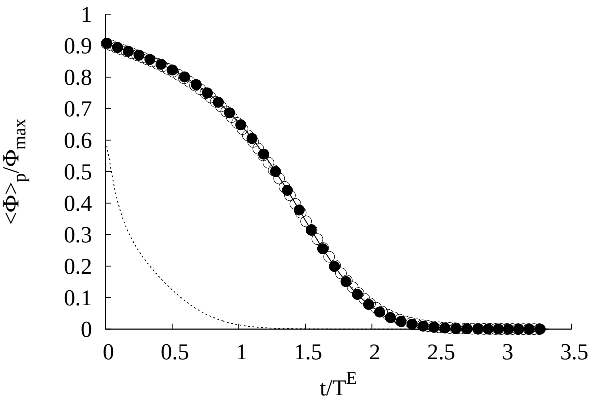

(a) $\langle \Phi \rangle_p / \Phi_{max}$

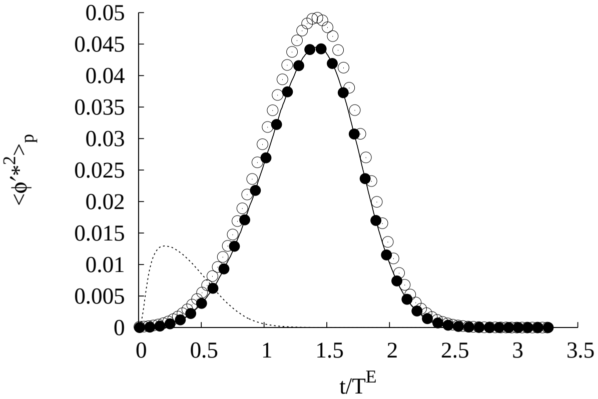

(b) $\langle \phi'^{*2} \rangle_p$

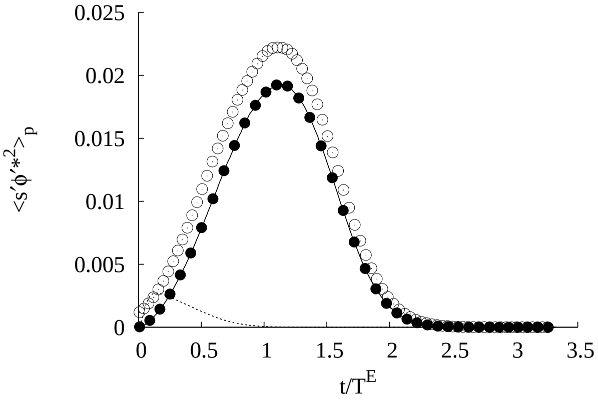

(c) $\langle \phi'^{*} s' \rangle_p$

Figure 5.40: Effect of the initial substrate field on the temporal evolution of the biological statistics for different initial substrate variances. (——) corresponds to the dynamic fields of simulations $R2$ with a uniform concentration $S_0 = 1\ \mathrm{kg_S \cdot m^{-3}}$ corresponding to $\langle s'^2 \rangle = 0$. The symbols refer to simulations $R2$ (•) and $G2$ (○) with $S_0 = 1\ \mathrm{kg_S \cdot m^{-3}}$ and the substrate concentration variance $\langle s'^2 \rangle = 2.78 \cdot 10^{-4}\ \mathrm{kg_S \cdot m^{-3}}$ and $\langle s'^2 \rangle = 7.02 \cdot 10^{-3}\ \mathrm{kg_S \cdot m^{-3}}$ respectively. The (········) line refers to simulation $R2$ with a uniform initial concentration $S_0 = 0.15\ \mathrm{kg_S \cdot m^{-3}}$.

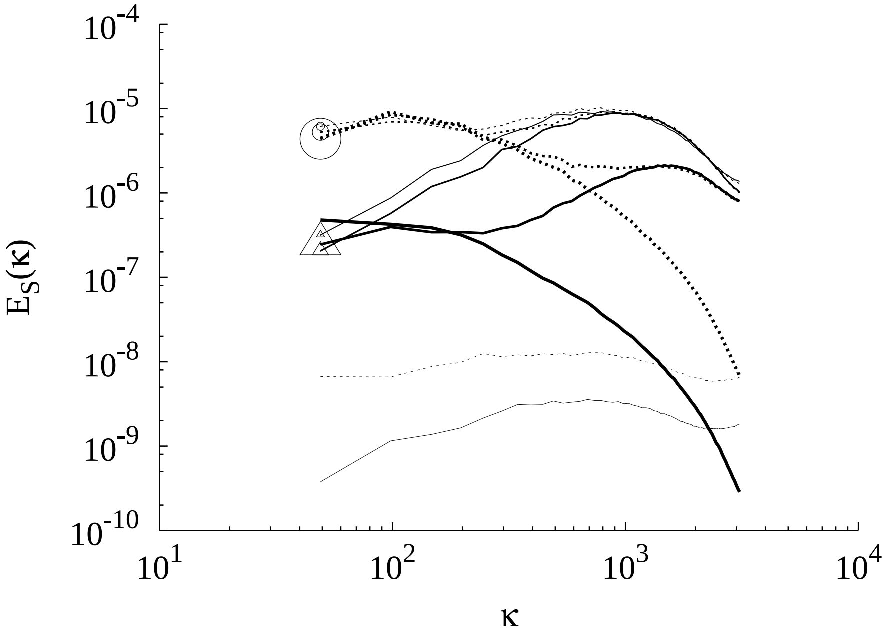

Figure 5.41: Evolution of the substrate energy spectra for initial substrate concentration field from simulations $R2$ (——) and $G2$ (········) with $S_0 = 1$ $\mathrm{kg_S \cdot m^{-3}}$ at different corresponding times of the simulations. The symbols size and lines thickness decrease for increasing times. The initial spectra are given by the bolder lines.

Finally we present in this paragraph the results for the assimilation rate as function of the averaged substrate concentration non-dimensional by the affinity constant for the substrate. The graphs must be read from right to left, meaningly from large to small concentrations.

First the assimilation evolution for small initial concentration is shown in Figure 5.42 for the dynamic fields $R1$ and $R2$. The dotted-dashed line corresponds to the uptake rate based on the fluid averaged concentration $\Phi(\langle S\rangle) = \Phi_{max}\frac{\langle S\rangle}{\langle S\rangle + k_S}$. It is observed that the obtained uptake rates are smaller compared to the uptake rate based on the mean concentration. These lower values are of prime importance considering that the usual determination of the uptake rate is experimentally obtained by measuring the residual averaged substrate concentration in the reactor. Moreover, the assimilation regime seems to differ from the usual hyperbolic law and the slope is slowed down for intermediate residual substrate concentrations.
Concerning the dynamics of the flow, it is shown that a more turbulent flow leads to higher assimilation rate. Finally, the effect of the substrate diffusion is represented by the × symbols. For the simulation $P2$ with the turbulent initial substrate field from simulation $P2$ with $S_0 = 0.15$ $\mathrm{kg_S \cdot m^{-3}}$. It is interesting to remark that for an increased diffusional coefficient $\mathcal{D}_{S,f}$, and the same dynamic field, the resulting uptake rate is smaller than for simulation $R1$ (equivalent to $P1$). Even if the resulting Schmidt number remains small for both simulations, for increasing Sc, the uptake rate decreases. This striking results is of prime importance for further developments considering the assumptions of the present work. Indeed, the scalar mixing below the Kolmogorov scale is expected to greatly impact the microorganisms assimilation. The effect of initial mixing state on assimilation is shown by the representation of the averaged uptake rate with respect to the averaged concentration in the case of the flow dynamics from simulation $R2$ parameters on Figure 5.43. As already observed, the resulting assimilation rate is smaller than the uptake rate based on the mean substrate concentration. Moreover, the effect of the initial mixing is observed for the initial substrate field from simulation $G2$. Indeed, the assimilation rate is slightly decreased accounting

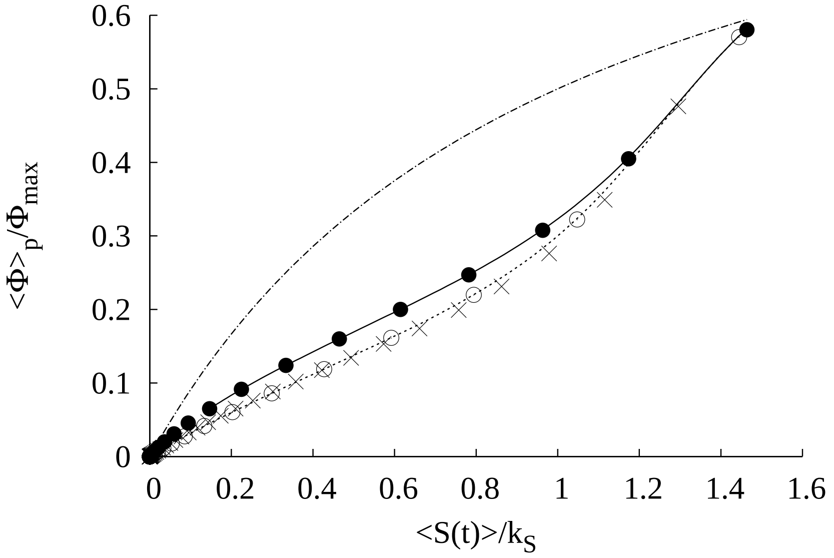

Figure 5.42: Evolution of the uptake rate with respect to the substrate concentration for different Reynolds-number flows.The dynamic fields are simulations $R2$ (——) and $R1$ (········) respectively with $S_0 = 0.15$ $\mathrm{kg_S \cdot m^{-3}}$ and $\langle s'^2 \rangle = 0$. The symbols refer to simulations $R2$ (•) and $R1$ (○) respectively with $S_0 = 0.15$ $\mathrm{kg_S \cdot m^{-3}}$ and $\langle s'^2 \rangle = 2.6 \cdot 10^{-4}$ $\mathrm{kg_S \cdot m^{-3}}$. The × symbols corresponds to the simulation $P1$ with $S_0 = 0.15$ and $k_S = 0.1$ $\mathrm{kg_S \cdot m^{-3}}$. $\Phi(\langle S \rangle)$: (-·-·-) is the uptake rate evolution based on the mean substrate concentration.

for the effect of substrate concentration fluctuations on the assimilation. The more fluctuations, the lower the uptake rate. This is an important result considering the strong substrate concentration fluctuations observed in industrial bioreactors. It is also interesting to observe that, below $\langle S(t) \rangle = 0.15$ $\mathrm{kg_S \cdot m^{-3}}$, the uptake rate decrease is not similar to the decrease observed for simulations $R1$ and $R2$ with $S_0 = 0.15$ $\mathrm{kg_S \cdot m^{-3}}$. This result is shown in Figure 5.44 and the observed shapes differ so that both history of microorganisms trajectories and initial substrate field impacts the assimilation.

Finally, for the present parameters of simulation, the same conclusion arise on the macroscopic law for the uptake rate. A hyperbolic evolution is found, but the macroscopic affinity constant differs from the microscopic affinity to the substrate k_S. Typically, the substrate fluctuations observed by the population globally result as a bigger affinity constant K_S, or a lower affinity to the substrate. The present conclusion has already been introduced in the second chapter of this work for an isolated microorganism exposed to fluctuating concentration.

Considering these conclusions, a further work could be to characterise the macroscopic affinity constant K_S in terms of the flow dynamics, the substrate mixing and the initial substrate field. But, this apparent affinity constant will also depend on the biological parameters such as k_S and the initial concentration in biomass for example. It would be interesting to introduce the adaptation of transport mechanisms (Ferenci, 1999b). In this part we only focused on the effect of the flow dynamics on the assimilation of one population of microorganisms and did not consider the effect of biological parameters. The next paragraph will scrutinise the effect of different populations on the biological assimilation.

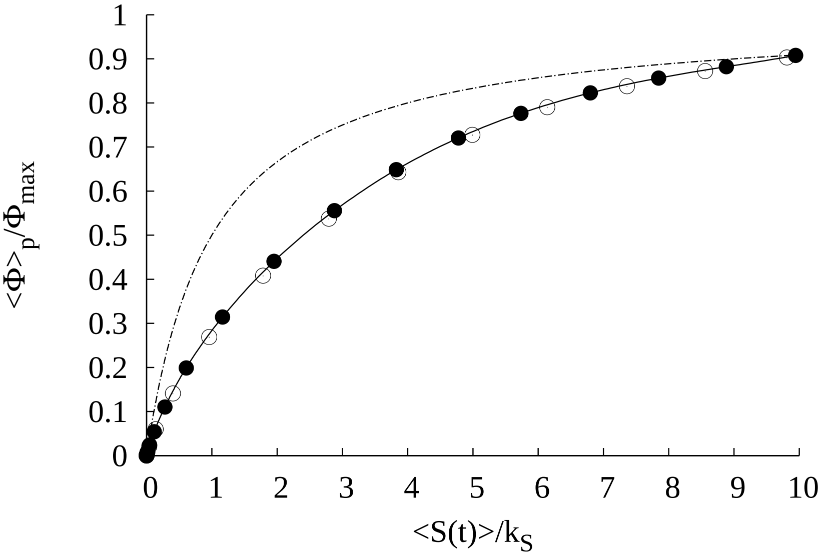

Figure 5.43: Evolution of the uptake rate with respect to the substrate concentration for different initial mixing states.(——) corresponds to the dynamic fields of simulations $R2$ with a uniform concentration $S_0 = 1$ kg$_S \cdot$ m^{-3} corresponding to $\langle s'^2 \rangle = 0$. The filled and empty symbols are for simulations $R2$ and $G2$ respectively with $S_0 = 1$ kg$_S \cdot$ m^{-3} and $\langle s'^2 \rangle = 2.78 \cdot 10^{-4}$ kg$_S \cdot$ m^{-3} and $\langle s'^2 \rangle = 7.02 \cdot 10^{-3}$ kg$_S \cdot$ m^{-3} respectively. (-·-·-) is the uptake rate evolution based on the mean substrate concentration.

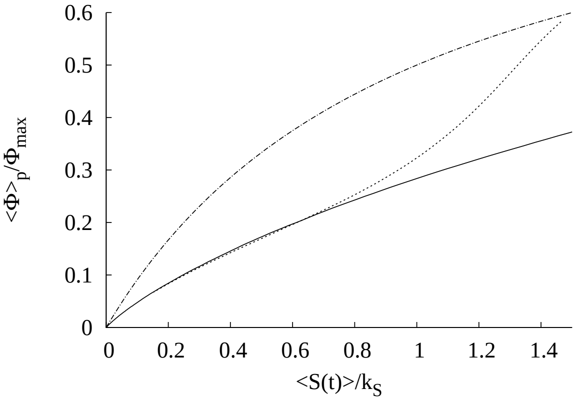

Figure 5.44: Evolution of the uptake rate with respect to the substrate concentration below $\langle S(t) \rangle = 0.15$ kg$_S \cdot$ m^{-3}. (——) corresponds to the dynamic fields of simulations $R2$ with a uniform initial concentration $S_0 = 1$ kg$_S \cdot$ m^{-3}. (········) is the uptake rate decrease for simulation $R2$ with an initial uniform substrate field $S_0 = 0.15$ kg$_S \cdot$ m^{-3}. (-·-·-) is the uptake rate evolution based on the mean substrate concentration.

5.5 Parametric study for biological phase

In the preceding paragraph, we investigated the effect of the flow dynamics and mixing on the assimilation by a population of microorganisms. The observed results are obtained with the biological parameters given in Table 5.3. The next study proposes to investigate the influence of the affinity

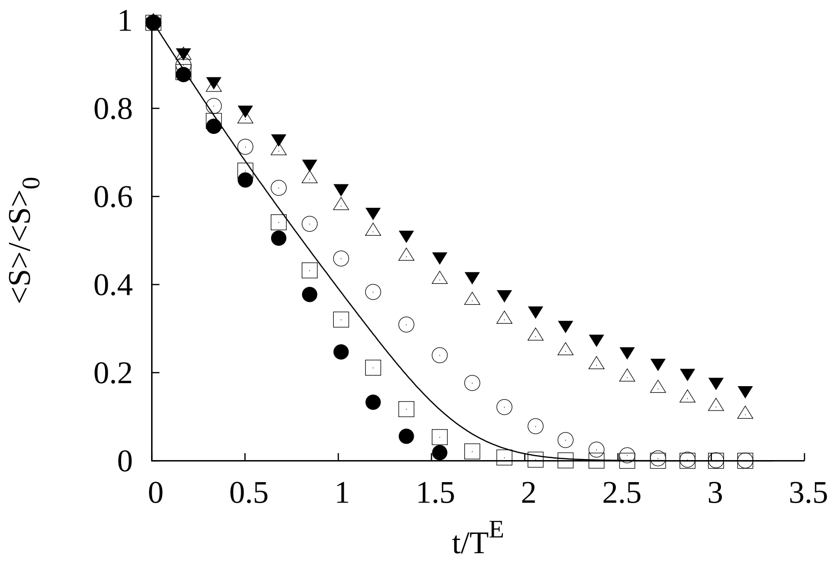

Figure 5.45: Time-evolution of the substrate concentration for different substrate affinities. The symbols legend can be found in Table 5.4.

for the substrate k_S and to the effect of particle heterogeneities and initial concentration on the results.

5.5.1 Different assimilation regime for different affinity constants

In the previous study an intermediate affinity constant was chosen for the microorganisms population with a ratio S_0/k_S at the initial state ranging from 1.5 to 10. For the bigger ratio ($S_0 = 1\ \mathrm{kg_S \cdot m^{-3}}$) the observed evolution for the macroscopic uptake rate is a hyperbolic law, whereas this hyperbolic shape is not found for smaller initial substrate concentration.

By using the substrate field obtained from simulation $R2$ and an initial mean concentration $S_0 = 1\ \mathrm{kg_S \cdot m^{-3}}$, the effect of different affinity constants on assimilation is scrutinised. The parameters for the simulations can be found in Table 5.3 and Table 5.4 gives the different affinity constant.

Table 5.4: Affinity constant for the simulations.

k_S	10^{-2}	$5 \cdot 10^{-2}$	10^{-1}	$2 \cdot 10^{-1}$	$5 \cdot 10^{-1}$	$6.6 \cdot 10^{-1}$
Symbol	●	□	——	○	△	▼

For $N_p = 2 \cdot 10^5$ microorganisms, the fluid substrate concentration evolution is plotted for different simulations with k_S ranging from 10^{-2} to $6.6 \cdot 10^{-1}\ \mathrm{kg_S \cdot m^{-3}}$. The lower the affinity constant, the higher the affinity for the substrate. Therefore, the substrate concentration decay is faster for lower k_S and the uptake rate remains more important for longer times but the slope of the decrease is bigger afterwards. The different statistics for the biological phase are given in Figure 5.46 where a general conclusion arises: if the initial assimilation is important, the resulting fluctuations are more important, whereas for small affinity to the substrate, the fluctuations are smaller because of smaller assimilation by the microorganisms and the mixing process dominate the assimilation.

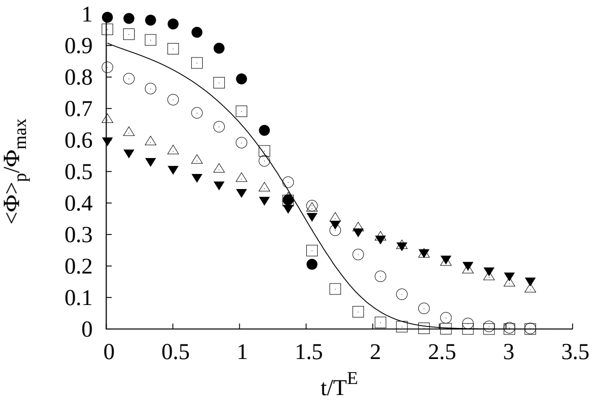

(a) $\langle \Phi \rangle_p / \Phi_{max}$

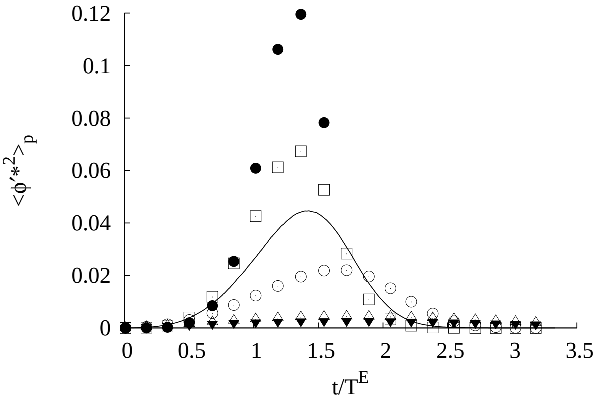

(b) $\langle \phi'^{*2} \rangle_p$

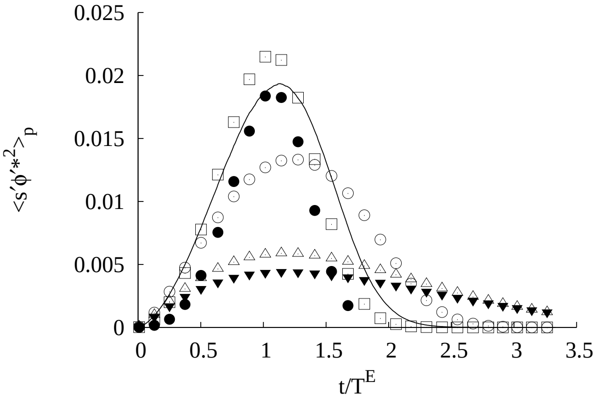

(c) $\langle s' \phi'^{*} \rangle_p$

Figure 5.46: Biological statistics for different substrate affinities. The meaning of the symbols can be found in Table 5.4.

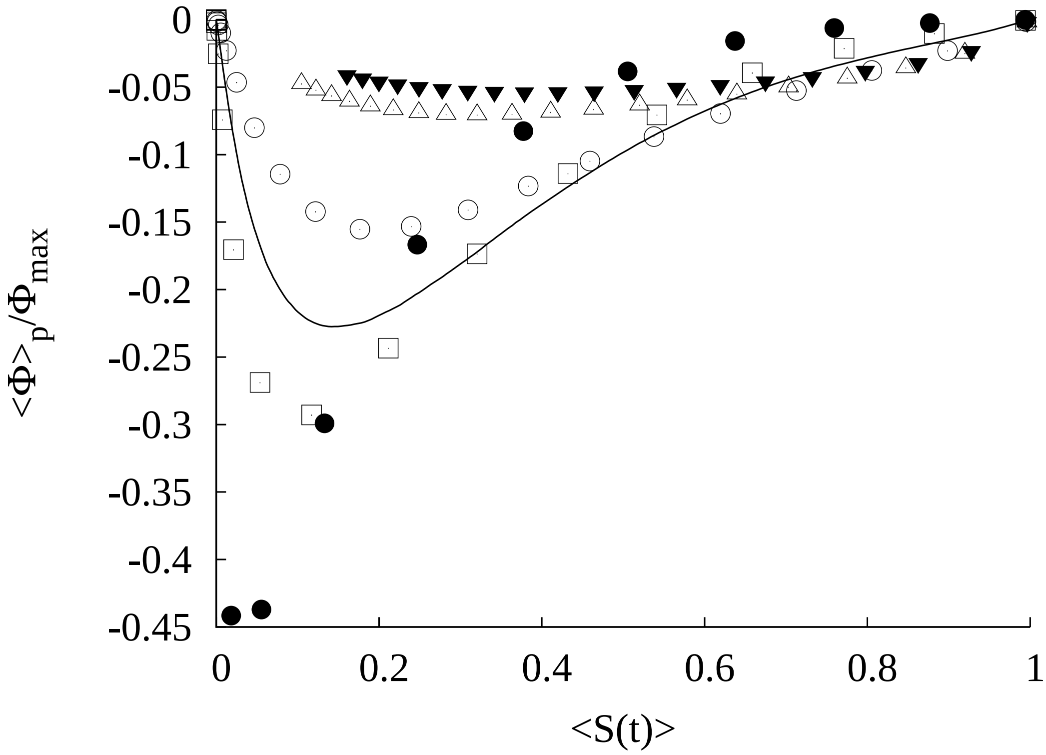

Figure 5.47: Time-evolution of $\langle \Phi \rangle_p - \Phi(\langle S \rangle)$ for different substrate affinities. The symbols legend can be found in Table 5.4.

Finally, the obtained average uptake rate $\langle \Phi^* \rangle_p$ are compared to the macroscopic uptake rate based on the mean substrate concentration $\Phi^*(\langle S \rangle)$. The difference between both uptake rates is given in Figure 5.47. For high concentrations, the differences are similar and small for all simulations. But as we can see, the difference gets bigger in time for smaller k_S. Meaningly, evaluating the uptake rate for one population on the mean substrate concentration is flawed especially for high affinity to the substrate because of the important substrate concentration gradient created due to assimilation.

From the differences observed by changing the affinity constant, we can wonder about the impact of the number of microorganisms in a population on the assimilation of the population. This problem is addressed in the next paragraph.

5.5.2 Influence of the particle loading

The initial microorganisms concentration X_0, more specifically the substrate concentration to biomass concentration initial ratio $\langle S \rangle / X$ is an important parameter for the study of biomass growth. Indeed, the more microorganisms, the higher the assimilation rate. Moreover, the biomass growth is also an important phenomenon that will affect the substrate field and in consequence the assimilation rate. Nevertheless we remind here that the microorganisms growth is not considered in this work and we will focus on the microorganisms initial concentration X.

The influence of different initial biomass concentrations is briefly analysed by changing the microorganisms number in the simulations. We decided to study the substrate concentration decay for double and half microorganisms. Based on the particle initial properties found in Table 5.3, the particle number is first $N_p = 10^5$ and then $N_p = 4 \cdot 10^5$. All simulations are performed for the

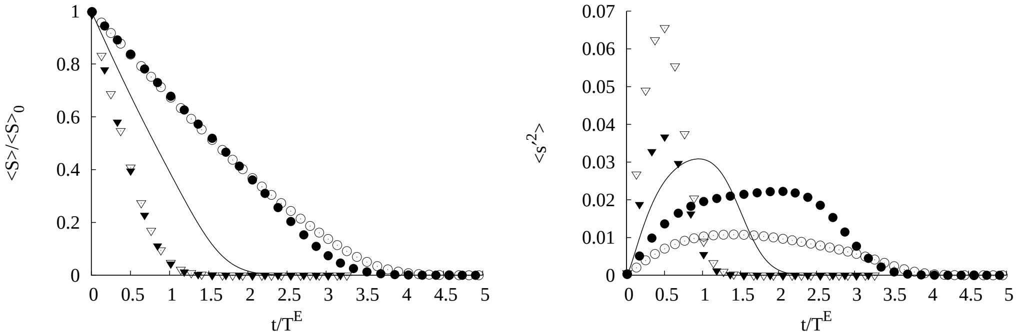

(a) $\langle S\rangle/S_0$ (b) $\langle s'^2\rangle$

Figure 5.48: Effect of the particle loading and maximum specific uptake rate on the temporal evolution of the mean substrate concentration and substrate variance. All simulations are performed for the dynamic fields and initial turbulent substrate field from simulation $R2$ with a uniform concentration $S_0 = 1\ \mathrm{kg_S\cdot m^{-3}}$. •: $N_p = 10^5$, (——): $N_p = 2\cdot 10^5$ and ▲: $N_p = 4\cdot 10^5$. And for $N_p = 2\cdot 10^5$, ○: $\Phi_{max} = 5\cdot 10^{-8}\ \mathrm{kg_S\cdot s^{-1}}$ and △: $\Phi_{max} = 2\cdot 10^{-7}\ \mathrm{kg_S\cdot s^{-1}}$.

dynamic flow and initial turbulent substrate concentration field from simulation $R2$ with a initial average concentration $S_0 = 1\ \mathrm{kg_S\cdot m^{-3}}$.

The different results for this change in the particles number can be found in Figures 5.48 and 5.49 with the filled symbols. First the mean substrate temporal evolution is plotted in Figure 5.48a. As expected, the substrate decay is slowed down if less microorganisms are injected in the bioreactor. But, the necessary time to reach a zero residual concentration is more than twice the corresponding time for the doubled particle number. For $N_p = 4\cdot 10^5$ microorganisms, the substrate decay is more pronounced but at least half an Eulerian time scale is required.

Concerning the mean averaged uptake rate for the microorganisms, the less microorganisms, the higher the assimilation rate. Indeed, for $N_p = 10^5$ microorganisms, the substrate concentration is higher as previously observed. This tendency is traduced by smaller uptake rate variance for small times. But for longer times, the variance increases. Nevertheless, the maximum is reached for longer time and remains less than the maximum uptake rate variance for $N_p = 2\cdot 10^5$.

On the opposite, the more microorganisms, the faster the increase in uptake rate variance. The maximum is higher than for $N_p = 2\cdot 10^5$ meaning that the more microorganisms, the wider uptake rate distribution in view of the precedent work. This result is in agreement with the substrate variance evolution shown in Figure 5.48b where the variance is maximum for the bigger microorganisms number. The microorganisms assimilation creates local gradients in the substrate concentration and the more microorganisms, the more fluctuations. The same conclusions arises for the substrate variance-uptake rate cross-correlation as seen in Figure 5.49c.

But if we look at the evolution of the mean uptake rate with respect to the fluid averaged substrate concentration, the results for the different simulations are confounded with each other. This means that all other biological and fluid parameters unchanged, the macroscopic assimilation law is identical, whatever the microorganisms number. In other words, the overall shape for assimilation law is unchanged and the apparent affinity constant would not depend on the biomass concentration. This observation should be verified for other simulations parameters in order to make a thoroughly conclusion.

But, the time required for complete assimilation of the initial substrate concentration is not equivalent in all cases. The more microorganisms, the faster the assimilation as observed in Figure 5.48.

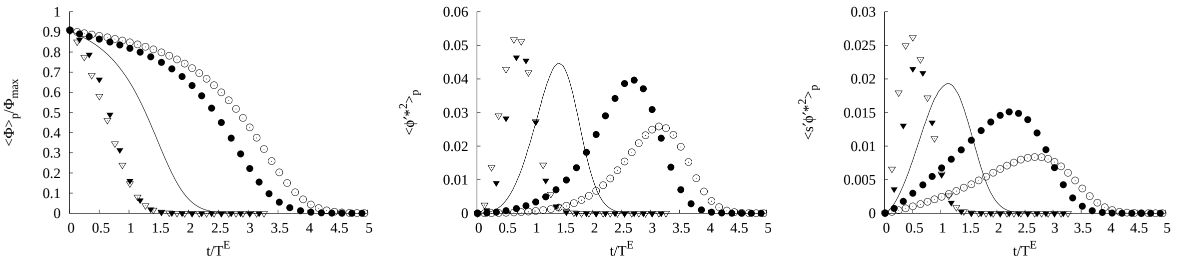

(a) $\langle\Phi\rangle_p/\Phi_{max}$ (b) $\langle\phi'^{*2}\rangle_p$ (c) $\langle s'\phi'\rangle_{*p}$

Figure 5.49: Effect of the particle loading and maximum specific uptake rate on the temporal evolution of the biological statistics. All simulations are performed for the dynamic fields and initial turbulent substrate field from simulation $R2$ with a uniform concentration $S_0 = 1\ \mathrm{kg_S \cdot m^{-3}}$. ●: $N_p = 10^5$, (——): $N_p = 2{\cdot}10^5$ and ▲: $N_p = 4{\cdot}10^5$. And for $N_p = 2{\cdot}10^5$, ○: $\Phi_{max} = 5{\cdot}10^{-8}\ \mathrm{kg_S \cdot s^{-1}}$ and △: $\Phi_{max} = 2 \cdot 10^{-7}\ \mathrm{kg_S \cdot s^{-1}}$.

The biomass growth or metabolite production can be directly affected by the exposure time to non-zero concentrations are to important concentration fluctuations, especially when the substrate concentration variance is important.

5.5.3 Effect of the maximum assimilation capacity of microorganisms

Finally, we just propose two results on the assimilation capacity of microorganisms. In the whole biological two-way coupling study, we kept the microorganisms maximum assimilation rate unchanged. The effect of different maximum capacities is shown by the empty symbols in Figures 5.48 to 5.50. We studied a two times higher and lower maximum assimilation capacity compared to the reference case $\Phi_{max} = 10^{-7}\ \mathrm{kg_S \cdot s^{-1}}$ with $N_p = 2 \cdot 10^5$ particles.

On the one hand, for the same particle loading ratio, the substrate concentration decrease is longer for the smaller maximum mass flux capacity because the overall assimilation rate is smaller. On the other hand, the substrate assimilation is faster for the bigger maximum mass flux and the substrate field concentration variance maximum is higher than for all simulations.

But we rather focus on non-dimensional biological statistics. The different statistics for the microorganisms population are shown in Figure 5.49 with empty symbols. The general evolution for the two considered simulations follow the remarks for the simulations with lower or higher particle loading ratio.

But regarding the non-dimensional averaged assimilation rate as function of the fluid averaged substrate concentration, the obtained overall assimilation law is not similar for the three prescribed maximum mass flux. Once again, this result can be discussed in term of apparent affinity constant K_S that accounts as well for the maximum capacity of assimilation of the different microorganisms. The smaller the maximum uptake rate capacity, the smaller the deviation to the expected macroscopic law because of the small amplitudes of local gradients due to assimilation. At the opposite the deviation is bigger for a higher maximum mass flux because of the large resulting variance of substrate concentration.

5.5.4 Dependance on initial conditions for the biological phase

It has been shown in this work that the statistical evolution of decaying substrate field is dependent on the initial conditions for the flow field. The effect of biological parameters on the decay has also

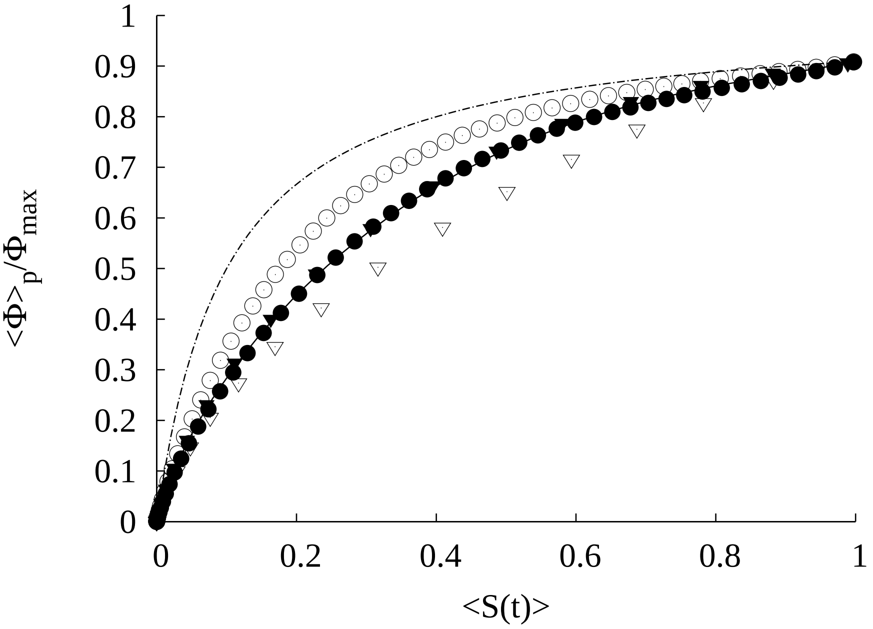

Figure 5.50: Effect of the particle loading and maximum specific uptake rate on the evolution of the mean uptake rate with respect to the mean concentration. All simulations are performed for the dynamic fields and initial turbulent substrate field from simulation $R2$ with a uniform concentration $S_0 = 1$ $\mathrm{kg_S \cdot m^{-3}}$. •: $N_p = 10^5$, (——): $N_p = 2 \cdot 10^5$ and ▲: $N_p = 4 \cdot 10^5$. And for $N_p = 2 \cdot 10^5$, ∘: $\Phi_{max} = 5 \cdot 10^{-8}$ $\mathrm{kg_S \cdot s^{-1}}$ and ▽: $\Phi_{max} = 2 \cdot 10^{-7}$ $\mathrm{kg_S \cdot s^{-1}}$.

been investigated. But the dependance on the initial dynamic properties of the microorganisms has not been investigated yet. we may remind here that the microorganisms are inertial-less and behave like tracers of the fluid. Thus, the initial particle velocity is not an accurate parameter to study the dependance on initial conditions for particles.

But, in fed-batch bioreactors, when the substrate is injected in the bioreactor, the microorganisms repartition is not homogeneous in the whole reactor. This configuration is mimicked by the injection of $N_p = 2 \cdot 10^5$ microorganisms at the bottom of the computational box. The microorganisms are approximately spread on 12 cells in the z-direction and it is chosen to have an initial density of one microorganism per computational cell in this bottom laden layer. Due to the velocity field, the microorganisms are dispersed in time. The initial and final particle fields are shown on Figures 5.51 and 5.52. In these figures, both initial particle fields for the simulations with initial randomly injected microorganisms are shown in Figures 5.51a and 5.52a. The final particle field for the initial localised injection is also shown in Figure 5.52b, where spatial heterogeneities are observed. Indeed, the initial heterogeneity affects the substrate concentration field. For short times, the substrate is assimilated by the microorganisms and the mass flux is important due to the available substrate concentration. But once this first high-assimilation phase is over, the microorganisms see lower substrate concentrations due to the assimilation of the neighbouring microorganisms. Moreover, the simulations are performed for less than 2 Eulerian times for the fluid corresponding to a simulation time of 0.26 s. As the microorganisms are tracers of the fluid, their position is impacted by the turbulent diffusion. Taylor (1922) proposes a work on the turbulent transport of a passive scalar, the turbulent diffusion is introduced by analysing the variance of displacement of a fluid elements ensemble. Batchelor (1953) later derives the asymptotical behaviour for large times as function of the fluid variance and Lagrangian time T^L (5.45) and displacement variance is also linked to the turbulent diffusion D^t (5.44).

$$\langle x_f^2(t)\rangle = 2\langle \mathbf{u}_f^2\rangle T^L t, \tag{5.43}$$

$$\langle x_f^2(t)\rangle = 6D^t t. \tag{5.44}$$

Finally the turbulent diffusion can be expressed as:

$$D^t = \frac{2}{3}q_f^2 T^L, \tag{5.45}$$

where the different parameters are know from our simulations. For simulation $R2$, the corresponding turbulent diffusion is: $D^t_{R2} = 1.246 \cdot 10^{-3}$ $\mathrm{m}^2 \cdot \mathrm{s}^{-1}$. We can then approximate the required time for one microorganism to travel in the whole box:

$$t_{D^t} = \frac{L_{box}^2}{D^t} = 1.68 \text{ s} \tag{5.46}$$

In comparison with the total simulation time, a non-homogeneous repartition is expected for the microorganisms position in the case of a localised initial repartition. This is observed in Figure 5.51b. This affects largely the substrate concentration field, as seen in Figure 5.52d.

If we now compare the uptake rate evolution with respect to the averaged concentration in the liquid, it is shown that the initial microorganisms concentration variance largely affects the macroscopic assimilation law as shown by Figure 5.53. The hyperbolic law is verified for small residual concentrations in the fluid, but a strong initial decrease is observed. At time $t = 0.64$ ms (corresponding to the vertical line in Figure 5.53), we plot the different distributions. The obtained substrate concentration distribution in the fluid are bimodal for both the total and fluctuating concentrations as seen in Figure 5.54. The total substrate concentration is distributed around S_0 and at $S = 0$ where there is no residual concentration due to assimilation. The substrate concentrations distributions seen by microorganisms present a different shape because of the substrate diffusion from the highly concentrated zone to the low concentrated zone. Finally, the distributions for the mass flux over the microorganisms is close to the concentration distribution seen by the microorganisms. Indeed, the uptake rate distribution can be directly linked to the distribution of substrate concentration seen by microorganisms as we proposed in the fourth chapter of this work.

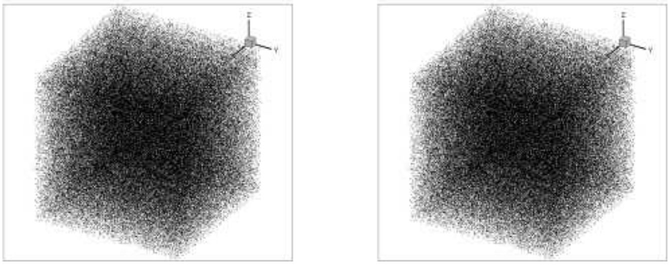

(a) Initial particle field, for initial random microorganisms repartition.

(b) Final particle field at $t = 0.26s$, for random initial microorganisms repartition.

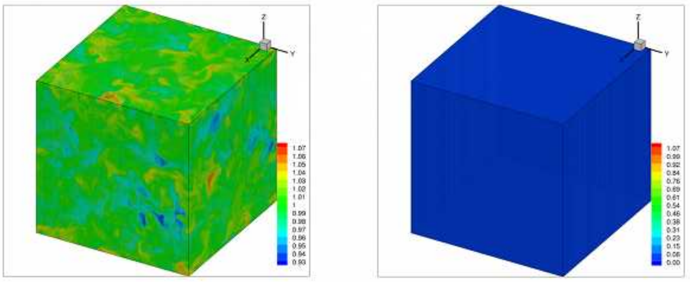

(c) S at $t = 0$

(d) S at $t = 0.26s$

Figure 5.51: 3D-view of the initial and final particle and substrate concentration fields for initial homogeneous microorganisms repartition.

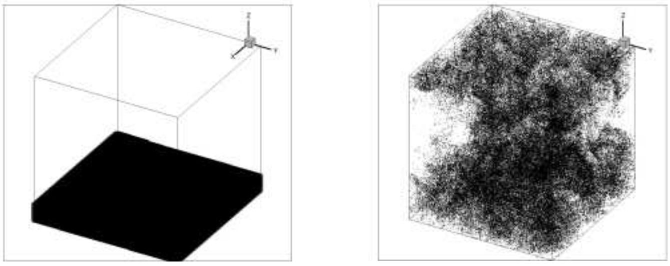

(a) Initial particle field, for localised microorganisms repartition.

(b) Final particle field at $t = 0.26s$, for the initial localised microorganisms injection.

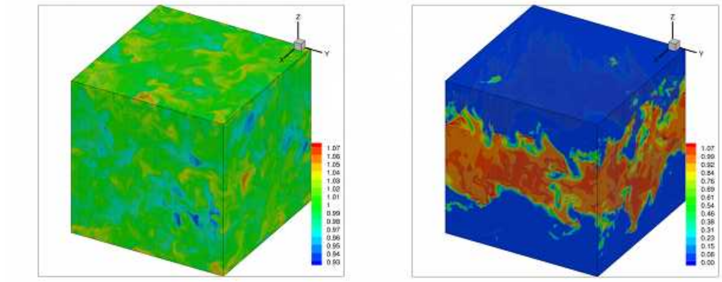

(c) S at $t = 0$

(d) S at $t = 0.26$, for localised initial microorganisms injection.

Figure 5.52: 3D-view of the initial and final particle and substrate concentration fields for initial inhomogeneous microorganisms repartition.

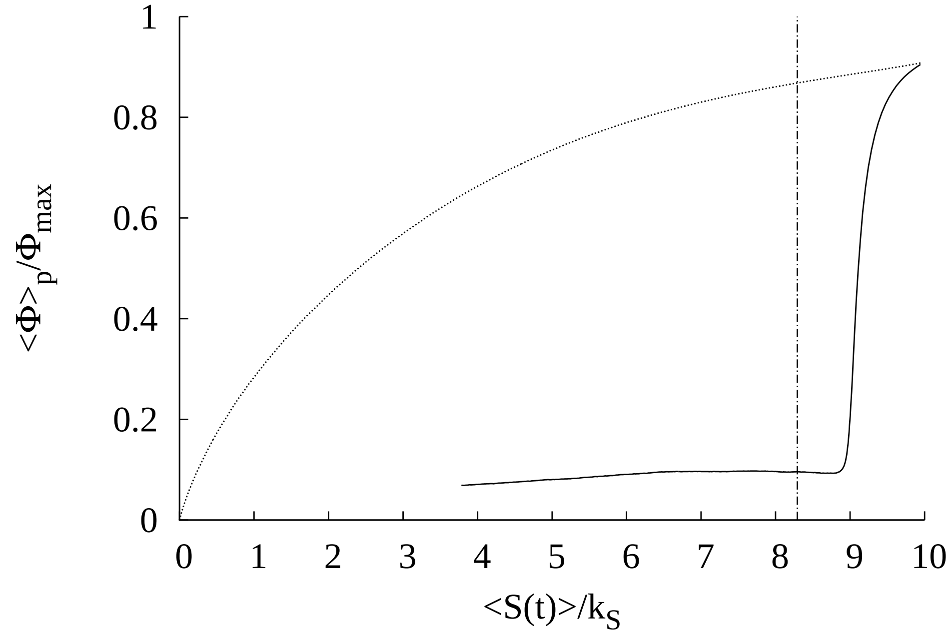

Figure 5.53: Evolution of the averaged assimilation rate with respect to the averaged concentration in the fluid for random (········) and localised (——) initial particle fields.

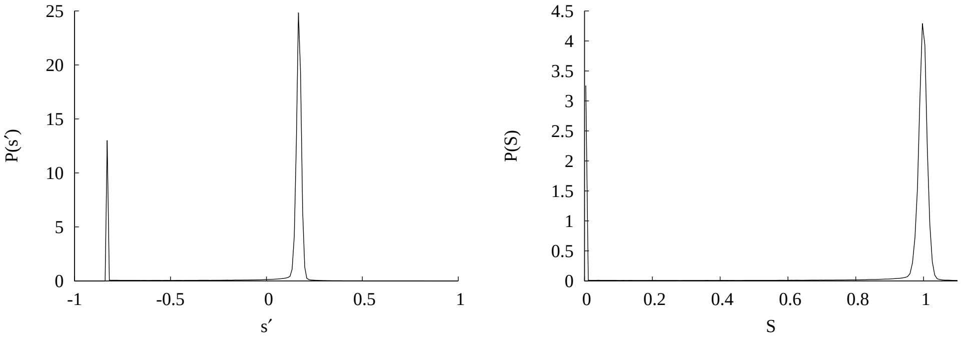

(a) $P(s')$ (b) $P(S)$

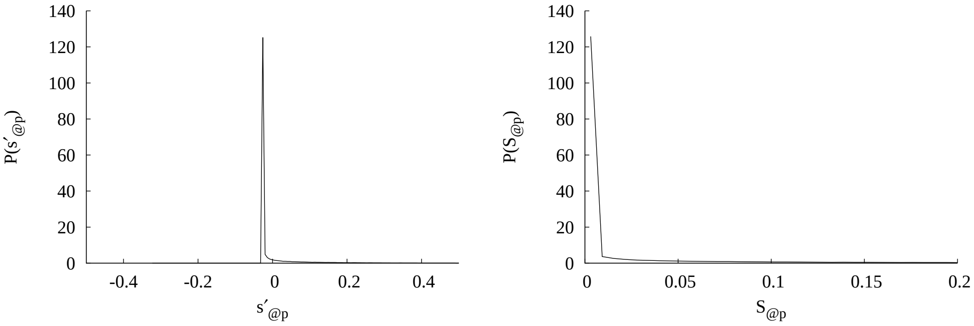

(c) $P(s'_{@p})$ (d) $P(S_{@p})$

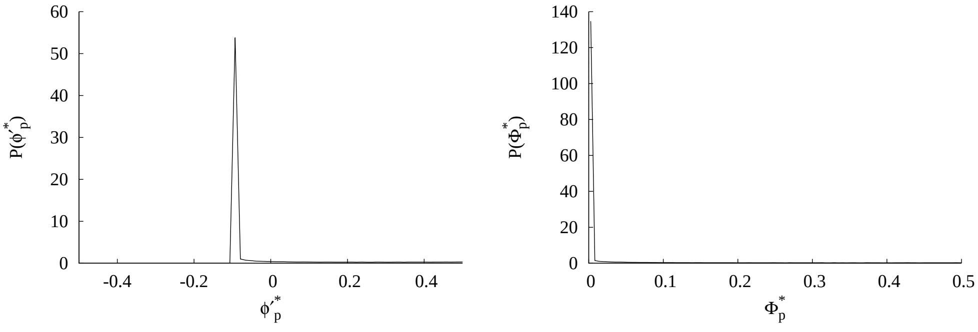

(e) $P(\phi'^{*}_p)$ (f) $P(\Phi^{*}_p)$

Figure 5.54: Normalised PDF for the fluid and microorganisms at $t = 64$ ms for the dynamic field and initial turbulent substrate field from simulation $R2$ with $S_0 = 1$ and $k_S = 0.1\ \mathrm{kg_S} \cdot \mathrm{m}^{-3}$.

Conclusion

This chapter was devoted to the analysis of the assimilation impact on the fluid in an unsteady configuration. Firstly the substrate concentration decay in a stationary fluid dynamics is studied. As expected the decay of the substrate concentration variance in a homogeneous isotropic turbulence is accurately described with the IEM model. Using this model, the temporal evolution of the substrate concentration variance is predictable as well as the concentration distribution that remains Gaussian throughout the simulation performed. The determination of the assimilated substrate distribution over the population of microorganisms can thus be deduced from the analytical law established n chapter 4.

Then, the biological two-way coupling configuration is presented. The numerical method is introduced and different numerical validations are performed using various hypothetical but informative configurations. First results in the absence of a velocity field show the effect of the microorganisms' spatial repartition in the computational domain on assimilation. Indeed, heterogeneities in the particle field concentration induce heterogeneities in the substrate concentration field. Local depletion in substrate directly influence the assimilation rate of some microorganisms. Thus, the specific assimilation rates obtained at the population scale are lower than obtained for homogeneously distributed particles.

Then, the biological two-way coupling is studied for a stationary HIT configuration, where the initial substrate concentration field is consumed by the microorganisms. This configuration mimics a batch reactor where the agitation is maintained and the substrate is no longer injected. A preliminary statistic analysis on the substrate concentration field show that the assimilation profoundly influences the scalar field. The averaged substrate concentration decreases in time as expected, so that the assimilation term in the averaged concentration transport equation is a sink term whereas it is found to be a source term in the substrate concentration variance evolution. Indeed, the substrate concentration variance reaches values up to 50 times the initial variance. This increase is the result of additional substrate gradients induced by the assimilation itself. Moreover the variance of the assimilation rate presents also an increase/decrease evolution, but on the opposite of the case without biological two-way coupling, the variance of the substrate concentration distribution in the fluid and that seen by the microorganisms are not similar. This results are further investigated by analysing the different PDF of the flow for the scalar. The distributions of the substrate fluctuations in the fluid, affected by the assimilation, are no longer Gaussian. Both distributions for the substrate concentration in the fluid and at the microorganisms' positions are not equal anymore. So, the prediction of the assimilation distribution over the microorganisms is flawed if one uses the substrate distribution in the fluid.

The influence of the flow dynamics and mixing on the assimilation rate is investigated. Intuitively, the higher the agitation (the higher the dissipation rate) the higher the obtained assimilated mass flux. This result gives support to experimental observations from the literature for the biomass growth, and enlightens the importance to achieve a good mixing state in order to increase the assimilation rate. The different results are presented in terms of averaged uptake rate with respect to the mean substrate concentration in the fluid. This choice is made in order to verify the validity of a macroscopic law based on the fluid averaged concentration and on the microscopic biological parameter k_S. Indeed, the usual approach for the determination of the assimilated uptake rate at the population scale is based on the averaged concentration in the reactor of the computational cell of a CFD calculation. The first striking results is the lower mass flux obtained for the simulations compared to the macroscopic law. But, following the observations made in the second chapter of this work the hyperbolic shape is still observed. A macroscopic assimilation law following a Monod equation can thus be found, but, the affinity constant must be adapted at the population scale. This apparent macroscopic affinity constant integrates the mixing effect on assimilation, or more specifically the competition between transport and assimilation. Indeed, for three different simulations where the dissipation rate and the substrate diffusion coefficient were modified, the obtained apparent affinity constants differ. This apparent affinity also accounts for the substrate initial concentration field.

Then a parametric study on the biological phase is performed. The influence of the affinity constant, maximum assimilation capacity, biomass concentration, as well as the influence of the initial repartition of microorganisms are investigated. They all are responsible for deviations of assimilation at the macroscopic scale. The initial particle field test is especially important for further development. Indeed, a homogeneous repartition of microorganisms is not realistic in bioreactors, and further heterogeneities of the substrate concentration field are expected due to heterogeneous assimilation of the population.

In the last case, the resulting macroscopic assimilation law is no longer hyperbolic. With the aim to understand this last result, the distributions of the substrate concentration in the fluid and seen by the microorganisms are studied. A bimodal distribution is found for the fluid substrate, whereas all microorganisms see one peak at small concentrations. The knowledge of the concentration distribution at the microorganisms' position is known in this configuration because of the Lagrangian tracking. But, at larger scales, the exact substrate concentration distribution at the microorganisms scale is out of reach. The determination of the effects of assimilation on both Lagrangian (at the microorganisms position) and Eulerian (in the fluid) substrate concentration fields remains one of the main perspectives of this part of the work.

We may also remark that this work was carried out considering the transport of one population of undifferentiated microorganisms. Meaningly, even if the microorganisms see different substrate concentrations along their trajectories, they are physiologically identical. But adaptation of the microorganisms to their environment and distinctions in terms of metabolisms can arise during the process. For example, for small residual concentration, the microorganisms can increase their affinity to the substrate, or the maximum capacity of assimilation can be adapted by the activation of specific transporters, resulting in a distribution of assimilation properties (affinity and maximum) within the population. Obviously, since this adaptation is dynamic, assimilation properties are expected to be dependent on the individual trajectories and on the quality of micro-mixing inside the bioreactor.

Figures

Conclusion

La mise au point et l'optimisation du fonctionnement des bioréacteurs industriels repose sur une phase d'extrapolation depuis l'échelle du laboratoire jusqu'à l'échelle industrielle. Or, la définition de critères objectifs garantissant le maintien des performances lors du changement d'échelle n'est actuellement pas possible étant donné la complexité des phénomènes biologiques à l'échelle cellulaire. De plus, les interactions entre la réaction biologique et le milieu de culture sont extrêmement sensibles à ces changements d'échelle.

La modélisation des bioréacteurs représente donc un enjeu majeur pour l'industrie, de même que l'identification de critères pertinents pour le suivi et l'analyse des cultures à grande échelle. De nombreuses approches expérimentales et numériques sont actuellement utilisées afin de produire des modélisations susceptibles a minima de représenter le fonctionnement à une échelle donnée. Parmi ces méthodes, le recours à la mécanique des fluides numériques pour prédire les transferts de masse, de quantité de mouvement et de chaleur dans des écoulements multiphasiques semble être une voie prometteuse, notamment en raison des succès obtenus dans de nombreux autres domaines d'application.

Ce travail a été réalisé dans le cadre de la fédération FERMaT en collaboration entre l'Institut de Mécanique des Fluides de Toulouse (IMFT) et le Laboratoire d'Ingénierie des Systèmes Biologiques et Procédés (LISBP). Les travaux de recherches se sont concentrés sur la simulation numérique des bioréacteurs et l'objectif principal de ce travail était de déterminer les effets des hétérogénéités spatiales de concentration dans un volume de fluide sur l'assimilation d'une population de microorganismes. En d'autre terme, on a cherché a caractériser l'influence de l'état de mélange du fluide sur la réaction biologique.

Cette problématique de micro-mélange est prépondérante pour la modélisation des bioréacteurs, notamment d'un point de vue numérique. En effet, les approches usuelles se basent sur la concentration moyenne calculée dans une maille de calcul CFD pour déterminer la croissance de la biomasse. Or, des hétérogénéités locales de concentrations influencent directement les microorganismes en terme d'assimilation et une diminution de la biomasse et l'apparition de sous-produits d'overflow sont observées expérimentalement.

Dans le premier chapitre, une étude bibliographique a permis de présenter différents travaux expérimentaux portant sur la problématique de l'influence du mélange sur la réaction biologique et les performances de bioréacteurs à différentes échelles. À l'aide de réacteurs scale-down (réacteurs de type industriels rapportés à l'échelle du laboratoire, mais prenant en compte les effets d'échelle à l'aide d'installations spécifiques), on cherche à reproduire les effets d'échelles à l'échelle du laboratoire et l'influence du mélange à l'échelle globale du réacteur est mise en évidence. Des études sur des bioréacteurs de laboratoire ont également cherché à montrer l'influence du micro-mélange sur le comportement de la biomasse. Ces effets de mélanges à l'échelle microscopiques ont été bien caractérisés, notamment du point de vue des conséquences biologiques. Mais les phénomènes physiques, concernant en particulier le transport du substrat ne sont que peu abordées.

Différentes études numériques sur les bioréacteurs sont également présentées au cours du premier chapitre. D'une part une approche génie des bioréacteurs est couramment employée pour modéliser les réacteurs à grande échelle, mais les phénomènes à l'échelle des micro-organismes ne sont pas pris en compte. Différents travaux en mécanique des fluides numérique (CFD) pour la modélisation des bioréacteurs sont également présentés. Or, dans la plupart des cas, les approches utilisées ne prennent pas en compte les effets d'hétérogénéités de concentration à l'échelle des microorganismes. Cependant, l'utilisation de la mécanique des fluides numérique est prometteuse, c'est pourquoi nous l'avons choisie pour notre étude, et ce dans le but de modéliser les effets de micro-mélange à l'échelle des microorganismes.

Le second chapitre de ce travail est consacré à étudier l'influence des fluctuations de concentration observées par un microorganisme le long de sa trajectoire en terme d'assimilation de substrat. Cette étude, pour un microorganisme isolé, couple transport diffusif du substrat jusqu'au microorganisme et consommation du substrat à l'interface de la cellule. La concentration en substrat loin du microorganisme est imposée et varie temporellement, tandis qu'une loi d'assimilation est imposée à l'interface liquide-cellule. Une loi d'assimilation classique où le flux assimilé est relié algébriquement à la concentration en substrat est utilisée (Monod), mais on propose également un modèle d'assimilation bilinéaire qui s'affranchit de la constante d'affinité au substrat et se base uniquement sur la capacité d'assimilation maximale du microorganisme. Pour des signaux de concentrations simples, on étudie les résultats dans le régime statistiquement stationnaire en termes de flux interfacial assimilé par le microorganisme.

Les observations, sur le flux moyen assimilé par le microorganisme, mettent en lumière l'existence d'une compétition entre transport de substrat et consommation par le microorganisme. Cette compétition se traduit en moyenne par une diminution du taux d'assimilation par rapport au cas où le microorganisme serait soumis à une concentration en substrat constante au cours du temps (les concentrations lointaines étant en moyennes identiques). De plus, les temps caractéristiques et la structure du signal de concentration du champ lointain influencent directement l'assimilation du microorganisme.

La compétition entre temps caractéristique de fluctuation et temps caractéristique de transport jusqu'au microorganisme est également un paramètre important à prendre en compte lors de la simulation numérique des réacteurs biologiques. Or, cette observation doit être prise en compte lors de la modélisation d'un réacteur industriel : par exemple si le temps de la réaction biologique est comparable au temps de circulation dans le bioréacteur, mais que l'échelle de temps est bien plus petite. Compte-tenu de la configuration choisie pour cette étude, il est tout à fait possible d'envisager de futurs travaux représentant un microorganisme dans une suspension, et d'approcher les transferts de matière dans le cadre d'un transport convectif-diffusif. La détermination de nombres sans dimension caractérisant la compétition entre transport et réaction biologique est alors envisagée. De plus, cette approche pourrait mener à une analyse plus fine des hétérogénéités d'assimilation à la surface d'un microorganisme, en terme d'activation de capteurs haute affinité lorsque le microorganisme voit de très faibles concentrations en substrat.

Dans le but d'étudier les effets d'hétérogénéités locales sur une population de microorganismes, des simulations numériques à une échelle plus grande ont été réalisées dans le troisième chapitre. La configuration d'une turbulence homogène isotrope statistiquement stationnaire a été retenue pour l'étude dans un volume de quelques litres. Celle-ci présente l'avantage de pouvoir dériver des grandeurs à l'échelle du domaine intégrant tous les effets locaux. En outre, la résolution par simulation numérique directe permet de s'affranchir de quelconque modélisation pour le mélange du substrat, ce dernier étant résolu comme un scalaire de l'écoulement.

Les différents champs fluides étudiés au cours de ce travail sont présentés, ainsi qu'une validation de l'outil utilisé et des différentes grandeurs statistiques utilisées. Il est important de rappeler ici, qu'en raison de limitations numériques, les simulations réalisées n'ont permis de prendre qu'une gamme restreinte de nombres de Reynolds et de Schmidt pour les écoulements. Ces configurations ne sont donc pas exactement représentatives des phénomènes intervenant dans les bioréacteurs. C'est notamment important en terme de micro-mélange car les mécanismes de mélange à l'échelle microscopique sont modifiés pour d'important nombre de Schmidt, dans le cas où la diffusivité du substrat est faible comparée à la viscosité du fluide. La simulation numérique de tels écoulements se révèle donc être un enjeu majeur pour une future étude sur l'influence du micro-mélange sur la réaction biologique.

Dans le quatrième chapitre la dynamique et l'assimilation de la biomasse dans les écoulements précédemment obtenus ont été étudiées. Les microorganismes sont suivis de manière Lagrangienne dans l'écoulement. Par interpolation du champ Eulérien, la concentration locale vue par les microorganismes est ainsi directement déterminée et une loi d'assimilation est appliquée à l'échelle microscopique pour chaque microorganisme. Le nombre de microorganismes choisis pour une population se situe aux alentours de 200000. Cette quantité représente un bon compromis entre analyse statistique et performances numériques.

Des simulations statistiquement stationnaires, dans lesquelles la consommation du substrat par les microorganismes n'agit pas sur le champ de concentration du fluide ont tout d'abord été réalisées. L'exploitation des simulations s'est concentrée sur la détermination de grandeurs biologiques globales à l'échelle de la population. Nous avons montré que dans le cadre de la configuration choisie, la loi d'assimilation macroscopique basée sur la concentration moyenne dans le domaine reste valable pour les paramètres de simulations considérés.

Cependant, les hétérogénéités au sein de la population ont été mises en évidence à travers une analyse statistique importante et par l'analyse des fonctions de distributions de la phase biologique. Ces hétérogénéités, en termes d'assimilation au sein d'une même population, trouvent leur origine dans l'état de micro-mélange du réacteur. Nous avons alors montré que les hétérogénéités au sein des microorganismes peuvent, dans cette configuration, être entièrement déterminées par la connaissance de la distribution de concentration en substrat au sein du champ turbulent.

À l'aide d'un modèle métabolique, nous avons alors réussi à prédire la croissance de la biomasse ainsi que la production de métabolites secondaires issues du mécanisme d'overflow en se basant sur les distributions de flux de sucre assimilés par les microorganismes. En raison des distributions de concentrations en substrat vues par les microorganismes, il a été montré qu'une diminution de la vitesse spécifique de croissance s'accompagne dans le même temps de la formation de métabolites secondaires, et ce en particulier pour de très fortes affinités au substrat.

L'extrapolation de ce résultat est envisageable pour des simulations RANS ou LES de réacteurs industriels. En effet, si les équations de transport du scalaire et de sa variance sont résolues, on peut par exemple modéliser le mélange à l'intérieur d'une maille de calcul par un champ homogène et isotrope de concentration et ainsi déterminer la distribution du taux d'assimilation pour les microorganismes à l'intérieur de cette maille.

De plus, en couplant un modèle métabolique, on peut arriver à prédire le taux de croissance à l'intérieur de cette même maille de calcul CFD. Même si les résultats présentés pour la croissance ne considèrent que les métabolismes purement oxydatifs, la prise en compte de la limitation en oxygène pourrait se faire en regardant les PDF jointes de flux de substrat et d'oxygène assimilés par les microorganismes. La résolution du champ gazeux et la prise en compte de l'effet des bulles sur l'oxygène seraient susceptibles de modifier l'écoulement, et plus particulièrement le champ de concentration en substrat.

Enfin, les simulations ont été réalisées pour de faibles nombres de Schmidt. Une étude de l'impact de ce dernier sur l'assimilation est en continuité directe avec le travail présenté. En effet, les zones de mélanges visqueux convectif et visqueux-diffusif sous l'échelle de Kolmogorov vont influencer directement les champs de concentration vus par les microorganismes. Une DNS+DPS dans laquelle on étudierait l'assimilation instationnaire par les microorganismes représente également une voie de continuité de ce travail.

Enfin, l'objectif initial de ce travail était d'utiliser la simulation numérique directe afin de com prendre et de modéliser le couplage inverse biologique. Ce dernier a été mis en place et des cas de validation simple ont été proposés. Une étude de l'effet de la dynamique et du mélange sur l'assimilation a été menée tout au long du chapitre 5 de ce travail. Cette étude montre que la loi d'assimilation, basée sur la concentration résiduelle moyenne en substrat, habituellement utilisée dans les réacteurs batch surestime l'assimilation si l'on considère un seul et unique paramètre biologique entre l'échelle microscopique et macroscopique.

En effet, la loi d'assimilation obtenue à l'échelle du réacteur intègre les effets locaux, de la dynamique, du mélange et du champ de concentration initial. Une étude menée sur les paramètres biologiques montre également que d'autres paramètres influencent l'assimilation, tels que la concentration initiale en microorganismes, mais également leur répartition, ou encore leur état physiologique, c'est-à-dire leur affinité au substrat par exemple. De futurs développements sont envisageables quant à la détermination de la constante d'affinité macroscopique, en réalisant par exemple des simulations où les nombres adimensionnels du problème sont conservés.

Au cours de ce travail plusieurs perspectives à plus ou moins long terme sont apparues. D'une part, dans le but de caractériser les transferts de masse à l'échelle des microorganismes, et les interactions entre transport et réaction, des simulations numériques directes diphasiques apparaissent comme une piste de continuité de ce travail en terme de développements théoriques et de modèles à l'échelle locale.

D'autre part, au vue des résultats obtenus concernant l'effet du micro-mélange sur l'assimilation de substrat par les microorganismes, il apparaît de première importance de prendre en compte les effets d'hétérogénéités microscopiques dans les calculs RANS ou LES pour la modélisation des bioréacteurs. Il est par exemple envisageable de prédire le taux de croissance de la biomasse dans une maille de calcul CFD en utilisant le modèle métabolique, proposé dans le chapitre quatre, couplé aux distributions de flux assimilés dans la maille. La détermination des distributions de flux assimilés est basée sur les distributions de concentration en substrat, comme présenté lors des simulations numériques stationnaires de ce travail. Enfin, ce travail a montré qu'une approche basée sur la résolution des équations de transport des différentes fonctions de densité de probabilité du problème ainsi que les termes de transferts se présente comme une voie majeur pour la modélisation des bioréacteurs, et plus particulièrement pour la modélisation du couplage inverse biologique.

Appendix A

Analytical solution for 1D spherical diffusion equation with Monod assimilation model

In the steady state, the radial component of the spherical diffusion equation yields:

$$\frac{\partial}{\partial r}\left(r^2\frac{\partial S}{\partial r}\right) = 0. \tag{A.1}$$

Using the Monod assimilation model the boundary conditions for the problem are:

- Constant far-field concentration:

$$S(r = R + L) = S_\infty \tag{A.2}$$

- Constant assimilation at the cell interface:

$$\frac{dS}{dr}|_{r=R} = \varphi_{max}\frac{S_{int}}{k_S + S_{int}} \tag{A.3}$$

The substrate concentration in the domain is:

$$S(r) = S_\infty + R^2\varphi_{max}\frac{S_{int}}{k_S + S_{int}}(\frac{1}{R+L} - \frac{1}{r}) \tag{A.4}$$

At $r = R$ the interfacial concentration yields:

$$S(r = R) = S_{int} = S_\infty + R^2\varphi_{max}\frac{S_{int}}{k_S + S_{int}}(\frac{1}{R+L} - \frac{1}{R}), \tag{A.5}$$

leading to a second-order equation for the interfacial concentration S_{int}. The positive solution finally gives S_{int} as a function of R , L , k_S , S_∞:

$$S_{int} = \frac{-(k_S - S_\infty + \frac{RL}{R+L}\varphi_{max}) + \sqrt{(k_S - S_\infty + \frac{RL}{R+L}\varphi_{max})^2 + 4k_S S_\infty}}{2}, \tag{A.6}$$

and the interfacial uptake rate is given by:

$$\varphi_{int} = \varphi_{max}\frac{-(k_S - S_\infty + \frac{RL}{R+L}\varphi_{max}) + \sqrt{(k_S - S_\infty + \frac{RL}{R+L}\varphi_{max})^2 + 4k_S S_\infty}}{2k_S - (k_S - S_\infty + \frac{RL}{R+L}\varphi_{max}) + \sqrt{(k_S - S_\infty + \frac{RL}{R+L}\varphi_{max})^2 + 4k_S S_\infty}2}. \tag{A.7}$$

Appendix B

Linear and SFM interpolation schemes

Linear interpolation

The interpolated quantity at the particle position is written $s_{@p}(x_p, y_p, z_p, t)$ and is linked to the Eulerian quantity $s(x_i, y_j, z_k, t)$, where the subscripts refers to the different nodes of the Eulerian grid. The approximation $s_{@p}$ is thus given by:

$$s_{@p} = (x_p, y_p, z_p, t) = \sum_{i=0}^{N} \sum_{j=0}^{N} \sum_{k=0}^{N} s(x_i, y_j, z_k, t) P_i(x_p) P_j(y_p) P_k(z_p) \tag{B.1}$$

where the coefficients are the quantity values at the grid points and the basis functions P_i are given hereafter:

$$\begin{array}{rcll} P_i(x) & = & 0; & x < x_{i-1} \\ & = & (1-\xi), \quad \xi = \frac{x - x_{i-1}}{\Delta}; & x_{i-1} \leqslant x \leqslant x_i \\ & = & \xi, \qquad\quad \xi = \frac{(x - x_i)}{\Delta}; & x_i \leqslant x \leqslant x_{i+1} \\ & = & 0; & x_{i+1} < x \end{array} \tag{B.2}$$

These basis functions are linear functions of the position and only the eight direct surrounding nodes are used to calculate the interpolated data.

SFM interpolation scheme

In the Shape Function Method, the data at the particle position and its spatial derivatives at the eight corners of the cube immediatly surrounding the particle are used to evaluated the local quantity at the particle position. The interpolated quantity is then written as:

$$\begin{aligned} s_{@p}(x_p, y_p, z_p, t) &= \textstyle\sum_{i=0}^{N}\sum_{j=0}^{N}\sum_{k=0}^{N}(s(x_i, y_j, z_k, t)H_i(x_p)H_j(y_p)H_k(z_p) \\ &+ \tfrac{\partial s}{\partial x}(x_i, y_j, z_k, t)G_i(x_p)H_j(y_p)H_k(z_p) \\ &+ \tfrac{\partial s}{\partial y}(x_i, y_j, z_k, t)H_i(x_p)G_j(y_p)H_k(z_p) \\ &+ \tfrac{\partial s}{\partial z}(x_i, y_j, z_k, t)H_i(x_p)H_j(y_p)G_k(z_p)) \end{aligned} \tag{B.3}$$

where H and G are the basis functions also called the shape functions. The basis functions for Hermite interpolation can be written as:

$$\begin{aligned} H_i(x) &= 0; && && x < x_{i-1} \\ &= \xi^2(3-2\xi), && \xi = \tfrac{(x-x_{i-1})}{\Delta}; && x_{i-1} \leqslant x \leqslant x_i \\ &= (1-\xi)^2(1+2\xi), && \xi = \tfrac{(x-x_i)}{\Delta}; && x_i \leqslant x \leqslant x_{i+1} \\ &= 0; && && x_{i+1} < x \end{aligned} \tag{B.4}$$

$$\begin{aligned} G_i(x) &= 0; && && x < x_{i-1} \\ &= h\xi^2(\xi-1), && \xi = \tfrac{(x-x_{i-1})}{\Delta}; && x_{i-1} \leqslant x \leqslant x_i \\ &= h(1-\xi)^2\xi, && \xi = \tfrac{(x-x_i)}{\Delta}; && x_i \leqslant x \leqslant x_{i+1} \\ &= 0; && && x_{i+1} < x \end{aligned} \tag{B.5}$$

The periodicity implies:

$$\begin{aligned} x_p &= x_{p+N} \quad \text{if } p < 0 \\ &= x_{p-N} \quad \text{if } p > N \end{aligned} \tag{B.6}$$

where N is the total number of points in the direction i.

Appendix C

Forcing scheme parameters

Table C.1: Forcing parameters for the different performed simulations.

Simulation name	$R1$, $P1$	$R2$, $G2$
Mesh	128^3	128^3
Re_Λ	68	110
Forcing parameters		
σ_F	0.02	0.1
T_F	0.2	0.05

Bibliography

Acrivos, A. and Taylor, T. (1962). Heat and mass transfer from single spheres in stokes flow. *Physics of Fluids*, 5:387.

Akiti, O. and Armenante, P. M. (2004). Experimentally-validated micromixing-based cfd model for fed-batch stirred-tank reactors. *AIChE Journal*, 50(3):566–577.

Al-Homoud, A. and Hondzo, M. (2008). Enhanced uptake of dissolved oxygen and glucose by escherichia coli in a turbulent flow. *Applied Microbiology and Biotechnology*, 79(4):643.

Amanullah, A., McFarlane, C. M., Emery, A. N., and Nienow, A. W. (2001). Scale-down model to simulate spatial ph variations in large-scale bioreactors. *Biotechnology and Bioengineering*, 73(5):390–399.

Ataai, M. M. and Shuler, M. L. (1985). Simulation of cfstr through development of a mathematical model for anaerobic growth of escherichia coli cell population. *Biotechnology and Bioengineering*, 27(7):1051–1055.

Bailey, J. E. and Ollis, D. F. (1986). *Biochemical Engineering Fundamentals*, volume Second. McGraw-Hill.

Balachandar, S. and Maxey, M. (1989). Methods for evaluating fluid velocities in spectral simulations of turbulence. *Journal of Computational Physics*, 83(1):96 – 125.

Baldyga, J. and Bourne, J. (1984). A fluid mechanical approach to turbulent mixing and chemical reaction part iii computational and experimental results for the new micromixing model. *Chemical Engineering Communications*, 28:259–281.

Baldyga, J. and Bourne, J. R. (2003). *Turbulent mixing and chemical reactions.* John Wiley and Sons, Chichester.

Baldyga J., B. J. (1986). *Encyclopedia of Fluid Mechanics: V, 1, Flow Phenomena and Measurement.* Gulf Houston.

Basset, A. (1888). A treatise on hydrodynamics (deighton bell, london, 1888). *Vol*, 2:285.

Batchelor, G. (1953). *The theory of homogeneous turbulence.* Cambridge Univ Pr.

Batchelor, G. (1980). Mass transfer from small particles suspended in turbulent fluid. *Journal of Fluid Mechanics*, 98(03):609–623.

Batchelor, G. K., Howells, I. D., and Townsend, A. A. (1959). Small-scale variation of convected quantities like temperature in turbulent fluid part 2. the case of large conductivity. *Journal of Fluid Mechanics*, 5(01):134–139.

Bauer, M. and Eigenberger, G. (1999). A concept for multi-scale modeling of bubble columns and loop reactors. *Chemical Engineering Science*, 54(21):5109 – 5117.

Bergstedt, M. S., Hondzo, M. M., and Cotner, J. B. (2004). Effects of small scale fluid motion on bacterial growth and respiration. *Freshwater Biology*, 49(1):28–40.

Bezzo, F., Macchietto, S., and Pantelides, C. C. (2003). General hybrid multizonal/cfd approach for bioreactor modeling. *AIChE Journal*, 49(8):2133–2148.

Boivin, M., Simonin, O., and Squires, K. (1998). Direct numerical simulation of turbulence modulation by particles in isotropic turbulence. *Journal of Fluid Mechanics*, 375(1):235–263.

Borgas, M., Sawford, B., Xu, S., Donzis, D., and Yeung, P. (2004). High Schmidt number scalars in turbulence: structure functions and Lagrangian theory. *Physics of Fluids*, 16:3888.

Bourne, J., Kozicki, F., and Rys, P. (1981). Mixing and fast chemical reaction: Test reactions to determine segregation. *Chemical Engineering Science*, 36(10):1643 – 1648.

Boussinesq, V. (1885). Sur la résistance qu'oppose un liquide indéfini en repos. In *Acad Sci*, volume 100, pages 935–7.

Bylund, F., Collet, E., Enfors, S.-O., and Larsson, G. (1998). Substrate gradient formation in the large-scale bioreactor lowers cell yield and increases by-product formation. *Bioprocess and Biosystems Engineering*, 18:171–180.

Chassagnole, C., Noisommit-Rizzi, N., Schmid, J. W., Mauch, K., and Reuss, M. (2002). Dynamic modeling of the central carbon metabolism of escherichia coli. *Biotechnology and Bioengineering*, 79(1):53–73.

Corrsin, S. (1951). On the spectrum of isotropic temperature fluctuations in an isotropic turbulence. *Journal of Applied Physics*, 22(4):469–473.

Corrsin, S. (1952). Heat transfer in isotropic turbulence. *Journal of Applied Physics*, 23(1):113 –118.

Crowe, C. T., Sharma, M. P., and Stock, D. E. (1977). The particle-source-in cell (psi-cell) model for gas-droplet flows. *Journal of Fluids Engineering*, 99(2):325–332.

Danckwerts, P. (1958). The effect of incomplete mixing on homogeneous reactions. In Garcia et al. (2009), pages 93–102.

Delafosse, A. (2008). *Analyse et étude numérique des effets de mélange dans un bioréacteur*. Phd thesis, Institut National des Sciences Appliquées.

Delafosse, A., Line, A., Morchain, J., and Guiraud, P. (2008). Les and urans simulations of hydrodynamics in mixing tank: Comparison to piv experiments. *Chemical Engineering Research and Design*, 86(12):1322 – 1330.

Delvigne, F., Boxus, M., Ingels, S., Thonart, P., et al. (2009). Bioreactor mixing efficiency modulates the activity of a prpos:: Gfp reporter gene in e. coli. *Microbial cell factories*, 8(1):15.

Delvigne, F., Destain, J., and Thonart, P. (2005a). Bioreactor hydrodynamic effect on *Escherichia coli*; physiology: experimental results and stochastic simulations. *Bioprocess and Biosystems Engineering*, 28:131–137.

Delvigne, F., Destain, J., and Thonart, P. (2005b). Structured mixing model for stirred bioreactors: An extension to the stochastic approach. *Chemical Engineering Journal*, 113(1):1 – 12.

Ducci, A. and Yianneskis, M. (2005). Direct determination of energy dissipation in stirred vessels with two-point lda. *AIChE journal*, 51(8):2133–2149.

Dunlop, E. and Ye, S. (1990a). Micromixing in fermentors: Metabolic changes in saccharomyces cerevisiae and their relationship to fluid turbulence. In Garcia et al. (2009), pages 854–864.

Dunlop, E. H. and Ye, S. J. (1990b). Micromixing in fermentors: Metabolic changes in saccharomyces cerevisiae and their relationship to fluid turbulence. *Biotechnology and Bioengineering*, 36(8):854–864.

Elghobashi, S. and Truesdell, G. (1993a). On the two-way interaction between homogeneous turbulence and dispersed solid particles. I: Turbulence modification. *Physics of Fluids A Fluid Dynamics*, 5:1790–1790.

Elghobashi, S. and Truesdell, G. C. (1993b). On the two-way interaction between homogeneous turbulence and dispersed solid particles. i: Turbulence modification. *Physics of Fluids A: Fluid Dynamics*, 5(7):1790–1801.

Enfors, S. O., Jahic, M., Rozkov, A., Xu, B., Hecker, M., Jürgen, B., Krüger, E., Schweder, T., Hamer, G., O'Beirne, D., Noisommit-Rizzi, N., Reuss, M., Boone, L., Hewitt, C., McFarlane, C., Nienow, A., Kovacs, T., Trägårdh, C., Fuchs, L., Revstedt, J., Friberg, P. C., Hjertager, B., Blomsten, G., Skogman, H., Hjort, S., Hoeks, F., Lin, H. Y., Neubauer, P., van der Lans, R., Luyben, K., Vrabel, P., and Manelius, Å. (2001). Physiological responses to mixing in large scale bioreactors. *Journal of Biotechnology*, 85(2):175–185.

Escudié, R. and Liné, A. (2003). Experimental analysis of hydrodynamics in a radially agitated tank. *AIChE Journal*, 49(3):585–603.

Esener, A. A., Roels, J. A., and Kossen, N. W. F. (1983). Theory and applications of unstructured growth models: Kinetic and energetic aspects. *Biotechnology and Bioengineering*, 25(12):2803–2841.

Eswaran, V. and Pope, S. (1988). Direct numerical simulations of the turbulent mixing of a passive scalar. *Physics of Fluids*, 31:506.

Fede, P. (2004). *Modélisation et simulation de l'influence de la turbulence sur les collisions dans les écoulements mono et bi-solides*. PhD thesis.

Feng, Z.-G. and Michaelides, E. E. (2000). A numerical study on the transient heat transfer from a sphere at high reynolds and peclet numbers. *International Journal of Heat and Mass Transfer*, 43(2):219 – 229.

Ferenci, T. (1996). Adaptation to life at micromolar nutrient levels: the regulation of escherichia coli glucose transport by endoinduction and camp. *FEMS Microbiology Reviews*, 18(4):301–317.

Ferenci, T. (1999a). 'growth of bacterial cultures' 50 years on: towards an uncertainty principle instead of constants in bacterial growth kinetics. *Research in Microbiology*, 150(7):431 – 438.

Ferenci, T. (1999b). Regulation by nutrient limitation. *Current Opinion in Microbiology*, 2(2):208 – 213.

Février, P. and Simonin, O. (2000). *Etude numérique des effets de concentration préférentielle et de corrélation spatiale entre vitesses de particules solides en turbulence homogene isotrope stationnaire*. PhD thesis.

Fox, R. (2003). *Computational models for turbulent reacting flows*. Cambridge Univ Pr.

Fox, R. and Yeung, P. (2003). Improved lagrangian mixing models for passive scalars in isotropic turbulence. *Physics of Fluids*, 15:961.

Frankel, N. A. and Acrivos, A. (1968). Heat and mass transfer from small spheres and cylinders freely suspended in shear flow. *Physics of Fluids*, Volume 11.

Fredrickson, A., Ramkrishna, D., and Tsuchiya, H. (1967). Statistics and dynamics of procaryotic cell populations. *Mathematical Biosciences*, 1(3):327 – 374.

Garcia, J., Cha, H., Rao, G., Marten, M., and Bentley, W. (2009). Microbial nar-gfp cell sensors reveal oxygen limitations in highly agitated and aerated laboratory-scale fermentors. *Microbial Cell Factories*, 8(1):6.

George, S., Larsson, G., Olsson, K., and Enfors, S.-O. (1998). Comparison of the baker's yeast process performance in laboratory and production scale. *Bioprocess and Biosystems Engineering*, 18:135–142.

Guillard, F., T. C. (1999). Modeling of the performance of industrial bioreactors with a dynamic microenvironmental approach: A critical review. *Chemical Engineering & Technology*, Volume 22, Issue 3:187–195.

Hansford, G. S. and Humphrey, A. E. (1966). The effect of equipment scale and degree of mixing on continuous fermentation yield at low dilution rates. *Biotechnology and Bioengineering*, 8(1):85–96.

Hartmann, H., Derksen, J., Montavon, C., Pearson, J., Hamill, I., and van den Akker, H. (2004). Assessment of large eddy and rans stirred tank simulations by means of lda. *Chemical Engineering Science*, 59(12):2419 – 2432.

Henson, M. A., Müller, D., and Reuss, M. (2002). Cell population modelling of yeast glycolytic oscillations. *The Biochemical journal*, 368:433–446.

Hewitt, C. J., Nebe-Von Caron, G., Axelsson, B., McFarlane, C. M., and Nienow, A. W. (2000). Studies related to the scale-up of high-cell-density e. coli fed-batch fermentations using multi-parameter flow cytometry: Effect of a changing microenvironment with respect to glucose and dissolved oxygen concentration. *Biotechnology and Bioengineering*, 70(4):381–390.

Hondzo, M. and Al-Homoud, A. (2007). Model development and verification for mass transport to escherichia coli cells in a turbulent flow. *Water Resources Research*, 43.

Insel, G., Celikyilmaz, G., Ucisik-Akkaya, E., Yesiladali, K., Cakar, Z., Tamerler, C., and Orhon, D. (2007). Respirometric evaluation and modeling of glucose utilization by escherichia coli under aerobic and mesophilic cultivation conditions. *Biotechnology and bioengineering*, 96(1):94–105.

Jaberi, F. (1998). Temperature fluctuations in particle-laden homogeneous turbulent flows. *International Journal of Heat and Mass Transfer*, 41(24):4081 – 4093.

Jaberi, F., Miller, R., Madnia, C., and Givi, P. (1996). Non-gaussian scalar statistics in homogeneous turbulence. *Journal of Fluid Mechanics*, 313:241–282.

Jaberi, F. A. and Mashayek, F. (2000). Temperature decay in two-phase turbulent flows. *International Journal of Heat and Mass Transfer*, 43(6):993 – 1005.

Jayesh, Tong, C., Warhaft, Z., et al. (1994). On temperature spectra in grid turbulence. *Physics of Fluids*, 6(1).

Jenne, M. and Reuss, M. (1999). A critical assessment on the use of $k - \varepsilon$ turbulence models for simulation of the turbulent liquid flow induced by a rushton-turbine in baffled stirred-tank reactors. *Chemical Engineering Science*, 54(17):3921–3941.

John, A., Bjalski, W., and Nienow, A. (1997). Mixing ix, multiphase systems. *Récents progrès en génie des procédés.*, 11(52):169.

Kàrmàn, T. d. and Howarth, L. (1938). On the statistical theory of isotropic turbulence. *Proceedings of the Royal Society of London. Series A, Mathematical and Physical Sciences*, 164(917):pp. 192–215.

Kim, B. G. and Shuler, M. L. (1990). A structured, segregated model for genetically modified escherichia coli cells and its use for prediction of plasmid stability. *Biotechnology and Bioengineering*, 36(6):581–592.

Kitano, H. (2002). Computational systems biology. *Nature: International weekly journal of science*, 420(6912):206–210.

Koch, A. L. and Houston Wang, C. (1982). How close to the theoretical diffusion limit do bacterial uptake systems function? *Archives of Microbiology*, 131(1):36–42.

Kolmogorov, A. (1941). The local structure of turbulence in incompressible viscous fluid for very large reynolds' numbers. In *Akademiia Nauk SSSR Doklady*, volume 30, pages 301–305.

Kolmogorov, A. (1962). A refinement of previous hypotheses concerning the local structure of turbulence in a viscous incompressible fluid at high Reynolds number. *Journal of Fluid Mechanics*, 13(01):82–85.

Kovàrovà-Kovar, K. and Egli, T. (1998). Growth kinetics of suspended microbial cells: From single-substrate-controlled growth to mixed-substrate kinetics. *Microbiol. Mol. Biol. Rev.*, 62:646–666.

Lapin, A. and Lübbert, A. (1994). Numerical simulation of the dynamics of two-phase gas-liquid flows in bubble columns. *Chemical Engineering Science*, 49(21):3661 – 3674.

Lapin, A., Muller, D., and Reuss, M. (2004). Dynamic behavior of microbial populations in stirred bioreactors simulated with euler-lagrange methods: Traveling along the lifelines of single cells. *Industrial & Engineering Chemistry Research*, 43(16):4647–4656.

Lapin, A., Schmid, J., and Reuss, M. (2006). Modeling the dynamics of e. coli populations in the three-dimensional turbulent field of a stirred-tank bioreactor – a structured - segregated approach. *Chemical Engineering Science*, 61(14):4783 – 4797.

Lara, A., Leal, L., Flores, N., Gosset, G., Bolívar, F., and Ramírez, O. (2006a). Transcriptional and metabolic response of recombinant escherichia coli to spatial dissolved oxygen tension gradients simulated in a scale-down system. *Biotechnology and bioengineering*, 93(2):372–385.

Lara, A. R., E., G., T., R. O., and L.A., P. (2006b). Living with heterogeneous bioreactors: understanding the effect of environmental gradients in cells. *Molecular Biotechnology*, 34(3):355–381.

Larsson, G., Törnkvist, M., Wernersson, E., Trägårdh, C., Noorman, H., and Enfors, S. (1996). Substrate gradients in bioreactors: origin and consequences. *Bioprocess and Biosystems Engineering*, 14(6):281–289.

Lavieville, J. and Berlemont, A. (1997). Simulations numériques et modélisation des interactions entre l'entraînement par la turbulence et les collisions interparticulaires en écoulements gaz-solide.

Legendre, D. (1996). *Quelques aspects des forces hydrodynamiques et des transferts de chaleur sur une bulle sphérique.* PhD thesis, INPT, Institut de Mécanique des Fluides de Toulouse (IMFT).

Lendenmann, U. and Egli, T. (1998). Kinetic models for the growth of escherichia coli with mixtures of sugars under carbon-limited conditions. *Biotechnology and Bioengineering*, 59(1):99–107.

Lien, R. and D'Asaro, E. (2002). The kolmogorov constant for the lagrangian velocity spectrum and structure function. *Physics of Fluids*, 74:4456–4459.

Lin, H. Y., Mathiszik, B., Xu, B., Enfors, S.-O., and Neubauer, P. (2001). Determination of the maximum specific uptake capacities for glucose and oxygen in glucose-limited fed-batch cultivations of escherichia coli. *Biotechnology and Bioengineering*, 73(5):347–357.

Lin, H. Y. and Neubauer, P. (2000). Influence of controlled glucose oscillations on a fed-batch process of recombinant escherichia coli. *Journal of Biotechnology*, 79(1):27 – 37.

Linkès, M., Martins Afonso, M., Fede, P., Morchain, J., and Schmitz, P. (2012). Numerical study of substrate assimilation by a microorganism exposed to fluctuating concentration. *Chemical Engineering Science*.

Magnaudet, J., Rivero, M., and J., F. (1995). Accelerated flows past a rigid sphere or a spherical bubble. part 1. steady straining flow. *Journal of Fluid Mechanics, , pp 97-135*, 284:pp 97–135.

Mantzaris, N. V., Liou, J.-J., Daoutidis, P., and Srienc, F. (1999). Numerical solution of a mass structured cell population balance model in an environment of changing substrate concentration. *Journal of Biotechnology*, 71:157–174.

Mashayek, F. (1998). Direct numerical simulations of evaporating droplet dispersion in forced low mach number turbulence. *International Journal of Heat and Mass Transfer*, 41(17):2601 – 2617.

Mayr, B., Horvat, P., Nagy, E., and Moser, A. (1993). Mixing-models applied to industrial batch bioreactors. *Bioprocess and Biosystems Engineering*, 9:1–12.

Merchuk, J. C. and Asenjo, J. A. (1995). The monod equation and mass transfer. *Biotechnology and Bioengineering*, 45(1):91–94.

Monod, J. (1949). The growth of bacterial cultures. *Annual Review of Microbiology*, 3(1):371–394.

Morchain, J., Gabelle, J.-C., and Cockx, A. (2012). Coupling of biokinetic and population balance models to account for biological heterogeneity in bioreactors. *AIChE Journal*.

Nagy, E., Neubeck, M., Mayr, B., and Moser, A. (1995). Simulation of the effect of mixing, scale-up and ph-value regulation during glutamic acid fermentation. *Bioprocess and Biosystems Engineering*, 12:231–238.

Namdev, P. K., Thompson, B. G., and Gray, M. R. (1992). Effect of feed zone in fed-batch fermentations of saccharomyces cerevisiae. *Biotechnology and Bioengineering*, 40(2):235–246.

Natarajan, A. and Srienc, F. (1999). Dynamics of glucose uptake by single escherichia coli cells. *Metabolic Engineering*, 1(4):320–333.

Natarajan, A. and Srienc, F. (2000). Glucose uptake rates of single e. coli cells grown in glucose-limited chemostat cultures. *Journal of Microbiological Methods*, 42(1):87–96.

Neubauer, P., Åhman, M., Törnkvist, M., Larsson, G., and Enfors, S.-O. (1995a). Response of guanosine tetraphosphate to glucose fluctuations in fed-batch cultivations of escherichia coli. *Journal of Biotechnology*, 43(3):195 – 204.

Neubauer, P., Häggström, L., and Enfors, S.-O. (1995b). Influence of substrate oscillations on acetate formation and growth yield in escherichia coli glucose limited fed-batch cultivations. *Biotechnology and Bioengineering*, 47(2):139–146.

Neubauer, P. and Junne, S. (2010). Scale-down simulators for metabolic analysis of large-scale bioprocesses. *Current opinion in biotechnology*, 21(1):114–121.

Nielsen, J. and Villadsen, J. (1992). Modelling of microbial kinetics. *Chemical Engineering Science*, 47(17-18):4225 – 4270.

Oseen, C. (1927). *Hydrodynamik*, volume 1. Akad. Verl.-Ges.

Overholt, M. and Pope, S. (1996). Direct numerical simulation of a passive scalar with imposed mean gradient in isotropic turbulence. *Physics of Fluids*, 8(11):3128–3148.

Overholt, M. and Pope, S. (1998). A deterministic forcing scheme for direct numerical simulations of turbulence. *Computers & Fluids*, 27(1):11 – 28.

Poe, G. and Acrivos, A. (1976). Closed streamline flows past small rotating particles: Heat transfer at high pï¿½clet numbers. *International Journal of Multiphase Flow*, 2(4):365 – 377.

Pohorecki, R. and Baldyga, J. (1983). New model of micromixing in chemical reactors. 1. general development and application to a tubular reactor. *Industrial & Engineering Chemistry Fundamentals*, 22(4):392–397.

Pohorecki, R. and Baldyga, J. (1988). The effects of micromixing and the manner of reactor feeding on precipitation in stirred tank reactors. *Chemical Engineering Science*, 43(8):1949–1954.

Pope, S. (2000). *Turbulent flows*. Cambridge Univ Pr.

Pumir, A. (1994). A numerical study of the mixing of a passive scalar in three dimensions in the presence of a mean gradient. *Physics of Fluids*, 6:2118.

Purcell, E. M. (1978). The effect of fluid motions on the absorption of molecules by suspended particles. *Journal of Fluid Mechanics*, 84(03):551–559.

Ramkrishna, D. (1979). Statistical models of cell populations. In *Advances in Biochemical Engineering, Volume 11*, volume 11 of *Advances in Biochemical Engineering/Biotechnology*, pages 1–47. Springer Berlin / Heidelberg.

Ramkrishna, D. (2011). The status of population balances. *Reviews in Chemical Engineering*, 3:49–95.

Ranade, V. (1997). An efficient computational model for simulating flow in stirred vessels: a case of rushton turbine. *Chemical Engineering Science*, 52(24):4473 – 4484.

Reuss, M. and Jenne, M. (1993). Compartment models. *U. Mortensen, & H. Noorman, Proceedings of bioreactor performance, Helsingor, Denmark*, 15:63.

Sawford, B. (1991). Reynolds number effects in lagrangian stochastic models of turbulent dispersion. *Physics of Fluids A: Fluid Dynamics*, 3:1577.

Schmalzriedt, S., Jenne, M., Mauch, K., and Reuss, M. (2003). Integration of physiology and fluid dynamics. In von Stockar, U., van der Wielen, L., Bruggink, A., Cabral, J., Enfors, S.-O., Fernandes, P., Jenne, M., Mauch, K., Prazeres, D., Reuss, M., Schmalzriedt, S., Stark, D., von Stockar, U., Straathof, A., and van der Wielen, L., editors, *Advances in Biochemical Engineering/Biotechnology*, volume 80 of *Advances in Biochemical Engineering/Biotechnology*, pages 19–68. Springer Berlin, Heidelberg.

Senn, H., Lendenmann, U., Snozzi, M., Hamer, G., and Egli, T. (1994). The growth of escherichia coli in glucose-limited chemostat cultures: a re-examination of the kinetics. *Biochimica et Biophysica Acta (BBA) - General Subjects*, 1201(3):424 – 436.

Singh, H., Fletcher, D. F., and Nijdam, J. J. (2011). An assessment of different turbulence models for predicting flow in a baffled tank stirred with a rushton turbine. *Chemical Engineering Science*, 66(23):5976 – 5988.

Squires, K. D. and Eaton, J. K. (1990). Particle response and turbulence modification in isotropic turbulence. 2(7):1191–1203.

Sreenivasan, K. (1995). On the universality of the kolmogorov constant. *Physics of Fluids*, 7:2778.

Sreenivasan, K. (1996). The passive scalar spectrum and the obukhov–corrsin constant. *Physics of Fluids*, 8:189.

Stokes, G. (1851). On the effect of the internal friction of fluids on the motion of pendulums.

Subramanian, G., Ramkrishna, D., Fredrickson, A., and Tsuchiya, H. (1970). On the mass distribution model for microbial cell populations. *Bulletin of Mathematical Biology*, 32:521–537.

Sundaram, S. and Collins, L. (1997). Collision statistics in an isotropic particle-laden turbulent suspension. part 1. direct numerical simulations. *Journal of Fluid Mechanics*, 335(75):109.

Taylor, G. (1922). Diffusion by continuous movements.

Tchen, C. (1947). *Mean value and correlation problems connected with the motion of small particles suspended in a turbulent fluid*. PhD thesis.

Thomson, N. and Ollis, D. (1980). Extracellular microbial polysaccharides. ii. evolution of broth power-law parameters for xanthan and pullulan batch fermentation. *Biotechnology and bioengineering*, 22(4):875–883.

Truesdell, G. C. (1993). *The interaction between decaying isotropic turbulence and dispersed solid particles*. PhD thesis, University of California, Irvine.

Truesdell, G. C. and Elghobashi, S. (1994). On the two-way interaction between homogeneous turbulence and dispersed solid particles. II. Particle dispersion. *Physics of Fluids*, 6:1405–1407.

Truskey, G. A., Yuan, F., and Katz, D. F. (2004). *Transport Phenomena in Biological Systems*. Pearson Prentice Hall Upper Saddle River, NJ, Upper Saddle River, 1st edition.

Villermaux, J. (1995). Future challenges in chemical engineering research: Chemical reaction engineering. *Chemical engineering research & design*, 73(2):105–109.

Villermaux, J. and Devillon, J. (1972). Représentation de la coalescence et de la redispersion des domaines de ségrégation dans un fluide par un modèle d'interaction phénoménologique. In *Proceedings of the 2nd International symposium on chemical reaction engineering*, pages 1–13.

Vlaev, D., Mann, R., Lossev, V., Vlaev, S., Zahradnik, J., and Seichter, P. (2000). Macro-mixing and streptomyces fradiae: Modelling oxygen and nutrient segregation in an industrial bioreactor. *Chemical Engineering Research and Design*, 78(3):354 – 362.

Vràbel, P., van der Lans, R. G., van der Schot, F. N., Luyben, K. C., Xu, B., and Enfors, S.-O. (2001). Cma: integration of fluid dynamics and microbial kinetics in modelling of large-scale fermentations. *Chemical Engineering Journal*, 84(3):463 – 474.

Warhaft, Z. and Lumley, J. (1978). An experimental study of the decay of temperature fluctuations in grid-generated turbulence. *Journal of Fluid Mechanics*, 88(04):659–684.

Warnaars, T. A. and Hondzo, M. (2006). Small-scale fluid motion mediates growth and nutrient uptake of selenastrum capricornutum. *Freshwater Biology*, 51(6):999–1015.

Wenger, K. and Dunlop, E. (1994). Coupling of micromixing, macromixing, and the glucose effect in continuous culture of saccharomyces cerevisiae. In *AIChE Symposium Series*, pages 166–166. American Institute of Chemical Engineers.

Wiskind, H. (1962). A uniform gradient turbulent transport experiment1based on a paper presented at the international symposium on fundamental problems in turbulence and their relation to geophysics sponsored by the international union of geodesy and geophysics and the international union of theoretical and applied mechanics, held september 4–9, 1961. *Marseilles, France., J. Geophys. Res*, 67(8):3033–3048.

Xu, B., Jahic, M., and Enfors, S.-O. (1999). Modeling of overflow metabolism in batch and fed-batch cultures of escherichiacoli. *Biotechnology Progress*, 15(1):81–90.

Yarin, L. and Hetsroni, G. (1994). Turbulence intensity in dilute two-phase flows. ii temperature fluctuations in particle-laden dilute flows. *International Journal of Multiphase Flow*, 20(1):17 – 25.

Yeung, P. (2001). Lagrangian characteristics of turbulence and scalar transport in direct numerical simulations. *Journal of Fluid Mechanics*, 427(-1):241–274.

Yeung, P., Sykes, M., and Vedula, P. (2000). Direct numerical simulation of differential diffusion with Schmidt numbers up to 4.0. *Physics of Fluids*, 12:1601.

Yeung, P., Xu, S., Donzis, D., and Sreenivasan, K. (2004). Simulations of three-dimensional turbulent mixing for schmidt numbers of the order 1000. *Flow, Turbulence and Combustion*, 72:333–347.

Yeung, P., Xu, S., and Sreenivasan, K. (2002). Schmidt number effects on turbulent transport with uniform mean scalar gradient. *Physics of Fluids*, 14:4178.

Yeung, G-J, P. and Pope, B. (1989). Lagrangian statistics from direct numerical simulations of isotropic turbulence. *J. Fluid Mech*, 207:531–586.

Yeung, P. K., Pope, S. B., and Sawford, B. L. (2006). Reynolds number dependence of Lagrangian statistics in large numerical simulations of isotropic turbulence. *Journal of Turbulence*, 7:58.

Yeung, P. K. and Zhou, Y. (1997). Universality of the kolmogorov constant in numerical simulations of turbulence. *Phys. Rev. E*, 56:1746–1752.

Yim, S. and Shamlou, P. (2000). The engineering effects of fluids flow on freely suspended biological macro-materials and macromolecules. In Schügerl, K., Kretzmer, G., Henzler, H., Kieran, P., Kretzmer, G., MacLoughlin, P., Malone, D., Schumann, W., Shamlou, P., and Yim, S., editors, *Influence of Stress on Cell Growth and Product Formation*, volume 67 of *Advances in Biochemical Engineering/Biotechnology*, pages 83–122. Springer Berlin / Heidelberg.

Zahradnik, J., Mann, R., Fialovà, M., Vlaev, D., Vlaev, S., Lossev, V., and Seichter, P. (2001). A networks-of-zones analysis of mixing and mass transfer in three industrial bioreactors. *Chemical Engineering Science*, 56(2):485 – 492.

Doctorat de l'Université de Toulouse

Délivré par l'**Institut National Polytechnique de Toulouse**

Ecole doctorale MEGeP
Spécialité Dynamique des Fluides
Soutenue le 06 décembre 2012
Marion Linkes

Simulation numérique et modélisation de l'assimilation de substrat par des microorganismes dans un écoulement turbulent.

Résumé Une des problématiques majeures dans l'industrie des bioprocédés réside dans l'extrapolation des procédés biologiques à grande échelle. On observe généralement à l'échelle industrielle des écarts de rendement de croissance de la biomasse, ainsi que la formation de sous-produits comparativement à l'échelle du laboratoire. Ces écarts sont en partie attribués à l'apparition de gradients de concentration en substrat à l'échelle des bioréacteurs. Mais à moindre échelle, le micro-mélange influence également la réaction biologique. En effet, les différents substrats sont assimilés à l'échelle des microorganismes. Une approche microscopique est donc choisie pour étudier l'influence des fluctuations vues par les microorganismes le long de leurs trajectoires. Un modèle couplant transport et assimilation à l'échelle d'un microorganisme est proposé pour de mettre en évidence l'apparition d'une compétition entre régime physique et biologique limitant l'assimilation du substrat par le microorganisme. La simulation numérique directe est ensuite utilisée pour caractériser un champ de turbulence homogène isotrope. Les effets des hétérogénéités de concentration vues par les microorganismes, suivi de manière Lagrangienne, sont étudiés sur l'ensemble de la population. On observe l'apparition de différents taux d'assimilation distribués sur l'ensemble des microorganismes. Une formule analytique, basée sur les distributions de concentration de substrat dans le fluide, est proposée. Un modèle métabolique explique les baisses de vitesse spécifiques de croissance, ainsi que la formation de sous-produits. Enfin, de premiers résultats sur le couplage inverse biologique sont présentés. L'effet des microorganismes sur le champ de concentration est caractérisé et une étude paramétrique sur les propriétés dynamiques et biologiques est réalisée.

Mots-clefs : *réacteurs biologiques, assimilation de substrat, microorganismes, simulation numérique, mélange, hétérogénéités.*

Numerical simulation and modelling of substrate assimilation by microorganisms in a turbulent flow.

Abstract: The scale-up of biological process is a critical issue in the bioprocess industry. When passing from a laboratory to an industrial scale, the conversion yields of substrate into biomass is often overestimated and by-products are formed. Different existing works attempt to predict the effect of mixing on biomass growth and the emergence of substrate concentration gradients at the reactor scale are a first explanation of the degraded performances. But, micro-mixing effects also impact the biological reaction. Indeed, the different substrates are assimilated at the microorganisms scale. Therefore a microscopic approach is chosen to study the influence of fluctuating events seen by microorganisms along their trajectories. A coupled transport-assimilation model is proposed for an isolated microorganism to evaluate the emergence of a competition between physical and biological limitations for assimilation. A second part of this work uses the direct numerical simulation approach to characterise a homogeneous isotropic turbulence field. The effects of local heterogeneities seen by microorganisms are addressed by discrete particle simulations and studied at the population scale. The heterogeneities lead to a distribution of assimilated rate over the microorganisms. The distributions are analytically derived from the substrate concentration in the domain, and explain the decreased specific growth rate, whereas by-products are formed. Then, first results on the biological two-way coupling are proposed. The effect of microorganisms on the substrate field is characterised and a parametric study on the dynamics as well as biological properties is realised.

Keywords: *biological reactors, substrate assimilation, microorganisms, numerical simulation, mixing, heterogeneities.*